NORTHWESTERN UNIVERSITY

Metal–Organic Frameworks as Well-Defined Crystalline

Heterogeneous Catalyst Supports

A DISSERTATION

SUBMITTED TO THE GRADUATE SCHOOL

IN PARTIAL FULFILLMENT OF THE REQUIREMENTS

for the degree

DOCTOR OF PHILOSOPHY

Field of Chemistry

By

Timothy A. Goetjen

EVANSTON, ILLINOIS

December 2022

Abstract

Industrial processes heavily rely on catalysts to control product selectivity and lower energy barriers required for chemical transformations. Catalysts are most commonly solid heterogeneous catalysts that facilitate separations from reaction mixtures and enhance recyclability. Heterogeneous catalysts used in industrial processes exhibit efficacious results, but in certain instances drawing structure-function relationships proves difficult. Without a clear picture of the catalytically active site structure, the exact mechanisms behind the observed catalytic results cannot be derived, which inhibits the development of next-generation catalysts.

Metal–organic frameworks (MOFs) are highly crystalline, porous materials constructed by organic linkers connected to metal nodes that self-assemble into multi-dimensional networks. Given their uniform structures and modular nature, MOFs are ideal materials as structurally well-defined catalysts or catalyst supports. MOFs have a wide variety of catalyst siting strategies including but not limited to 1) installation of active metal species at the metal oxide node *via* reactive hydroxyl and aqua ligands, 2) installation of active metal species into an organic structural linker, and 3) encapsulation of molecular or nanoparticle catalysts within the pores of the framework. Single crystals of certain MOFs can be grown and therefore catalyst structures can be determined at an atomic level by experimental X-ray diffraction measurements. Even bulk spectroscopic measurements become relatively easier to analyze when dealing with more structurally well-defined materials.

With the onset of increased availability of "wet" shale gas, hydrocarbon transformations combining small chain molecules rather than breaking down crude oil has received higher interest. Therefore, reactions involving carbon-carbon coupling have gained more interest, and the fundamental understanding of those reaction mechanisms is widely desired. In my research, I

aimed to develop MOF-supported catalysts for different carbon-carbon coupling reactions and take advantage of the structural uniformity of MOFs to build platforms to derive structure-function relationships wherever possible, to provide that knowledge for those who are developing next-generation catalysts.

Overall, this work advances the field of heterogeneous catalysis by providing structurally well-defined platforms for identifying trends in reactivity and selectivity in chemical transformations, including mechanistic studies. The knowledge gained and subsequent use of platform methodologies will funnel into the development of next-generation catalysts.

Acknowledgments

I have a great many people to thank for supporting me in my journey to this point, all of whom have led me to become the person/scientist I am today, and for that I am ever grateful. I also want to acknowledge how very fortunate I am to be in a position to be able to continue my education in a graduate program without additional obligations that would preclude me from pursuing my graduate degree. It is a privilege provided by many circumstances, for which I am very thankful. I'll try to organize my acknowledgments here in some chronological and/or geographical fashion, because that is how my brain is deciding to organize it for me, but it may just become a jumbled mess as I pour out my thanks for all those that have supported me over the years. Bear with me as I ramble in this non-scientific portion of writing.

Without a doubt, I would not be here today pursuing a passion for chemistry and research had it not been for Charles "Mr. Mac" McInerney of Somerville High School (SHS) in Somerville, NJ. I was fortunate to have him as a teacher for both Chemistry and AP Chemistry in my time at SHS, and through both classes he instilled a curiosity and a passion for chemistry that has burned in me to this day. He taught lessons creatively in such a manner that his excitement engaged the students, despite having done so for years prior, and supported us as we developed interest and passion for chemistry as a subject. Mr. Mac, thank you for inspiring me and being one of the best teachers I have ever had.

In the same vein I must thank Prof. G. Charles "Chuck" Dismukes for taking a chance on an inexperienced undergraduate student making his first foray into scientific research and providing a supportive environment to grow my passion for chemistry. Being in your lab, surrounded by a team of excited undergraduates and experienced graduate students and postdocs was a unique and fulfilling experience that led to my decision to pursue a Ph.D. in chemistry. Not

only was that the case, but also I would not be at Northwestern today if not for you. I remember going into your office with a list of schools I was looking to apply to, knowing I had a specific professor at Stanford in mind for whom I wanted to work, and asked you if you had any suggestions to add to the list. You recommended Northwestern and I took that advice, and I am forever grateful for that, because I would not trade my grad school experience for the world.

I would be remiss if I did not thank Dr. Karin U. D. Calvinho immediately after. Karin, you were the best mentor an undergraduate could ask for. Your unwavering support in the face of finicky electrochemistry and whatever troubles came my way was exactly what I needed. I am thankful every day that we got paired up when I was brought into the lab, and that we have continued to stay in touch even after I left Rutgers. Who would have thought that we would both end up at Argonne years later, for two different reasons, just one cubicle away from each other. You have treated me with nothing but respect and regarded me as an equal in the pursuit of scientific research. It was working with you, especially that summer during the Rutgers Energy Institute internship which gave me a peak into grad student life, that has led to where I am today.

Omar, thank you for providing a home for me in your research group as one of your first few students as you began your very successful independent career. Seeing your excitement for the science as you presented to us incoming first years during orientation is what drew me in to join your lab. You have provided me the opportunity to develop as an independent scientific researcher, for which I am grateful.

Joe, you have been such a kind and gracious mentor during my graduate studies. Your knowledge and wisdom have helped me many a time in adapting my approach to problems in both science and group interactions. Your positive attitude and calm demeanor is a force of good in the

scientific community and more specifically within your research group, a culture of which I am very fond and thankful to have been a part of.

Justin, thank you for being a genuine human being in all my interactions with you as a committee member and as part of the Catalysis Club of Chicago. I appreciate the advice you've given me and your willingness to just sit down with me for lunch and have a chat about careers.

Neil K., as a committee member you have been nothing but kind and engaging with me. I remember my quad chart meeting with you, where we had a very open and honest discussion about the research topics where I genuinely felt more like your colleague having a chat rather than a student pitching an idea. Thank you for providing that support.

Max, thank you for being my host scientist at Argonne and for allowing me to come into your group to conduct cutting edge research at a national lab. My experience for that year was one of a kind and I will always remember how welcoming you were and how willing you were to sit down and chat science with me as I drew upon your polymerization and catalysis expertise.

Jeremy, as my direct supervisor at Argonne, you took me under your wing to teach me all about a very complex analytical technique. I thoroughly enjoyed our time working together, including the countless hours at the APS trying to fit in all the experiments we wanted, and very much appreciate the time you spent teaching me and answering my many (probably repetitive) questions about working on my own data. I knew I enjoyed analytical techniques, but through working with you I found that it is in fact a passion of mine.

The rest of the Argonne National Laboratory (ANL) Catalysis group – Alon, Dave, Magali, Tabitha, Alejandra, Jess, Katie, Prajay, Jason, Jeff, Cong, Ted, Ryan, Robert, and Uddhav – I cannot express how thankful I am for how welcoming you all were when I joined the group for my year-long fellowship. I never felt like an outsider, the transition was natural, and I always felt

that I could ask anyone for help without a second thought. You all are a very talented and generous group of scientists that I am thankful to have had the chance to work with, however brief it was.

To all the staff of the core facilities at Northwestern University, you play a crucial role in research at NU and often go unacknowledged, or not nearly acknowledged as much as you should be. You have my thanks for any role you have played in aiding my work and all assistance you have provided me, from training to data analysis or collection. From IMSERC – Dr. Christos "Chris" Malliakas, Dr. Charlotte Stern, Dr. Saman Shafaie, Dr. Yuyang Wu, and Dr. Yongo Zhang. From KECK II – Dr. Xinqi Chen. From QBIC – Rebecca "Becky" Sponenburg. From REACT – Prof. Neil Schweitzer and Dr. Selim Alayoglu. For Neil and Selim – given the nature of my research you both played a significant role in providing me guidance and assisting with my research projects. Neil, your class prepared for a graduate school experience with catalysis research, and your calm and methodical approach to problems made you very easy to talk to and be someone to go to for advice. Selim, you always seem to have some knowledge of whatever experiment or measurement I am doing at the time, and always have an interest in it which leads to asking the right questions that get us down to the root of the matter.

Not only do the staff at the core facilities deserve praise, but so do those in non-technical positions within the Chemistry department who have supported me and others in their graduate careers. Sophie – thank you for being a constant in the department, for all you do to keep the department up and running, and for always being so excited to say hi in the hallway no matter what is going on. Mike – thank you for dealing with my numerous emails and phone calls when anything happened with the lab, it is truly impressive how you handle everything that is thrown at you and remain organized and calm. And of course, Jonathan, I cannot thank you nearly enough for the support you have provided to me. Being a person I can go to in order to vent about a tough day,

talk about the good times, or ask what exactly do I have to do to get this done, you know it all and what to say, and you keep us grad students sane and in good standing with Northwestern and the department.

To the students who have been involved with the student organizations I have had the fortune of being a part of, thank you for taking on an extra task to try to improve the graduate student experience and provide useful social and professional development opportunities. I thank both the members of the Graduate Liaison Committee and the board of Phi Lambda Upsilon – it has been a pleasure to work with you all. In addition to the students, thank you to Prof. Regan Thomson, who has been a staunch advocate for the students and voice of the students by bringing concerns and solutions to the faculty and department admin.

To the Farhomies and Huppsters both current and past – I chose the two groups not only for the mentors but also for the people they surrounded themselves with. While every day in grad school and research is not easy, having supportive and encouraging colleagues makes it just that little bit easier. There are too many of you to name individually, but there are those who helped me at the start – Louis, Hyun, Zhanyong, Riki,, Lee, and Aaron – I am grateful for your support and for you not judging me as I fumbled my way through the start of grad school. Kaikai and Xingjie, no matter what you always have positive attitudes and have always been quick to call me kind – this has meant the world to me. In the recent years with my newer officemates – it has been a pleasure to chat and make coffee and work each day alongside you. Thank you to everyone and thank you to all of the Farhomies and Huppsters that have become my dear friends – Flo, Zoha, Kira, Madeleine, Courtney, and Kent. At the heart of the groups there is kindness and empathy that drives everyone to work together to accomplish great things. Please hold on to that feeling, that empathy for others and team spirit to work together. Science is never a solitary endeavor, even

though at times grad school feels that way. Give each other the benefit of the doubt and try not to get too annoyed when someone is making an adjustment to interacting with the group. I would remiss if I did not talk about seal frits and sorption common supplies - while I may have sent a record number of emails about seal frits and sorption common supplies, something I certainly will not miss, there have been fewer as of late as we all work together to share and give everyone's work priority, not just our own.

Friends I have made in grad school, whether in passing or from the very beginning, thank you for providing me with a support system outside of the lab. From going on an adventure to a magic show in downtown Chicago one of my first few days here to now sitting in at your defenses and watching what brilliant scientists you have grown to become; I am proud to call you all my friends.

Peter, Jon, Jenny, Nils, and many more – I appreciate you and your friendship in my early years and know that you will accomplish great things moving forward.

Sylvia and Wassy – from the jokes about NJ or Pittsburgh to watching really ridiculous reality television together during happy hours, you two have been a source of support and friendship that have made my time in Evanston all the better. I am so happy you have been a part of my scientific and personal life, and that I got to grow through grad school with you.

Meghan and Cory – Thank you for being two of the kindest human beings on the planet. You both are two of the most genuine people I know, and I am thankful to have become your friend. I am also so happy that you both welcomed Kim into our little crew after having only met her I think the one time. I am excited to see you both go on to the next adventure in Memphis and I know both Kim and I look forward to the next time when the four of us can get together to watch another baseball game.

Kenton and Craig – I took a chance in choosing to live with people I didn't really know at the start of grad school and wow am I glad I did. I never expected at the start for us to live together for the majority of our grad school careers, but it was an absolute pleasure. I owe my sanity to you both as I navigated the beginning of grad school and a long-distance relationship. Craig – from random conversations to playing board games at home, you made my first few years happier, thank you. Kenton – you have always been a hype-man for me no matter what and that support means the world to me.

Waleed – though we have drifted to not hanging out as often or being in touch as much lately, seeing you the other day twice felt like no time had passed. Because of this I know we will remain friends and I hope that we get the chance to live in the same area again soon.

Rodrigo – your humor, your friendship, your willingness to be up for anything, and of course recently your proclivity to convince me to take (needed) breaks in work have been a constant in my life for my time in grad school and now especially the past two years living with you. Thanks for dealing with all of me, I know I am not always easy – I wouldn't want to trade away our time together for anything.

My friends from undergrad at Rutgers, I thank you for understanding the times I could not come visit or that I could only do so for a short period of time as I worked through grad school, especially those who happened to be in Chicago – Sweta and Ali. Hopefully now that I am getting closer to the East coast I can pop by NYC more often and take trips out to Colorado. Thank you for making it seem like no time has passed when I visit for the first time in a couple years when I am at a conference. There are many of you to name, but thank you – Hai-Kinh, Ariel, Ashni, Anish, Michelle, Alex, Charlie, and many more.

To my friends from back home, you've known me the longest and have stuck with me this far, even as I grew distant with being busy with grad school. Thank you for all the support you've given me, through sharing memes on Instagram, burning off steam playing video games, and just being there to talk. Thank you Mike, Elliott, and Sarah. You are most definitely my friends for life.

To the Parker/Pindar families – your acceptance of me from the very start of me dating Kim has seen my family double and then some. My heart is full with the support you all have provided. You have made me feel at home with you all these past almost eight years, which somehow manages to feel like it has been my whole life.

To my extended family – thank you for being there when I have the free time to visit and for understanding when I couldn't make the trip. I look forward to a more balanced work life that allows me to stop by more often, not just for the weddings and big events like that.

To my brother, Mike, someone who understands the pressures of the Ph.D. degree the most, thanks for understanding everything. I love how much closer we have gotten in recent years and that we manage to find time for each other to play games and catch up – I promise that will happen more again after the defense. I am so proud of you for making the journey to achieve your Ph.D. and am so very excited to share the Dr. Goetjen title with you. I love you.

To my Mom and Dad, I would not be here without your support. From raising me to be the man I am today, to providing me with the guidance to pursue the career I desire, no matter what – thank you. I am so very thankful to have you two as my parents and in my corner every day. I aspire to be as kind and caring as parents as you have been. From Mom teaching me a love for reading and learning through books to Dad finding old electronics for us to take apart together (and never put back together), you both supported my education and inquisitive spirit from a very

early age. Learning was obviously important to you and that drove me to learn as much as I could. I swear aiming for the Ph.D. was not just to one-up both of you, but in fact for my love of chemistry. I cannot thank you enough for always being there for me no matter what. I love you both, always.

Last, but most certainly not least, Kim, my rock and unwavering supporter. Never in a million years could I have imagined I would find a lifelong partner in undergrad, much less one who was also going to pursue a Ph.D. and be able to understand the level of commitment involved in science-based grad school. I know these past five years of long-distance have been anything but easy or perfect. We've had good times and bad, but throughout all of it we have understood that we are partners as well as individuals. Tackling problems together as a team is what makes relationships strong, and I think that mindset is one of the reasons we both have stuck together through the tough times. You have seen me grow and change as a scientist and person. You have been there for me through the times when I am not the easiest person to support, when the job hunt is not going well or my experiments are just not cooperating – I appreciate you. I also appreciate the many Snapchats of our cats and their quirky behavior – making me smile even on days I might not want to. You have certainly made this dog person turn into a cat person as well, loving them as much as you do. You are my ultimate hype-person, the person who always has my back, and my very best friend. I could not have made it through this Ph.D. without you. I cannot wait to move to Cleveland to live with you and start the next chapter of our lives together. I love you to the moon and back.

Table of Contents

List of Figures

List of Schemes

List of Tables

Chapter 1. Introduction

Portions of this chapter appear in the following manuscripts:

Goetjen, T. A.; Liu, J.; Wu, Y.; Sui, J.; Zhang, X.; Hupp, J. T.; Farha, O.K., Metal–Organic Framework (MOF) Materials as Polymerization Catalysts: A Review and Recent Advances. *Chem. Commun*. **2020**, *56*, 10409-10418.

Liu, J.; **Goetjen, T. A.**; Wang, Q.; Knapp, J. G.; Wasson, M. C.; Yang, Y.; Syed, Z. H.; Delferro, M.; Notestein, J. M.; Farha, O.K.; Hupp, J. T., MOF-Enabled Confinement and Related Effects for Chemical Catalyst Presentation and Utilization. *Chem. Soc. Rev*. **2022**, *51*, 1045-1097.

Liu, J.; Yang, Y.; **Goetjen, T. A.**; Hupp, J. T., Carbon-Efficient Conversion of Natural Gas and Natural-Gas Condensates to Chemical Products and Intermediate Feedstocks *via* Catalytic Metal–Organic Framework (MOF) Chemistry. *Energy Environ. Sci*. **2022**, *15*, 2819-2842.

1.1 Chapter Summary

Heterogeneous catalysts serve to lower the energy input needed to attain a chemical transformation, or to alter the product selectivity towards the desired product(s). While current industrial catalysts serve to enable these efficient transformations, they suffer from drawbacks such as a lack of structural uniformity which inhibits deriving structure-function relationships that lead to the development of next-generation catalysts. The precise synthetic control over chemical functionality and crystalline structural order offered by metal–organic frameworks (MOFs) make them ideal scaffolds for systematically investigating structure-function relationships in heterogeneous catalysis. Herein, I highlight the benefits of heterogeneous catalysts in industrial processes, currently implemented catalysts and their drawbacks, metal–organic frameworks (MOFs), and the increasing interest for chemical transformations related to shale gas conversion. I also introduce the methods I employed throughout my thesis research to study MOF-supported catalysts and their structure-function relationships, including crystallographic and *operando* spectroscopic studies.

1.2 Relevance of Heterogeneous Catalysts

The impact of catalysis in chemical industry is immense. Chemical industry produces a wide variety of products that are essential feedstocks for many other industries including those in the manufacturing and transportation sectors. These products feed into supplies or packaging for food, technology, medicine, and much more. The economical production of these materials, through both energy input and product selectivity metrics, is needed to ensure affordability of manufacturing and consumer goods. In the past 100 years, the use of catalysts in industry has grown, with more than 85% of chemical processes utilizing at least one catalytic step. Of those catalytic steps, approximately 80% use heterogeneous catalysts.[1]

Heterogeneous catalysts have been employed because it was found that supporting active metals on a solid material not only made the catalyst more active and stable, but also lowered the price of the final product and facilitated catalyst recycling. They are actively used in a wide variety of industrial processes including Fischer-Tropsch (syngas to hydrocarbons),[2] Haber-Bosch (ammonia synthesis),[3] and Phillips (ethylene polymerization).[4] Without any of these processes, which rely on heterogeneous catalysts, life as we know it would be drastically different.

1.3 Drawbacks of Current Heterogeneous Catalysts

Obviously, given the rich history and impetus for innovation, great strides have been made in the development of heterogeneous catalysts. Yet, the elucidation of mechanisms and active site structures often take decades of painstaking research to identify.[5-6] Perhaps one of the most commonly known industrial-scale catalysts is the heterogeneous Cr-based Phillips catalyst; it accounts for ca. 50% of global PE production.[7] However, due to the amorphous nature of the catalyst's SiO_2 support, the precise chemical identity of the active species and the mechanism of its action are still debated.[6] The absence of this kind of information, unfortunately, is inhibitory toward scientific-hypothesis-based advancement and development of catalysis science. Clearly desirable for fundamental studies are chemically and structurally well-defined supports and, where possible, equally well-defined catalyst active sites. Therefore, there is a need to develop such platforms and methodology that allows for the uniform deposition of catalytic sites and subsequent atomic level interrogation of catalyst structures which enables the determination of structure-function relationships.

1.4 Metal–Organic Frameworks as Catalysts and Catalyst Supports

MOFs are typically crystallographically well-defined, and microporous, mesoporous, or both.[8] At a minimum, they comprise multitopic organic linkers and metal-containing inorganic

nodes, inter-connected in alternating fashion by coordination bonds. Nodes can consist of single metal ions, pairs of metal ions, linker-isolated metal-ion-containing clusters, or shared-linker-terminus-connected one-dimensional rods; see **Figure 1.1**. Periodically arranged linkers and nodes can yield uniform arrays of pores that are interconnected at the pore-to-pore level by apertures that are similarly uniform. Relevant to heterogeneous catalysis, pores and apertures are often of molecular width. Pores can take the form of distinct cages; channels extending in 1, 2, or 3 directions; pillaring-linker-defined spaces between two-dimensional sheets; or other constructs, see **Figure 1.1**.
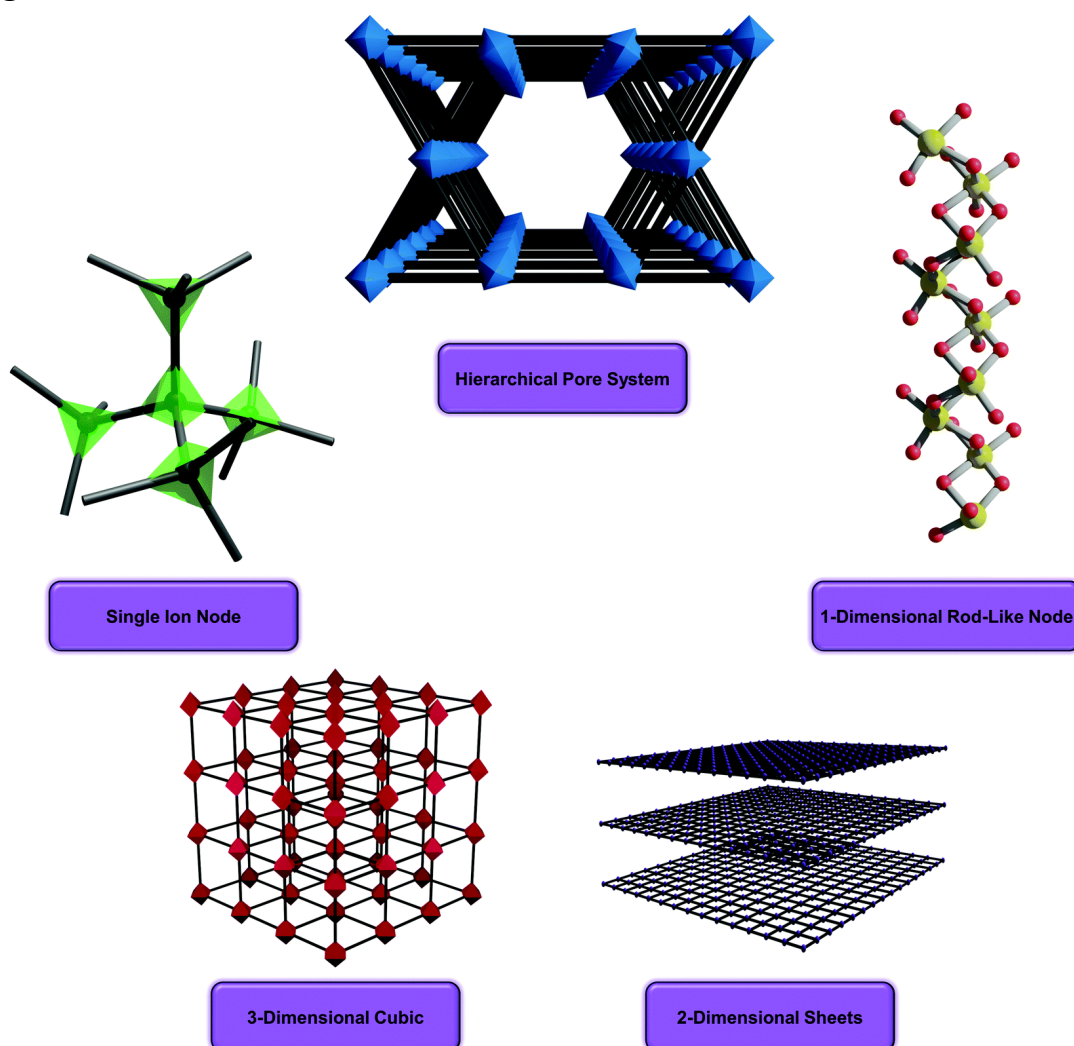
Figure 1.1 Representative MOF and MOF-component archetypes: ZIF-type single-atom-node architectures, 1D channel with rod-like structures, 2D layered dimensions, 3D cubic structures with high porosity and metal-cluster nodes, and hierarchical porous topologies.

Tens of thousands of MOFs have been described experimentally, with a couple orders of magnitude more having been virtually screened computationally.[9-10] Roughly five thousand experimental examples have been curated and then described in terms that facilitate their computational or experimental evaluation regarding pore volume, pore size, gravimetric or volumetric surface–area, density, node accessibility, pore-connectivity, approximate topology, and so on.[11] Many are potentially suitable for broad application in heterogeneous catalysis,[12] but the suitability of a particular MOF for heterogeneous catalysis is reaction-specific. To generalize, however, useful MOFs for heterogeneous catalysis will offer: (a) molecular-scale porosity,[13] (b) good chemical stability toward exposure to H_2, O_2, H_2S, H_2SO_4, HX, NH_3, H_2O_2, N_2O, hydroxide, steam, and/or condensed water,[14] (c) good thermal stability,[15] (d) good mechanical stability, including stability toward solvent evacuation and associated capillary forces,[16] (e) overall crystallinity, and (f) uniformity of active-site composition and structure, even at the scale of single atoms.

Good to excellent thermal stability for MOFs translates as sustained retention of framework crystallinity and porosity (days or weeks) at 350 or 400 °C. We can conclude then that MOFs are best viewed as complementary to zeolites, high-surface-area metal-oxide powders, and related materials, as catalysts or catalyst supports, as MOFs are ill-suited for reactions at temperatures more than a few hundred degrees above room temperature. Nevertheless, it is remarkable that frameworks consisting largely of hydrocarbon linkers can be usefully deployed as catalysts or catalyst supports for substrate oxidation by O_2 at a few hundred degrees Celsius without being lost to combustion. MOF-catalyzed oxidative dehydrogenation of propane to propene at 230 °C[17] and cyclohexene to benzene at 350 °C[18] are two such examples.

As shown qualitatively in **Figure 1.2**, depending on the identity of the MOF, active-sites for heterogeneous catalysis can consist of functionalized linkers, coordinatively unsaturated metal ions on nodes, enshrouded nanoparticles, noncovalently linker-adhering polyoxometalates, non-structural ligands such as metal complexes intentionally grafted after framework synthesis, or node-grafted metal ions, metal-oxy clusters, metal-sulfide clusters, or other species.[19-28] Thus, the MOF itself can be viewed as either a catalyst or a catalyst support. Relevant to catalytic chemistry, commonly encountered support-like nodes are hexa-zirconium(IV) species having a core structure of $Zr_6(\mu_3\text{-}O)_4(\mu_3\text{-}OH)_4$. The node can accommodate up to twelve linker-terminating carboxylate groups, and MOFs are known with 4-connected,[29] 5-connected,[30] 6-connected,[31] 8-connected,[32] 9-connected,[33-34] and 10-connected nodes,[35-36] in addition to nominally 12-connected nodes.[37] Connection sites not occupied by linker carboxylates are typically occupied by non-structural ligands and/or terminal aqua/hydroxo pairs.[31, 38-39] These ligands, together with bridging hydroxo ligands are ideal for grafting metal-ions or clusters. If these ligands are displaced by candidate reactants or removed thermally, the underlying metal(IV) sites can function as Lewis acids,[40-42] or, in the case of displacement by sulfate, nodes can be made highly Brønsted-acidic.[43-45]
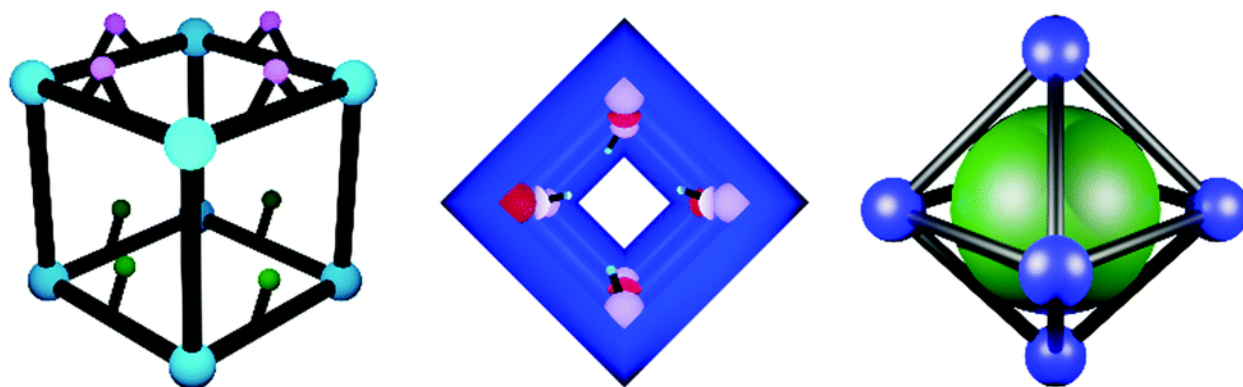
Figure 1.2 Representation of modes of use of MOFs as catalysts or catalyst-supports, including linker-supported catalysts (left), nodes as catalysts or node-supported catalysts (middle), and MOF encapsulated or enshrouded nanoparticles (right).

Thus, nodes within MOFs of this kind can be viewed as tiny pieces of zirconia or other metal-oxides having well-defined and uniform composition.[46] In many cases the uniformity translates into atomically precise single-crystal X-ray diffraction (SCXRD) structures featuring subsequently grafted catalytic ions and clusters.[21, 26, 44, 47-58] In a few cases, SCXRD measurements reveal how a grafted catalyst evolves over the course of catalytic runs, or changes in response to catalytically relevant thermal or chemical pre-treatment.[57, 59] Analogous core structures and support behavior have been described for hafnia-, ceria-, and thoria-like fragments/nodes[21, 49, 60-61] and for nodes featuring twelve rather than six M(IV) ions.[62-63] For less oxophilic metals in lower oxidation states, stable frameworks can often be obtained by enlisting anionic nitrogen ligands, such as di-, tri-, or tetra-azolates, as linkers.[64-65]

A mechanistically useful feature of linker-isolated nodes is their propensity to block node-to-node migration and sintering of grafted ionic catalysts – for example, metal ions or metal-ion-containing clusters.[36, 53, 55, 66-69] This behavior contrasts with the typical behavior of metal-oxide powders as supports; the absence of migration and sintering is potentially quite powerful for answering questions relating to the effects of metal-nuclearity in defining catalytic activity and selectivity, and for distinguishing between mechanisms for catalyzed reactions.[70-71] As structural understanding of MOFs continues to increase and synthetic techniques become more sophisticated, we will be able to better target ideal MOF structures and identify active species. Ideally this will drive a deeper mechanistic understanding of catalytic reactions with respect to catalysts on amorphous supports in an effort to provide fundamental understanding that feeds into the development of next-generation catalysts.

1.5 Shale Gas Conversion

Early in this century a convolution of technological, political, and economic considerations kicked off, in North America, a tremendous acceleration of the pace of fracking-based extraction of shale-trapped natural gas from known enormous reserves; see **Figure 1.3**. The scale of the still ongoing extraction was sufficient to shift the United States from being a massive importer to a net exporter of fossil fuels. Furthermore, the extraction accelerated the decommissioning of coal-fired electrical power plants and their replacement by gas-fired plants and renewable sources. It also led to: (a) large regional economic dislocations, both positive and negative, in the extraction sector of the U.S. economy, (b) a net reduction in the cost of electrical energy and in the cost of gas-based heating, (c) more efficient combustion-based production of electrical energy, and consequently, a diminished output of CO_2 per unit of electrical power, and (d) an attenuation of other environmental burdens associated with burning coal, including release of heavy metals, oxy-sulfur compounds, and aerosols, and generation of thorium-contaminated fly-ash as a combustion residue.[72] It has been suggested that while combustion of natural gas produces CO_2, its use could prove to be a beneficial transitional step toward net-zero carbon emissions – pending the build-out of renewable energy production capacity and attendant energy storage capabilities, together with economical carbon-capture and -sequestration.

U.S. dry shale gas production
billion cubic feet per day
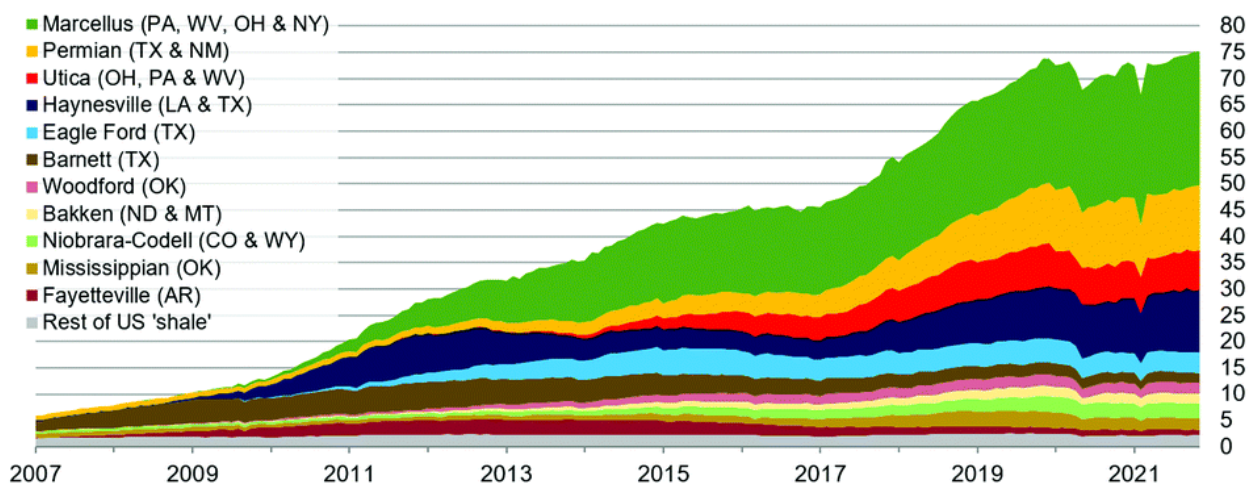
Figure 1.3 The production of shale gas in the U.S. Source: EIA (2021).

Curiously, a mid-century net-zero carbon emission scenario will not end the extraction of fossil hydrocarbons. Remaining will be a sizable need for hydrocarbons as feedstocks for commodity chemicals destined for transformation into polymers and other value-added chemicals, *i.e.* consumption unrelated to the use of hydrocarbons as fuels. In this realm, the realization of economical extraction of large quantities of natural gas has already resulted, in North America, in extensive replacement of oil by natural gas as a chemical feedstock; see **Figure 1.4**.[73] Thus, the focus has shifted away from the breakdown of large-hydrocarbon components of crude oil into manufacturing-relevant intermediates, such as naphtha (saturated C_5 to C_{10} mixtures), and toward the build-up of natural gas into manufacturing-relevant intermediates. Notably, shale-derived natural gas, especially from the enormous Marcellus formation, is wet gas – meaning that in addition to methane, it comprises significant fractions of ethane, propane, and butane. Since even ethane, with a critical temperature of 305 K, is liquefiable at room temperature (albeit, only at

pressures approaching 50 bar), ethane, propane, and butane are sometimes termed natural-gas

liquids, while propane and butane are also termed condensates.
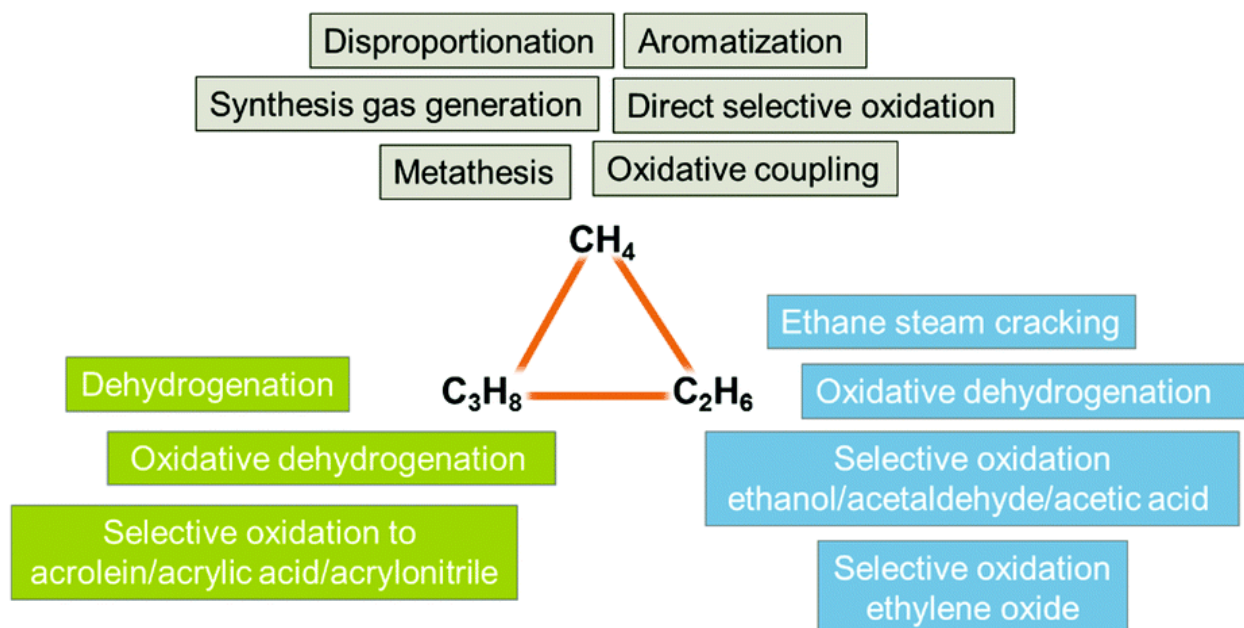
Figure 1.4 Potential approaches to converting methane and light alkanes, the major component of natural gas, into other valuable products. CH_4 = methane, C_2H_6 = ethane, and C_3H_8 = propane.[73]

1.6 Outlook for Future Development of Next-Generation Catalysts

The shift from oil to natural gas has transformed the chemistry, and especially the catalytic

chemistry, of commodity chemical manufacturing. To oversimplify, the breakdown of crude oil

starts with energy-intensive separations, typically distillations, and is followed by high-

temperature cracking that converts the heaviest and longest components into lighter hydrocarbons.

The common catalysts are zeolites or other alumino-silicates.[74] The harsh conditions for cracking

more-or-less guarantee that: (a) catalysts will be "nonuniform" (catalyst evolution or aggregation),

(b) catalyst active-sites will be difficult to identify and characterize with atomic-scale precision,

and (c) catalyst structures will evolve both with time-on-stream and with regeneration. In contrast,

the conditions associated with build-up of useful intermediates from C_1, C_2, C_3, and C_4

hydrocarbons typically are much less harsh, the reactive mixtures are less complex, and the

required thermal energy input is less.[75] These are conditions that hold out the possibility of full characterization of catalysts; *operando* observation of catalyst interactions with reactants, intermediates, and products; and *operando* observation and subsequent mechanistic understanding of the chemical and structural evolution of catalysts. More realistically, they hold out these promises for functional model systems, such as metal–organic frameworks, that have sufficient stability for such investigations, even if they lack the stability needed for extended, practical utilization. To the extent that these promises are realizable, they may enhance hypothesis-driven design and understanding of heterogeneous catalysts at the atomic or near-atomic scale. In turn or in parallel they can empower both the explanative and predictive capabilities of contemporary computational chemistry. Obviously, the application of computational chemical tools to experimental heterogeneous catalysis becomes much more useful when catalysts are compositionally and structurally uniform, when the compositions and structures are known, when their evolution over time can be accurately followed, and when the corresponding catalyst-synthesis chemistry is well enough developed for desired new or modified catalysts and supports to be realizable experimentally.[76]

1.7 Thesis Outline

The work described in this Thesis involves the synthesis, characterization, and catalytic evaluation of catalytic metal species deposited into a MOF. Focused on generating well-defined structures that otherwise could not be uniformly prepared on traditional amorphous supports, the work presented here takes advantage of using MOFs as a crystalline support to make unique structures that are competent catalysts for gas-phase carbon-carbon coupling reactions. The primary reactions of focus are ethylene oligomerization (used for the generation of liquid hydrocarbon fuels), ethylene polymerization (used for the generation of polyethylene plastics), and

acetylene dimerization (used to generate "green oil" products such as 1,3-butadiene for adhesives and rubber).

Chapter 2 demonstrates the solvent-based installation of a Cr-based single-site catalyst at the Zr_6 node of NU-1000, termed Cr-SIM-NU-1000. Careful structural characterization, including the synthesis of catalyst single crystals and the collection of X-ray diffraction data leads to developing an atomic-level picture of the as-synthesized catalyst. Ethylene oligomerization reactivity is then screened, providing activity and selectivity information for the well-defined catalytic system.

In Chapter 3, the limits of X-ray diffraction on single crystal MOF systems are explored further by collecting data and solving the structure of NU-1000 single crystals after Cr deposition and treatment with the necessary diethylaluminum chloride (DEAC) co-catalyst. The DEAC treated MOF-supported Cr catalyst, DEAC@Cr-SIM-NU-1000 is then employed for ethylene polymerization yielding linear high-density polyethylene in the manner of a single-site catalyst, providing a well-defined platform for further systematic studies in modulating catalyst environment and identifying the effect on polymer properties.

Chapter 4 seeks to provide further understanding of the structural evolution of DEAC@Cr-SIM-NU-1000 under reaction conditions. Taking DEAC@Cr-SIM-NU-1000 to a synchrotron source, *operando* X-ray absorption spectroscopy data is collected under exposure to high-pressure ethylene. The catalyst structure, compared to the co-catalyst pre-treated single crystal structure remains the same after ethylene exposure, confirming active site structure of the catalyst. A kinetic study was also performed to enhance mechanistic understanding of the catalyst system having filled out the details of the structural characterization.

In Chapter 5, a different catalyst system, copper nanoparticles confined with the pores of NU-907 is modified by the addition of cationic indium as a promoter. The copper nanoparticles

were structurally characterized by X-ray absorption and infrared spectroscopies before being utilized for acetylene dimerization. The cationic indium served to enhance the overall production of 1,3-butadiene, a desired commodity chemical in the rubber and adhesives industries.

Chapter 2. Metal–Organic Framework Supported Single Site Chromium(III) Catalyst for Ethylene Oligomerization at Low Pressure and Temperature

Portions of this chapter appear in the following manuscript:

2.1 Chapter Summary

A chemically and thermally stable, mesoporous, crystalline metal–organic framework, NU-1000, serves as a structurally well-defined support for catalytic reactions. Depositing chromium(III), a metal widely used in homogeneous ethylene oligomerization catalysts, onto the Zr_6 node of NU-1000 allows for the atomically precise determination of the structure of the Cr^{3+} catalyst through single-crystal X-ray diffraction studies. Chromium modification of NU-1000 was accomplished via solvothermal deposition in MOFs (SIM); termed Cr-SIM-NU-1000, the elaborated material features individual Cr atoms directed in single-site fashion into the mesopore of NU-1000. It was found that NU-1000 serves to stabilize the catalyst against both the typical chemical deactivation of homogeneous systems and leaching from heterogeneous systems. Cr-SIM-NU-1000 exhibits superior catalytic activity, as compared to Cr_2O_3, for ethylene oligomerization, with 20% conversion at a turnover frequency of about $60 \ h^{-1}$ and products ranging from C_8–C_{28}. Given that this catalysis occurs at low temperature (ambient) and low pressure (1 bar C_2H_4), along with minimal quantity of cocatalyst, the high activity shown by Cr-SIM-NU-1000 enables significant reduction in materials usage and waste. Postcatalytic characterization reveals Cr-SIM-NU-1000 remains intact with no leaching under the reaction conditions.

2.2 Utilization of Natural Gas Components as a Chemical Feedstock

With its recent declining cost, natural gas has garnered increased attention as a more efficient resource for generating electricity than coal, including a reduction in harmful emissions.[77] However, the infrastructure to convert and/or transport the highly abundant resource is lacking, therefore obligating flaring at the mining source, which results in unnecessary combustion of 140 billion cubic meters of potential methane fuel and generation of atmospheric CO_2 each year.[78] Crude oil is used instead and is distilled into shorter-chain hydrocarbons for use in naphtha[79] (C_5–

C_7), vehicle fuel[80-81] (C_5–C_{11}), jet fuel[82] (C_{10}–C_{18}), diesel fuel[83] (C_{12}–C_{24}), and lubricating oil[84] (C_{10}–C_{30}); however, natural gas remains largely underutilized as a feedstock for these valuable fuels and chemicals.[85] Thus, conversion of natural gas to liquid or oil facilitates its transport.

Composed primarily of methane (60–90%) and ethane (0–20%), natural gas is predominantly converted to liquid fuel via oligomerization of short-chain carbon molecules into long-chain molecules (>C_6). Additionally, dehydrogenation of natural gas yields ethylene, an ideal starting reagent in the synthesis of longer chain liquid hydrocarbons.[86] The promise of efficient conversion of natural gas to liquid hydrocarbons underscores the potential practical value of designing, interrogating, and understanding the behavior of structurally well-defined catalysts for alkene oligomerization. Molecular chromium(III) complexes have proven to exhibit high activity and selectivity,[87-88] but catalyst deactivation is common.[89] Current industrial catalysts, such as the Cr-based Phillip's catalyst, for ethylene oligomerization or polymerization, often utilize traditional solid-phase supports, such as silica.[7, 90] Although heterogeneous support of metal-atom-containing catalysts facilitates separation of catalysts from products, standard supports, such as silica, often lack homogeneity, resulting in nonuniform spatial distribution of catalyst sites and, because of sintering, nonuniform catalyst cluster or particles. Additionally, conventional supports are typically not amenable to characterization by single-crystal X-ray diffraction and therefore incomplete structural characterization inhibits our understanding of the mechanism by which the catalysts function.

2.3 Metal–Organic Frameworks as Well-Defined Catalyst Supports

In contrast to traditional porous oxide supports, porous metal–organic frameworks (MOFs) are highly crystalline. Furthermore, many present, as inorganic structural nodes, well-defined and chemically accessible, periodic arrays of metal–oxide clusters. Thus, these highly porous materials

are, in many respects, ideal model scaffolds/supports for heterogeneous catalysts.[91-92] Notably, MOF crystallinity facilitates atomic scale characterization and mechanistic investigations by single-crystal X-ray diffraction.[14] Recently, MOF supports have been shown to stabilize homogeneous catalysts and eliminate the need for expensive separations when used in heterogeneous systems.[93] The variety of MOF building blocks available affords the realization of materials with an expanse of physical properties and chemical functionalities. Postsynthetic modification strategies employing vapor and liquid-phase techniques have been reported to deposit metals and install or exchange ligands.[48, 94-95]

NU-1000, a Zr-based MOF composed of eight-connected $Zr_6(\mu_3\text{-O})_4(\mu_3\text{-OH})_4(H_2O)_4(OH)_4$ nodes and tetratopic 1,3,6,8-(*p*-benzoate)pyrene (TBAPy) linkers (**Figure 2.1**), has proven to be a suitable support for catalysis due to its 31 Å diameter mesopores that allow for facile substrate diffusion as well as its high chemical and thermal stability.[96] The spatial distribution of the metal nodes allows for postsynthetic modification to develop uniform single-site and/or single-metal-atom catalysts.[59, 67] Metalation of the NU-1000 Zr_6 nodes can be accomplished *via* vapor-phase atomic-layer deposition in MOFs (AIM)[94] or the analogous condensed-phase solvothermal deposition in MOFs (SIM).[59]

In this work, we present a unique ethylene oligomerization catalyst, stabilized on the metal–organic framework, NU-1000. NU-1000 modified with Cr^{3+} serve as the support and catalyst, respectively. Providing more accessible active sites due to the porosity of the framework, catalyst activity is increased, thus reducing the necessary partial pressure of ethylene from 30 to 50 bar[97-98] to only 1 bar. In addition, the catalyst is sufficiently active at ambient temperature, whereas industrial catalysts are generally not active or selective until 80–110 °C.[90] Contributing to the reduction in resource usage and waste through low pressures and temperatures, the quantity of

aluminum cocatalyst is also drastically reduced, requiring only 3 mol Al:1 mol Cr while comparable systems go as high as 500 mol Al:1 mol Cr.[97, 99] By drastically decreasing the reactant partial pressure and cocatalyst amount, along with being able to operate at ambient temperature, Cr-SIM-NU-1000 represents an active, attractive, and functional model system for investigating chromium-catalyzed ethylene oligomerization.
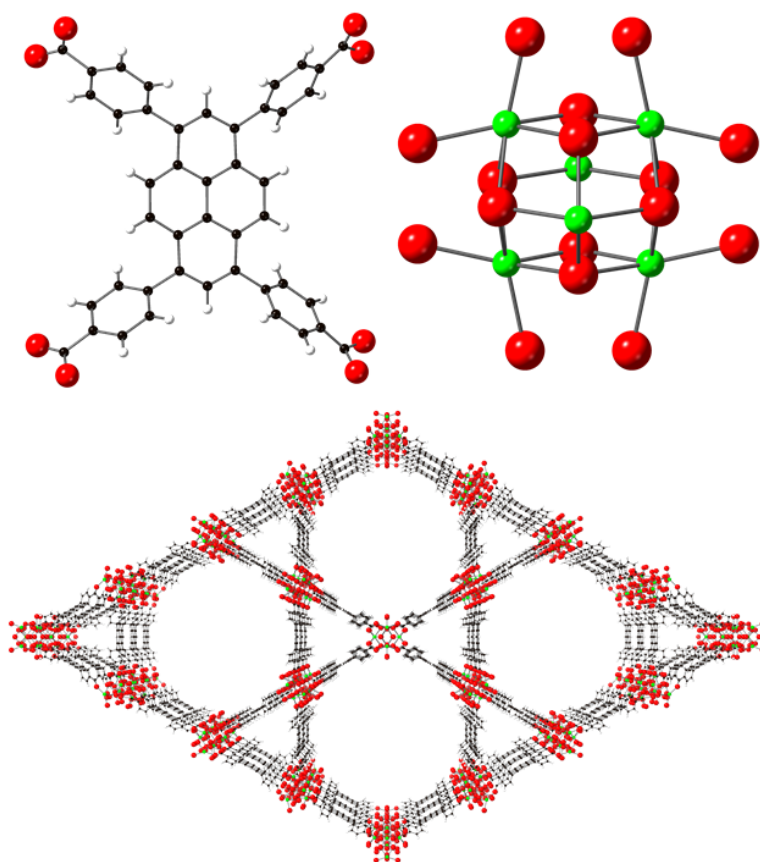
Figure 2.1 Structural representation of the Zr_6 node (right) and pyrene-based linker (left) of NU-1000 (bottom). Zr (green), O (red), C (black), H (white). Hydrogens omitted on the node for clarity.

2.4 Deposition of Chromium on MOF Support and Bulk Characterization

Cr-SIM-NU-1000 was prepared by the SIM method, where the chromium dichloride (initially Cr (II)) reacts with bridging oxo and terminal aqua and hydroxo groups on the Zr_6 node of NU-1000. A distinct color change from yellow to green was observed after the SIM process. After sufficient washing with *N,N*-dimethylformamide (DMF) and acetone to remove excess unreacted Cr, Cr loading was determined, via inductively coupled plasma optical emission spectroscopy (ICP-OES), to be 1.4 ± 0.1 Cr per Zr_6 node. Powder X-ray diffraction (PXRD) data confirm that the support remains crystalline after metalation (**Figure 2.2**). Scanning electron microscopy (SEM) images of the material show retention of the morphology and physical characteristics of the NU-1000 crystallites, while energy-dispersive spectroscopy (EDS) indicates uniform distribution of the Cr across the NU-1000 crystallites (**Figure 2.6**).
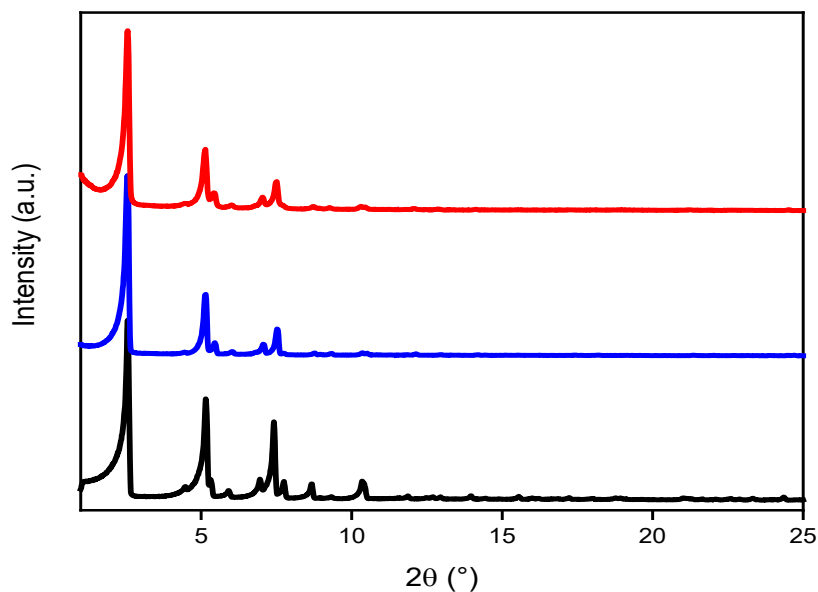
Figure 2.2 Powder X-ray diffraction data of NU-1000 (black), Cr-SIM-NU-1000 (blue), and Cr-SIM-NU-1000 post catalysis (red).

The Brunauer–Emmett–Teller (BET) surface area, as determined from the N_2 adsorption/desorption isotherm at 77 K (**Figure 2.3a**), decreases from 2120 to 1820 m^2/g as a result of the metalation of the node. DFT calculated pore size distributions confirm that mesoporosity is retained with an average mesopore size close to 3 nm, but slightly decreased relative to the chromium-free version (**Figure 2.3b**). The structure of Cr-SIM-NU-1000 was analyzed by single-crystal X-ray diffraction after growth of single-crystals of NU-1000 and subsequent metalation by the SIM method.
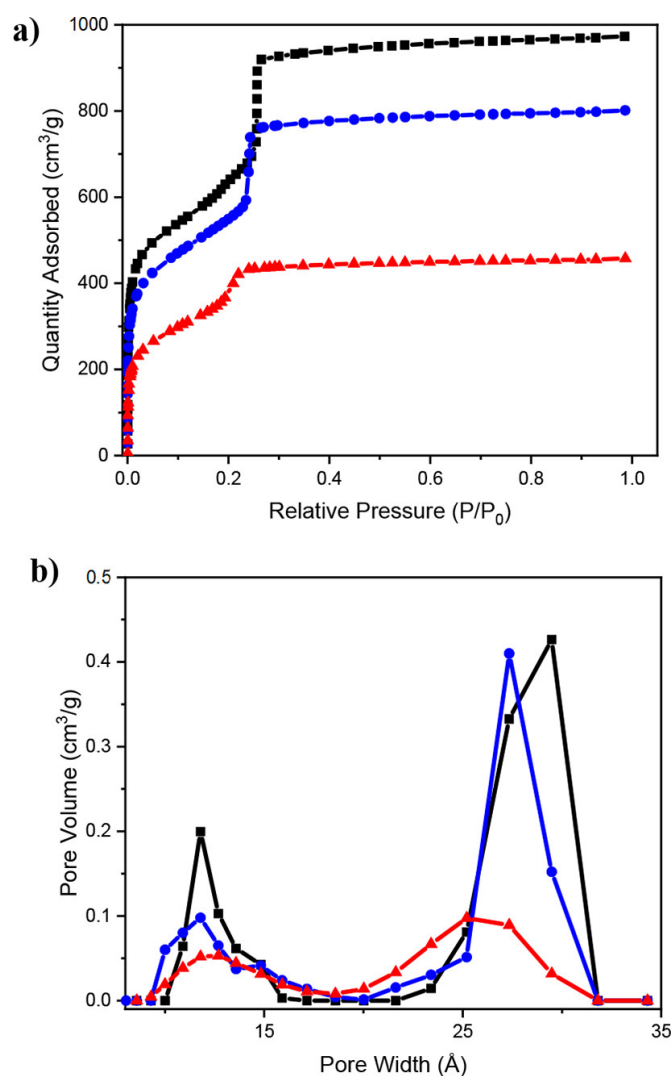
Figure 2.3 (a) N_2 adsorption isotherms of NU-1000 (black), Cr-SIM-NU-1000 (blue), Cr-SIM-NU-1000 post catalysis (red). (b) Pore-size distributions of NU-1000 (black), Cr-SIM-NU-1000 (blue), and Cr-SIM-NU-1000 post catalysis (red).

2.5 Structural Characterization of Cr-SIM-NU-1000 by Single-Crystal X-ray Diffraction

Structural analysis showed four crystallographically equivalent Cr sites with 1/4 occupancy each, as confirmed by the 1.0 Cr/Zr_6 loading from ICP-OES analysis of the single-crystal batch. Siting of the chromium ions entails interaction with three of the six available zirconium(IV) atoms, *via* a μ_3-oxo, μ_2-oxo, and μ_2-hydroxo ligands (nominally derived from node bridging oxo, terminal hydroxo, and terminal aqua ligands). These ligands direct the proposed tetrahedrally coordinated, single chromium atom into the MOF mesopore; see **Figure 2.4**. Based on EDS (**Figure 2.6**) and XPS (indicating Cr (III); **Figure 2.5**) analyses, the last occupied coordination site in the tetrahedral geometry is proposed to contain a charge balancing chloride ion. Knowing the coordination environment of the Cr should facilitate future mechanistic studies and help guide the design of future generations of the catalyst.
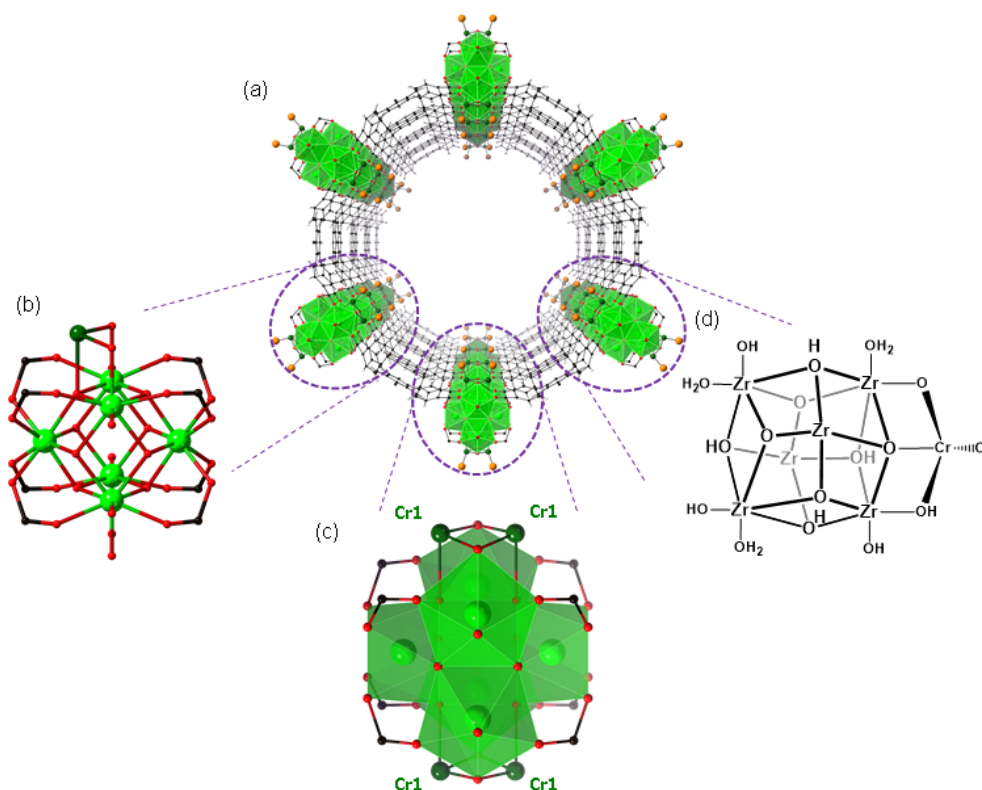
Figure 2.4 Crystal structures of Cr-SIM-NU-1000 collected at 210 K. (a) 3D structure (b) the magnified figure of the node where one Cr (dark green) binding is shown considering crystallographic occupancy (c) the magnified node showing all four equivalent Cr sites with 1/4 occupancy (d) structure representation shown for clarity. Hydrogens omitted in (b-c) for clarity. H (white), C (black), O (red), Cl (orange), Cr (dark green), Zr (light green).

2.6 Ethylene Oligomerization Reactivity Testing

Catalytic testing of Cr-SIM-NU-1000 for ethylene oligomerization was performed in a Parr reactor at ambient temperature. H_2 is fed into the reactor along with ethylene at a ratio of 4:1 H_2:C_2H_4 to inhibit polymer production. After the reactor vessel was charged with 0.3 mol % catalyst, 5 mL heptane (solvent), and 0.1 mmol of a diethylaluminum chloride cocatalyst inside of an argon-filled glovebox, the vessel was sealed. At the Parr reactor apparatus, the reactor was connected to a mechanical stirrer set to 300 rpm, and then charged with 4 bar H_2 followed by 1 bar C_2H_4.

Cr-SIM-NU-1000 showed about 20% conversion after a reaction time of only 1 h with a turnover frequency of 60 h^{-1} at ambient temperature and 5 bar of total pressure. Most notable though are both the amount of cocatalyst utilized, only a ratio of 3 mol Al:1 mol Cr compared to recent studies exceeding 100 times as much,[97, 99] and the low pressure compared to other Cr-based catalysts ranging from 30 to 50 bar of ethylene.[97-98] After the reaction, the solution was analyzed for liquid products by gas chromatography mass spectrometry (GC–MS) and longer chain hydrocarbons in a range from C_8–C_{28} were observed. The product distribution followed a Schulz–Flory distribution, with 79% C_8–C_{18} and the remaining 21% C_{20}–C_{28}. The distribution broken down by carbon number can be seen in the Additional Information (**Figure 2.9**). No solid product (polyethylene) was observed under the reaction conditions. Control reactions with unmodified NU-1000 (i.e., the support alone) showed no detectable conversion under the same reaction conditions; unsupported Cr_2O_3 showed only 3% conversion with a turnover frequency of 2 h^{-1} after 1 h, despite increasing to 1.5 mol %, with products ranging from C_8–C_{18} (**Table 2.1**). Compared with Cr_2O_3 (which delivers only C_8–C_{18}), the Cr-SIM-NU-1000 catalyst shows significantly greater activity and an ability to sustain catalytic oligomerization up through products as long as 28 carbons. This increase in activity, along with suppression of polymer production, points to the promise of Cr-SIM-NU-1000 and its successors as efficient ethylene oligomerization catalysts that reduce the quantity of required resources and diminish chemical waste.

Table 2.1 Conversion, selectivity, and turnover frequency values for the tested catalysts for the oligomerization of ethylene.

Catalyst	Conversion [%]	Selectivity [%]		TOF [h^{-1}]
		C_8-C_{18}	C_{20}-C_{28}	
Cr-SIM-NU-1000[a]	20	79	21	60
Cr$_2$O$_3$[a]	3	100	0	2
NU-1000	<1	-	-	-

[a]The cocatalyst was added with a n_{Al}:n_{Cr} ratio of 3:1. For NU-1000, the same amount of diethylaluminum chloride was added as for Cr-SIM-NU-1000.

2.7 Post-Catalysis Characterizations

Extensive postcatalysis characterization of Cr-SIM-NU-1000 was performed utilizing PXRD, SEM with EDS, XPS, ICP-OES, and N_2 physisorption. PXRD (**Figure 2.2**) and SEM (**Figure 2.6**) revealed that crystallinity is maintained along with morphology of the crystallites. ICP-OES confirmed the absence of Cr-leaching and EDS (**Figure 2.6**) still showed a spatially uniform distribution of Cr. XPS (**Figure 2.5**) showed that the oxidation state of Cr remains (or returns to) 3+. N_2 physisorption (**Figure 2.3**) showed a significant decrease in MOF surface area. An explanation is suggested by the results of further ICP-OES measurements. These revealed 2.7 ± 0.3 Al atoms, derived from the added cocatalyst, are present per Cr atom, and thus are eliminating a portion of the MOF's porosity while the framework retains crystallinity.

Extending the batch reaction run time to 24 h resulted in formation of not only oligomers, but also crystalline polyethylene (as evidenced by PXRD measurements (**Figure 2.8**) and, indirectly, by a significant decrease in MOF porosity (**Figure 2.7**)). The observation of crystalline polyethylene as a product in the extended run, but not in the shorter run, is consistent with the vastly increased catalyst contact time associated with the latter.

2.8 Chapter Conclusions

In summary, a Cr-based ethylene oligomerization catalyst supported on the highly stable metal–organic framework, NU-1000, was synthesized by liquid-phase metalation and thoroughly characterized including by single-crystal X-ray diffraction. This catalyst, Cr-SIM-NU-1000, exhibited ethylene oligomerization activity at ambient temperature, low pressure, and significantly lower cocatalyst additions compared with conventional catalysts, however it still followed the Schulz–Flory distribution. Further mechanistic studies will be conducted that, given the well-defined structure of the catalyst, will provide useful insight into the ethylene oligomerization

reaction and direct future catalyst development. Finally, future optimization to the reaction system that will lead to taming the selectivity and thus narrowing the product distribution will be studied and reported on in due time.

2.9 Additional Information

2.9.1 Materials

1,3,6,8-tetrabromopyrene, (4-(ethoxycarbonyl)phenyl)boronic acid, tetrakis(triphenylphosphine) palladium(0), tripotassium phosphate, zirconyl chloride octahydrate, benzoic acid, anhydrous heptane, chromium(II) chloride, and diethylaluminum chloride (1.0 M in heptane) were purchased and used as is from Sigma Aldrich (St. Louis, MO). Hydrochloric acid, nitric acid, acetone, N,N-dimethylformamide, 1,4-dioxane were purchased and used as it from Fisher Scientific (Hampton, NH). Chromium (III) oxide (Surface Area ~325 m^2/g) was purchased and used as is from Alfa Aesar (Haverhill, MA). Ultrapure deionized water (18.2 MΩ.cm resistivity) was obtained from a Millipore Milli-Q-Biocel A10 instrument (Millipore Inc., Billerica, MA). Argon gas used during the reactor charging, nitrogen gas used for the adsorption/desorption measurements, and hydrogen gas for catalysis were ordered from Airgas (Radnor, PA) with Ultra High Purity Grade 5. Ethylene gas (99.9%) used for catalysis was ordered from Airgas (Radnor, PA).

2.9.2 Synthetic Methods

NU-1000. 1,3,5,8-(p-benzoate)pyrene, was synthesized according to the reported procedure.[96] NU-1000 was synthesized according to the procedure by Wang et al.[96]

Cr-SIM-NU-1000. Cr-SIM-NU-1000 was prepared by mixing 200 mg NU-1000 into 25 mL of a 0.1 M $CrCl_2$ solution in N,N-dimethylformamide (DMF) and heated overnight at 100°C. $CrCl_2$ was used since it oxidizes readily in air or moisture, and is more soluble in DMF than $CrCl_3$. The sample was washed with fresh DMF until the green supernatant turned colorless. Then the sample was washed with acetone to exchange the solvent and remove DMF. The sample was dried at 80°C in a vacuum oven for 2 hours, and then thermally activated at 120°C under dynamic vacuum for 12 hours.

Single Crystal Cr-SIM-NU-1000. Single crystal NU-1000 was prepared by mixing 70 mg ZrCl$_4$ and 2 g benzoic acid into 6 mL of N,N-diethylformamide (DEF) in one vial and 40 mg of 1,3,5,8-(p-benzoate)pyrene in 4 mL DEF in a separate vial after which both vials were heated at 100 °C for 1 h. The vials were then cooled to room temperature and the solutions mixed along with 150 μL of trifluoroacetic acid, and subsequently placed in an oven at 120 °C for 1 day. The solution was then cooled to room temperature again, and the solvent was exchanged to DMF. An acid wash was performed as per the reported NU-1000 procedure.[96] After washing the crystals with DMF 3 times, the Cr-SIM procedure was performed as described above.

2.9.3 Catalytic Measurement Details

Ethylene Oligomerization. In an argon glovebox, 10 mg Cr-SIM-NU-1000, 5 mL anhydrous heptane, and 0.1 mL of diethylaluminum chloride (1.0 M in heptane) were charged into a 50 mL 4590 micro bench top autoclave Parr reactor. The reactor was then sealed, transferred out of the glovebox and connected to the gas inlet, pressure gauge, and thermocouple at the reactor station. The reactor was then set to stir at 300 rpm and pressurized with 4 bar H$_2$ and 1 bar C$_2$H$_4$. After 1 hour, gas samples were taken by airtight gas syringe and analyzed by gas chromatography. The reactor was then cooled to -20°C with a mixture of dry ice and acetone before being vented and opened, after which the solvent was collected to be analyzed on by gas chromatography mass spectrometry.

2.9.4 Instrumental Methods

Measurements. N$_2$ adsorption isotherms were measured on a Micromeritics Tristar II 3020 (Micromeritics, Norcross, GA) at 77K with 30-50 mg pre-activated sample at 120 °C for 12 h under high vacuum using a SmartVac Prep (Micromeritics, Norcross, GA). BET surface area was calculated in the region P/Po = 0.005-0.05 and pore-size distributions were obtained via DFT calculations using a carbon slit-pore model with a N$_2$ kernel.

Inductively coupled plasma optical-emission spectroscopy (ICP-OES) was performed at the QBIC facility on a Thermo iCAP 7600 Spectrometer (ThermoFisher, Waltham, MA). In each preparation, ~3 mg samples were digested in 2 mL concentrated nitric acid in a 2-5 mL Biotage (Uppsala, Sweden) microwave vial. Biotage SPX microwave reactor (software version 2.3, build 6250) was used to heat the mixture to 150 °C for 5 min. 300 µL of the digested sample was removed and diluted to 10 mL with ultrapure deionized water.

Powder X-ray Diffraction (PXRD) data were collected at the IMSERC X-ray Facility at Northwestern University on a Stoe-STADI-P powder diffractometer equipped with an asymmetric curved Germanium monochromator (CuKα1 radiation, λ = 1.54056 Å) and one-dimensional silicon strip detector (MYTHEN2 1K from DECTRIS). The line focused Cu X-ray tube was operated at 40 kV and 40 mA. Powder was packed in a 3 mm metallic mask and sandwiched between two layers of polyimide tape. Intensity data from 1 to 25 degrees 2θ were collected over a period of 10 mins. The instrument was calibrated against a NIST Silicon standard (640d) prior the measurement.

Single-crystal X-ray diffraction (SC-XRD) data was collected at 210 K using a Bruker KAPPA APEX II (Bruker, Billerica, MA) equipped with an APEX2 CCD detector, Cryostream 80-400K (Oxford Cryosystems, Oxford, United Kingdom), and CuKα IµS microfocus source with MX Optics and a Kappa geometry goniometer. Refinement results are summarized in Table S1 and S2. Crystallographic data in CIF format have been deposited in the Cambridge Crystallographic Data Centre (CCDC) under deposition number CCDC1874677. The data can be obtained free of charge via www.ccdc.cam.ac.uk/data_request/cif (or from the Cambridge Crystallographic Data Centre, 12 Union Road, Cambridge CB2 1EZ, U.K.)

Scanning electron microscopy (SEM) images and energy dispersive spectroscopy (EDS) line scans were collected at Northwestern University's EPIC/NUANCE facility using a Hitachi SU8030 FE-SEM (Dallas, TX) microscope. All samples were coated with 8 nm OsO_4 before imaging.

X-ray photoelectron spectra were collected at Keck-II/NUANCE facility at NU using a Thermo Scientific ESCALAB 250Xi (Al Kα radiation, 1486.6 eV). All measurements were performed with an electron flood gun and were calibrated to C1s peak at 284.8 eV.

Gas chromatography mass spectrometry was conducted at the IMSERC facility at NU on an Agilent 6890 GCMS (Agilent Technologies, Santa Clara, CA) equipped with an Agilent J&W DB-5 capillary column and 5973 MS.

Gas chromatography for conversion analysis was conducted at the CleanCat facility at NU on an Agilent 7890A GC (Agilent Technologies, Santa Clara, CA) with an Agilent GS-GasPro capillary column and FID detector using helium carrier gas (99.999%, Airgas, Radnor, PA).

Catalysis was conducted at the CleanCat facility at NU using a 50 mL 4590 micro bench top autoclave Parr reactor (Parr Instruments, Moline, IL) connected to a gas manifold and a 4838 Reactor Controller (Parr Instruments, Moline, IL).

2.9.5 Single-crystal X-ray Diffraction Analyses

Single crystals of Cr-SIM-NU-1000 were mounted on MicroMesh (MiTeGen) with paratone oil. The data was collected on a 'Bruker APEX-II CCD' diffractometer with a Cu Kα microfocus X-ray source. The crystals were kept at 210 K under a nitrogen stream during data collection. Using Olex2 software,[100] the structure was solved with the ShelXS[101] structure solution program using Direct Methods and refined with the ShelXL[102] refinement package using Least Squares minimization. The disordered non-coordinated solvents were removed using the PLATON SQUEEZE program. The refinement results are summarized in **Table 2.2**. Crystallographic data

for the Cr-SIM-NU-1000 crystal structure in CIF format has been deposited in the Cambridge Crystallographic Data Centre (CCDC) under deposition number CCDC-1874677. The data can be obtained free of charge via www.ccdc.cam.ac.uk/data_request/cif (or from the Cambridge Crystallographic Data Centre, 12 Union Road, Cambridge CB2 1EZ, U.K.).

Table 2.2 Crystallographic data for Cr-SIM-NU-1000.

Identification code	Cr-SIM-NU-1000
Empirical formula	$C_{21.46}H_{10}Cl_{0.25}Cr_{0.25}O_8Zr_{1.5}$
Formula weight	554.48
Temperature/K	210.0
Crystal system	hexagonal
Space group	P6/mmm
a/Å	39.100(2)
b/Å	39.100(2)
c/Å	16.7147(9)
$\alpha/°$	90
$\beta/°$	90
$\gamma/°$	120
Volume/Å^3	22131(3)
Z	12
ρ_{calc}g/cm^3	0.499
μ/mm^{-1}	2.261
F(000)	3276.0
Crystal size/mm^3	0.18 × 0.066 × 0.063
Radiation	CuKα (λ = 1.54178)
2Θ range for data collection/°	2.608 to 121.834
Index ranges	-43 ≤ h ≤ 43, -44 ≤ k ≤ 41, -18 ≤ l ≤ 18
Reflections collected	88732
Independent reflections	6316 [R_{int} = 0.2081, R_{sigma} = 0.0681]
Data/restraints/parameters	6316/106/100
Goodness-of-fit on F^2	1.401
Final R indexes [I>=2σ (I)]	R_1 = 0.1403, wR_2 = 0.3816
Final R indexes [all data]	R_1 = 0.1642, wR_2 = 0.4006
Largest diff. peak/hole / e Å^{-3}	1.48/-2.13
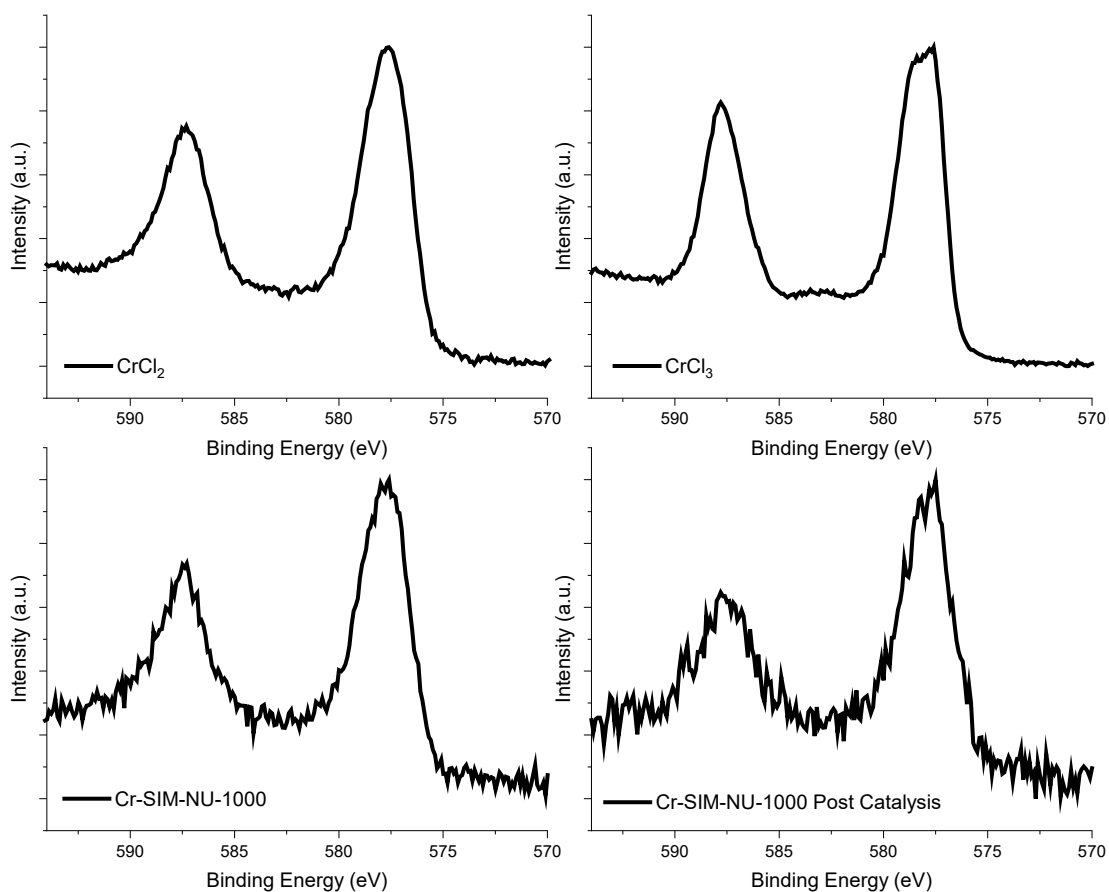
Figure 2.5 Cr 2p XPS spectra of $CrCl_2$ (top-left) and $CrCl_3$ (top-right) precursors as well as Cr-SIM-NU-1000 (bottom-left) and Cr-SIM-NU-1000 post catalysis (bottom-right).   In each spectrum, left-hand peak refers to Cr $2p_{1/2}$ and right-hand peak refers to Cr $2p_{3/2}$.   For Cr^{3+} compounds in the NIST database, a general binding energy for the Cr $2p_{3/2}$ in chloride compounds is shown to be ~577.6 eV. In all the above spectra, the Cr $2p_{3/2}$ peaks line up with 577.6 eV very well, implying that the Cr^{2+} chloride precursor used for synthesis has been oxidized to Cr^{3+} (presumably by air) before or during installation in NU-1000, and that the Cr ion retains (or returns to) the oxidation state of 3+, post-catalysis – again presumably due to exposure to air.
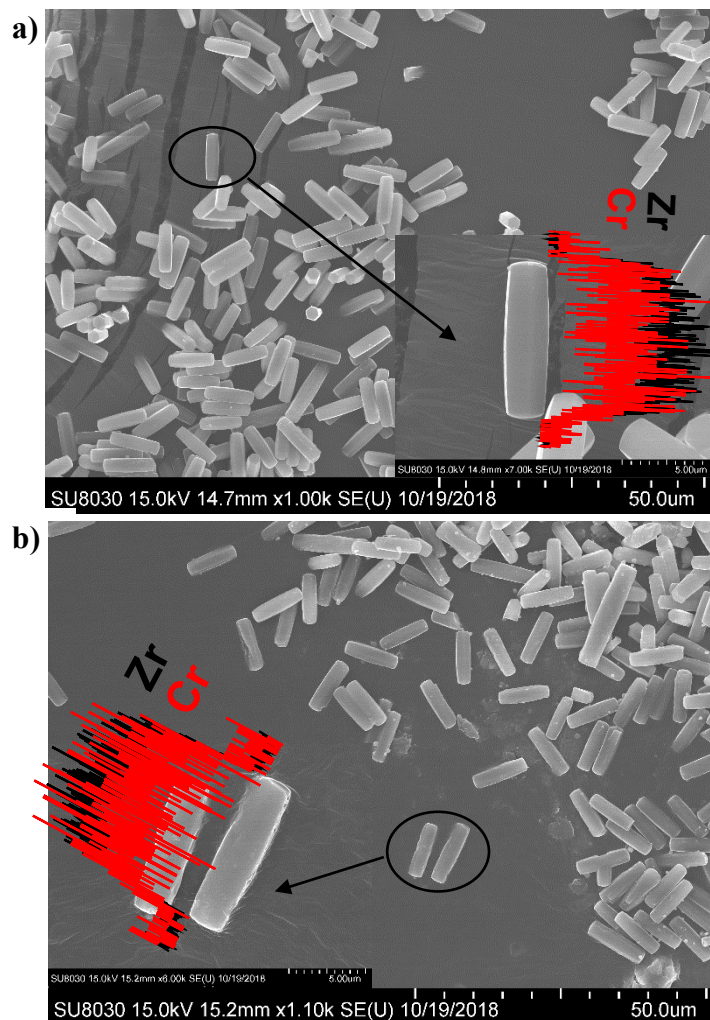
Figure 2.6 SEM images and EDS line scans of (a) Cr-SIM-NU-1000 and (b) Cr-SIM-NU-1000 post catalysis.
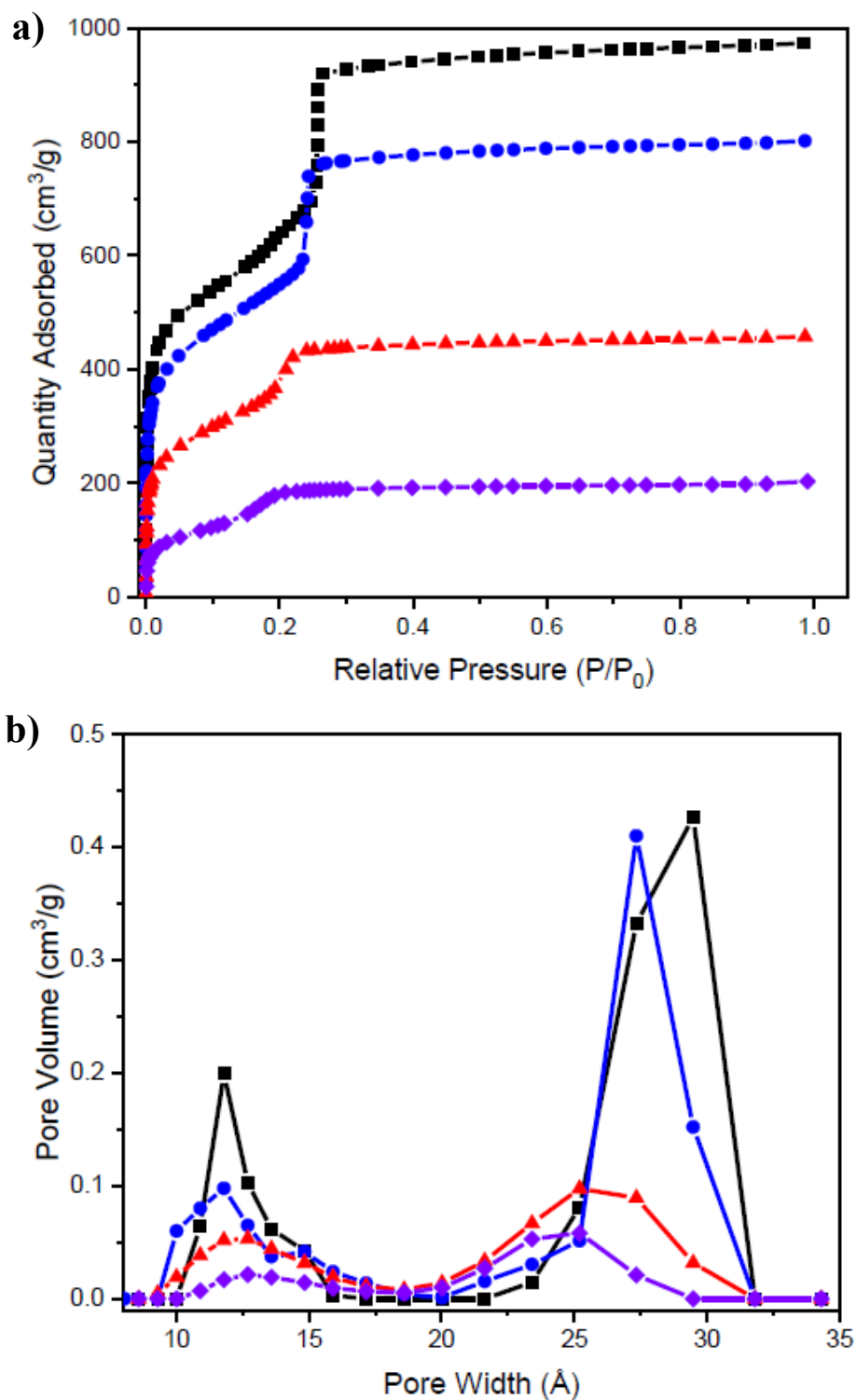
Figure 2.7 (a) N_2 adsorption isotherms and (b) Pore-size distributions of NU-1000 (black), Cr-SIM-NU-1000 (blue), Cr-SIM-NU-1000 post catalysis (red), and Cr-SIM-NU-1000 post 24 hours of catalysis (purple).
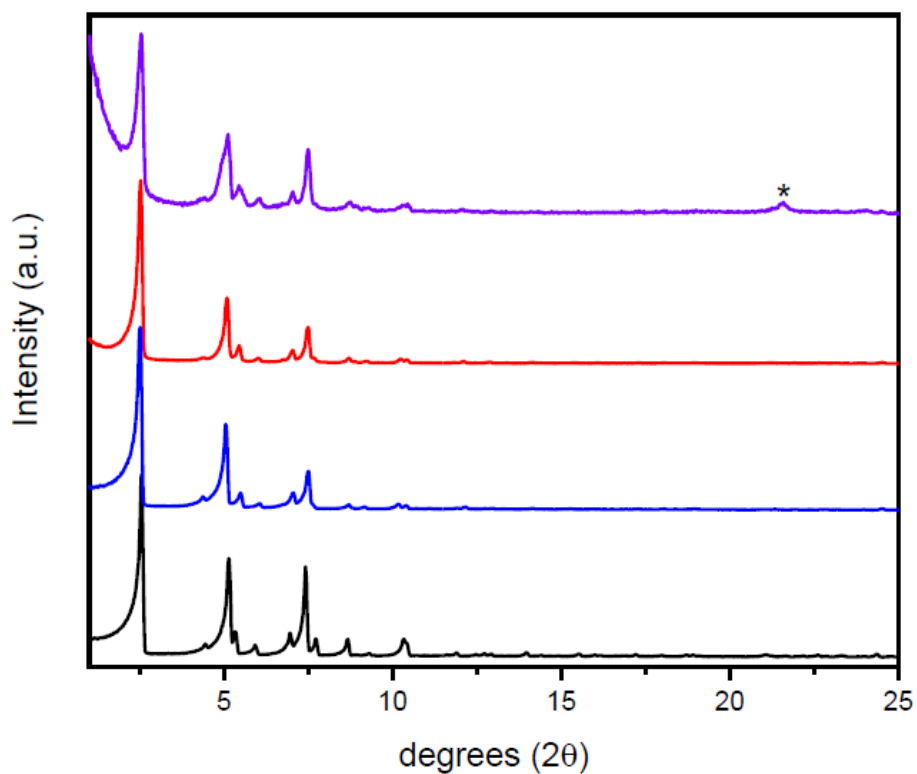
Figure 2.8 Powder X-ray diffraction patterns for NU-1000 (black), Cr-SIM-NU-1000 (blue), Cr-SIM-NU-1000 post catalysis (red), and Cr-SIM-NU-1000 post 24 hours of catalysis (purple). The post 24 hours of catalysis sample shows amorphous character at the beginning of the pattern in addition to a new peak at 21.5 degrees (*) corresponding to amorphous and crystalline polyethylene respectively.
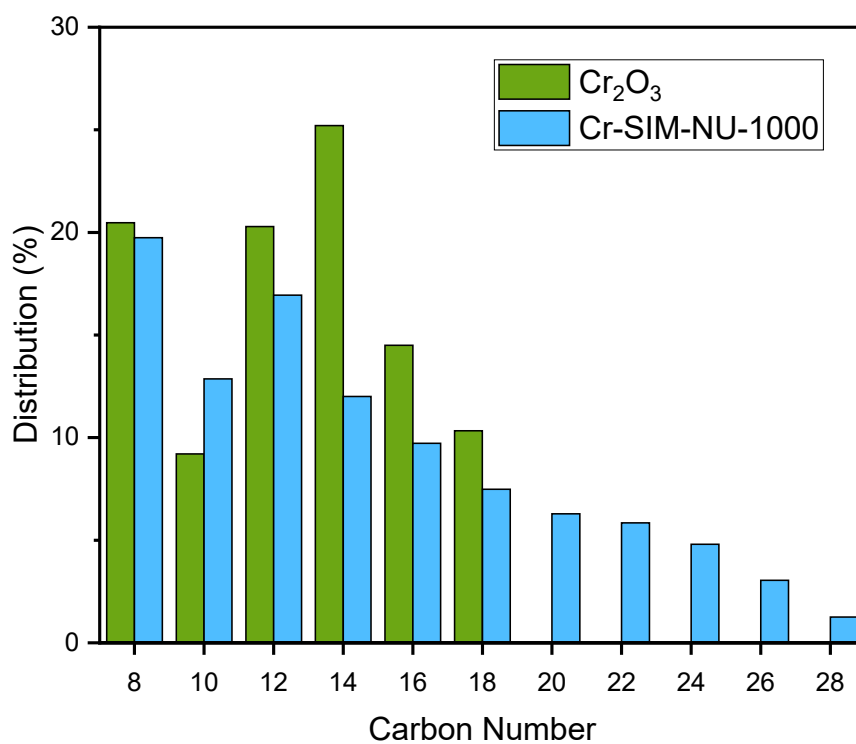
Figure 2.9 Percent distribution of hydrocarbon products by chain length for Cr-SIM-NU-1000 (blue) and Cr_2O_3 (green).

Chapter 3. Ethylene Polymerization with a Crystallographically Well-Defined Metal–Organic Framework Supported Catalyst

Portions of this chapter appear in the following manuscript:

3.1 Chapter Summary

The inherent crystallinity of metal–organic framework (MOF) catalysts offers the possibility to understand the structure of the active site at the molecular level. This property is often lacking in traditional amorphous supports. Cr-SIM-NU-1000, a MOF-supported Cr^{3+} heterogeneous catalyst, is shown to be competent for ethylene polymerization after activation with $AlEt_2Cl$ (DEAC), producing crystalline linear polyethylene (PE). The polymer produced has a low polydispersity ($Đ = 2.0$), in marked contrast to the Phillips supported chromium catalyst, $Cr@SiO_2$ ($Đ \sim 8–65$). Cr-SIM-NU-1000 achieves a turnover frequency of $2.6 \times 10^3\,h^{-1}$ under 40 bar ethylene pressure at room temperature, with corresponding PE productivity of 1.3×10^5 g PE mol^{-1} Cr per h. Single crystal X-ray diffraction (SC-XRD) of the pre-catalyst was conducted by collecting a structure of alkyl aluminum (DEAC) co-catalyst treated Cr-SIM-NU-1000. This crystal structure provides insight into the interactions between DEAC co-catalyst and Cr active site, revealing a Cr–C bond after treatment with DEAC. Furthermore, DEAC is crystallographically resolved at the terminal oxy-ligands of the node and likely also exists within the window pores of the framework between nodes, based on electron density mapping. Cr-SIM-NU-1000 offers the opportunity to study a structurally well-defined olefin polymerization system, with atomically precise characterization of the pre-catalyst structure. This allows the proposal of a mechanism and feeds into future development of next-generation heterogeneous catalyst systems.

3.2 Polymerization in Societal Context

Polymers play an integral role in today's society.[103] Efficient and selective synthesis of these polymers, especially of polyethylene (PE) for which there are hundreds of specialized grades, is essential for the economical manufacturing of desired products.[7] To achieve this, heterogeneous catalysts are desired to enhance the activity and selectivity of these transformations (**Scheme**

3.1).[104] In the realm of olefin polymerization, a canonical example of a successful industrial heterogeneous catalyst is the Phillips catalyst ($Cr@SiO_2$), which is responsible for approximately 50% of global polyethylene production.[7, 105] While this is an efficacious demonstration of industrial heterogeneous catalysis, structural understanding and derivation of structure–activity relationships remain elusive.[106]
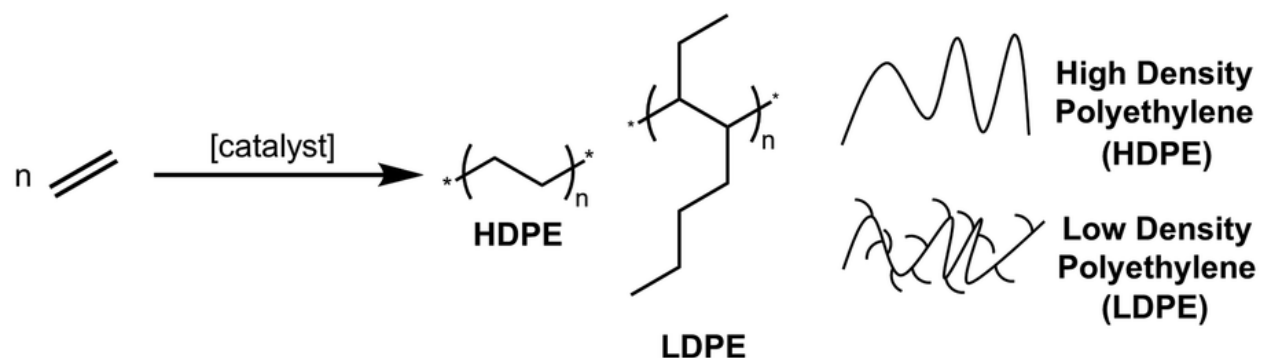
Scheme 3.1 Ethylene polymerization reaction aided by a heterogeneous catalyst with examples of polymers. Visual representation of polymers shows the contrast between minimal to no branching (HDPE) and substantial branching (LDPE) in the two example types.

3.3 Ambiguous Catalyst Structures Offer Opportunity for New Model Systems

There is widespread debate on the nature of the pre-catalyst species and active site(s) of systems such as the Phillips catalyst.[6] While non-diffractive spectroscopic techniques aim to elucidate the pre-catalyst structure and nature of the active site(s),[107] and provide some mechanistic insight,4 a comprehensive understanding through these methods is nontrivial.[6] The need for atomically precise insight into structure is evidenced by the drastic effect variations in catalyst structure have on activity and product selectivity.[108-109] Therefore, to better understand the influence of structure on polymer properties, an analogous crystalline support can be envisioned, affording numerous additional characterization techniques for probing catalyst speciation.

3.4 Metal–Organic Frameworks as Model Catalyst Systems with Structural Uniformity

Metal–organic frameworks (MOFs) are a highly tunable class of porous materials, comprised of inorganic nodes (metal ions, clusters, etc.) and multi-topic organic linkers (carboxylates, phosphonates, pyridines, etc.).[110] Due to the modularity of their structures and functions,[14, 111-115] MOFs have proven useful for a wide suite of potential applications[116] including gas separations and storage,[117-119] chemical sensing,[120-121] water purification,[122-123] and catalysis.[15, 124-128] Among these applications, catalysis has largely capitalized upon the tailorable nature of MOFs to enhance activity and selectivity across various transformations.[129-136] Notably, MOFs are crystalline and thus can be characterized *via* single crystal X-ray diffraction (SC-XRD), even after post-synthetic modification.[48-49, 57-59, 137-138] This allows MOFs to be used as crystalline analogues capable of yielding information that is complementary to what can be learned structurally by anchoring catalysts on traditional materials such as amorphous oxides including silica, alumina, and zirconia.[139] Zr-Based MOFs, in particular, are desirable as catalyst supports due to high chemical and thermal stabilities, as well as providing uniform and spatially isolated catalyst deposition sites.[14, 140] In particular, NU-1000 ($[Zr_6(\mu_3\text{-}O)_4(\mu_3\text{-}OH)_4(OH)_4(OH_2)_4](TBAPy)_2$, $TBAPy^{4-}$ = 1,3,6,8-tetrakis(*p*-benzoate) pyrene, NU = Northwestern University),[96] comprised of Zr_6 nodes and pyrene-based tetratopic carboxylate linkers, offers terminal hydroxyl and aqua groups as grafting sites.[94]

3.5 Crystallographically Resolved MOF-Supported Cr Catalyst Polymerizes Ethylene

Herein, we demonstrate the activity of a MOF-supported Cr catalyst, Cr-SIM-NU-1000, for ethylene polymerization. Upon exposure to pure (99.9%) ethylene at room temperature with diethylaluminum chloride (DEAC) as a co-catalyst (for structure see **Figure 3.6**), Cr-SIM-NU-

1000 yields crystalline, linear polyethylene. Ethylene polymerization activity of Cr-SIM-NU-1000 was screened across a range of ethylene pressures (5–40 bar), and polymer samples were characterized by gel permeation chromatography (GPC), differential scanning calorimetry (DSC), solution-phase ^{1}H and ^{13}C nuclear magnetic resonance (NMR) spectroscopy, and solid-state ^{13}C cross polarization/magic angle spinning (CP/MAS) NMR spectroscopy. Applying to macroscopic single crystals of Cr-SIM-NU-1000 the same co-catalyst treatment as that for the microcrystalline powders used here for catalysis experiments, affords DEAC@Cr-SIM-NU-1000 single crystals. SC-XRD analysis reveals that the alkyl aluminum co-catalyst is sited on the MOF node and directed into the void space (or "c-pore") that cross-connects triangular and hexagonal channels.

Previously considered as an ethylene oligomerization catalyst,[50] Cr-modified NU-1000, called Cr-SIM-NU-1000, showed activity implying that the catalyst could efficiently polymerize ethylene under different catalytic conditions. Furthermore, the reported single crystal structure of Cr-SIM-NU-1000 revealed siting of the catalyst upon the Zr_6 nodes of the MOF support, providing an opportunity to probe the reactivity of a Cr-based ethylene polymerization catalyst with a known uniform structure (**Figure 3.1**),[50] and propose a plausible mechanism.
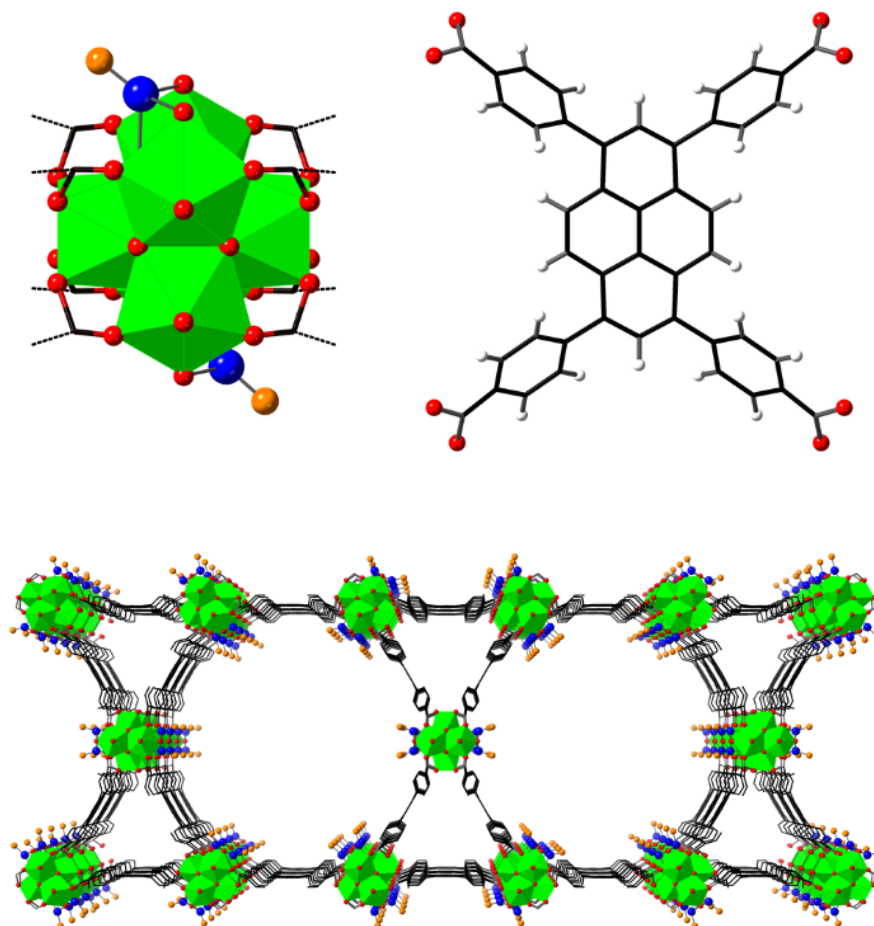
Figure 3.1 Visual representation of Cr-SIM-NU-1000 from experimental crystal structure.[50] Node (top right) and linker (top left) components, and overall structure of Cr-SIM-NU-1000 (bottom). Cr shown at the node in two of four crystallographically equivalent sites with 0.25 occupancy, while the MOF structure shows all four sites. Atom colors: H (white), C (black), O (red), Cl (orange), Cr (blue), and Zr (green). Hydrogens omitted from node and MOF structure for clarity.

3.6 Catalyst Synthesis and Characterization

Cr-SIM-NU-1000 was synthesized using a previously reported solvothermal deposition procedure with $CrCl_2$ as the Cr precursor.[50] Powder X-ray diffraction (PXRD) confirmed bulk phase purity, N_2 physisorption was performed to confirm porosity, and scanning electron microscopy (SEM) was used to confirm retention of crystallite morphology (**Figure 3.2**). Inductively coupled plasma-optical emission spectroscopy (ICP-OES) analysis revealed a Cr loading of 2.5 ± 0.3 Cr atoms per Zr_6 node or 5.4 ± 0.6 wt% Cr. These bulk characterizations confirm that framework integrity remains after the metalation step as reported previously,[50] and

that remaining porosity can facilitate substrate diffusion to installed Cr sites and subsequent polymer formation.
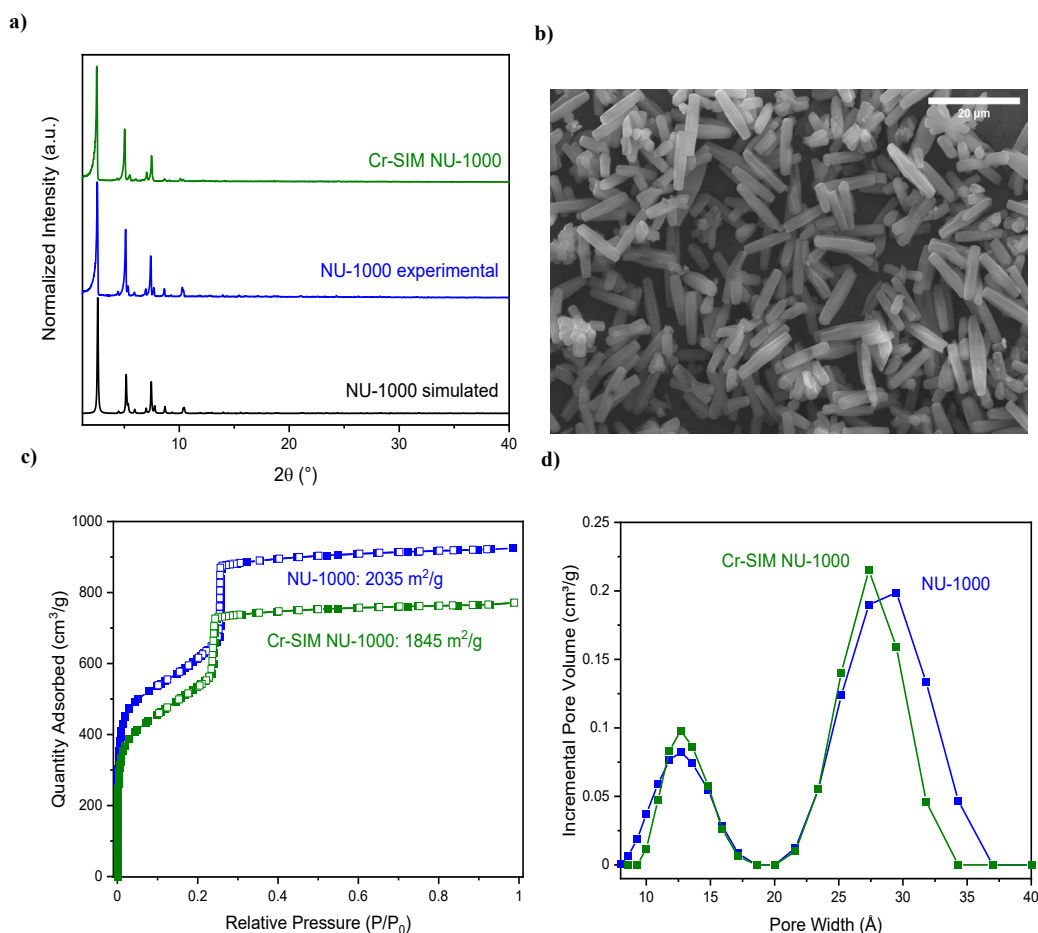
Figure 3.2 Bulk characterization of NU-1000 and Cr-SIM-NU-1000. (a) Powder X-ray diffraction patterns, (b) SEM image of Cr-SIM-NU-1000 with scale bar 20 μm, (c) N$_2$ isotherms at 77 K, and (d) density functional theory computed pore size distributions.

3.7 Interactions of Alkyl Aluminum Co-Catalyst Probed by Bulk Spectroscopy

With the addition of the DEAC co-catalyst necessary for catalytic activity at room temperature, as demonstrated previously,[50] the interactions between DEAC and the MOF catalyst were initially characterized using non-diffractive spectroscopic techniques. Specifically, X-ray photoelectron spectroscopy (XPS) and diffuse reflectance infrared Fourier transform spectroscopy (DRIFTS) were used to determine the electronic effect and potential interactions of DEAC with

the node upon DEAC treatment at the same conditions as catalysis experiments (287 : 1 Al : Cr).

Al 2p XPS (**Figure 3.10**) of DEAC and DEAC@Cr-SIM-NU-1000 exhibit nearly identical binding

energies (75.3 and 75.2 eV) which are also 0.3–0.4 eV lower than other Al^{3+} salt standards,

indicative of more electron rich Al species. Interestingly, looking into Cr 2p XPS (**Figure 3.11**) of

the as-synthesized catalyst and DEAC treated catalyst materials shows a lower binding energy in

the DEAC treated material (577.2 eV) compared to as-synthesized (577.7 eV), suggesting a more

electron rich Cr species after DEAC treatment. This lower binding energy is in alignment with the

binding energy of the $CrCl_2$ precursor used to synthesize the catalyst material, suggesting an

electrodeficient $Cr^{\delta+}$ active catalyst. Notably, there is also a slight increase in the Cr–O bond

lengths in going from the as-synthesized catalyst to the DEAC treated material (**Table 3.5**).

DRIFTS analysis of the as-synthesized catalyst and DEAC treated materials (**Figures 3.8** and **3.9**)

show a loss of the remaining hydroxo peak (3690 cm^{-1}) in the Cr-SIM-NU-1000 spectrum after

exposure to DEAC. This peak loss suggests that DEAC has interacted with the remaining hydroxo

species through proton scavenging and/or node-grafting.

3.8 Interactions of Alkyl Aluminum Co-Catalyst Probed by X-ray Crystallography

Taking the structural characterization a step further, single crystals of Cr-SIM-NU-1000

were treated with DEAC at the same exposure level as the catalysis experiments (287 : 1 Al : Cr),

and subsequently characterized by SC-XRD. The species retains the *P6/mmm* space group and has

very similar unit cell parameters to untreated Cr-SIM-NU-1000, with only a slight increase along

a and b axes ($a = b = 39.433$ Å), and a slight decrease on the c axis ($c = 16.256$ Å). To confirm

and quantify DEAC loading into the single crystal of the framework, we performed ICP-OES

measurements on the treated single crystals. These measurements indicated DEAC loading at a

level corresponding to 10 Al atoms per Zr_6 node. Additionally, the loss of the hydroxo peak in the

DRIFT spectrum suggests that Al is depositing at the remaining terminal positions of the Zr_6 nodes located in the inter-node space (c-pore).

Notably, the atom bound to Cr is best assigned as carbon in the DEAC treated crystal structure, rather than the as-synthesized Cl^- ligand, yielding a Cr–C bond of 1.59 Å, confirming the transfer of the ethyl group from DEAC to Cr. Additionally, the DEAC can be partially resolved in the crystal structure bound to terminal oxy-ligands at the node (**Figure 3.3** and **3.23**). Unfortunately, exposure to DEAC degraded the crystals, and only the first C of the Cr–ethyl, and the Al and Cl of node deposited DEAC, were visible in the structure. However, all resolved Al atoms sit within the window, or c-pore, of the framework at the terminal hydroxyl and aqua groups of the Zr_6 node; Cr sits at 6.00 Å from the resolved Al atoms, and as such continuing interactions between Al and Cr are unlikely, since an Al–Cr coordination bond of this length is unrealistic. No substantial residual electron density can be seen in the hexagonal or triangular pores (**Figure 3.24**), but in addition to the resolved Al atoms at the node there is still some residual unassigned electron density located within the c-pore (**Figure 3.25**). This residual electron density is likely more DEAC sited within the pore but not coordinated to the Zr_6 node. Large distances between trivalent metal chlorides and Zr nodes have been previously seen in MOFs,[141] and DEAC dimers are reasonably stable at room temperature against dissociation to the monomeric species.[142-144] As has been shown with other alkyl aluminum species,[142] diethylaluminum chloride (DEAC) exists as a dimer in solution at room temperature. The co-catalyst solution used for these studies is 1.0 M DEAC in heptane, with catalyst treatment using DEAC always occurring at room temperature. Thus, while crystallographically resolved as coordinating to the node, we propose that DEAC also inhabits the window pore as a dimer when it no longer has surface hydroxo or aqua ligands with which to react. To our knowledge, this represents the first crystallographic study to identify a Cr–

C bond after DEAC treatment of a heterogeneous catalyst/porous support and resolve the DEAC co-catalyst, at least partially, within such a system.
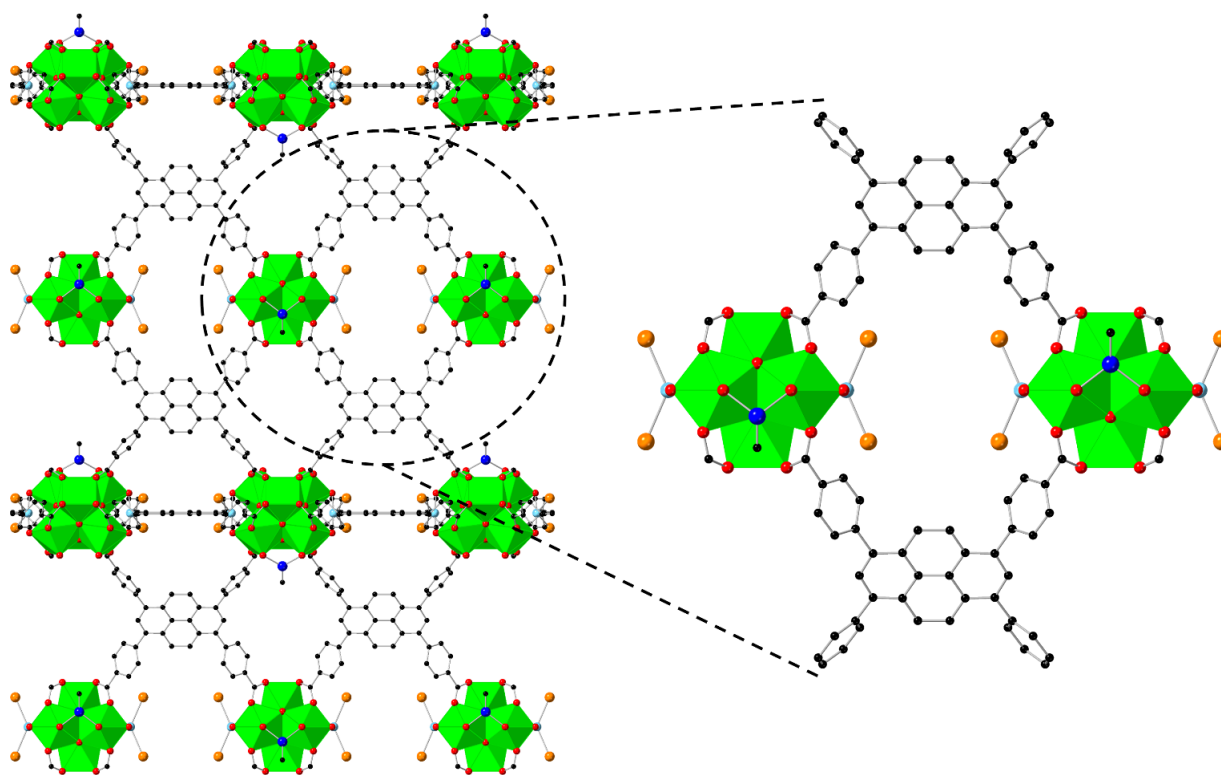
Figure 3.3 Experimental single crystal X-ray diffraction structure of DEAC@Cr-SIM-NU-1000. View of window between the nodes that occurs across the framework exhibiting occupation by DEAC sited at the oxy-ligands of the node (left). Zoomed in view of the c-pore showing crystallographically equivalent sites for both Cr (0.25 occupancy) and Al (right). Atom colors: carbon (black), oxygen (red), aluminum (light blue), chlorine (orange), chromium (dark blue), zirconium (green). Hydrogen omitted for clarity.

3.9 Catalytic Ethylene Polymerization by Cr-SIM-NU-1000

To test the activity of Cr-SIM-NU-1000 for ethylene polymerization, the catalyst was evaluated in a Parr pressure vessel over a range of ethylene pressures. To perform these reactions, the vessel was charged with catalyst, DEAC co-catalyst (287 : 1 Al : Cr), and 5 mL heptane in an Ar-filled glovebox before being pressurized to between 5 and 40 bar with ethylene. The reactor was then left at room temperature for 1 hour, before the reaction was quenched and the polymer and catalyst were collected on the benchtop. Polymer yield was determined by isolated mass. As

ethylene pressure was increased, the average turnover frequency as well as productivity metric (g PE mol^{-1} Cr per h) showed an apparent increasing trend, reaching the highest activity at 40 bar ethylene with a turnover frequency of 2.6×10^3 h^{-1} and polyethylene productivity of 1.3×10^5 g PE mol^{-1} Cr per h (**Figure 3.4a**). In fact, plotting log(TOF) vs. log(C$_2$H$_4$ pressure) yields a slope of ~1 (**Figure 3.4b**), evidence of a linear dependence of turnover frequency on ethylene pressure and evidence against intrapore condensation of ethylene seen in other MOF materials.[135, 145-146]
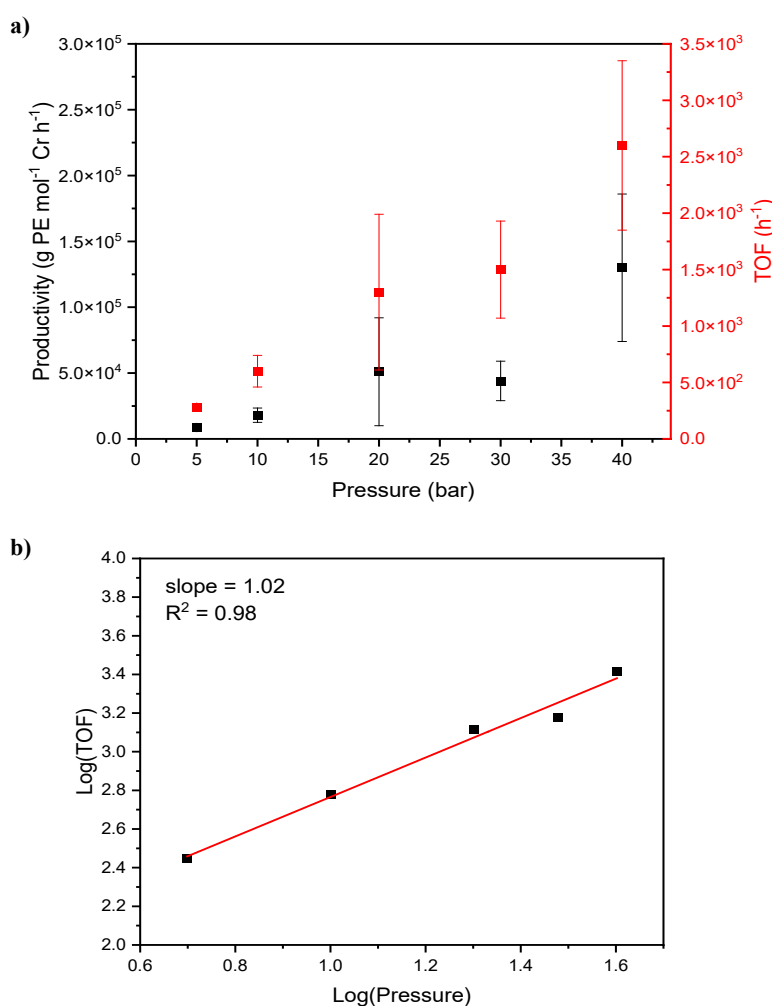
Figure 3.4 (a) Plot of productivity and turnover frequency (TOF) of Cr-SIM-NU-1000 for ethylene polymerization vs. starting ethylene pressure. Error bars consist of five replicates. Reaction conditions: 0.006 mol% catalyst (10 mg), 1.0 mL 1.0 M Et$_2$AlCl in heptane (287 eq.), and 5 mL heptane in pressurized Parr vessel at room temperature with 200 rpm stirring for 1 hour. (b) Log plot of TOF vs. C$_2$H$_4$ pressure.

3.10 Polymer Product Characterizations

Polymer samples produced by Cr-SIM-NU-1000 can be described as linear polyethylene as evidenced by a single peak, assignable to the polymer, and lack of branched peaks observed in the solid-state ^{13}C CP/MAS NMR (**Figure 3.18**)[147-150] and solution ^{13}C NMR (**Figure 3.21**) spectra. Heat of fusion calculations from DSC measurements[151] (**Table 3.2**) further indicate that the polymer produced is high-density, having an average melting temperature of 137 °C and 42% crystallinity. GPC analysis revealed that the polymer produced has an average molecular weight that depends on the initial pressure of ethylene. In general, with increasing ethylene pressure, the molecular weight of the polymers increased while the polydispersity decreased, reaching a weight average molecular weight (M_w) of 920 kDa with a polydispersity of 2.0 (see **Table 3.3**). It is important to note that prior to GPC analysis, the catalyst was removed (by filtration) as a necessary step during sample preparation. Conceivably, MOF removal could have resulted in the removal of ultra-high molecular weight polymer and polymer trapped within the pores of the framework. Extensive washing of the post-catalysis material (MOF and polymer) leads to substantial removal of surface polymer (**Figures 3.14-3.17**);[152-154] however, complete removal of polymer from the framework was not achieved. Nonetheless, it remains that Cr-SIM-NU-1000 is a competent catalyst for ethylene polymerization, with a uniformly active single site as indicated by the low polydispersity generally seen with other single-site catalysts such as metallocenes.[7]

3.11 Mechanistic Insights

Furthermore, given the defined structures of the MOF and supported catalyst, connections can be drawn to the polymer properties and a mechanism can be proposed (**Figure 3.5**). Supported Cr-based ethylene polymerization catalysts have been proposed to proceed through Cossee–

Arlman (linear insertion) and metallacycle chain growth mechanisms, and can subsequently terminate through a variety of methods including β-H elimination to the metal, β-H transfer to the monomer, or chain transfer to aluminum.[90, 155] With Cr-SIM-NU-1000, given the lack of activity without addition of DEAC, the alkyl aluminum co-catalyst serves to activate the Cr species within the MOF by providing an initial ethyl group and generating an alkyl–Cr species. This activation by alkylation is supported by the Cr–C bond resolved in the crystal structure of DEAC@Cr-SIM-NU-1000. Next, after ethylene coordination to the Cr, or in a concerted manner, linear insertion (Cossee–Arlman) of ethylene occurs. Linear insertion is the most likely mechanism since substantial α-olefin production, rather than polymer, is expected for the metallacycle mechanism.[156] The geometry of the framework support, namely the 1-dimensional channels of the **csq** topology that NU-1000 exhibits,[32] is likely to facilitate the linear insertion chain growth mechanism, noting that the Cr species exclusively faces into the hexagonal 3 nm mesopore, as shown in **Figure 3.1**. Based on solution ^{1}H NMR spectra of the polyethylene product (**Figures 3.20** and **3.22**), the absence of olefinic signals indicates that the termination step of the polymerization is exclusively chain transfer to aluminum species, as seen by other ethylene polymerization systems activated by DEAC.[157] In addition, chain walking – and subsequent branching – is not observed in this system by ^{13}C NMR (**Figure 3.21**), an important component to be expected in the β-hydrogen elimination pathway, more commonly seen with late transition metal catalysts.[156]
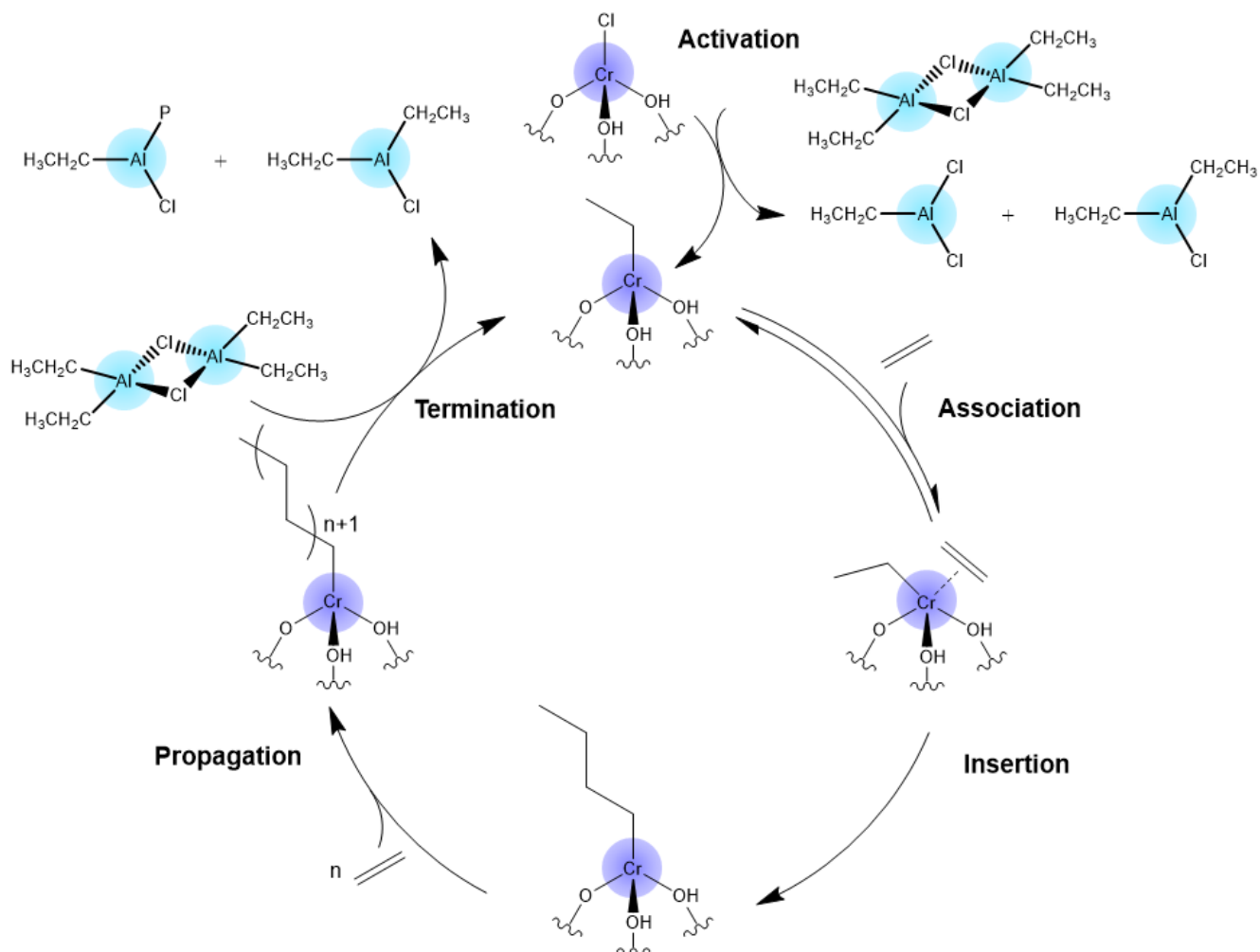
Figure 3.5 Proposed mechanism of ethylene polymerization using Cr-SIM-NU-1000 as the catalyst and diethyl aluminum chloride as the activator and chain termination agent. Cr-SIM-NU-1000 is first activated by DEAC to provide Cr-ethyl which allows subsequent chain growth through linear insertion of ethylene into the Cr–alkyl bond. Chain termination occurs through transfer to DEAC. P = polymer chain.

3.12 Chapter Conclusions

Cr-SIM-NU-1000 serves as a structurally well-defined Cr-based ethylene polymerization catalyst that offers insight into the inner workings of similar heterogeneous catalysts unable to be characterized crystallographically. While this report resolves the Cr–C bond and the approximate crystallographic location of the DEAC within a heterogeneous ethylene polymerization catalyst structure, it should be acknowledged that this is a pre-catalyst structure, and not the operando catalyst structure. By collecting diffraction data that leads to structural elucidation of the pre-

catalyst material, this MOF-supported catalyst shows the potential for improving upon our understanding of heterogeneous polymerization systems. With that in mind, we are able to provide a proposed mechanism for this catalyst and co-catalyst system, wherein the polymerization proceeds through a linear insertion chain growth and terminates via chain transfer to the alkyl aluminum co-catalyst. There is still more to be done to fully elucidate the mechanism and influence of co-catalyst concentrations or identity on the resulting activity of this system and polymer produced. Subsequent work looking at in-situ crystallographic and spectroscopic techniques can aid in the determination of the oxidation state and potential structural changes of the catalyst during the process of the reaction, something unable to be obtained without the structural definition of this uniformly supported catalyst. Efforts to this end are ongoing in our laboratories.

3.13 Additional Information

3.13.1 Materials

Acetone, N,N-dimethylformamide (DMF), hydrochloric acid were purchased from Fisher Scientific (Waltham, MA) and used as received. Benzoic acid, trifluoroacetic acid (TFA), zirconyl chloride octahydrate, chromium(II) chloride (99.99% trace metals), and 1.0 M diethylaluminum chloride (DEAC) in heptane were purchased from Sigma-Aldrich (St. Louis, MO) and used as received. **Caution diethylaluminum chloride is pyrophoric and should only be handled under an inert atmosphere and with care**. Anhydrous heptane was purchased from Sigma-Aldrich and further dried by soaking over 3 Å molecular sieves. N,N-Diethylformamide (DEF) was purchased from TCI America (Portland, OR) and used as received. UHP N_2 (99.999%), UHP Ar (99.999%), and UHP ethylene (99.9%) were purchased from Airgas (Radnor, PA) and used as received. 1,3,6,8-Tetrakis(p-benzoic acid)pyrene (H₄TBAPy) was synthesized based on literature procedure.[96]

3.13.2 Synthetic Methods

NU-1000 powder synthesis. 1,3,5,8-Tetrakis(p-benzoic acid)pyrene, was synthesized according to reported procedure.[96] NU-1000 was synthesized, acid activated, and washed according to previously published procedures.[32, 96]

Cr-SIM-NU-1000 powder synthesis. Cr-SIM-NU-1000 was prepared by previously reported procedure.[50] Cr-SIM-NU-1000 was prepared by mixing 200 mg NU-1000 into 25 mL of a 0.1 M $CrCl_2$ solution in N,N-dimethylformamide (DMF) and heated overnight at 100 °C. The sample was washed with fresh DMF (3 × 40 mL). Then the sample was washed with acetone (3 × 40 mL) to exchange the solvent to remove DMF and left to soak overnight in fresh acetone. The sample was dried at 80 °C in a vacuum oven for 2 hours, and then thermally activated at 120 °C under dynamic vacuum on a Smart VacPrep for 16 hours.

DEAC@Cr-SIM-NU-1000 powder synthesis. Freshly DMF washed Cr-SIM-NU-1000 powder was solvent exchanged to acetone by washing 3 times and then soaking overnight. Then, after decanting the acetone, the powder was placed in a vacuum oven at 80 °C for 3 hours. Then, it was thermally activated at 120 °C under dynamic vacuum on a Smart VacPrep for 16 hours. The powder was then transferred into an Ar filled glovebox. Next, it was soaked in anhydrous heptane before decanting the solvent and exposing the powder to 1.0 M diethylaluminum chloride in heptane consistent with the catalysis experiments. After 1 h, the solvent was decanted and exchanged for fresh heptane 3 times with a 30 min soaking period in between. The solvent was then exchanged to pentane, where the powder was allowed to soak for a total of 1.5 h during which 3 washes and subsequent soaks were performed. After decanting as much pentane as possible, the powder was held under dynamic vacuum on a Smart VacPrep for 16 hours.

NU-1000 Single Crystal Synthesis. Single crystals of NU-1000 were prepared by previously reported procedure.[50] 70 mg $ZrCl_4$ and 2 g benzoic acid were dissolved in 6 mL *N,N*-diethylformamide (DEF) *via* sonication in an 8-dram vial. 40 mg H_4TBAPy was suspended in 4 mL DEF *via* sonication in a separate 8-dram vial. Both vials were incubated in a preheated oven at 100 °C for 1 h. The vials were then removed from the oven and allowed to cool to room temperature. Subsequently, the linker solution was added to the node solution and 40 µL TFA was also added. After brief sonication to ensure homogeneous distribution of the solutions, the vial was placed in a sand bath before being placed in a preheated oven at 120 °C overnight. After allowing the vial to cool to room temperature the crystals were DMF washed and acid activated similarly to the powder, with 0.5 mL 8 M HCl in 12 mL DMF at 100 °C overnight. Lastly, they were washed 3 times with fresh DMF.

Cr-SIM-NU-1000 Single Crystal Synthesis. Freshly washed NU-1000 single crystals were subjected to a 0.1 M $CrCl_2$ solution in DMF at 100 °C overnight. After cooling to room temperature, the unreacted $CrCl_2$ was washed away with fresh DMF aliquots.

DEAC@Cr-SIM-NU-1000 Single Crystal Synthesis. Freshly DMF washed Cr-SIM-NU-1000 single crystals were solvent exchanged to ethanol by washing 3 times and then soaking overnight. Then, in as minimal ethanol as possible, the crystals were transferred to a glass dish for supercritical CO_2 activation. Using a supercritical CO_2 drier, the ethanol was exchanged with liquid CO_2 and dry crystals were obtained. The crystals were then transferred into an Ar filled glovebox. Next, they were soaked in anhydrous heptane before decanting the solvent and exposing the crystals to 1.0 M diethylaluminum chloride in heptane consistent with the powder experiments. After 1 h, the solvent was decanted and exchanged for fresh heptane 3 times with a 30 min. soaking period in between.

3.13.3 Catalysis Details

Ethylene polymerization. In an Ar filled glovebox, 10 mg Cr-SIM-NU-1000, 5 mL anhydrous heptane, and 1.0 mL of diethylaluminum chloride (1.0 M in heptane) were charged into a 50 mL 4590 micro bench top autoclave Parr reactor. The reactor was then sealed, transferred out of the glovebox and connected to the gas inlet, pressure gauge, and thermocouple at the reactor station. The reactor was then set to stir at 200 rpm and pressurized to between 5 and 40 bar with C_2H_4. After 1 hour, the reaction was vented and opened, after which the solid polymer was recovered for analysis.

3.13.4 Physical Characterization and Instrumentation

Powder X-ray diffraction (PXRD) data was collected at the IMSERC X-ray Facility at Northwestern University on a STOE-STADI-P powder diffractometer equipped with an asymmetric curved germanium monochromator (CuKα1 radiation, λ = 1.54056 Å) and one-

dimensional silicon strip detector (MYTHEN2 1K from DECTRIS). The line focused Cu X-ray tube was operated at 40 kV and 40 mA. Powder was packed in a 3 mm metallic mask and sandwiched between two layers of polyimide tape. Intensity data from 1 to 40 degrees 2θ were collected over a period of 5 min.

N_2 adsorption isotherms were measured on a Micromeritics Tristar II 3020 (Micromeritics, Norcross, GA) at 77 K with 30–80 mg pre-activated sample at 120 °C for 16 h under high vacuum using a Smart VacPrep (Micromeritics, Norcross, GA). BET area was calculated in the region P/P_0 = 0.005–0.05 and pore-size distributions were obtained via density functional theory (DFT) calculations using a carbon slit-pore model with a N_2 kernel.

Inductively coupled plasma optical-emission spectroscopy (ICP-OES) was performed at the QBIC facility at Northwestern University on a Thermo iCAP 7600 spectrometer (ThermoFisher, Waltham, MA). In each preparation, ~3 mg samples were digested in 2 mL concentrated nitric acid in a 2–5 mL Biotage (Uppsala, Sweden) microwave vial. Biotage SPX microwave reactor (software version 2.3, build 6250) was used to heat the mixture to 150 °C for 15 min. 300 μL of the digested sample was removed and diluted to 10 mL with ultrapure Millipore water.

Supercritical CO_2 drying was performed using a Tousimis Samdri-PVT-3D supercritical CO_2 drier, exchanging ethanol for supercritical CO_2 five times with a minimum soaking time of 1 h between exchanges. The temperature was then increased to the supercritical point and the instrument pressure was bled at 0.5 cm^3 min^{-1}.

Single-crystal X-ray diffraction (SC-XRD) intensity data of a yellow-green rod crystal were collected at 200 K. A suitable single crystal was mounted on a MiTeGen loop with paratone oil on

an XtaLAB Synergy diffractometer equipped with a micro-focus sealed X-ray tube PhotonJet (Cu) X-ray source and a hybrid pixel array detector (HyPix) detector. Temperature of the crystal was controlled with an Oxford Cryosystems low-temperature device. Data reduction was performed with the CrysAlisPro software using an empirical absorption correction. The structure was solved with the ShelXT structure solution program using the Intrinsic Phasing solution method and by using Olex2 as the graphical interface. The model was refined with ShelXL using least squares minimization.

Scanning electron microscopy (SEM) images were collected at Northwestern University's EPIC/NUANCE facility using an FEI Quanta 650 ESEM microscope. All samples were coated with 9 nm OsO_4 before imaging.

Gel permeation chromatography (GPC) measurements were conducted in the Chemical Science and Engineering Division at Argonne National Laboratory (ANL) using a high-temperature GPC (Agilent-Polymer Laboratories 220) equipped with refractive index and viscometer detectors. Monodisperse polystyrene standards were used for calibration (ranging from 400 Da to 1.1 MDa). The column set included 3 Agilent PL-Gel Mixed B columns and 1 PL-Gel Mixed B guard column. 1,2,4-Trichlorobenzene (TCB) containing 0.01 wt% 3,5-di-tert-butyl-4-hydroxytoluene (BHT) was chosen as the eluent with a flow rate of 1.0 mL min^{-1} at 150 °C. Samples were prepared in TCB at a concentration of ~1–2 mg mL^{-1} and heated at 130 °C for 24 h prior to injection.

^{13}C cross polarization/magic angle spinning (CP/MAS) solid-state nuclear magnetic resonance (NMR) spectroscopy was conducted at room temperature on a Bruker Avance III 400 MHz spectrometer equipped with a 4 mm HX probe. Sample data was acquired using TopSpin™ by

Bruker. ^{13}C CP/MAS NMR data were collected using a spin rate of 10 kHz and a contact time (p15) of 5 ms at room temperature. D1 was set to 5.00 s, SW was set to 296 ppm, and O1P was set to 100 ppm. 12 000 scans were used for ^{13}C CP/MAS NMR data collection. Samples were loaded neat into a 4 mm cylindrical zirconia rotor sealed with a Kel-F cap, both from Bruker. ^{13}C CP/MAS NMR spectra were referenced to an external adamantane peak at δ 38.3 and were converted to tetramethylsilane at δ 0.0. NMR spectra were reported after phase correction in MestReNova (MNova) by Mestrelab Research.

^{1}H and ^{13}C solution state NMR spectroscopy was conducted on a Bruker Avance III 600 MHz system equipped with two RF channels (^{1}H = 600 MHz, ^{13}C = 150 MHz). Sample data was acquired using TopSpin™ by Bruker. All collected spectra were referenced to residual solvent signals. NMR spectra were processed and integrated using Mnova by Mestrelab Research, following phase correction and baseline correction (Whittaker smoother). Initial ^{1}H solution state NMR spectra of the polymer product were collected in 1,1,2,2-tetrachloroethane-d$_2$ at 120 °C with 25 scans. D1 was set to 5.00 s, SW was set to 16 ppm, and O1P was set to 6 ppm. Next, ^{13}C solution state NMR spectra of the polymer product were collected in 1,1,2,2-tetrachloroethane-d$_2$ at 120 °C with 18 000 scans. D1 was set to 2.00 s, SW was set to 240 ppm, and O1P was set to 100 ppm. After ^{13}C solution state NMR data collection finished, final ^{1}H solution state NMR spectra of the polymer product were collected in 1,1,2,2-tetrachloroethane-d$_2$ at 120 °C with 25 scans. D1 was set to 5.00 s, SW was set to 16 ppm, and O1P was set to 6 ppm. The polymer product was heated at 120 °C in 1,1,2,2-tetrachloroethane-d$_2$ prior to NMR data collection to aid in solubilization.

Differential scanning calorimetry (DSC) experiments were conducted using a Mettler Toledo TGA/DSC 1 LF and corresponding STARe software (v16.10). For DSC of polymers, samples

were heated in 70 μL alumina crucibles under N_2 at 10 °C min^{-1} from 25 °C to 200 °C and then cooled from 200 °C to 25 °C for two cycles.

Diffuse reflectance infrared Fourier transform spectroscopy (DRIFTS) experiments were conducted using a Thermo Scientific Nicolet iS50 FT-IR spectrometer equipped with an MCT-A detector cooled to 77 K. A Harrick Scientific Praying Mantis™ diffuse reflectance accessory was used to acquire spectra under air- and moisture-free conditions. Samples were prepared inside of a glovebox with argon atmosphere and DRIFT spectra were collected under this atmosphere. KBr was used as a background for spectra. The collected spectra were processed using the Kubelka–Munk function.

X-ray photoelectron spectra were collected at the Keck-II/NUANCE facility at Northwestern University using a Thermo Scientific ESCALAB 250Xi (Al Kα radiation, 1486.6 eV). All measurements were performed with an electron flood gun and were calibrated to C 1s peak at 284.8 eV.

3.13.5 Calculations

Productivity Calculations

Productivity (g PE mol^{-1} Cr h^{-1}) = mass of polymer isolated / (mol Cr in MOF catalyst * experiment duration)

Turnover Frequency Calculations

TOF (h^{-1}) = mol ethylene consumed / (mol Cr in MOF catalyst * experiment duration)
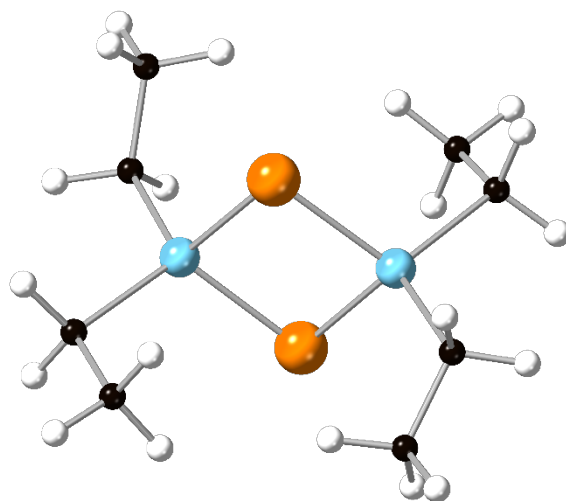
Figure 3.6 Structure of diethylaluminum chloride, which exists as a dimer at room temperature. Atom colors: Hydrogen (white), Carbon (black), Chlorine (orange), Aluminum (light blue).
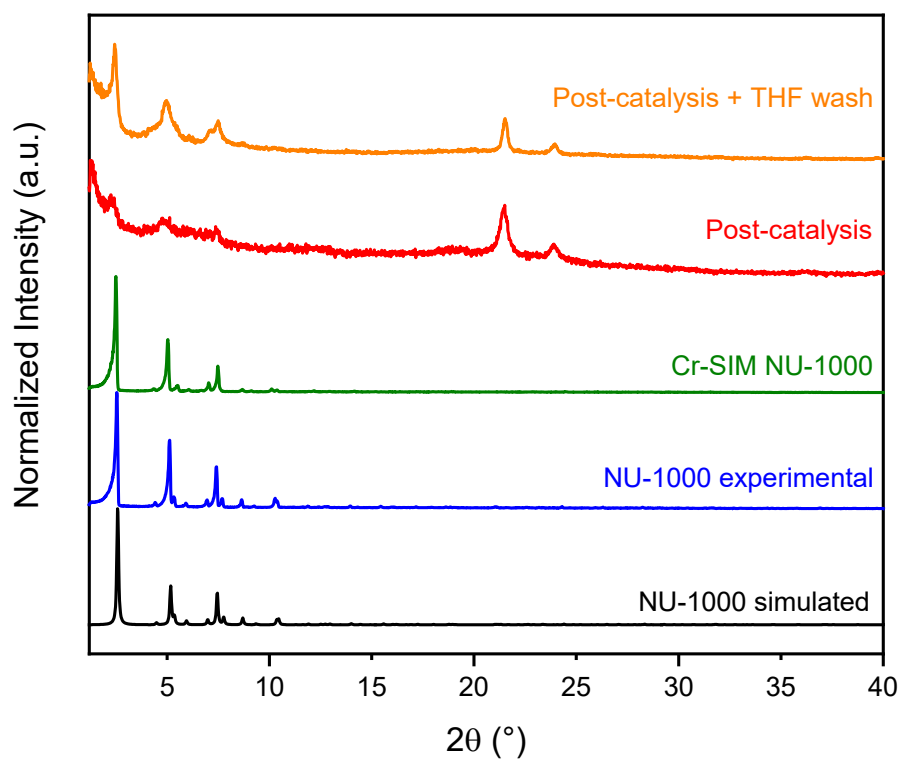
Figure 3.7 Powder X-ray diffraction patterns of NU-1000 simulated (black) and experimental (blue), Cr-SIM-NU-1000 (green), Cr-SIM-NU-1000 post-catalysis (red), and Cr-SIM-NU-1000 post-catalysis washed with THF (orange).
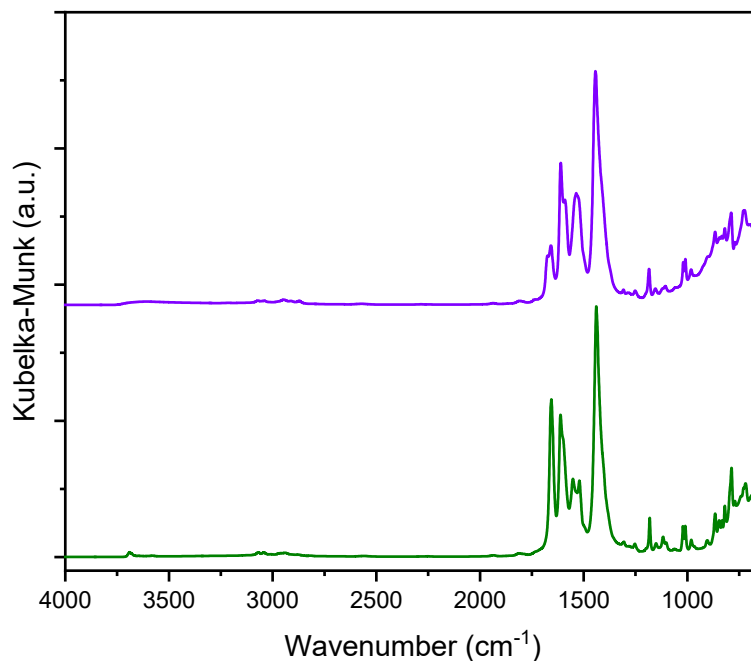
Figure 3.8 Diffuse reflectance infrared Fourier transform (DRIFT) spectra of Cr-SIM-NU-1000 (green) and DEAC@Cr-SIM-NU-1000 (purple).
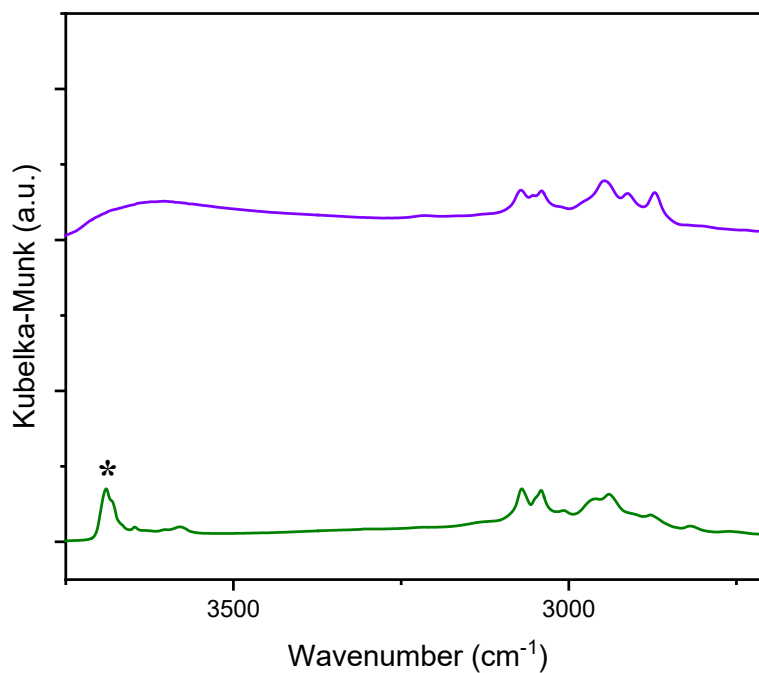
Figure 3.9 Zoomed in higher wavenumber region of the diffuse reflectance infrared Fourier transform (DRIFT) spectra of Cr-SIM-NU-1000 (green) and DEAC@Cr-SIM-NU-1000 (purple) showing the loss of the hydroxyl peak upon treatment with DEAC.
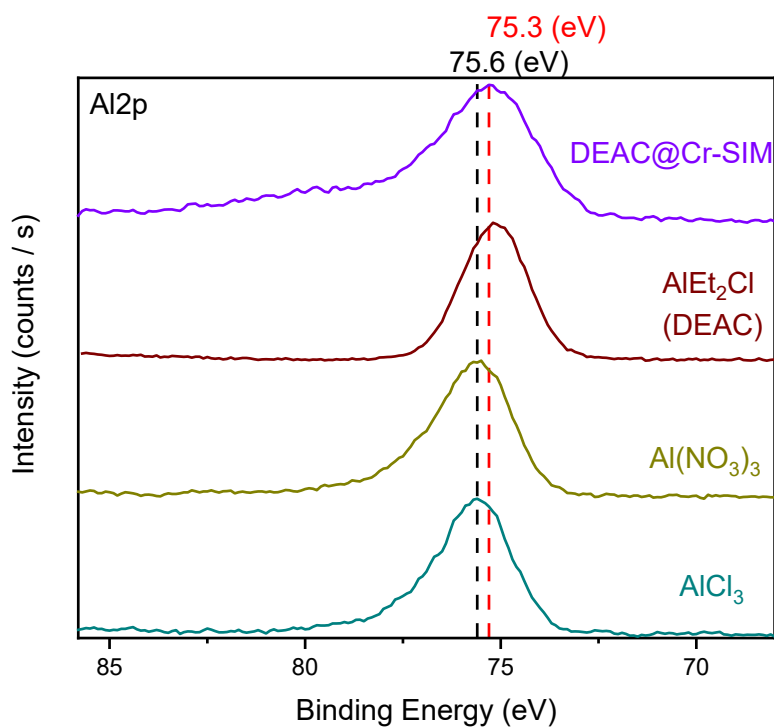
Figure 3.10 Al 2p X-ray photoelectron spectra (XPS) of DEAC@Cr-SIM-NU-1000 (purple), DEAC (brown), and two other Al salts: $Al(NO_3)_3$ (yellow) and $AlCl_3$ (teal).
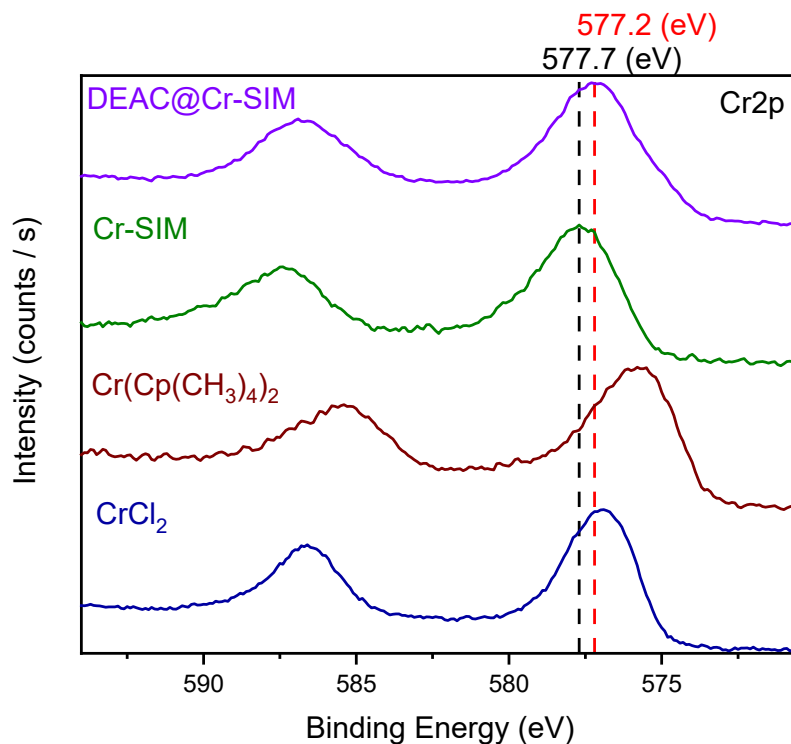
Figure 3.11 Cr 2p X-ray photoelectron spectra (XPS) of DEAC@Cr-SIM-NU-1000 (purple), Cr-SIM-NU-1000 (green), and two Cr precursors: $Cr(Cp(CH_3)_4)_2$ (brown) and $CrCl_2$ (navy blue).
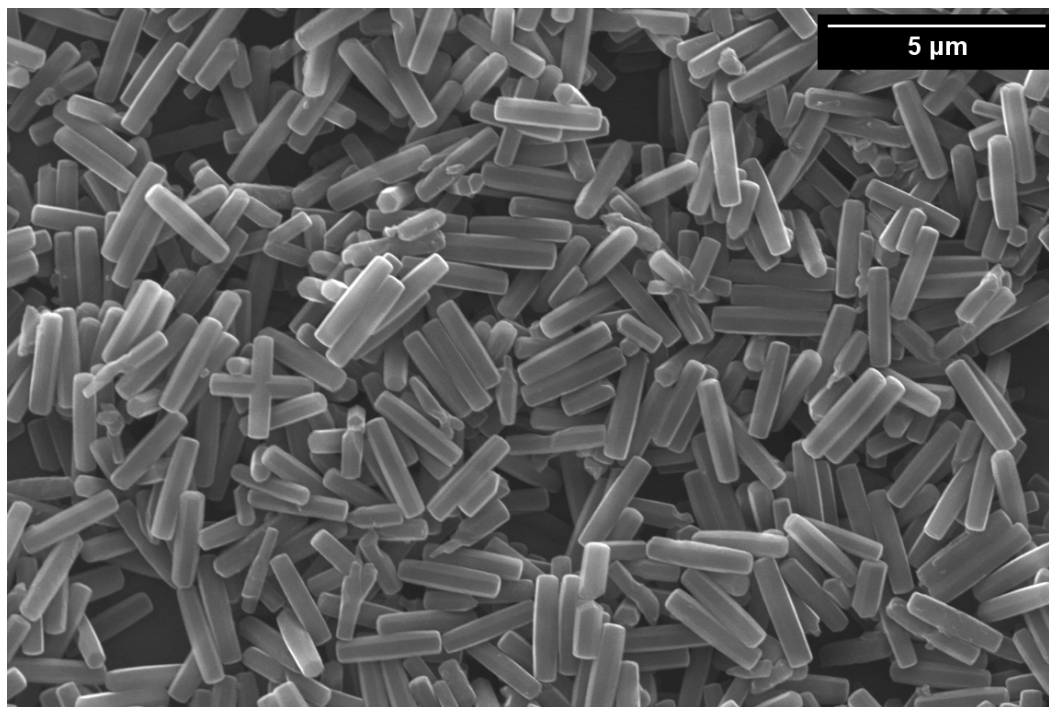
Figure 3.12 SEM image of NU-1000. Scale bar 5 micron.
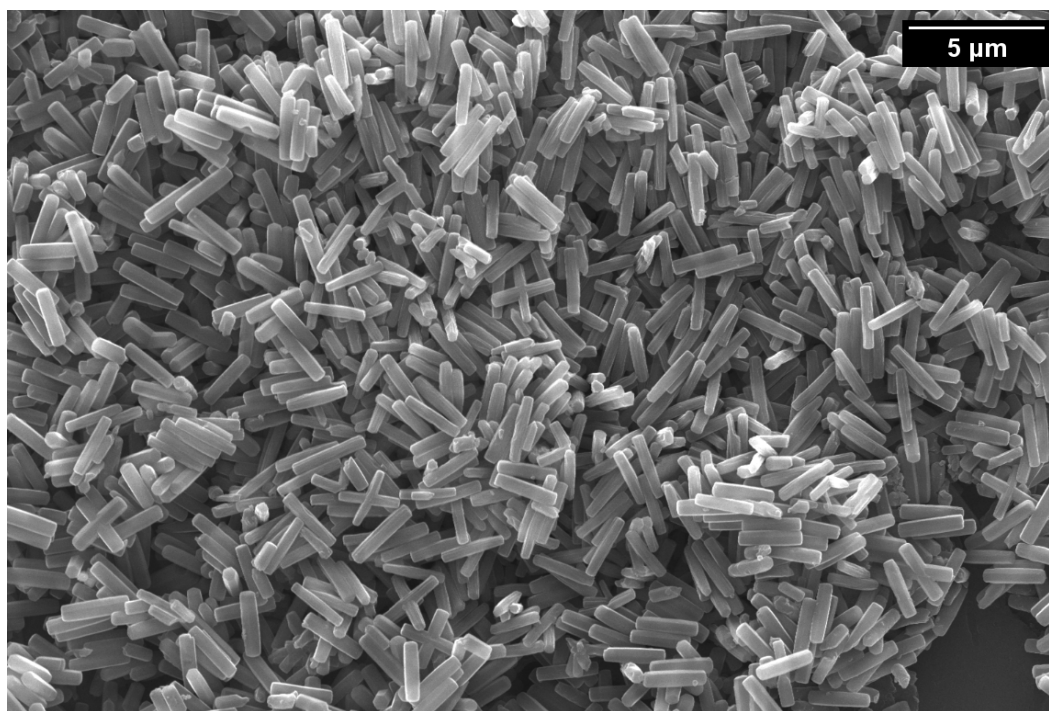
Figure 3.13 SEM image of Cr-SIM-NU-1000. Scale bar 5 micron.
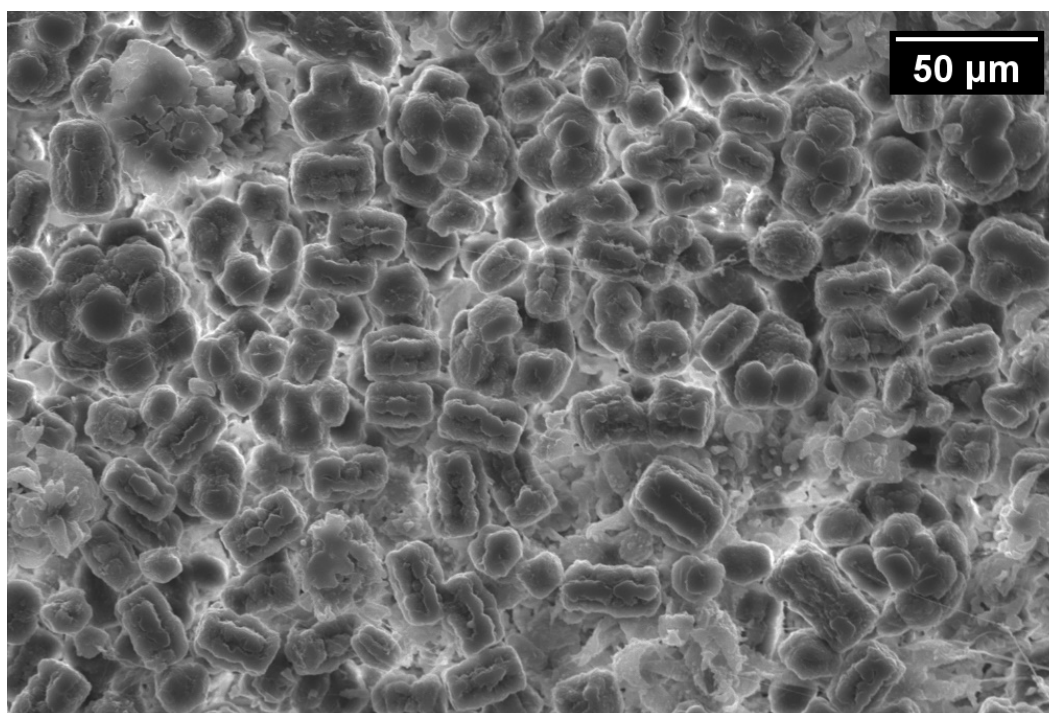
Figure 3.14 SEM image of post-catalysis Cr-SIM-NU-1000. Scale bar 50 micron.
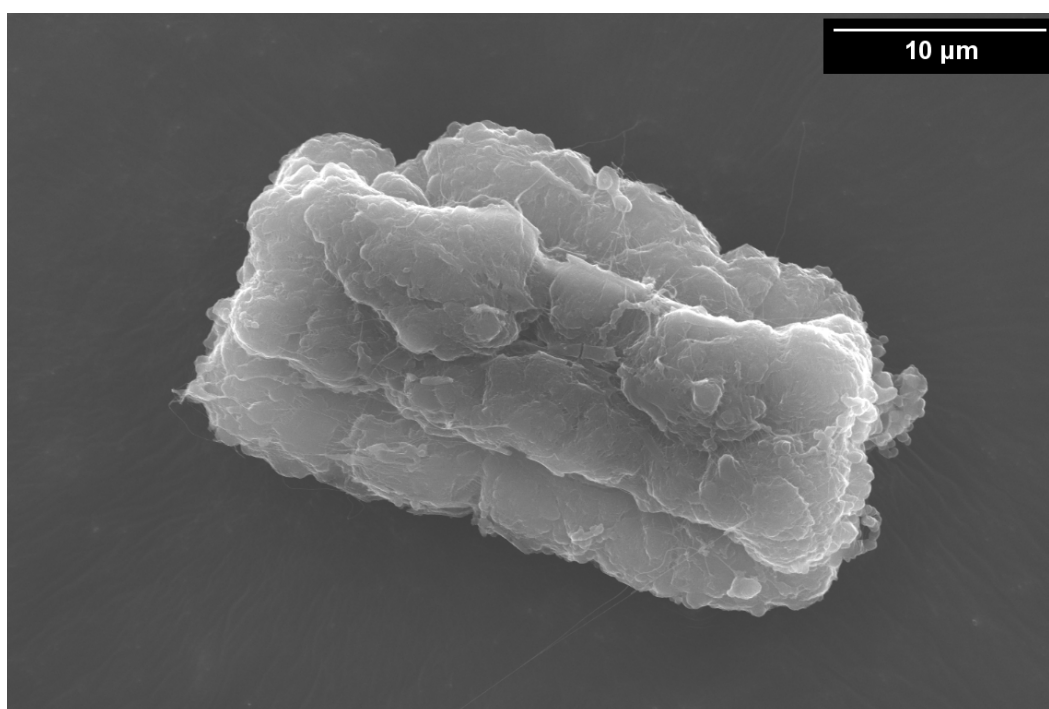
Figure 3.15 SEM image of post-catalysis Cr-SIM-NU-1000 at higher magnification. Scale bar 10 micron.
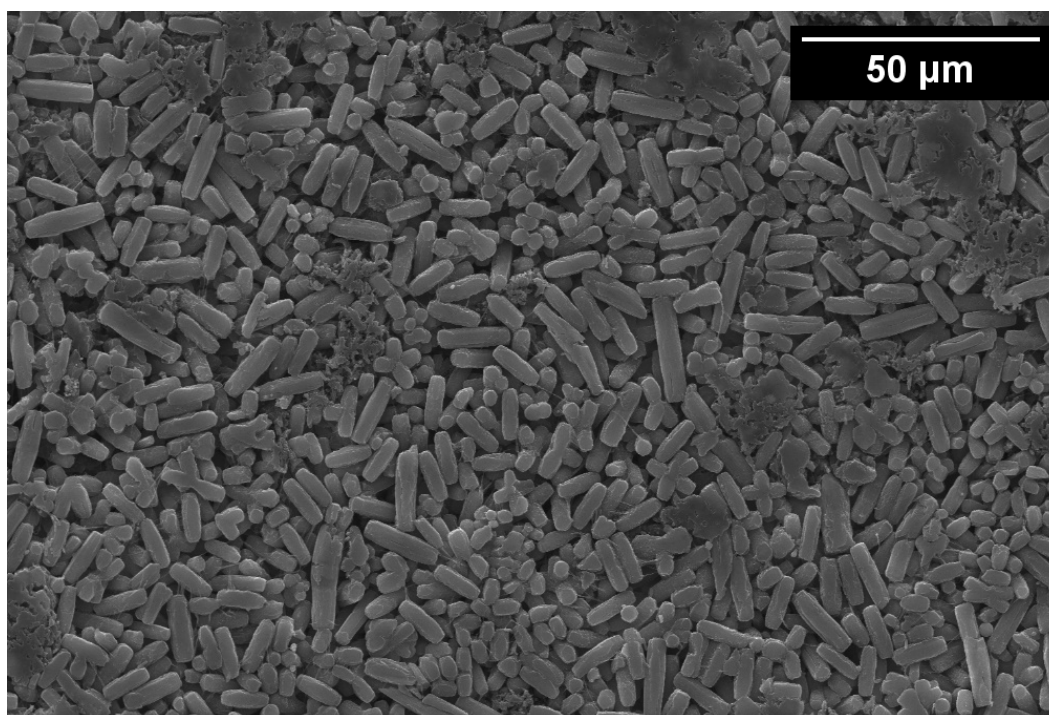
Figure 3.16 SEM image of post-catalysis Cr-SIM-NU-1000 washed with THF. Scale bar 50 micron.
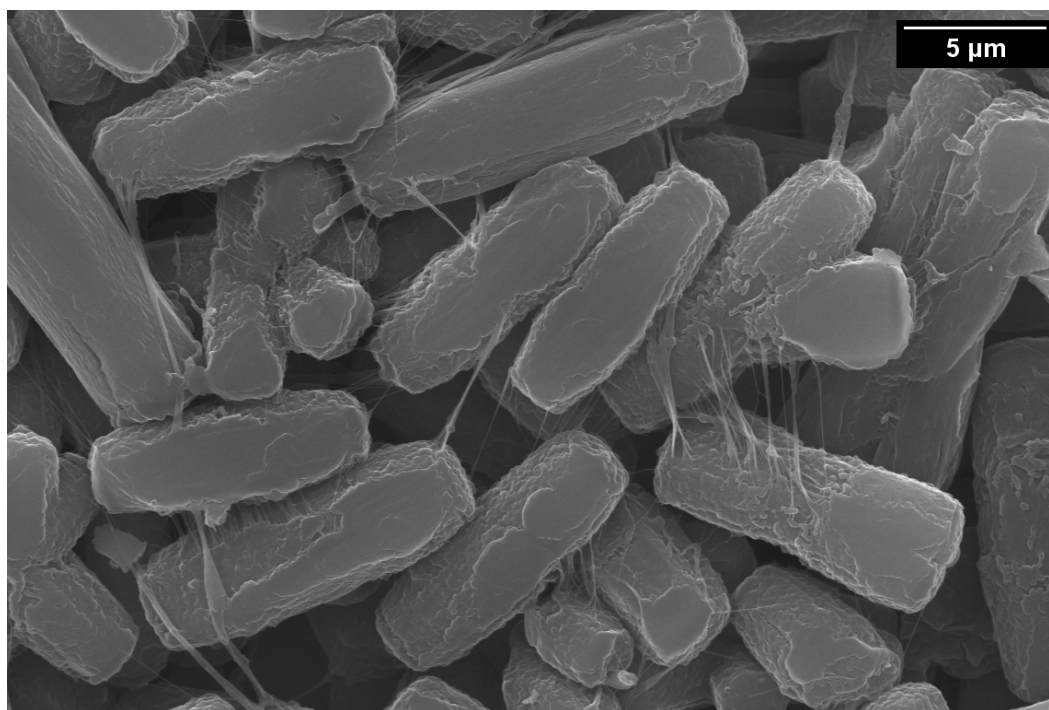
Figure 3.17 SEM image at higher magnification of post-catalysis Cr-SIM-NU-1000 washed with THF. Scale bar 5 micron.

Table 3.1 Productivity and turnover frequencies of Cr-SIM-NU-1000 compared to relevant literature materials.

Metric (@ RT)	Cr-SIM-NU-1000	Cr-MFU-4*l* [135]	MIL-101(Cr)-NDC[136]	MIL-53(Cr)[136]
Productivity*	4	90	5	17
TOF*	0.7	14	9×10^{-5}	2×10^{-4}

*Productivity shown in g PE g_{cat}^{-1} h^{-1} atm^{-1}
**TOF shown in s^{-1}

Table 3.2 Melting temperatures, heats of fusion, and percent crystallinity of polymer samples produced by Cr-SIM-NU-1000 at various ethylene pressures.

Ethylene Pressure (bar)	Melting Temperature (°C)	Heat of Fusion (J/g)	Crystallinity* (%)
5	136.9 ± 0.3	103 ± 38	35 ± 13
10	136.7 ± 0.3	108 ± 12	37 ± 4
20	136.4 ± 0.3	152 ± 31	52 ± 10
30	136.8 ± 0.6	139 ± 16	48 ± 6
40	136.9 ± 1.3	118 ± 30	40 ± 10

*Determined by the melting enthalpy calculated from DSC in comparison to $\Delta H°_m = 293$ J/g for 100% crystalline UHMWPE.

Table 3.3 Gel permeation chromatography data for polymer samples produced by Cr-SIM-NU-1000 at various pressures.

Reaction Pressure (bar)	Number Average Molecular Weight, M_n (kDa)	Weight Average Molecular Weight, M_w (kDa)	Polydispersity
5	0.54	3.2	7.1
10	1.4	2.2	2.4
20	3.2	7.8	2.5
30	2.6	4.6	1.9
40	440	920	2.0
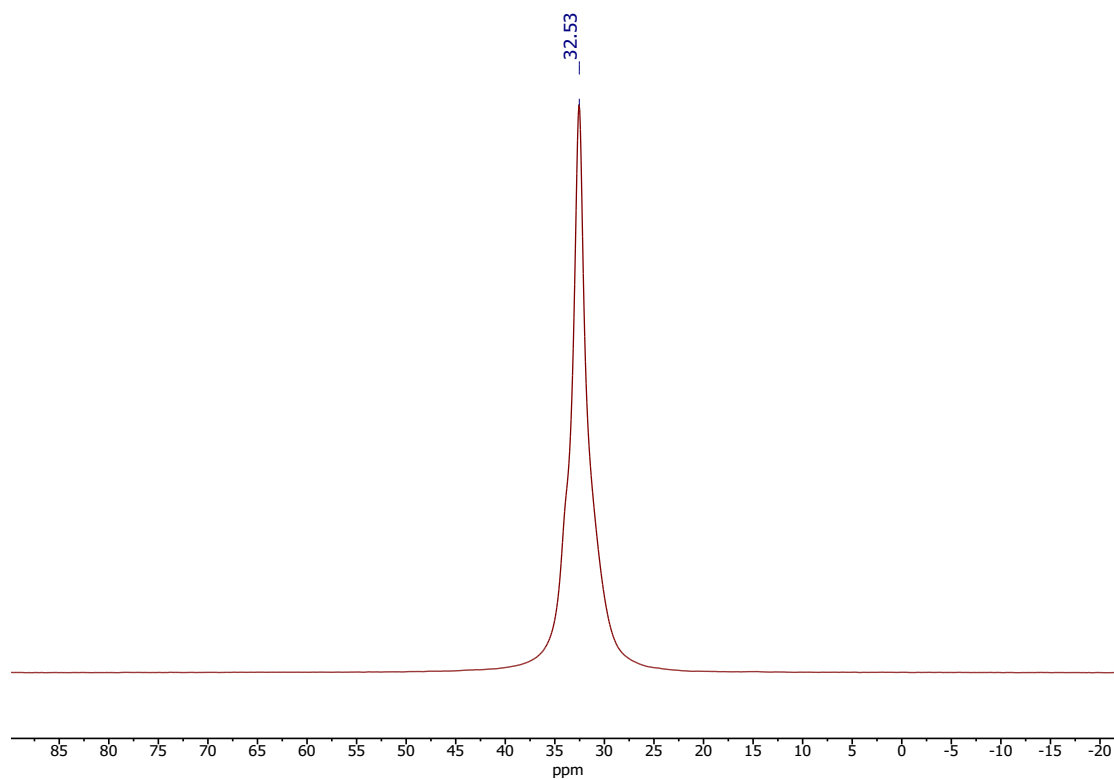
Figure 3.18 ^{13}C CP/MAS NMR spectrum of polyethylene product.
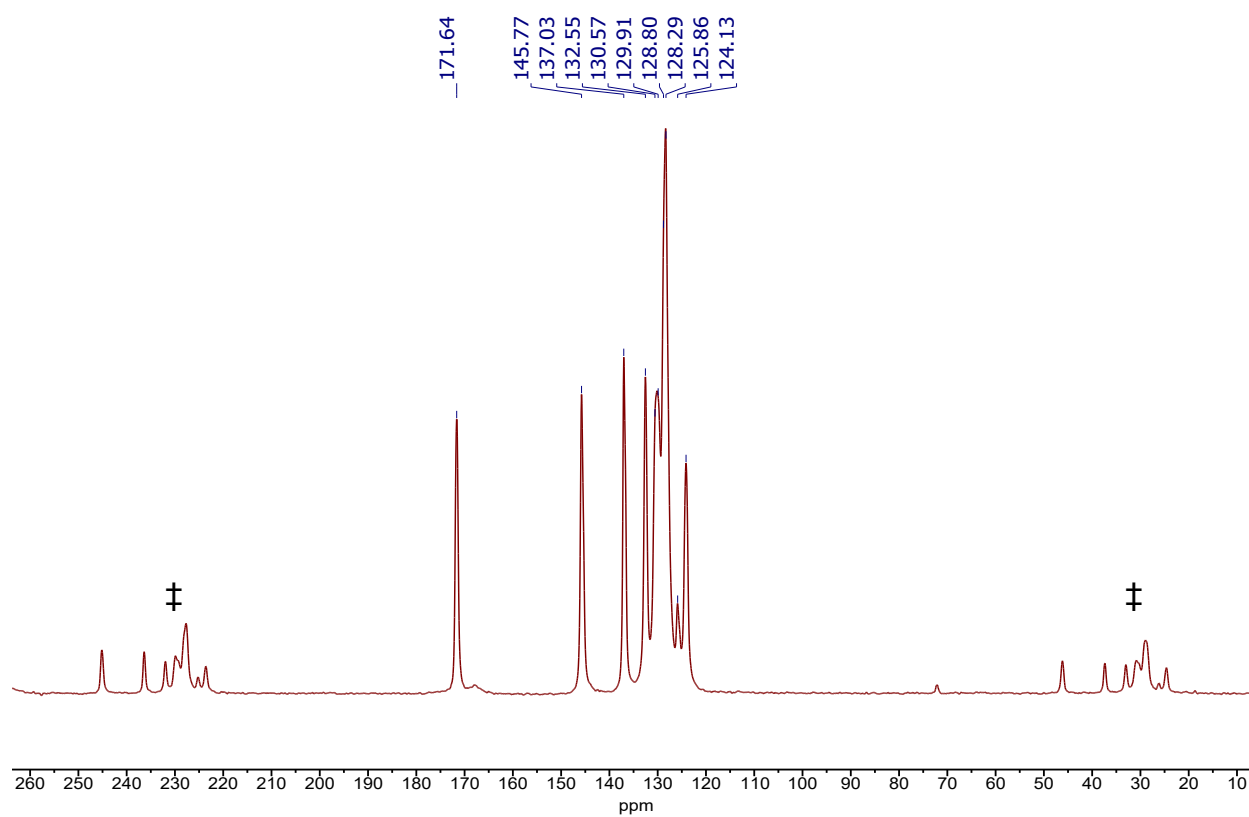
Figure 3.19 ^{13}C CP/MAS NMR spectrum of NU-1000 (spinning side bands indicated by ‡).
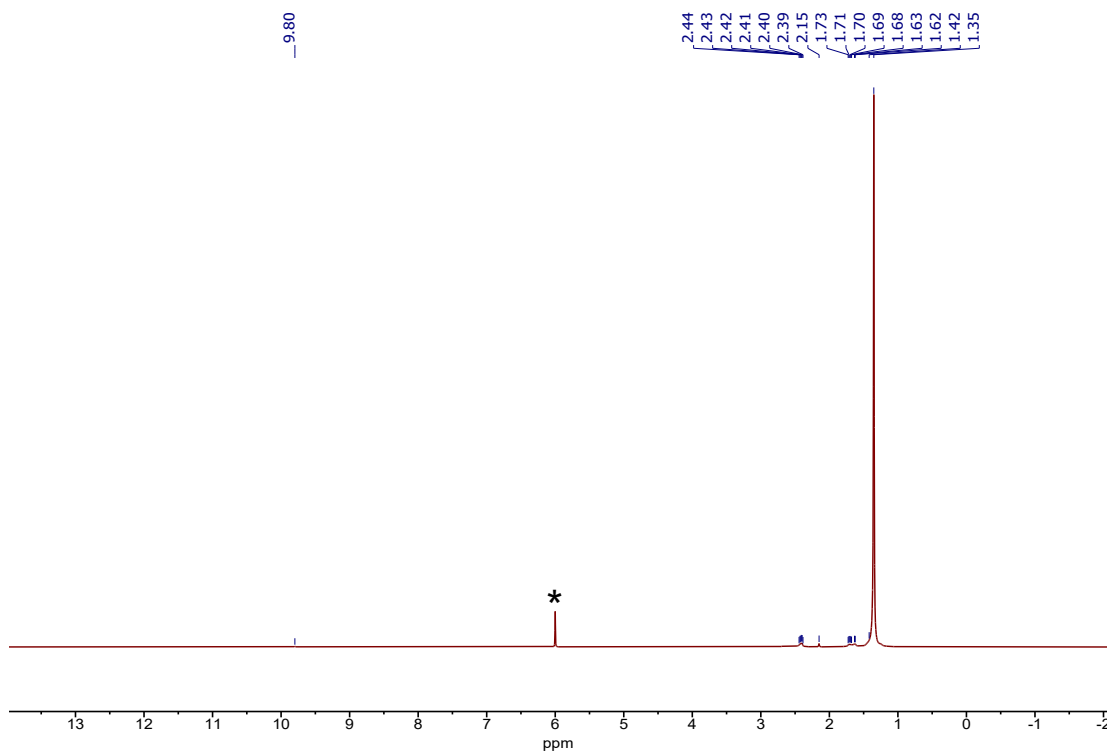
Figure 3.20 Initial ^{1}H NMR spectrum of polyethylene product in 1,1,2,2-tetrachloroethane-d_2 at 120 °C. * indicates residual solvent signal for 1,1,2,2-tetrachloroethane-d_2.
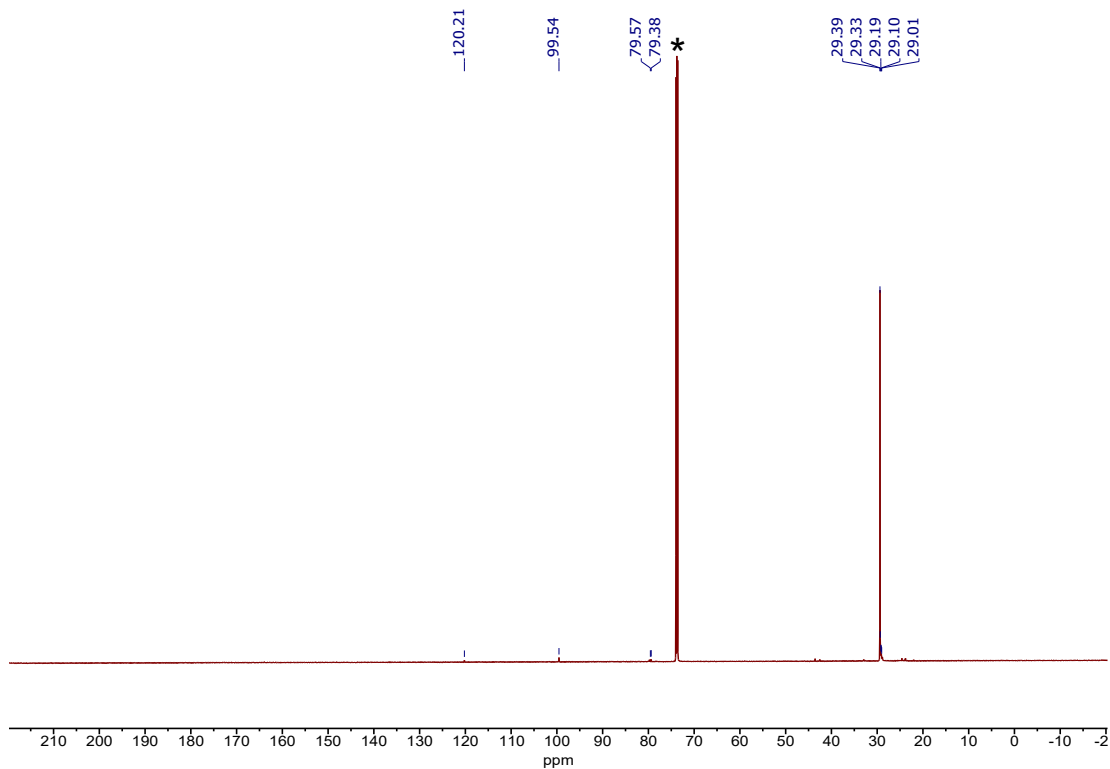
Figure 3.21 ^{13}C NMR spectrum of polyethylene product in 1,1,2,2-tetrachloroethane-d_2 at 120 °C. * indicates residual solvent signal for 1,1,2,2-tetrachloroethane-d_2.
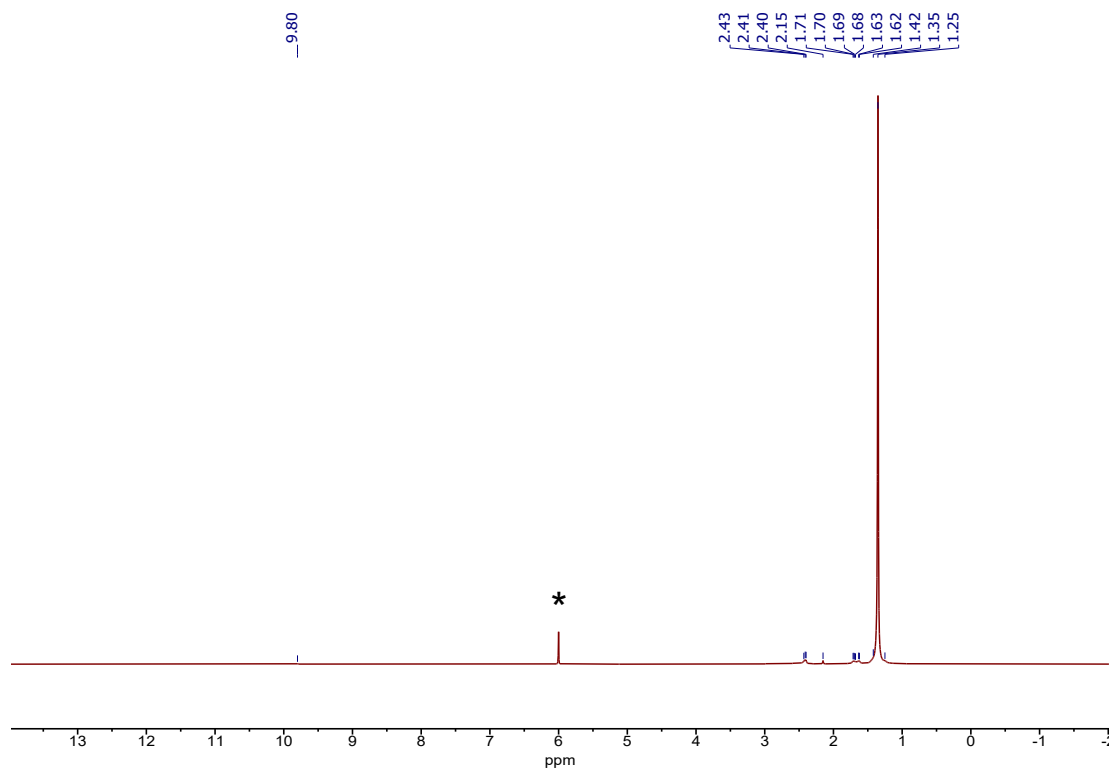
Figure 3.22 Final ^{1}H NMR spectrum of polyethylene product in 1,1,2,2-tetrachloroethane-d_2 at 120 °C. * indicates residual solvent signal for 1,1,2,2-tetrachloroethane-d_2.

Table 3.4 Crystal data and structure refinement for DEAC@Cr-SIM-NU-1000.

Identification code	DEAC@Cr-SIM-NU-1000_final
Empirical formula	$C_{45.27}H_{22}AlCl_2Cr_{0.18}O_{15.33}Zr_3$
Formula weight	1192.25
Temperature/K	200.15
Crystal system	hexagonal
Space group	P6/mmm
a/Å	39.433(3)
b/Å	39.433(3)
c/Å	16.2564(5)
α/°	90
β/°	90
γ/°	120
Volume/Å^3	21891(3)
Z	6
ρ_{calc}g/cm^3	0.543
μ/mm^{-1}	2.419
F(000)	3526.0
Crystal size/mm^3	0.101 × 0.039 × 0.018
Radiation	CuKα (λ = 1.54184)
2Θ range for data collection/°	6.848 to 79.946
Index ranges	-32 ≤ h ≤ 32, -32 ≤ k ≤ 32, -7 ≤ l ≤ 13
Reflections collected	29356
Independent reflections	2583 [R_{int} = 0.1309, R_{sigma} = 0.0374]
Data/restraints/parameters	2583/246/167
Goodness-of-fit on F^2	1.021
Final R indexes [I>=2σ (I)]	R_1 = 0.0859, wR_2 = 0.2454
Final R indexes [all data]	R_1 = 0.1033, wR_2 = 0.2678
Largest diff. peak/hole / e Å^{-3}	0.55/-1.22

Table 3.5 Cr-O bond distances comparison between Cr-SIM-NU-1000 and DEAC@Cr-SIM-NU-1000 structures.

Cr-SIM-NU-1000 Cr-O Distances (Å)	DEAC@Cr-SIM-NU-1000 Cr-O Distances (Å)
1.968	1.992
2.270	2.508
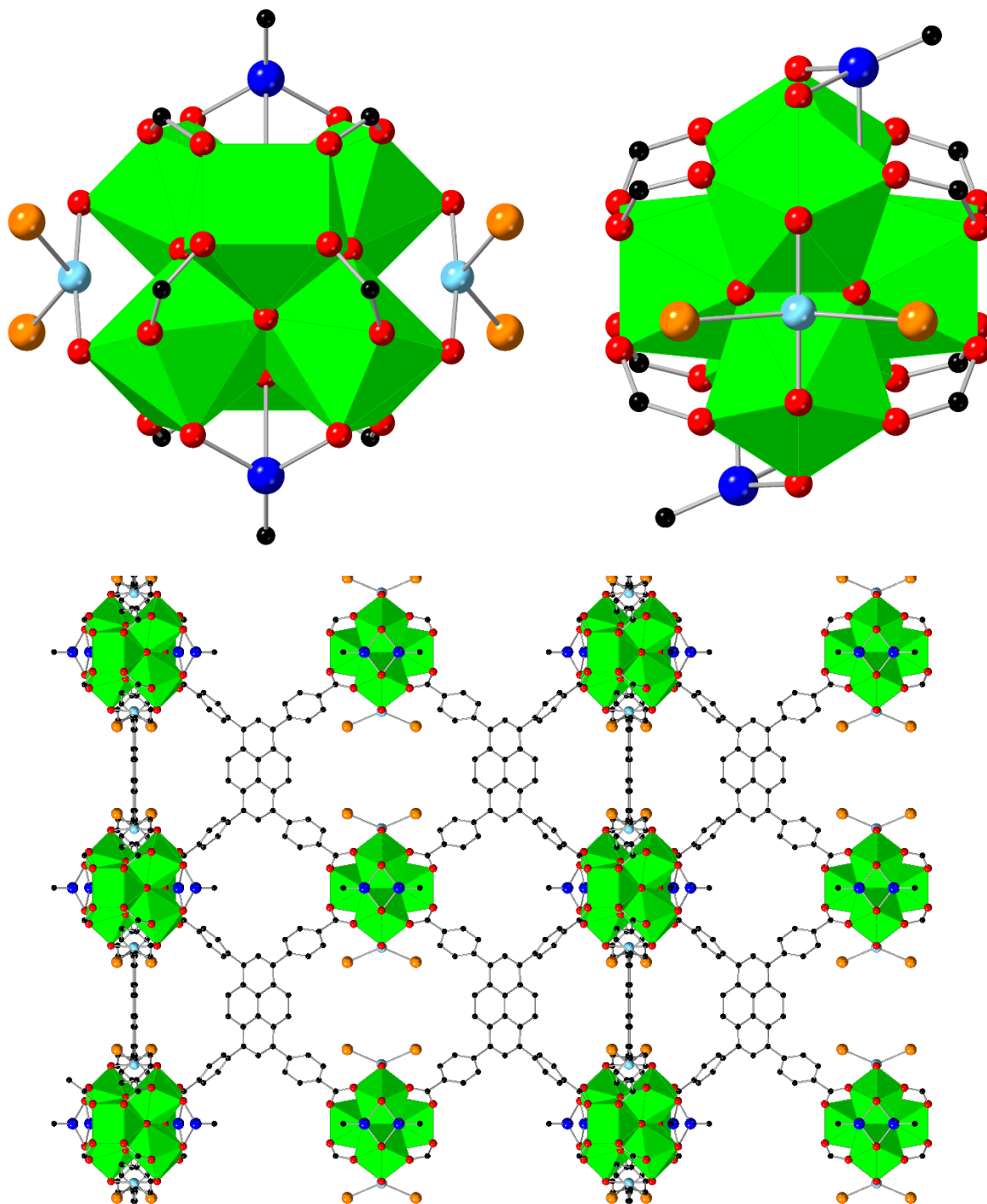
Figure 3.23 Views of the node (top) and window, or c-pore, along the a-axis (bottom) of DEAC@Cr-SIM-NU-1000 single crystal structure. DEAC viewed in crystallographically equivalent positions. Atom colors: C (black), O (red), Cl (orange), Al (light blue), Cr (dark blue), Zr (green), with hydrogens omitted for clarity.
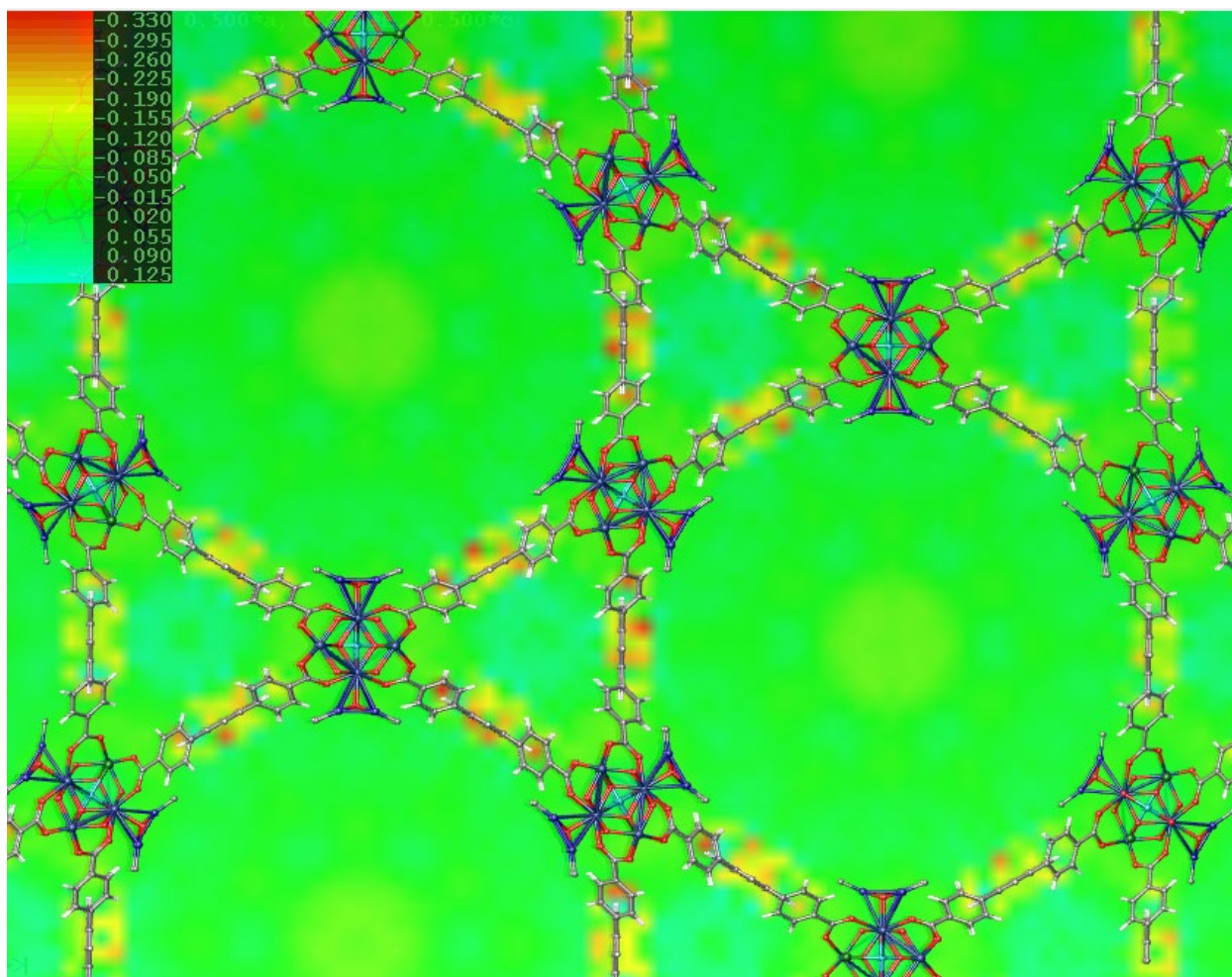
Figure 3.24 Residual electron density map of DEAC@Cr-SIM-NU-1000 single crystal structure viewing the hexagonal and triangular pores. Map shows minimal unassigned electron density within the hexagonal and triangular pores suggesting no remaining Al co-catalyst left within these pores. Electron density map generated by Olex2.
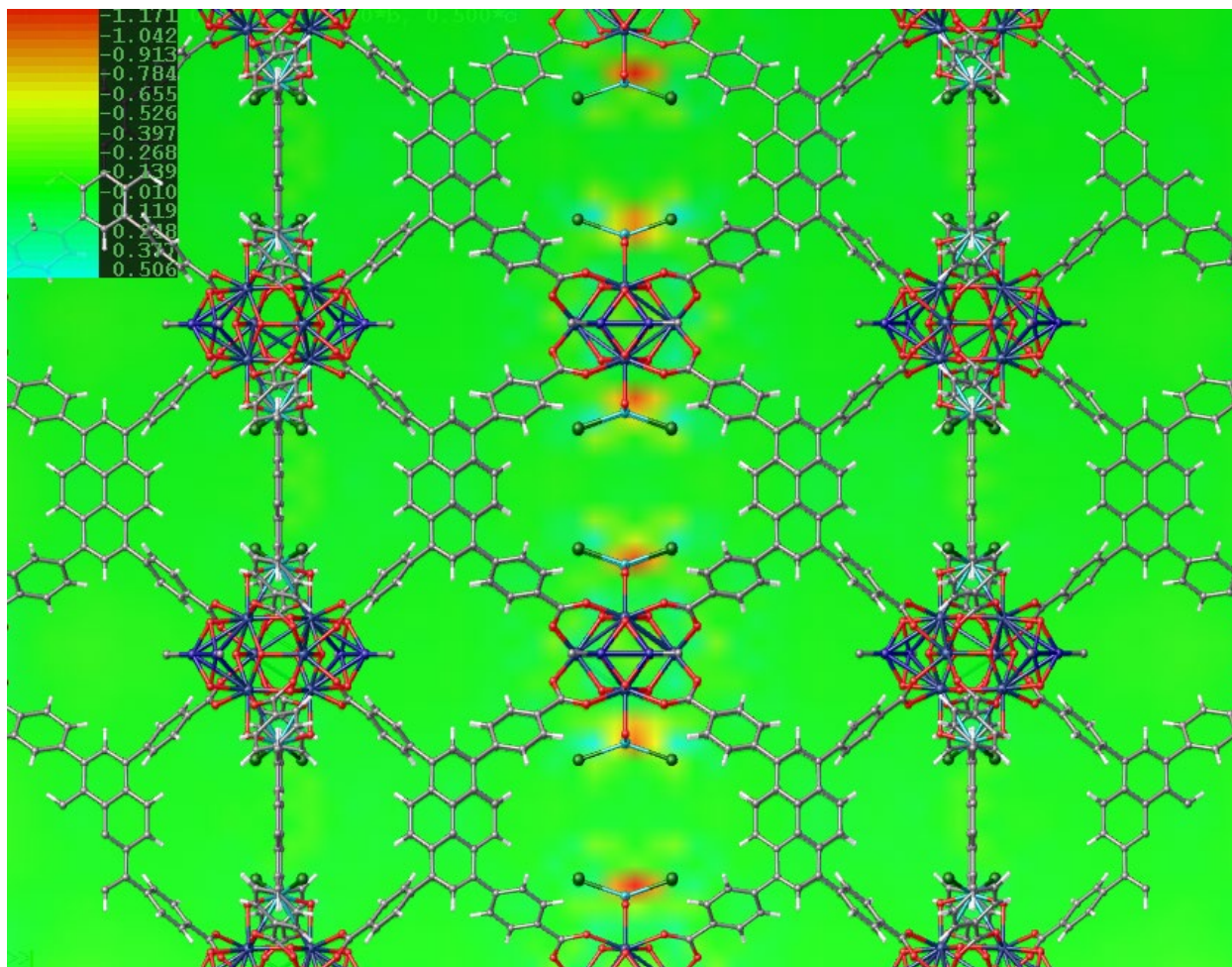
Figure 3.25 Residual electron density map of DEAC@Cr-SIM-NU-1000 single crystal structure viewing the internode spaces, or c-pores. Map shows additional unassigned electron density within c-pores indicating remaining Al co-catalyst left within these pores. Electron density map generated by Olex2.

Chapter 4. Active Site Determination and Mechanistic Insights in a MOF-Supported Polymerization Catalyst

Portions of this chapter appear in the following manuscript:

<u>Goetjen, T. A.</u>; Ferrandon, M. S.; Kropf, A. J.; Lamb, J. V.; Delferro, M.; Hupp, J. T.; Farha, O.K., Active Site Determination and Mechanistic Insights in a MOF-Supported Polymerization Catalyst. *Submitted.*

4.1 Chapter Summary

The structural elucidation of catalyst active sites in heterogeneous catalysts when supported by traditional metal oxides remains a challenge despite the advanced characterization techniques that have been developed. The catalyst deposition site nonuniformity in metal oxides inhibits clear structural characterization through bulk spectroscopic methods and rules out the use of single crystal X-ray diffraction. However, for metal–organic framework(MOF)-supported catalysts the crystallinity and uniform structures of the underlying support enhance our ability to identify pre-catalyst and catalytically active sites and open the door to using single crystal X-ray diffraction coupled with spectroscopy under reaction conditions. The use of *in-situ* X-ray absorption spectroscopy identifies the catalytically active site in diethylaluminum chloride (DEAC) pre-treated DEAC@Cr-SIM-NU-1000 to be a Cr-ethyl when used for ethylene polymerization. Further kinetics experiments elucidate the effects of ethylene pressure, temperature, catalyst loading, and co-catalyst loading, furthering mechanistic knowledge and helping to deconvolute the structure-function relationship.

4.2 Heterogeneous Catalysis and Structure-Function Relationships

Heterogeneous catalysts serve numerous purposes in our daily lives. From being the active component in the catalytic convertors in our vehicles to enabling the process to generate fertilizer to feed our global population, heterogeneous catalysts are essential in society.[158] Through the use of solid supports heterogeneous catalysts exhibit enhanced stability, recyclability, and processability, as well as more recent success towards sustainability.[159] However, with rising demand for more economically efficient transformations, and those that adapt to generate fine chemicals,[160-161] the next generation of catalyst materials is targeted to improve upon the previous generation and achieve these goals.[162-163]

The study of structure-function relationships in catalysis research leads to the development of design rules for the next generation of catalyst materials.[164] Of great importance to this process is obtaining knowledge of the structure of the catalytically active site at the atomic level. While typically facile with homogeneous molecular catalyst species,[165] the definitive determination of the active site structure of catalysts deposited on traditional heterogeneous catalyst supports such as silica, alumina, or other bulk metal oxides, is non-trivial due to the non-uniformity of catalyst deposition sites. One high profile example is the Phillips catalyst, Cr on SiO_2, which accounts for approximately 50% of world polyethylene[7] production yet the true active site structure and electronic environment is debated to this day,[6] sometimes with great intensity.[166-168] The burgeoning field of surface organometallic chemistry (SOMC) strives to bridge the gap between both homogeneous and heterogeneous catalysis,[169-170] in order to take advantage of the benefits of both fields including the well-defined structures of molecular catalysts. SOMC has yielded insights into the nature of active sites of a number of industrially relevant catalysts,[171] however it still relies upon metal oxide supports which often lack ordered structures. The use of crystallographically well-defined, porous solid supports approaches the same method of bridging the gap from the starting point of the catalyst support and building up.

4.3 Metal–Organic Frameworks for Deriving Structure-Function Relationships

Metal–organic frameworks (MOFs) have become increasingly studied as ordered and uniform catalysts or catalyst supports in the field of heterogeneous catalysis.[12, 71, 172-174] Comprised of inorganic nodes, either metal ions or clusters, and organic linkers, ligands that form coordination bonds to the nodes, MOFs are multidimensional, hybrid, porous networks that have been studied for many applications.[14, 110, 175] MOFs importantly provide a platform for fundamental understanding of structure-function relationships due to their crystallinity and therefore the ability

to develop an atomic-level picture of catalyst sites by single-crystal X-ray diffraction.[59, 137, 176-177] In addition, their tunable structural components and wide variety of 3-dimensional structures allow for the tailor-made development of catalyst supports.[178] Using MOFs as a structurally well-defined platform, even bulk spectroscopic data, coupled with crystallographic characterization, can provide unique insight into structure-function relationships.[179-180] The key benefit to spectroscopic measurements is the ability to perform *in-situ* or *operando* experiments that enable the determination of catalyst structures under relevant reaction conditions. The pairing of a crystal structure before exposure to reaction conditions with a spectroscopic measurement during exposure to reaction conditions provides useful insight into the evolution of catalyst structures and the identification of the catalytically active site. [181]

Herein, we utilized a previously demonstrated MOF-based ethylene polymerization catalyst,[50, 176] Cr-modified NU-1000 as a structurally well-defined system to probe structural evolution under reaction conditions. Additionally, kinetic experiments that look at the role of catalyst loading, temperature, ethylene pressure, and co-catalyst loading were performed to further interrogate the mechanism of polymerization. A well-informed mechanism is suggested based on the kinetic data in this study and *in-situ* X-ray absorption spectroscopy (XAS) measurements under high-pressure ethylene. The catalytically active site is determined to be the Cr-ethyl that is formed after treatment with alkyl aluminum co-catalyst since the *in-situ* XAS shows no change upon exposure to ethylene. This finding also indicates strongly that the polymerization mechanism follows the linear chain insertion mechanism since a change in the EXAFS spectrum is expected for a metallacycle mechanism which would include multiple metal-carbon bonds.

4.4 Active Site Determination Using *In-Situ* X-ray Absorption Spectroscopy

Definitive determination of catalyst active-site structures is a challenge with most heterogeneous catalysts. For the DEAC@Cr-SIM-NU-1000 system, the as-synthesized Cr-SIM-NU-1000[50] and DEAC@Cr-SIM-NU-1000[176] have both been crystallographically characterized (see **Figure 4.1**). The former includes a tetrahedrally coordinated Cr ion ligated to three oxygen-containing node grafting species along with a charge-balancing chloride ion. The latter retains that same structure but for the charge balancing chloride ion, which is replaced by an ethyl group transferred by DEAC, shown by the Cr-C resolved in the structure. While these insights are very useful in determining structure-function relationships, they fall short of identifying the catalyst structure under relevant reaction conditions.
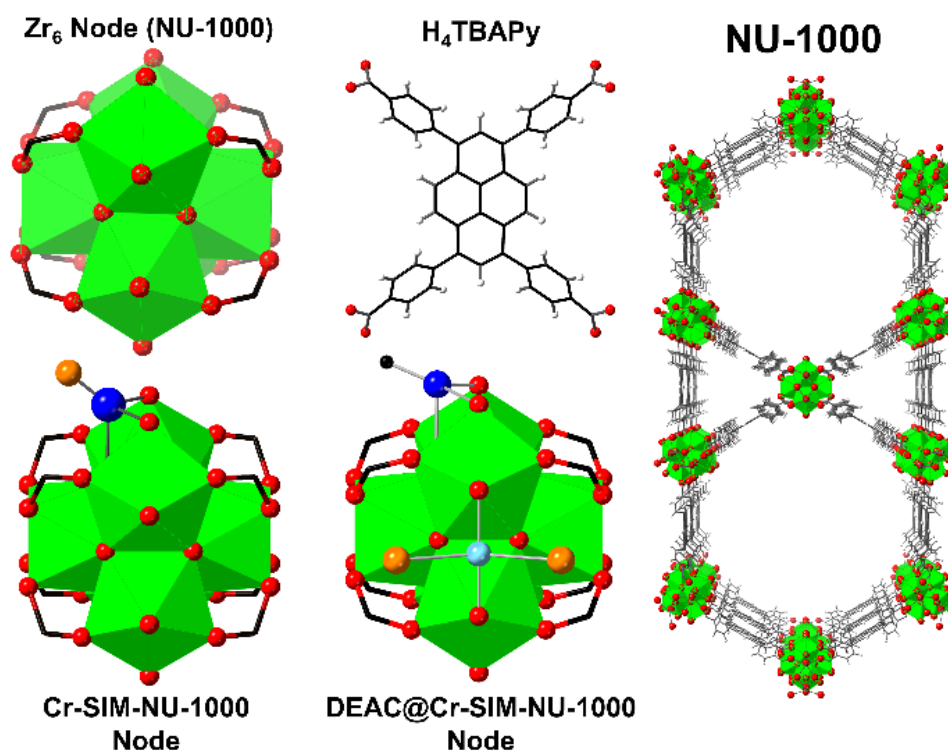
Figure 4.1 Structural representation of components of MOF NU-1000, NU-1000 structure, Cr-SIM-NU-1000 node, and DEAC@Cr-SIM-NU-1000 node based on experimental single crystal X-ray diffraction data. Atom colors: H (white), C (black), O (red), Cl (orange), Al (light blue), Cr (dark blue), Zr (green). MOFid for NU-1000: Zr.HVCDAMXLLUJLQZ.MOFkey-v1.csq.[182]

Therefore, we turned to *in-situ* X-ray absorption spectroscopy to lend us insight into the catalytically active site under high pressure ethylene at conditions relevant to ethylene polymerization reactions. After treating bulk Cr-SIM-NU-1000 with DEAC to generate DEAC@Cr-SIM-NU-1000, it was then diluted with carbon black and packed into a Kapton capillary to be used in a home-built high-pressure capillary reactor setup. Cr-SIM-NU-1000 was also measured using the same setup to serve as a baseline material.

Spectra for Cr-SIM-NU-1000 were collected at room temperature under air since the material had not yet been treated with the air-sensitive co-catalyst. Subsequent spectra for DEAC@Cr-SIM-NU-1000 were collected under either N_2 or C_2H_4. Before exposure to ethylene, spectra under N_2 were collected for DEAC@Cr-SIM-NU-1000. Then, DEAC@Cr-SIM-NU-1000 was subjected to ethylene flow at 100 psi over the course of 6 hours, with multiple spectra being collected during that time. The spectra were then processed and the XANES and EXAFS data were analyzed to assess electronic and structural changes in the materials (see **Figures 4.10-4.12** for *k*-space spectra).
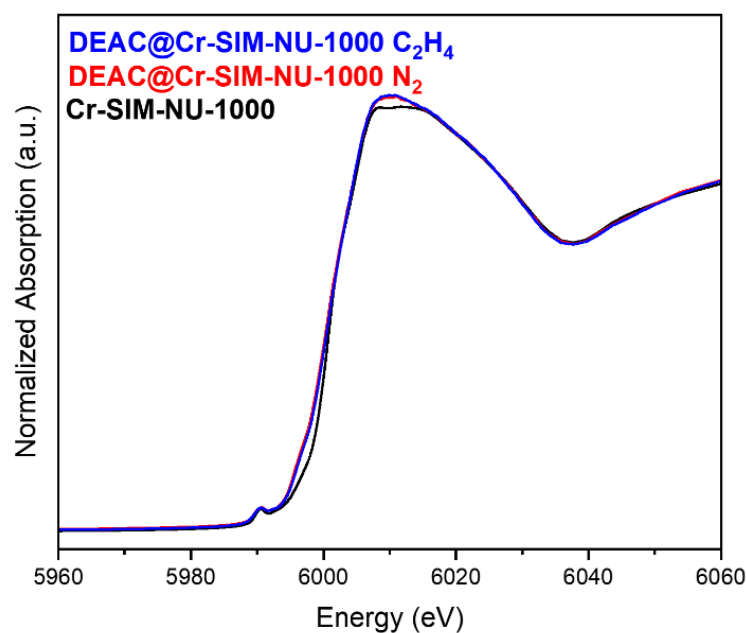
Figure 4.2 XANES region of normalized X-ray absorption spectra of Cr-SIM-NU-1000 (black), DEAC@Cr-SIM-NU-1000 under N_2 (red), and DEAC@Cr-SIM-NU-1000 under C_2H_4 (blue).

First, looking at the XANES region (see **Figure 4.2**), there is a slight difference in edge energy for Cr-SIM-NU-1000 versus DEAC@Cr-SIM-NU-1000, indicating a difference in Cr electronic environment, even before exposure to ethylene. A lack of substantial change in EXAFS indicates that there is not a large difference in structure, nor is there a detectable change in coordination number. This finding is consistent with available single-crystal X-ray structural data for Cr-SIM versus DEAC@Cr-SIM, there being a difference in the chemical identity of one ligand, but no change in the total number of ligands or in their geometric arrangement around the chromium center. Full fitting of the EXAFS Fourier transform was found to be non-trivial due to the proximity of the node and various scattering paths that would convolute those for the ligands of the Cr species. Additionally, the inclusion of the number of paths for the expected structure based on the single-crystal structure would exceed the number of independent points allowed for proper fitting.

Following this analysis, we looked at differences between spectra for DEAC@Cr-SIM-NU-1000 under N_2 versus C_2H_4. If the active-site differs from the Cr-ethyl found in the crystal structure of DEAC@Cr-SIM-NU-1000, then there would be a noticeable change in the XAS spectrum compared to the N_2 spectrum. However, if the active site is the single Cr-ethyl unit, then there would be no significant change in the XAS spectra. Furthermore, if the operant catalytic mechanism were the metallacycle-based mechanism, then one would expect to see an increase in the Cr coordination number and therefore a substantial change in the XAS spectrum. On the other hand, if the operative polymerization mechanism is linear chain insertion, the active-site would look essentially no different from the Cr-ethyl unit in terms of the local coordination environment that is probed by XAS. In fact, a lack of change after exposure to ethylene is what was observed.

Polyethylene formation was evidenced, in part, by the increasing absorption in the transmission XAS data with time (see **Figure 4.3**). Increases are expected as the polymer fills voids between particles and thereby increases X-ray absorption.
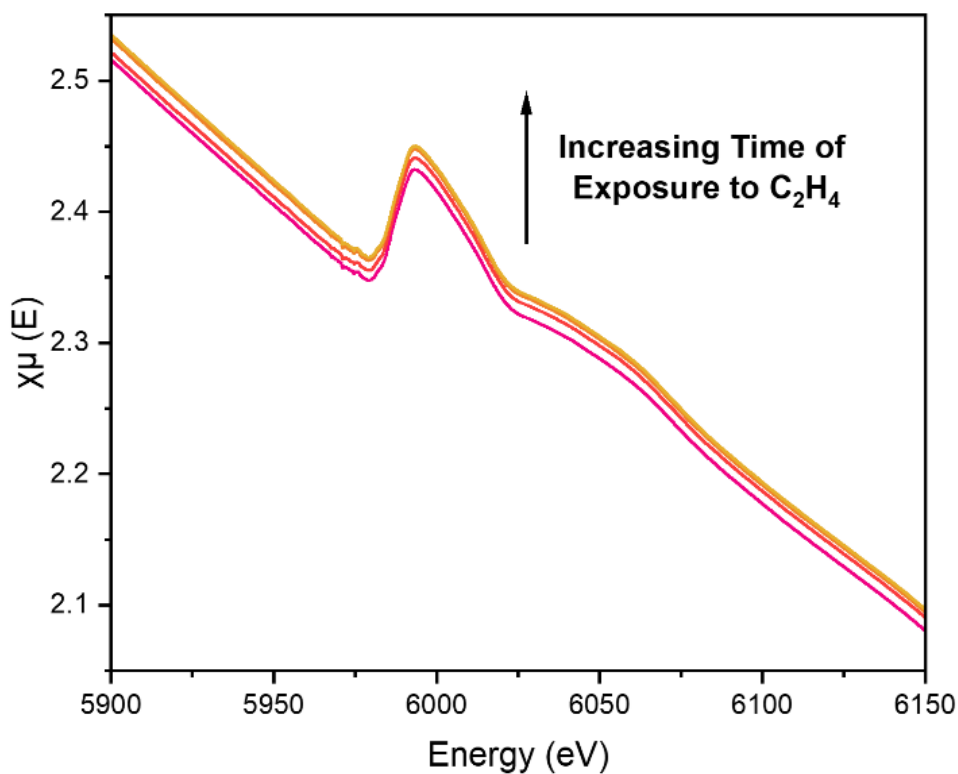
Figure 4.3 Transmission X-ray absorption spectra for DEAC@Cr-SIM-NU-1000 under flowing C_2H_4 at 100 psi over the course of 6 hours.

Looking further to the fluorescence data, the spectra for the N_2 vs. C_2H_4 exposed DEAC@Cr-SIM-NU-1000 show essentially no differences. Fourier transforms of the two EXAFS spectra reveal only very slight differences (see **Figure 4.4**). This finding tells us that the active-site of this catalyst is in fact the Cr-ethyl generated by DEAC treatment, and that Cr-catalyzed ethylene polymerization proceeds through a linear-chain-insertion, rather than metallacycle-formation, mechanism.
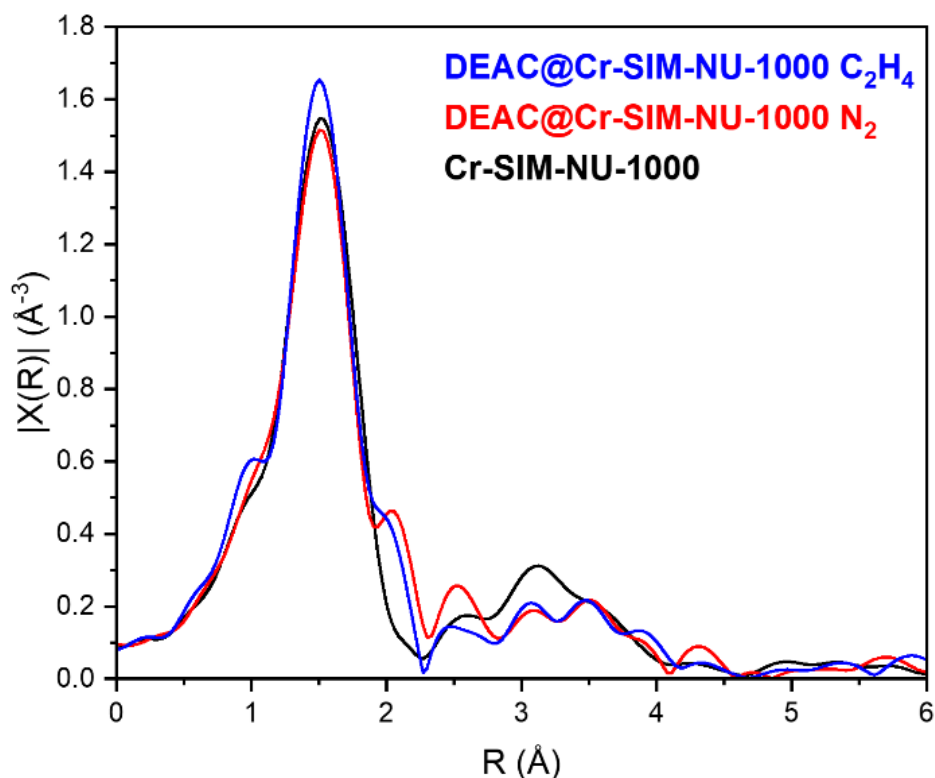
Figure 4.4 The k^2-weighted magnitude of the Fourier transforms of EXAFS spectra for Cr-SIM-NU-1000 (black), DEAC@Cr-SIM-NU-1000 under N_2 (red), and DEAC@Cr-SIM-NU-1000 under C_2H_4 (blue). FT was generated using a k-range of $3 - 11$ Å^{-1}.

4.5 Ethylene Polymerization Kinetics

Unlike our previous study of the ethylene polymerization activity of DEAC@Cr-SIM-NU-1000, the following kinetics studies were performed on DEAC pre-treated isolated powders without the use of solvent. Using conditions from the earlier study, monitoring reaction progress via ethylene pressure was complicated by the solubility of ethylene in the solvent, *i.e.* heptane.[183] To circumvent that issue we pre-treated Cr-SIM-NU-1000 samples with DEAC, isolated the modified MOF powders, and then ran the ethylene polymerization reactions neat.

The reaction parameters evaluated were catalyst loading, ethylene pressure, reaction temperature, and co-catalyst loading (see **Table 4.3** for reaction parameters). Each reaction was performed in glass finned vials within a high-throughput series of pressure vessels with glass beads to break up generated polymer granules (**Figure 4.9**). Ethylene pressure was tracked over the time

course of the reactions and polymer was collected to determine isolated yield. Thus, we evaluated kinetics via both continuous consumption of ethylene and integrated production of polymer.

The collected data present a complex picture. Catalyst loading, reaction temperature, ethylene pressure, and co-catalyst loading all seem to have an impact on overall polymer production, as well as on ethylene consumption; see **Figure 4.5**. Panel **e** shows broadly that, at least at longer reaction times, rates of ethylene consumption (at constant ethylene pressure) increase with increasing catalyst loading (as one would qualitatively anticipate). Looking more closely at the panel, with a catalyst loading of 20 mg we see an apparent partial induction period of *ca.* 10 minutes, suggesting either a need for catalyst activation, despite the pre-incorporation of DEAC, or a delay in ethylene access to the catalyst, possibly due to slow initial ethylene permeation of excess DEAC enshrouding the active-site. Shortly after the induction period, the rate of ethylene consumption begins slowing – dropping by about 2-fold between t = 20 min. and t = 60 min., despite a constant ethylene pressure. For a stable catalyst, and absent any complications relating to active-site accessibility, we would anticipate an unchanging rate. The observed progressive decrease is perhaps suggestive of catalyst chemical deactivation, although other possibilities such as DEAC depletion, MOF-pore-blocking by product polymer, or more localized, polymer-product-based physical blocking of access catalyst active-sites cannot be discounted.

Plotted in panel *a* is the integrated (1 hour) productivity for polymer formation as a function of catalyst loading. In the simplest instance, because productivity is presented on a per-mole-of-catalyst basis, we would anticipate no variation with catalyst loading. Instead, the normalized productivity sharply increases as the catalyst loading increases. The chemical basis for this behavior is unclear, but presumably is entangled or enmeshed with whatever factors are responsible for the induction behavior shown in panel *e*. Close inspection of the panel seems to

indicate induction behavior with not only 20 mg catalyst loading, but also 10 and 5 mg; however, the induction time appears to be longer with the lower loadings.
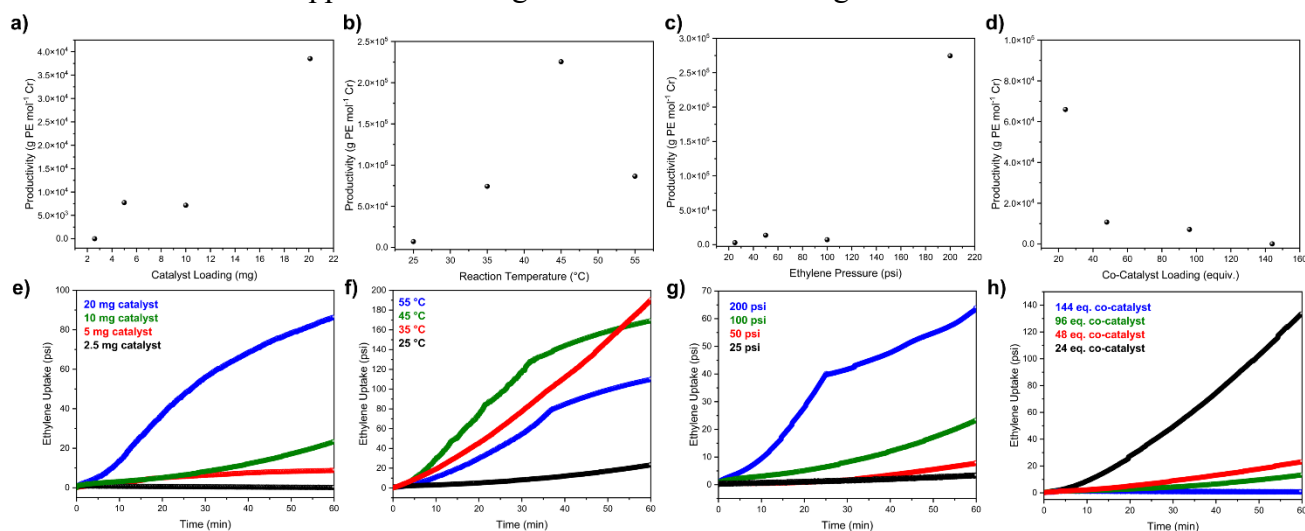
Figure 4.5 (a-d) polymer productivity vs. various reaction parameters (catalyst loading, reaction temperature, ethylene pressure, and equivalents of DEAC co-catalyst per equivalent of Cr catalyst), and (e-h) ethylene uptake vs. time, where the same four reaction parameters have been varied. Polymer production was evaluated after 1 hour. Note that plots in panels a-d are normalized for the moles of catalyst present, but that plots in panel e-h are not normalized. For ease of scaling across panels, note that the 1st point in panel a, the first point in panel b, the third point in panel c, and the third point in panel d, are presentations of the same experimental result and necessarily correspond to the same set of reaction conditions and parameters. Unless otherwise specified, reaction conditions are: 10 mg catalyst, 96 equivalents DEAC, C$_2$H$_4$ continuously refilled to a constant pressure of 100 psi, 25 °C. For conversion from psi to bar, divide by 14.5.

By increasing the reaction temperature from 25 °C to 35 °C, both ethylene consumption and polymer production increase significantly. However, when increased to 45 °C, polymer production drastically increases but ethylene consumption changes rates after 30 minutes likely indicating some form of catalyst deactivation. Further raising reaction temperature to 55 °C shows a decrease in both polymer production and ethylene consumption, with the latter having a similar change in rate after 35 minutes of reaction time. Therefore, the increased temperatures appear to accelerate the deactivation pathway of this catalyst, whether that is through polymer formation blocking the pores of the MOF, or decomposition of the active site. This is likely an impact of the temperature because a stability test of this reaction at 25 °C over the course of 5 hours shows continued

reactivity measured by the consumption of ethylene over time, without an inflection point indicating some form of deactivation under these standard conditions (see **Figure 4.6**).
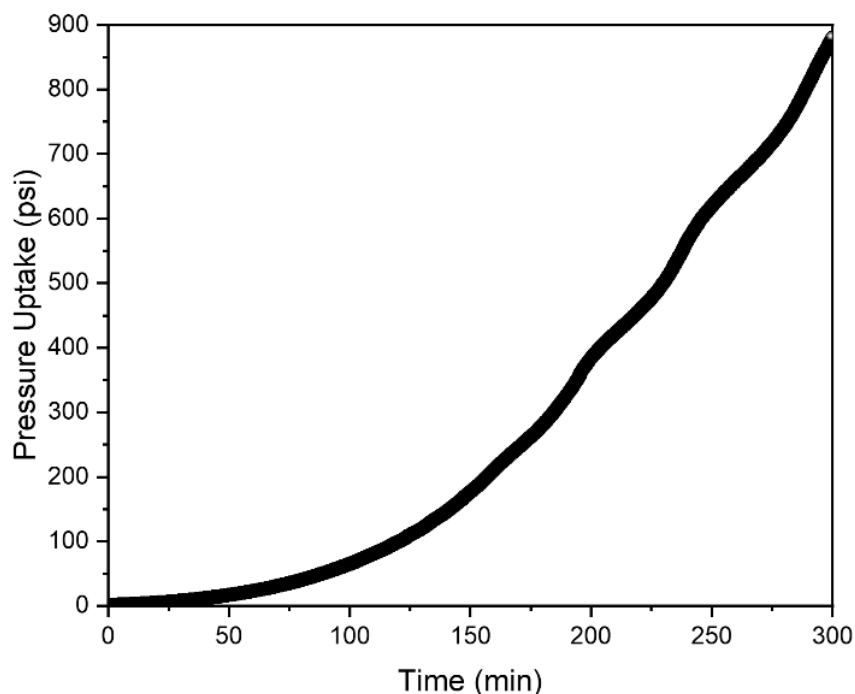
Figure 4.6 Ethylene consumption profile of ethylene polymerization reaction using 10 mg DEAC@Cr-SIM-NU-1000 treated with 96 eq. DEAC run under 100 psi ethylene at 25 °C for 5 h.

Next, the effect of ethylene pressure was investigated. To be expected, ethylene consumption increases, albeit slightly, with increasing ethylene pressure from 25 psi to 100 psi. When increased from 100 psi to 200 psi, a significant change in initial rate is observed and an inflection point in the ethylene consumption profile is seen, similar to that seen in the temperature screening reactions. It is clear too, based on polymer productivity, that between 100 and 200 psi there is a change in catalyst behavior. Finer grain screening of pressure would be needed to identify the precise pressure at which this change occurs, but it would make sense if a higher rate caused fast polymer formation that then led to blocking of the MOF pores at an earlier time than with reactions run at lower ethylene pressures. Lastly, the effect of co-catalyst loading was screened. Most ethylene polymerization catalysts using alkyl aluminum co-catalysts are run in a slurry with substantial excess of the co-catalyst (up to 1000 equivalents, relative to the catalyst) which is

soluble in the solvent used. In this study, the catalyst was pre-treated with the co-catalyst, diethylaluminum chloride, and the reaction was run neat with isolated powder catalyst treated at a range of 24 to 144 equivalents of Al:Cr (see **Table 4.1**). As the co-catalyst treatment equivalents is increased, there is an inverse correlation to the ethylene consumption, where the quickest and highest amount of ethylene consumed is at 24 equivalents and the lowest amount is at 144 equivalents. Both 48 and 96 equivalents show significantly lower ethylene consumption than 24 equivalents and essentially overlap. The polymer productivity follows a similar trend to the ethylene consumption. This is contrary to the results typically seen in slurry-phase reactions where additional co-catalyst equivalents show enhanced activity and is likely due to excess aluminum remaining within the pores and blocking access to catalyst sites through deposition of aluminum in the powder isolation process. It appears that each reaction parameter has an impact on the polymerization activity to a certain extent, with some parameters only showing significant differences at the bookend conditions. A possible explanation for the apparent deactivation observed and changes is ethylene consumption rates is a difference in rate of polymer formation, either insertion or propagation, versus chain termination. In the previous study of a slurry-phase reaction using this catalyst, the chain termination mechanism was chain transfer to the aluminum, a route which could be inhibited here since there is not additional DEAC free in solution to follow that step.

4.6 Polymer Characterizations

Characterization of the polymer products was inhibited by lack of solubility in solvents at high temperature for gel permeation chromatography (GPC). It is therefore likely that the polymer formed is of substantially large molecular weight or significantly cross-linked such that solubility is impeded. This lends insight into the possibility that termination of the polymer chains is strongly

disfavored and follows a potentially different mechanism than the chain transfer to the alkyl aluminum seen in solution-based experiments. This is likely due to the pre-treatment with DEAC rather than having free DEAC in solution during the reaction, causing the termination step of this polymerization to either be substantially slower chain transfer to the aluminum or an alternative such as β-hydride elimination. Characterization by NMR proved difficult for some samples for the same reason as GPC, however a representative sample under extended time conditions was able to be measured (see **Figures 4.14-4.15**). The presence of a peak in the ^{1}H-NMR at 3.95 δ, characteristic of olefins, provides support for a termination mechanism that follows β-hydride elimination. Additionally, ^{13}C-NMR shows a major peak at 29.6 δ which dominates others on either side of it, indicating that the polymer is predominantly linear. Differential Scanning Calorimetry (DSC) measurements reveal that the polymer produced at all conditions is high-density and moderately crystalline (46 – 63 %; see **Table 4.2**), with melting temperatures ranging from 132 – 136 °C.

4.7 Conclusions

We find from comparative isolated, versus *in-situ* structural characterization of the MOF-supported catalyst, DEAC@Cr-SIM-NU-1000, that the catalyst enables ethylene polymerization via linear-chain-insertion rather than via metallacycle formation. Generally speaking, increases in catalyst loading and ethylene pressure cause increases in catalyst-loading-normalized productivity, boosting the reaction temperature from 25 °C to 35 °C, as one would anticipate for a thermally activated catalytic process. Further increases, however, only diminish reactivity. From these and other results, we conclude that catalysis itself eventually renders catalyst active-sites physically inaccessible, either by $AlCl_3$ from degradation of DEAC or by product polyethylene – or, at high DEAC loadings, by DEAC itself. From polymer characterization, we find the presence of olefins

which supports a termination step of β-hydride elimination, different from the initial slurry study most likely due to the lack of free DEAC in solution. DEAC@Cr-SIM-NU-1000 was further characterized by *in-situ* X-ray absorption spectroscopy under high-pressure ethylene to determine the Cr-ethyl to be the active catalyst structure. Overall, this study demonstrates how structurally well-defined catalyst supports such as metal–organic frameworks enable the structural characterization of catalyst active sites under relevant reaction conditions using synchrotron spectroscopic techniques not convoluted by multiple catalyst sites.

4.8 Additional Information

4.8.1 Materials

Acetone, *N,N*-dimethylformamide (DMF), hydrochloric acid were purchased from Fisher Scientific (Waltham, MA) and used as received. Benzoic acid, trifluoroacetic acid (TFA), zirconyl chloride octahydrate, chromium(II) chloride (99.99% trace metals), and 1.0 M diethylaluminum chloride (DEAC) in heptane were purchased from Sigma-Aldrich (St. Louis, MO) and used as received. ***Caution diethylaluminum chloride is pyrophoric and should only be handled under an inert atmosphere and with care***. Anhydrous heptane and pentane were purchased from Sigma-Aldrich and further dried by soaking over 3 Å molecular sieves. UHP N_2 (99.999%), UHP Ar (99.999%), and UHP ethylene (99.9%) were purchased from Airgas (Radnor, PA) and used as received. 1,2,4-trichlorobenzene (TCB) was purchased from Fisher Scientific International, Inc. and used as received. 1,1,2,2-tetrachloroethane-d_2 (TCE-d_2) was purchased from Cambridge Isotope Laboratories, Inc. and used as received. 1,3,6,8-tetrakis(p-benzoic acid)pyrene (H4TBAPy) was synthesized based on literature procedure.[96]

4.8.2 Synthetic Methods

NU-1000 powder synthesis. 1,3,5,8-Tetrakis(p-benzoic acid)pyrene, was synthesized according to reported procedure.[96] NU-1000 was synthesized, acid activated, and washed according to previously published procedures.[32, 96]

Cr-SIM-NU-1000 powder synthesis. Cr-SIM-NU-1000 was prepared by previously reported procedure.[50] Cr-SIM-NU-1000 was prepared by mixing 200 mg NU-1000 into 25 mL of a 0.1 M $CrCl_2$ solution in N,N-dimethylformamide (DMF) and heated overnight at 100 °C. The sample was washed with fresh DMF (3 × 40 mL). Then the sample was washed with acetone (3 × 40 mL) to exchange the solvent to remove DMF and left to soak overnight in fresh acetone. The sample

was dried at 80 °C in a vacuum oven for 2 hours, and then thermally activated at 120 °C under dynamic vacuum on a Smart VacPrep for 16 hours.

DEAC@Cr-SIM-NU-1000 powder synthesis. DEAC@Cr-SIM-NU-1000 was prepared by previously reported procedure.[4][176] Freshly DMF washed Cr-SIM-NU-1000 powder was solvent exchanged to acetone by washing 3 times and then soaking overnight. Then, after decanting the acetone, the powder was placed in a vacuum oven at 80 °C for 3 hours. Then, it was thermally activated at 120 °C under dynamic vacuum on a Smart VacPrep for 16 hours. The powder was then transferred into an Ar filled glovebox. Next, it was soaked in anhydrous heptane before decanting the solvent and exposing the powder to 1.0 M diethylaluminum chloride in heptane consistent with the catalysis experiments. After 1 h, the solvent was decanted and exchanged for fresh heptane 3 times with a 30 min. soaking period in between. The solvent was then exchanged to pentane, where the powder was allowed to soak for a total of 1.5 h during which 3 washes and subsequent soaks were performed. After decanting as much pentane as possible, the powder was held under dynamic vacuum on a Smart VacPrep for 16 hours. The material was subsequently stored in an Ar-filled glovebox.

4.8.3 Catalysis Details

Ethylene Polymerization Kinetic Measurements in High Throughput Batch Reactor. For kinetic measurements, the Optimization Sampling Reactor (OSR, Unchained Labs Inc., Figure S1, left) located in a N_2-filled glovebox (MB 200B, MBraun) at the Argonne National Laboratory High-throughput Research Facility was used. It has 8 parallel batch reactors (40 mL each) with independent temperature and pressure control and common overhead stirring, which was set at 700 rpm for all experiments. The 25 mL OSR vials which have 8 indentations (Figure S1, right) were loaded with 10 glass beads to ensure proper mixing and breaking down of the polymer formed.

The ethylene pressure was monitored during each experiment. The procedure is automated and controlled by LEA software.

In-Situ X-ray Absorption Spectroscopy. X-ray absorption spectroscopy measurements were performed at Sector 10 BM-D of the Advanced Photon Source at Argonne National Laboratory. Samples (~ 10 wt%) were diluted with carbon black and ground into a uniform powder before being loaded into a Kapton capillary (ID: 1.47 mm, OD: 1.56 mm, Wall: 0.047 mm, Length: 70 mm) between quartz wool plugs. The capillary was loaded into a custom-built capillary reactor setup either within an Ar-filled glovebox (for DEAC@Cr-SIM-NU-1000) or on benchtop (for Cr-SIM-NU-1000). Samples were first purged with N_2 before initial fluorescence spectra were taken. Both transmission and fluorescence spectra were collected during exposure to C_2H_4 at 2 mL/min with the reactor pressurized to 100 psig over the course of 6 hours. Data analysis was performed using the Demeter XAS software package (v 0.9.26).[184]

4.8.4 Physical Characterization and Instrumentation

Powder X-ray diffraction (PXRD) data was collected at the IMSERC X-ray Facility at Northwestern University on a STOE-STADI-P powder diffractometer equipped with an asymmetric curved Germanium monochromator (CuKα1 radiation, λ = 1.54056 Å) and one-dimensional silicon strip detector (MYTHEN2 1K from DECTRIS). The line focused Cu X-ray tube was operated at 40 kV and 40 mA. Powder was packed in a 3 mm metallic mask and sandwiched between two layers of polyimide tape. Intensity data from 1 to 40 degrees 2θ were collected over a period of 5 mins.

Inductively coupled plasma optical-emission spectroscopy (ICP-OES) was performed at the QBIC facility at Northwestern University on a Thermo iCAP 7600 Spectrometer (ThermoFisher, Waltham, MA). In each preparation, ~3 mg samples were digested in 2 mL concentrated nitric acid in a 2-5 mL Biotage (Uppsala, Sweden) microwave vial. Biotage SPX microwave reactor

(software version 2.3, build 6250) was used to heat the mixture to 150 °C for 15 min. 300 µL of the digested sample was removed and diluted to 10 mL with ultrapure Millipore water.

^{1}H and ^{13}C{^{1}H} solution state NMR spectroscopy was conducted on a Bruker Avance III 500 MHz system spectrometer (11.7 T) equipped with two RF channels (1H = 500 MHz, 13C = 125 MHz). Sample data was acquired using TopSpin™ by Bruker. All collected spectra were referenced to residual solvent signals. NMR spectra were processed and integrated using Mnova by Mestrelab Research, following phase correction and baseline correction (Whittaker smoother). Initial ^{1}H solution state NMR spectra of the polymer product were collected in 1,1,2,2-tetrachloroethane-d_2 at 120 °C with 25 scans. D1 was set to 5.00 sec, SW was set to 16 ppm, and O1P was set to 6 ppm. Next, ^{13}C{^{1}H} solution state NMR spectra of the polymer product were collected in 1,1,2,2-tetrachloroethane-d_2 at 120 °C with 18,000 scans. D1 was set to 2.00 sec, SW was set to 240 ppm, and O1P was set to 100 ppm. After ^{13}C{^{1}H} solution state NMR data collection finished, final ^{1}H solution state NMR spectra of the polymer product were collected in 1,1,2,2-tetrachloroethane-d_2 at 120 °C with 25 scans. D1 was set to 5.00 sec, SW was set to 16 ppm, and O1P was set to 6 ppm. The polymer product was heated at 120 °C in 1,1,2,2-tetrachloroethane-d_2 prior to NMR data collection to aid in solubilization.

Differential scanning calorimetry (DSC) experiments were conducted using a TA Instruments Discovery DSC-25 and corresponding Trios software (v5.3.0.48151). For DSC of polymers, samples were heated in alumina crucibles under N_2 at 10 °C/min. from 25 °C to 200 °C and then cooled from 200 °C to 25 °C for two cycles.

Figure 4.7 Optimization Sampling Reactor (left) and vial with indentation (right).
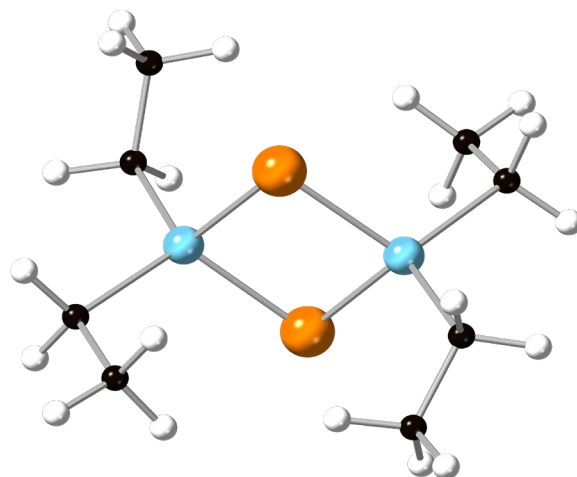
Figure 4.8 Structure of diethylaluminum chloride, which exists as a dimer at room temperature. Atom colors: Hydrogen (white), Carbon (black), Chlorine (orange), Aluminum (light blue).

Table 4.1 Cr and Al loading of DEAC@Cr-SIM-NU-1000 samples.

Targeted Al:Cr Treatment	Cr Loading (per Zr$_6$ node)	Al Loading (per Zr$_6$ node)	Al:Cr Measured
24	2	6.2	3.1
48	2	6.2	3.1
96	2	6.5	3.3
144	2	6.4	3.2

Table 4.2 Melting temperatures, heats of fusion, and percent crystallinity of polymer samples produced by DEAC@Cr-SIM-NU-1000 at various ethylene pressures.

Experiment #	Melting Temperature (°C)	Heat of Fusion (J/g)	Crystallinity* (%)
0	134.6	151	52
1	132.5	-**	-
2	134.2	151	52
3	134.5	165	56
4	134.2	134	46
5	133.9	162	55
6	135.1	185	63
7	132.6	176	60
8	132.3	183	62
9	133.8	177	60
10	135.1	163	56
11	134.0	186	63
12	132.7	-**	-
13	132.1	178	61

*Determined by the melting enthalpy calculated from DSC in comparison to $\Delta H°_m = 293$ J/g for 100% crystalline UHMWPE.

**Heats of fusion were unable to be determined due to the limited amount of sample.

Table 4.3 Reaction conditions for ethylene polymerization kinetics experiments.

Experiment #	Reaction Temperature (°C)	Catalyst Amount (mg)	Co-Catalyst Equivalents (Al:Cr)	Ethylene Pressure (psi)	Reaction Time (h)
0	25	10	96	100	1
1	25	**2.5**	96	100	1
2	25	**5**	96	100	1
3	25	**20**	96	100	1
4	25	10	96	**25**	1
5	25	10	96	**50**	1
6	25	10	96	**200**	1
7	**35**	10	96	100	1
8	**45**	10	96	100	1
9	**55**	10	96	100	1
10	25	10	**48**	100	1
11	25	10	**24**	100	1
12	25	10	**144**	100	1
13	25	10	96	100	**5**

*Reaction condition being varied in **green**.
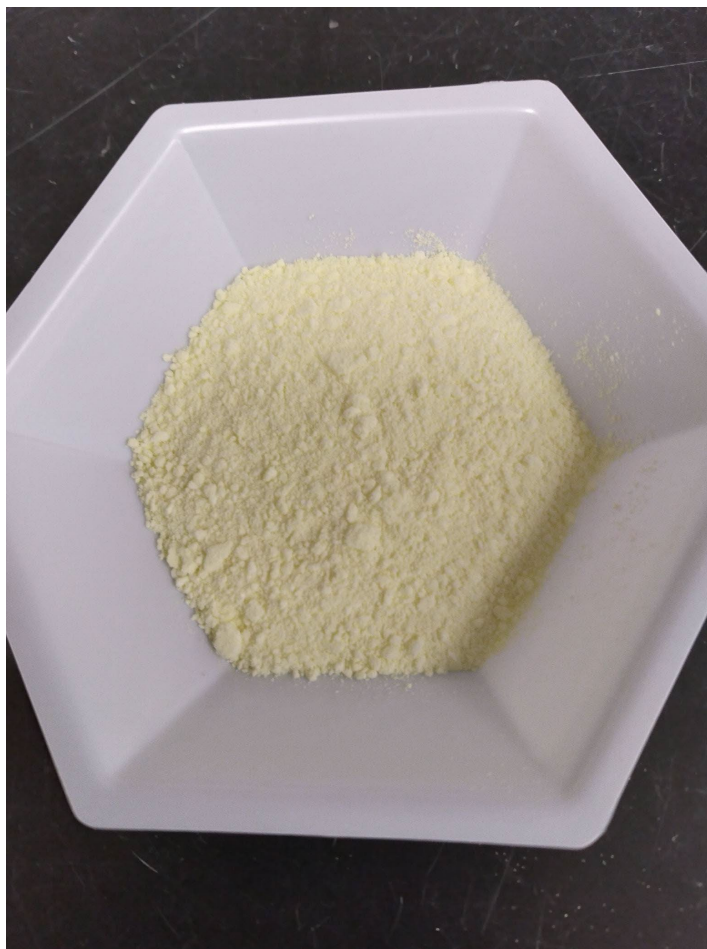
Figure 4.9 Representative image of polymer and MOF collected post-catalysis.
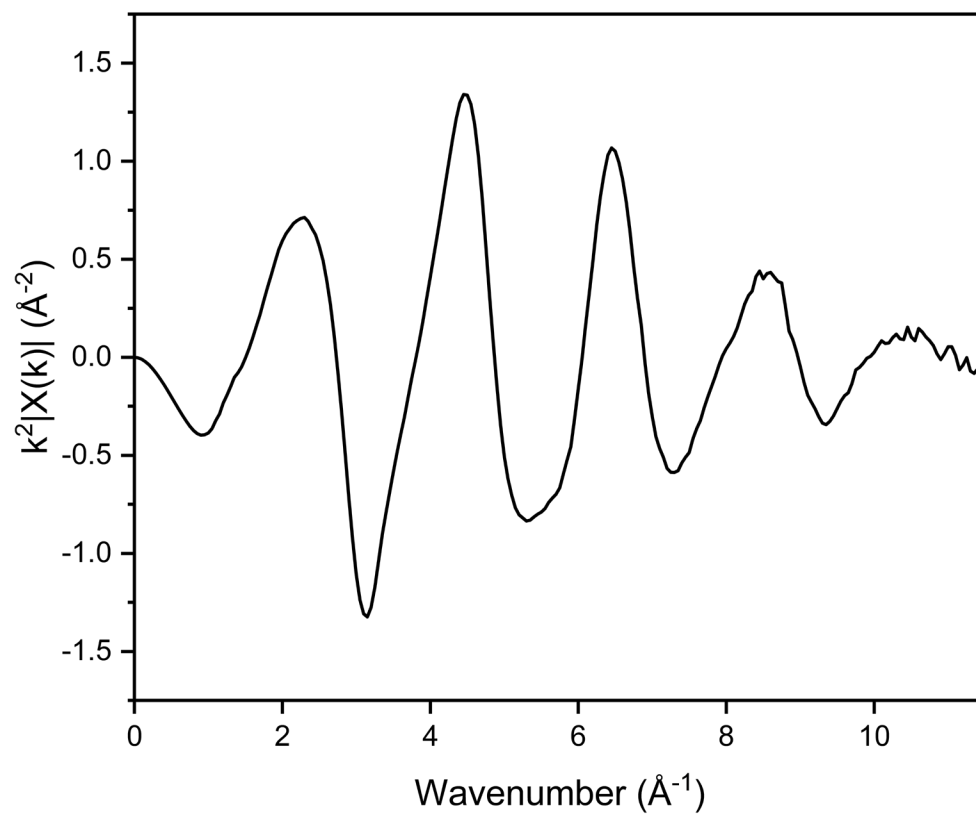
Figure 4.10 Cr-K edge EXAFS spectrum of Cr-SIM-NU-1000 in *k*-space.
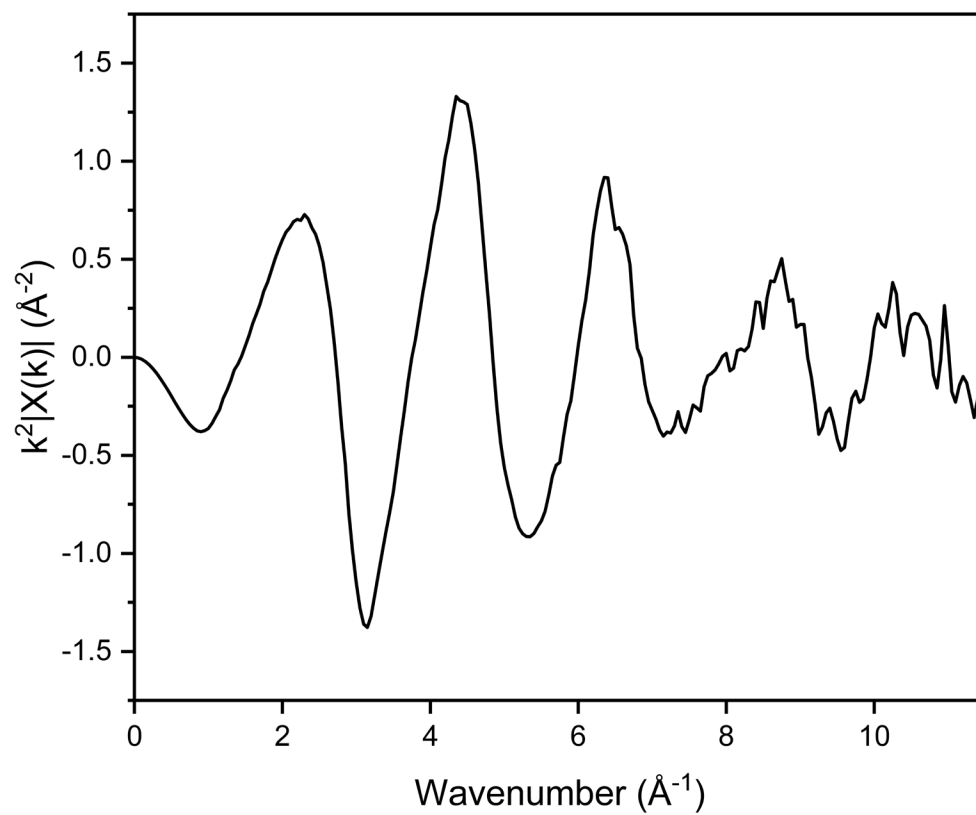
Figure 4.11 Cr-K edge EXAFS spectrum of DEAC@Cr-SIM-NU-1000 under N_2 in *k*-space.
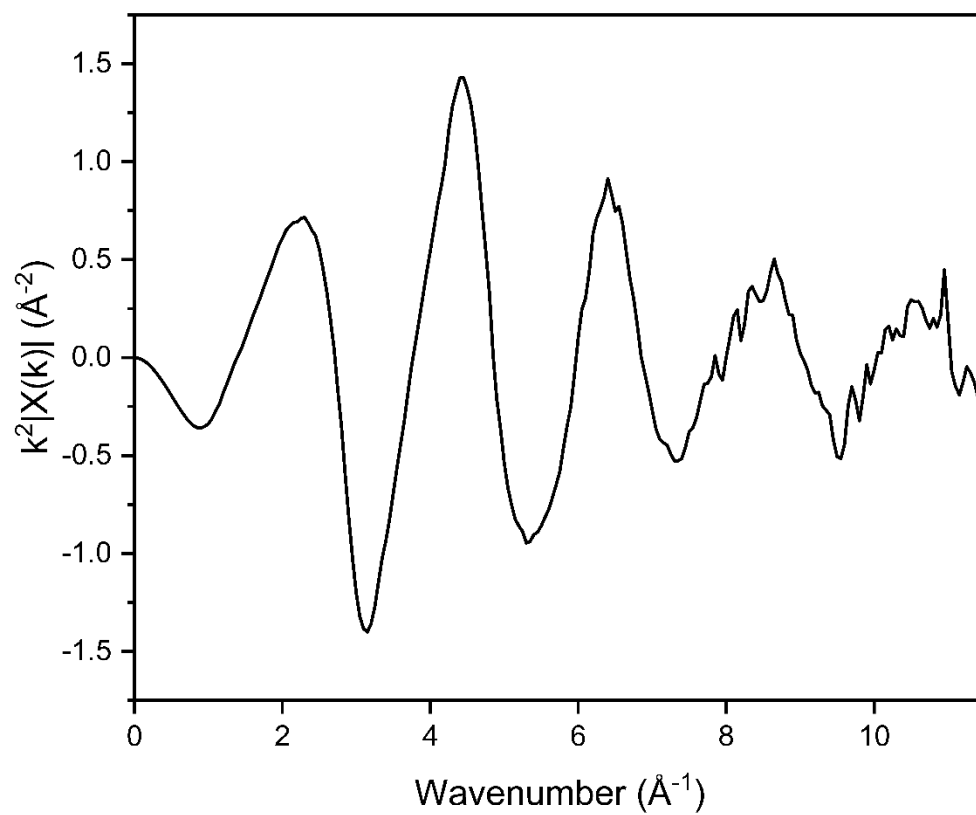
Figure 4.12 Cr-K edge EXAFS spectrum of DEAC@Cr-SIM-NU-1000 under C_2H_4 in *k*-space.
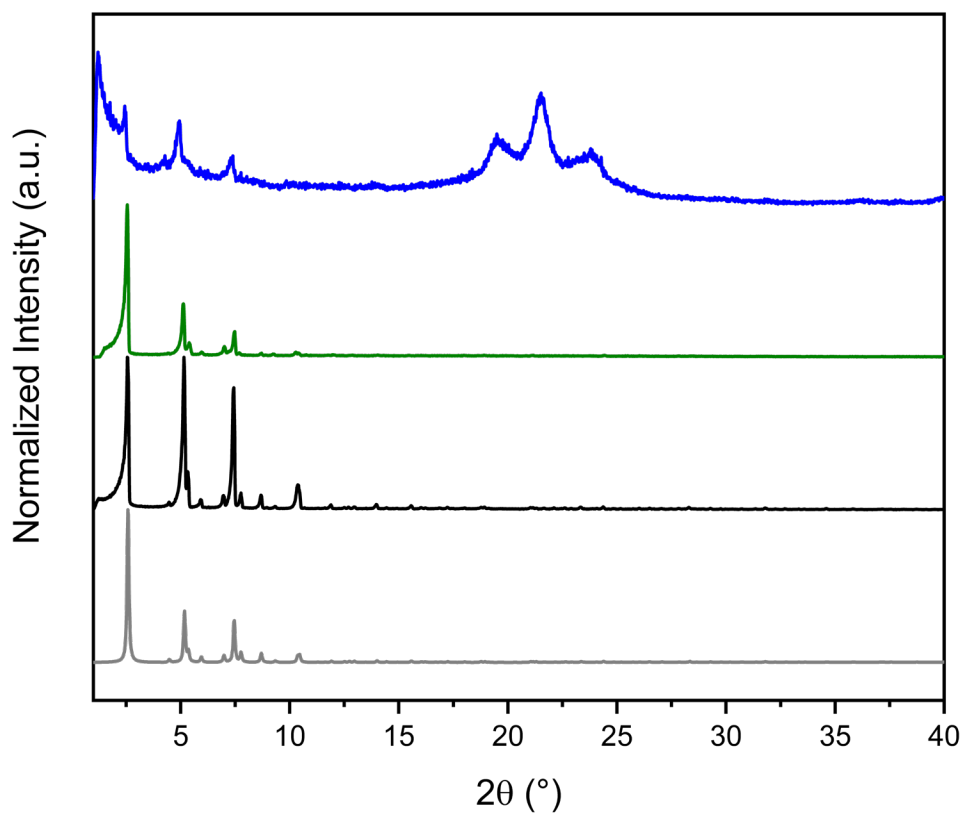
Figure 4.13 Powder X-ray diffraction (PXRD) patterns of NU-1000 simulated from crystal structure (gray), NU-1000 as synthesized (black), Cr-SIM-NU-1000 as synthesized (green), and DEAC@Cr-SIM-NU-1000 post catalysis (blue). Note: crystalline polyethylene can be seen and dominates in the pattern for DEAC@Cr-SIM-NU-1000 post catalysis.
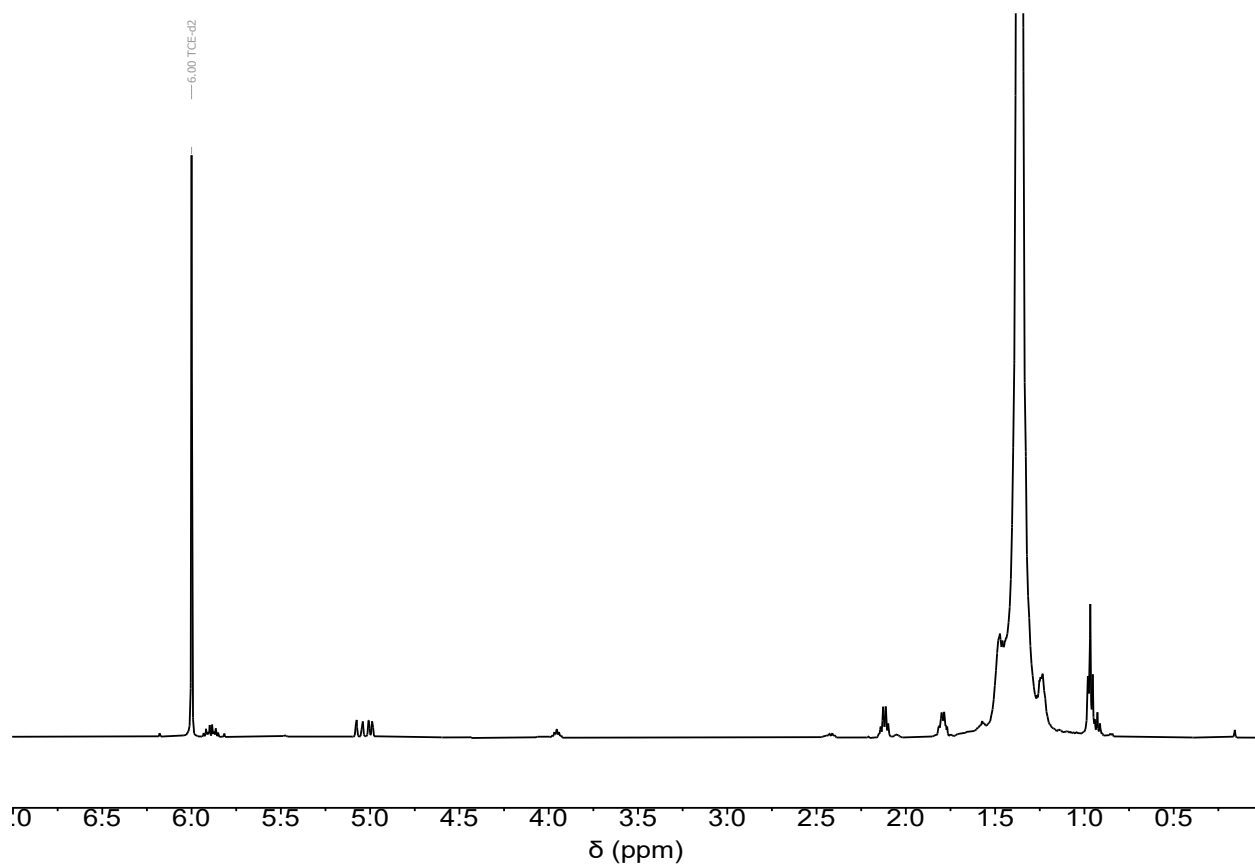
Figure 4.14 Representative ^{1}H-NMR of polyethylene product in 1,1,2,2-tetrachloroethane-d_2 at 120 °C.
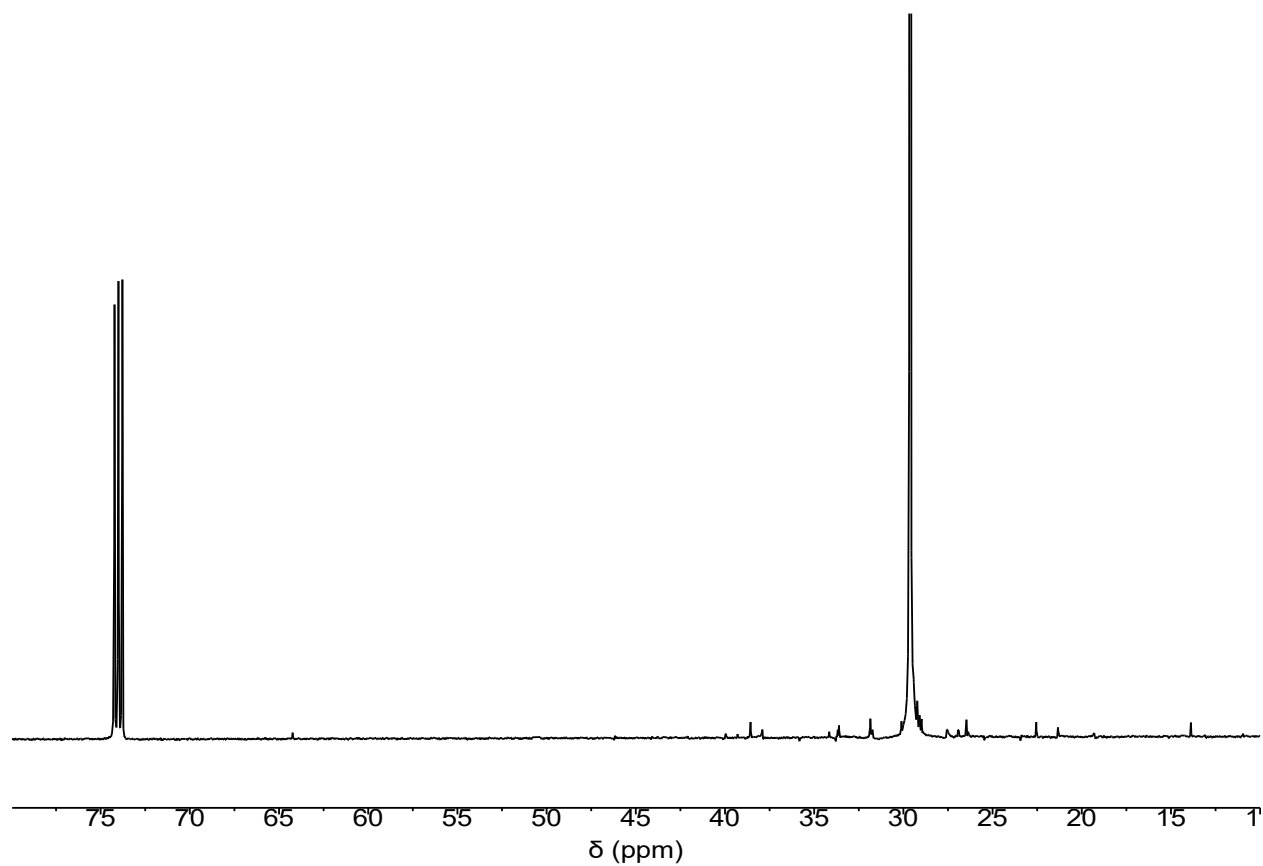
Figure 4.15 Representative ^{13}C-NMR of polyethylene product in 1,1,2,2-tetrachloroethane-d_2 at 120 °C.

Chapter 5. Tuning the Product Distribution of Acetylene Dimerization Through Bimetallic MOF-Supported Systems

Portions of this chapter appear in the following manuscript:

5.1 Chapter Summary

Metal−organic frameworks (MOFs) are receiving increased attention due to their well-defined structures that allow the determination of structure−property relationships. MOFs have been used as heterogeneous catalyst supports in a variety of fashions including for confinement of metal nanoparticles, which have demonstrated enhanced resistance to aggregation, a common issue in amorphous metal oxide supports. Cu and In catalysts were installed in the Zr-based MOF NU-907, being confined within the nanoporous structure. The Cu catalyst is known to, under various conditions, either selectively hydrogenate acetylene to ethylene or generate C_4 products such as butenes and 1,3-butadiene, an important feedstock for rubber and adhesives. The addition of indium to the Cu catalyst is intended to serve as a promoter to produce C_4 products by decreasing the surface coverage of copper while still allowing for C−C coupling. When employed for acetylene dimerization, InCu-NU-907 shows slightly decreased C_4 production overall but enhanced 1,3-butadiene production compared to all other catalysts studied herein. These catalysts were thoroughly characterized by a range of techniques to confirm structural integrity and porosity and probe the nature of the interactions of indium with the Cu nanoparticle active site.

5.2 Background

Catalysis continues to be ubiquitous in our daily lives in processes such as Haber-Bosch (ammonia from N_2 and H_2), Fisher-Tropsch (hydrocarbons from syngas), and catalytic converters (toxic vehicle emissions mitigation). In fact, catalysts are used in approximately 85% of industrial processes, with 80% of them being heterogeneous catalysts.[185] While homogeneous catalysts serve many uses and work to great effect, heterogeneous catalysts often serve to facilitate product separation more efficiently as well as provide enhanced catalyst recyclability. Traditional supports used for heterogeneous catalysts are those such as silica (SiO_2), alumina (Al_2O_3), and other bulk

metal oxides (MO_x). In the past couple of decades, metal–organic frameworks (MOFs) have become widely studied as catalyst support materials.[139, 186-187]

5.3 Metal–Organic Frameworks as Catalyst Supports

Metal–organic frameworks are a class of hybrid materials that self-assemble into 2D or 3D networks composed of inorganic metal nodes and organic linkers. Due to their ordered structures and high porosity, among many other desirable properties, MOFs have been studied for various applications such as gas storage/separations, chemical sensing, and heterogeneous catalysis.[110] Within the field of catalysis, MOFs have been applied to a wide variety of reactions ranging from methane oxidation[188] and olefin polymerization[176] to chemical warfare agent degradation[130] and electrochemical hydrogen evolution.[189] MOFs have shown excellent promise for the structural determination of catalytic species due to their crystalline nature, and displayed unique confinement effects enabled by their ordered porous networks.[12, 137]

A host of methods for synthesizing nanoparticles (NPs) within MOFs have been employed, and the subsequent materials have been used not only for catalysis but also for sensing and gas separations.[190] Within the realm of catalysis, metal or metal–oxide nanoparticles supported by the nanoporous structures of MOFs have been used for a wide range of reactions, from oxidation and hydrogenation to carbon–carbon coupling.[191] Nanoparticles in general have been broadly used within the heterogeneous catalysis field since they have higher surface area to unit volume ratios, especially desirable when scaling up in industrial catalysis.[192] However, on traditional supports such as SiO_2, Al_2O_3, and other bulk metal oxides, the nanoparticles tend to migrate and aggregate under relevant reaction conditions, leading to significant deactivation of the catalyst and therefore diminished activity, loss of selectivity, and/or reduced overall recyclability.[193] While substantial progress and efforts into combating these deactivation pathways have been made,[194-195] MOFs

offer a unique advantage such that nanoparticles can be confined within the pore and/or the framework itself, providing a substantial barrier to aggregation by means of walls of organic linker surrounding the cavities of the MOFs.[190] This enhanced resistance to nanoparticle aggregation has been demonstrated in MOF-supported catalysts, in addition to the ability to control or template nanoparticle growth to a uniform size within preformed MOF pores.[12]

5.4 Shale Gas and Acetylene Dimerization

As of the rise in "wet" shale gas availability within the United States, the heterogeneous catalysis community has become interested in the building up of smaller hydrocarbons into longer chain hydrocarbons through carbon-carbon coupling. Such reactions include olefin metathesis,[196-197] olefin polymerization,[135, 176] and alkyne oligomerization[198-199] to name a few. Often seen as a detrimental side reaction in acetylene semi-hydrogenation systems seeking to purify ethylene streams,[200-201] acetylene dimerization (**Scheme 5.1**) can generate products such as butenes or even 1,3-butadiene, a major feedstock in the adhesives and rubber industries.[202] Advancements beyond the gas/liquid-based Nieuwland catalyst system, which suffers from low conversion and facile polymer fouling, have been made recently with the development of solid catalysts mainly involving supported Cu species akin to the Nieuwland system.[203] Additionally, Cu NPs confined within MOFs have been previously demonstrated to selectively hydrogenate acetylene to ethylene[204] and have also shown promise for the production of C_4 products including 1,3-butadiene.[205] Enhancement of the C_4 reactivity, in particular 1,3-butadiene, will require catalyst modifications most commonly done by promoter ions in heterogeneous catalyst systems. Cationic indium has shown promise for carbon–carbon coupling reactions and also served to limit the size of Cu nanoparticles, which has been demonstrated to affect product selectivity and therefore is of interest for elevating the production of 1,3-butadiene in our MOF system.[206-207]

Scheme 5.1 Acetylene Dimerization Pathways to Partially Hydrogenated C_4 Products
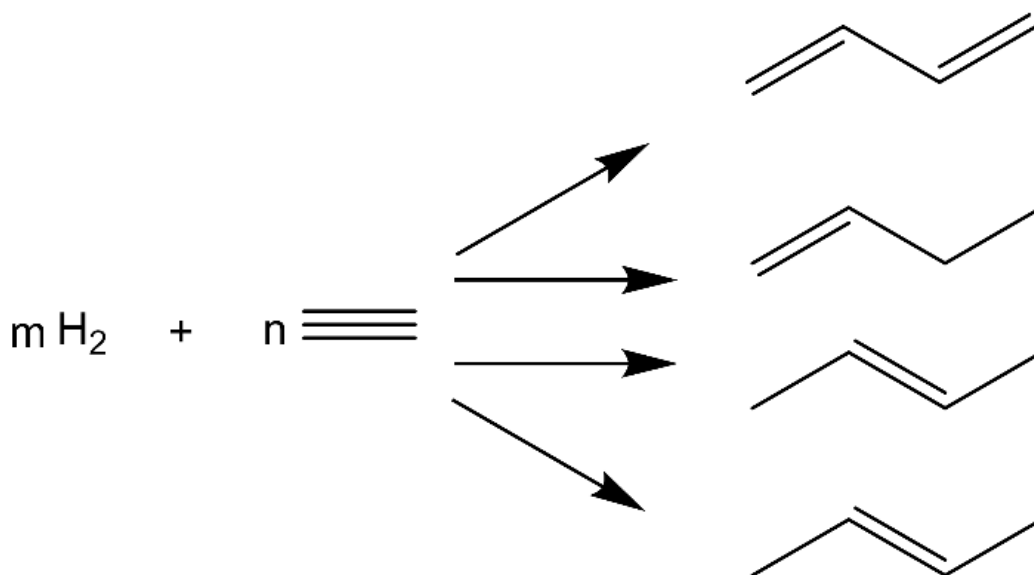
5.5 Modifying Catalysts with Promoters

In the realm of nanoparticles, the synthesis of bimetallic nanoparticles as well as metal nanoparticles incorporated with metal oxide rafts or overcoats[208-210] is the most common method of incorporating an additional metal species in a promoter-like fashion. Both of these bimetallic systems provide different reactivity from monometallic analogues and, when incorporated into MOFs, offer an opportunity to derive structure–property relationships. Herein, we demonstrate the activity and selectivity of a MOF-supported Cu NP catalyst promoted by cationic In for the oligomerization of acetylene compared to the monometallic counterparts and provide characterization to identify the reason for the resulting reactivity differences.

5.6 Catalyst Synthesis and Characterization

The catalysts of interest in this study are Cu-NU-907, In-NU-907, and InCu-NU-907. NU-907 (see **Figures 5.1** and **5.2** for MOF and NP@MOF structural representation) was initially synthesized on a small scale (~30 mg) and then scaled up to yield 300–400 mg (see the Additional Information for synthesis details, **Figure 5.8** for PXRD patterns, and **Figures 5.9** and **5.10** for N_2 adsorption isotherms and pore size distributions). This larger scale procedure was used for the

solvothermal post-synthetic modification to incorporate copper and/or indium. Before being

utilized for acetylene dimerization, the catalysts were subjected to reducing conditions at 200 °C

under dilute H_2 flow.
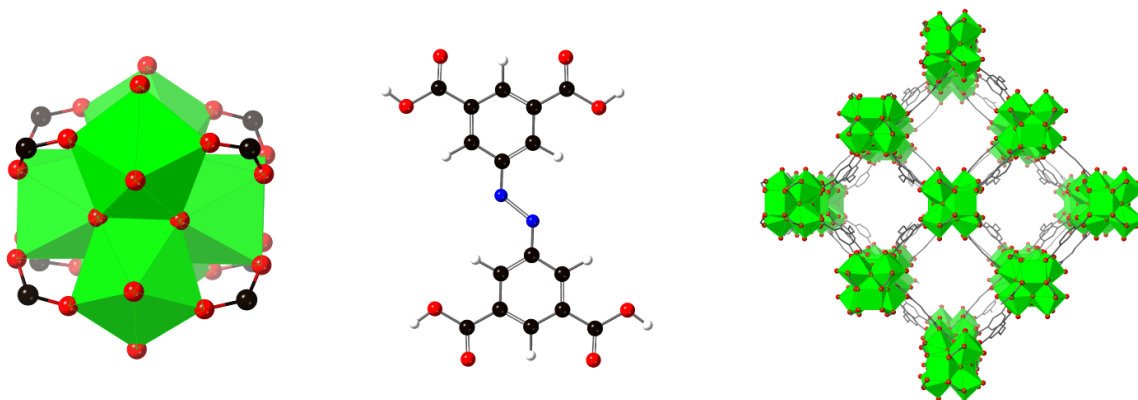
Figure 5.1 Structural models of the scu topology of NU-907(right) and the node (left) and linker (middle) components. Zirconium (green), oxygen (red), nitrogen (blue), carbon (black), and hydrogen (white).
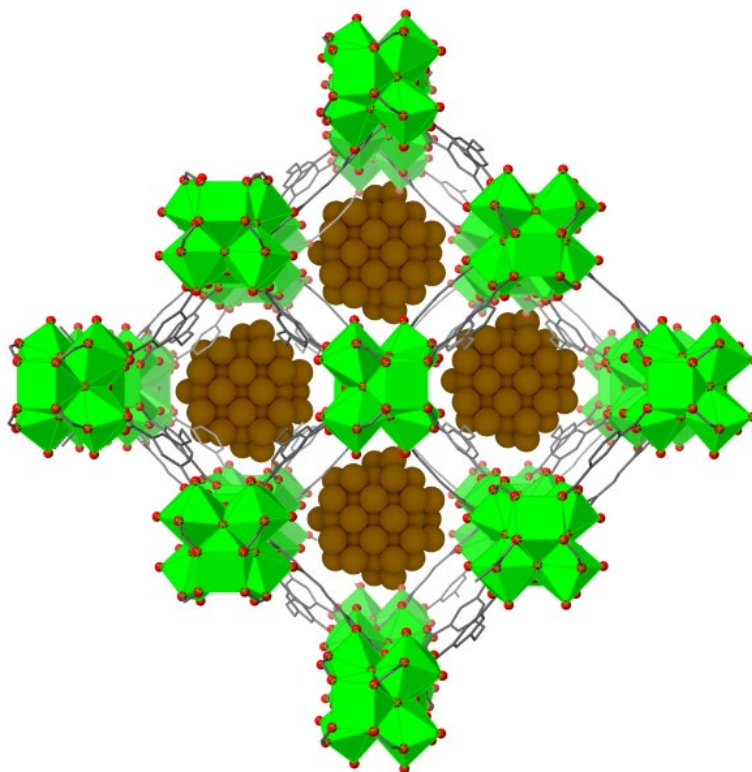
Figure 5.2 Structural model of metal nanoparticles encapsulated within the pores of NU-907. Zirconium (green), oxygen (red), nitrogen (blue), carbon (black), hydrogen (white), and metal nanoparticle (orange).

5.6.1 Crystallinity and Porosity

The modified frameworks were characterized by powder X-ray diffraction (PXRD) and N_2 isothermal adsorption isotherms at 77 K after metal deposition and after catalysis to determine retention of bulk crystallinity and porosity after metalation and nanoparticle formation (**Figure 5.3**). PXRD patterns of the as-synthesized Cu and In modified materials match well with the simulated and as-synthesized NU-907 patterns (**Figure 5.3a**), as do the post-catalysis materials (see **Figure 5.22**), indicative of retention of bulk phase purity and crystallinity. In addition, the N_2 adsorption isotherms show sufficient retention of the high porosity of the frameworks (**Figure 5.3b**) and an expected reduction in Brunauer–Emmett–Teller (BET) area upon metal installation within the framework (**Table 5.2**). The density functional theory (DFT)-computed pore size distributions show an expected decrease in pore width in the singular micropore of the NU-907 framework (see **Figure 5.11**). Based on inductively coupled plasma optical emission spectroscopy (ICP-OES), metal loadings per Zr_6 node were 0.9 ± 0.1 Cu atoms in Cu-NU-907, 2.6 ± 0.3 In atoms in In-NU-907, 0.9 ± 0.1 Cu atoms in InCu-NU-907, and 1.7 ± 0.4 In atoms in InCu-NU-907.
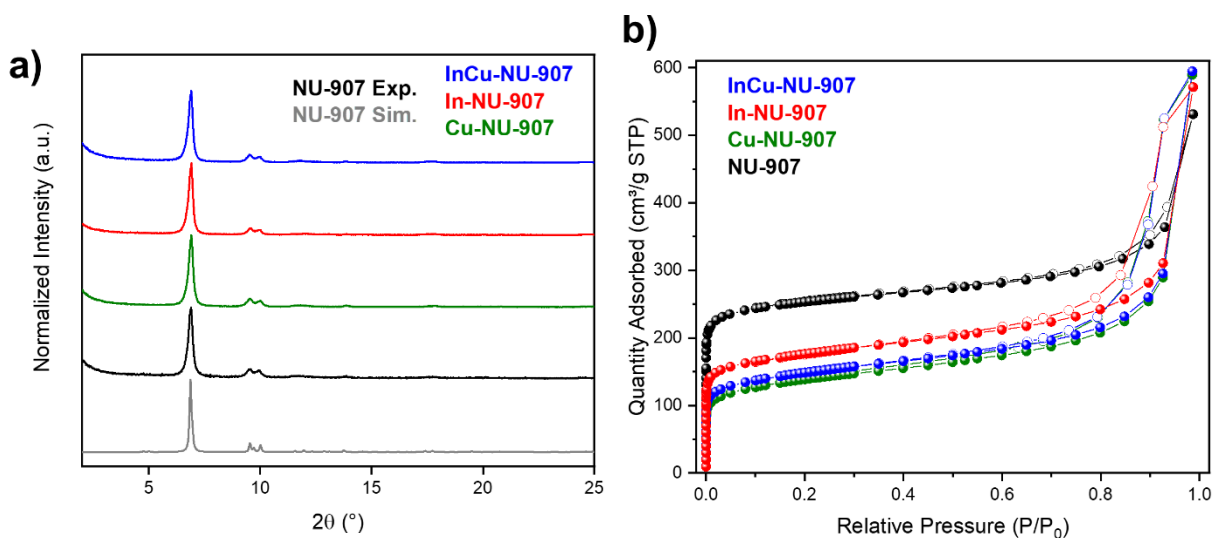
Figure 5.3 (a) Simulated and experimental PXRD patterns and (b) N_2 adsorption isotherms for NU-907 (black), Cu-NU-907 (green), In-NU-907 (red), and InCu-NU-907 (blue).

5.6.2 Electronic Environment by XPS

Further characterization of the Cu and/or In modified materials leads to X-ray photoelectron spectroscopy (XPS) to elucidate the electronic environment prior to reduction to nanoparticles. XPS reveals the deposited Cu to be Cu^{2+} in both the monometallic and bimetallic samples, and the In species are In^{3+} (**Figure 5.4**). After H_2 treatment which is done prior to the catalysis, the XPS shows a reduced Cu species of Cu^0, with some small presence of oxidized Cu likely due to surface oxidation during sample transfer. In the case of both indium samples, no metallic In^0 is observed, though it should be noted that there is a slight shift to lower binding energy in both In-containing materials after the reduction treatment, which could suggest interactions with the Cu nanoparticles changing the electronic environment. However, XPS is largely a surface technique, so a more complete picture can be derived about the bulk from subsequent X-ray absorption spectroscopy (XAS) experiments.
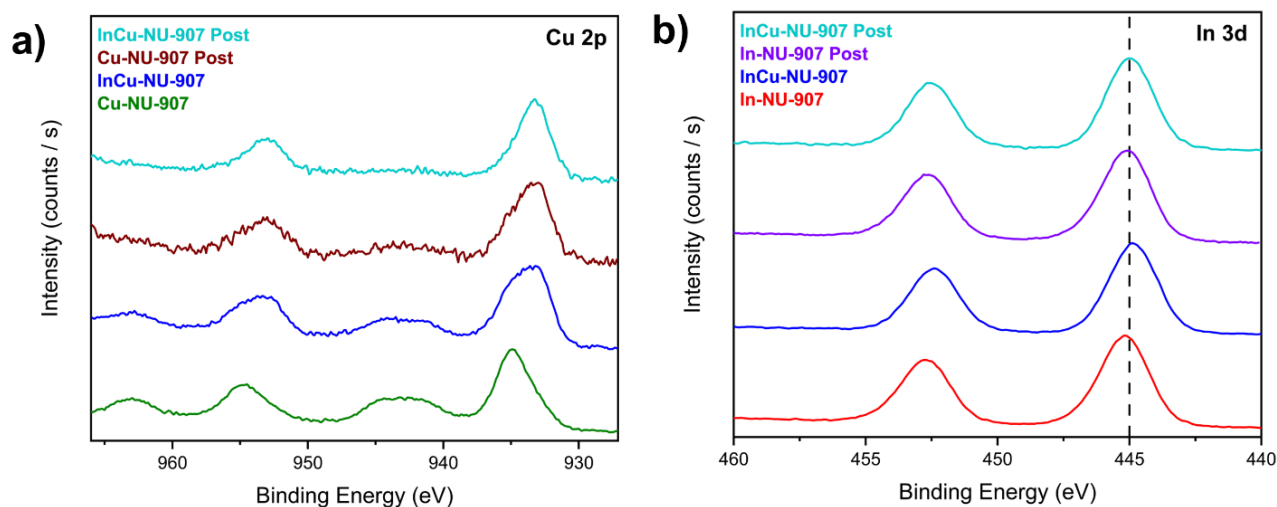
Figure 5.4 XPS spectra before and after reduction of (a) Cu samples and (b) In samples. Vertical dashed line in (b) is at 445 eV.

Given in both the Cu-NU-907 and InCu-NU-907 materials, the Cu is reduced to metallic Cu^0 based on XPS, a surface technique, further confirmation of nanoparticle formation was needed. Unfortunately, due to the size of the nanoparticles (< 2 nm) and the susceptibility of the MOF to

beam damage under transmission electron microscopy (TEM) conditions, clear micrographs were unable to be obtained. However, both diffuse reflectance infrared Fourier transform spectroscopy (DRIFTS) using CO as a probe molecule, and in situ XAS under reducing conditions were able to be performed to characterize and confirm the formation of Cu nanoparticles.

5.6.3 CO-DRIFTS Characterization of Cu Nanoparticles

Cu-NU-907 and InCu-NU-907 materials were pre-reduced at 200 °C under dilute H_2 flow before collecting CO DRIFT spectra. The samples were exposed to flowing gaseous CO and then purged with Ar to leave only adsorbed CO species. Stable spectra after an Ar purge were collected to characterize the Cu surfaces in Cu-NU-907 and InCu-NU-907 (see **Figure 5.12** for full spectra and **Figure 5.13** for the comparison of spectra under CO and after an Ar purge with gas-phase CO). As shown in **Figure 5.5**, Cu-NU-907 exhibits a peak centered at 2090 cm^{-1} corresponding to CO_{atop} bound to the Cu nanoparticles. For InCu-NU-907, there is a similar feature, however it is shifted to higher wavenumber, centered at 2094 cm^{-1}. This could be explained by several factors including nanoparticle size, extent of surface oxidation, or direct interactions with indium at Cu NP edge interfaces.[211] Unfortunately, it is difficult to deconvolute these factors to come to a definitive conclusion without additional characterization. However, we can turn to in situ XAS and extended X-ray absorption fine structure (EXAFS) fitting to provide further insight, including a particle size comparison between the two materials.
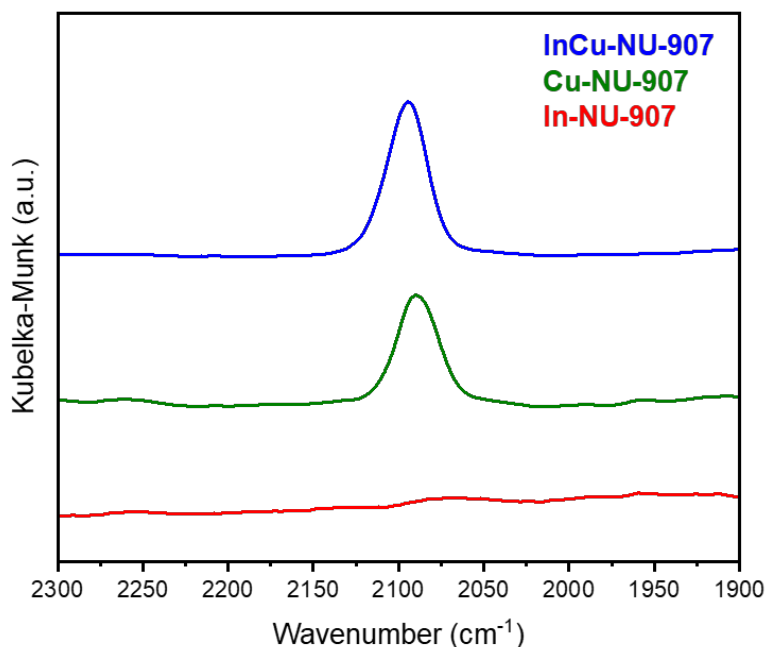
Figure 5.5 DRIFT spectra of CO treated Cu-NU-907 (green), In-NU-907 (red), and InCu-NU-907 (blue).

5.6.4 XAS Characterization of Cu Nanoparticles

X-ray absorption spectra for both Cu containing samples were collected at the Cu K-edge before, during, and after high temperature reduction (see **Figures 5.14** and **5.15** for full spectra). In addition, spectra were collected under the same conditions at the In K-edge for both In-containing samples (see **Figures 5.16-5.17** for full spectra). Using both sets of data we can identify from X-ray absorption near-edge spectroscopy (XANES) the extent of reduction for both Cu and In, and therefore the formation of mono- or bimetallic nanoparticles. Furthermore, we can determine an average nanoparticle size from fitting the EXAFS data.

As can be seen in the comparison of XANES spectra in **Figure 5.6a,c**, the as-synthesized Cu-NU-907 and InCu-NU-907 catalysts are an oxidized form of Cu with higher edge energy and white line intensity than the reference Cu foil. The extent of reduction was tracked during the experiment, but the final spectrum of the reduced species was taken at room temperature under inert gas flow. The reduced XANES spectra of both Cu-NU-907 and InCu-NU-907 indicate

complete reduction to metallic Cu, based their shift to lower edge energy, diminished white line intensity, and the presence of the 1s to 4p transition (which occurs in the $3d^{10}$ configuration)[212] in addition to comparison to the reference Cu foil. The complementary In-K edge measurements (**Figure 5.6b,d**) show some changes in the white line intensity and edge energies, but ultimately exhibit no In–In or In–Cu scattering in the EXAFS Fourier transform (**Figure 5.6f,h**).

With confirmation of reduction to Cu metal by XANES, data reduction and fitting of the Fourier transform (FT) of the EXAFS data was performed. For clarity, only the Fourier transform of the EXAFS is shown in the main text, **Figure 5.6e,g**, but additional information including the magnitude and imaginary components of the Cu K edge spectra and their resulting fits can be found in the Additional Information (see **Figures 5.18-5.21**). Compared to the Fourier transform of the Cu foil, it is qualitatively evident that the Cu–Cu scattering paths in the nanoparticle materials exhibit smaller magnitudes, indicating lower coordination number and, therefore, confirmation of the presence of nanoparticles rather than bulk Cu. Upon fitting the Cu–Cu path in Cu-NU-907, a coordination number of 8.8 ± 0.7 is obtained, which can be used to determine a nanoparticle size of approximately 1.7 nm.[213-214] On the other hand, fitting the Cu–Cu path in InCu-NU-907 provides a coordination number of 6.7 ± 0.8, which yields a smaller nanoparticle size of 1.0 nm (see **Table 5.1**). Knowing that the two materials differ in nanoparticle size brings further insight to the CO-DRIFTS experiment, where the smaller nanoparticle material exhibits a higher wavenumber CO stretch that is counterintuitive if particle size effects were the only contributing factor. Therefore, there must be an additional effect that is of greater impact shifting the CO stretch to even higher wavenumber despite a smaller nanoparticle which should cause a shift to lower wavenumber. Ultimately, the CO-DRIFTS and in situ XAS tell us that Cu nanoparticles are formed, In does not reduce to metal and form bimetallic nanoparticles with Cu, and the Cu

nanoparticles in Cu-NU-907 and InCu-NU-907 have different sizes and present different CO stretching frequencies.
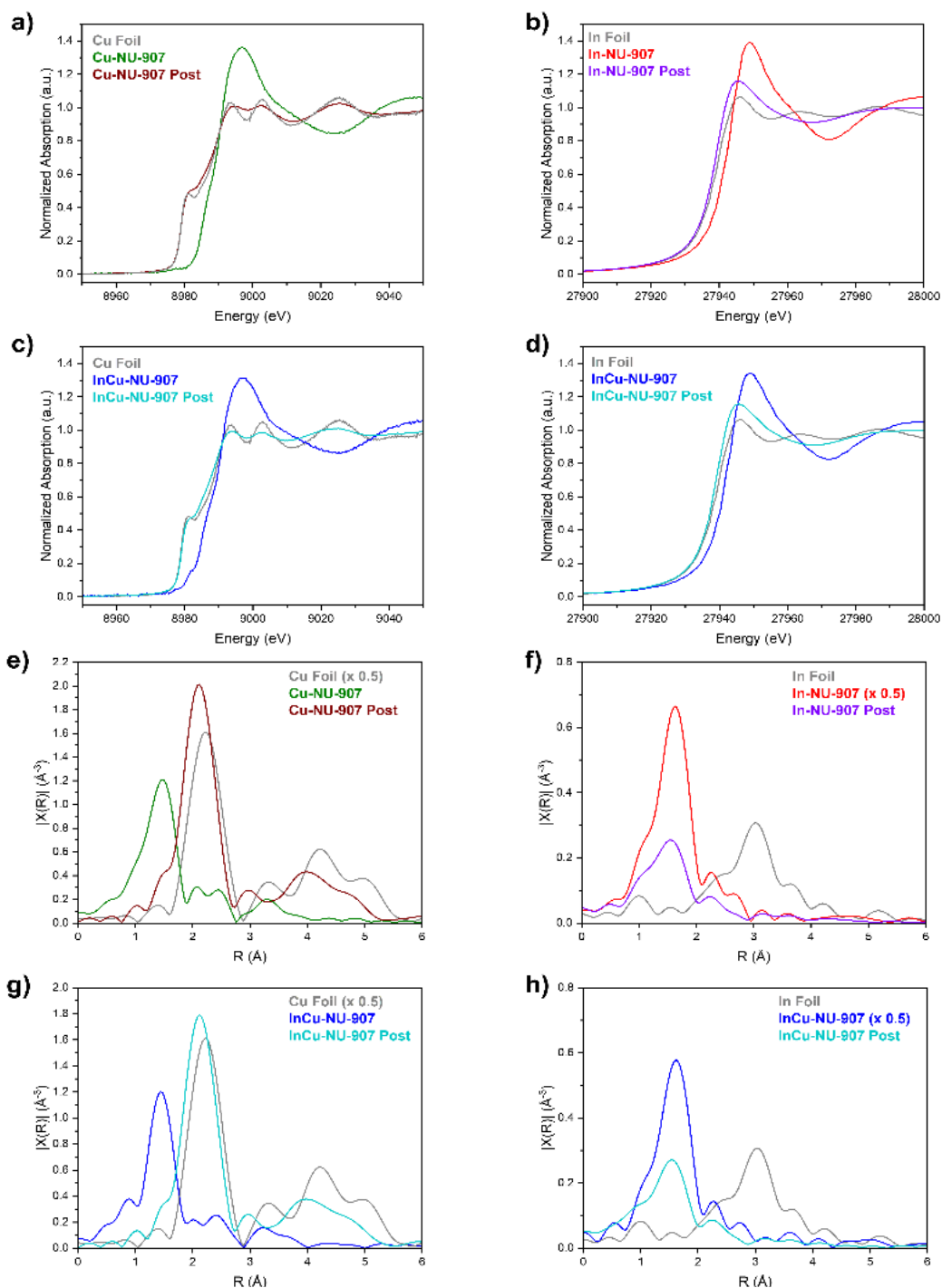
Figure 5.6 (a-d) Normalized XANES spectra at the Cu K and In K edges of as-synthesized and post reduction step materials compared to relevant reference foils. (e-h) The k^2-weighted magnitudes of the FT of EXAFS spectra for as-synthesized and post reduction step materials compared to relevant reference foils. FT was generated using a k-range of 3 – 11.5 Å^{-1}.

Table 5.1 Edge Energy and EXAFS Data at the Cu K Edge for the Fully Reduced Cu Catalysts

Catalyst	Scattering Path	R (Å)	CN	ΔE_0	σ^2	R-factor
Cu-NU-907 Reduced	Cu–Cu	2.53 ± 0.01	8.8 ± 0.7	3.3 ± 0.8	0.010 ± 0.001	0.006
InCu-NU-907 Reduced	Cu–Cu	2.53 ± 0.01	6.7 ± 0.8	2.9 ± 1.2	0.009 ± 0.001	0.013

5.7 Acetylene Dimerization Catalysis

With the catalyst materials of interest extensively characterized, we turned to their application for acetylene dimerization in a gas-phase fixed bed reactor setup. We hypothesized that the addition of cationic indium to the Cu NP system would affect the product selectivity through altering the Cu NP size as well as providing edge sites at the interface between Cu NPs and In species. Ideally, the introduction of In to the Cu catalyst material would alter the reactivity such that the production of C_4 products and 1,3-butadiene in particular would be favored. InCu-NU-907 does not form a bimetallic metal nanoparticle under the pre-reaction reduction conditions, retaining cationic indium. The In incorporation does also generate smaller Cu NPs than Cu-NU-907 and changes the Cu NP environment as evidenced by CO-DRIFTS.

Through initial reaction condition screening, we identified that including H_2 in the reactant feed was necessary to lower the production of additional oligomers of C_{6+} and reduce the amount of coke formation. Therefore, a ratio of 3:1 H_2:C_2H_2 flow was employed for the subsequent acetylene dimerization reactions. After a 4 h reduction under dilute H_2 at 200 °C, the flow was switched to the mixture of H_2 and acetylene, and various flowrates were tested to screen a range of space velocities. **Figure 5.7a** shows that In-NU-907 has similar acetylene conversion to the parent MOF NU-907 itself, while both Cu containing materials have higher conversion at all space velocities. Unsurprisingly, given the presence of H_2 and proclivity of Cu nanoparticles to hydrogenate acetylene, Cu-NU-907 nearly quantitatively converts acetylene at all conditions.

InCu-NU-907 exhibits different reactivity than the other catalysts, having moderate acetylene conversion at higher space velocity but increasing to nearly quantitative conversion at low space velocity. All catalyst materials were characterized post-catalysis by PXRD and retained bulk crystallinity (see **Figure 5.22**).

5.7.1 Catalyst Selectivity

While this trend of increasing conversion with decreasing space velocity is to be expected in general for catalysts, it is the product selectivity that exhibits some intriguing results. Each catalyst produces a majority of C_2 products, including both ethane and ethylene with catalyst selectivities in the order of In-NU-907 (89%) > InCu-NU-907 (86%) > Cu-NU-907 (61%). While there are some differences in individual (ethane vs ethylene) and overall C_2 product selectivities, the focus of incorporating In with Cu in the catalyst system was to affect the C_4 product distribution. With In-NU-907 there is <10% selectivity towards C_4 products with no production of 1,3-butadiene at all conditions. Cu-NU-907 similarly does not produce any 1,3-butadiene but does have a higher selectivity (~12–16%) towards C_4 products and even produces C_6 products accounting for 4–7% of product selectivity. On the other hand, InCu-NU-907 produces a smaller overall portion of C_4 products, but generally more than half of the C_4 product selectivity is accounted for by 1,3-butadiene. The comparison of 1,3-butadiene selectivity among all catalyst materials is shown in **Figure 5.7b**. We attribute this enhanced 1,3-butadiene selectivity to the interactions of Cu NPs with cationic In species in the pores of the MOF. It is likely that there are small portions of indium oxide that reside at the Zr_6 nodes where the indium was deposited, while the Cu NPs formed within the pores have been brought in close proximity to the indium. While this initial study of a MOF-confined bimetallic system provides some evidence of the interactions between Cu and In, future work is necessary to fully elucidate the active site structure.
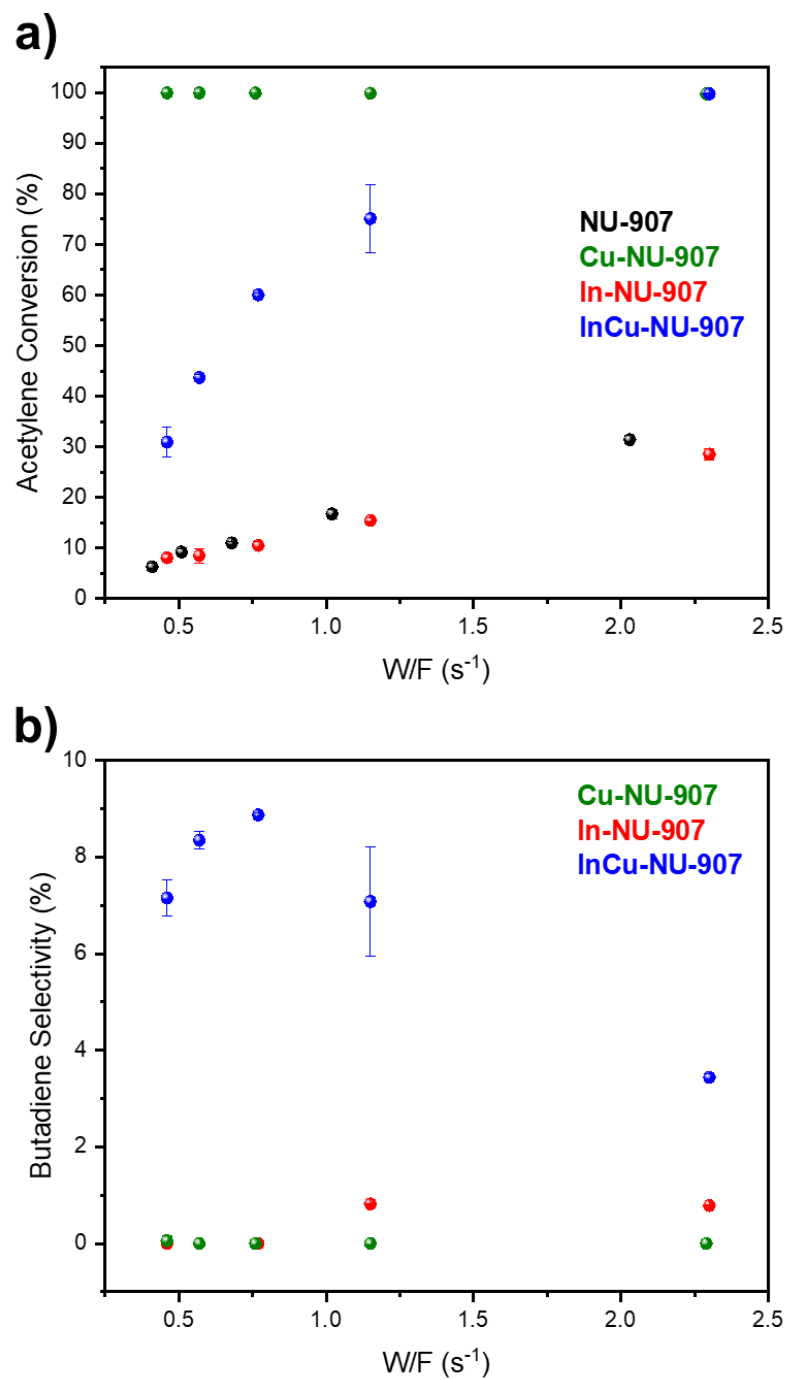
Figure 5.7 (a) Acetylene conversion profiles and (b) 1,3-butadiene selectivity profiles for NU-907 (black), In-NU-907 (red), Cu-NU-907 (green), and InCu-NU-907 (blue) over a range of space velocities.

5.8 Conclusions

A series of catalysts supported by Zr_6-based MOF, NU-907, were synthesized by depositing In, Cu, or Cu and In before reducing the material to generate Cu nanoparticles within a nanoporous structure. PXRD and N_2 adsorption confirmed retention of the structure and porosity of the MOF after deposition. Additional extensive characterization of the catalyst materials by XPS revealed retention of cationic indium but reduction of cationic copper to metal upon reduction pretreatment. CO-DRIFTS and in situ XAS served to confirm the presence of and distinguish between two different sizes of Cu NPs in different chemical environments existing in the Cu-NU-907 and InCu-NU-907 catalysts, with the latter containing smaller nanoparticles albeit with a higher CO stretching frequency. Compared to the monometallic catalysts, InCu-NU-907 exhibited higher selectivity for 1,3-butadiene, accounting for more than 50% of C_4 products generated. While the precise interactions of In with the Cu nanoparticle catalyst remain unclear, it is evident that there is an effect on the catalyst selectivity by incorporating both In and Cu before reduction. Future work building upon this will look to probe the precise interactions between the In and Cu in the nanoconfined environment through developing a range of catalysts with varying In:Cu ratios paired with density functional theory calculations to identify possible catalyst interfaces.

5.9 Additional Information

5.9.1 Materials

Acetone and *N,N*-dimethylformamide (DMF) were purchased from Fisher Scientific (Waltham, MA) and used as received. Formic acid (FA) and zirconyl chloride octahydrate were purchased from Sigma-Aldrich (St. Louis, MO) and used as received. Indium (III) oxide was purchased from Alfa Aesar (Ward Hill, MA) and used as received. Bis(dimethylamino-2-propoxy)copper(II) (Cu(dmap)$_2$) and trimethyl indium (In(Me)$_3$) were purchased from Strem Chemicals (Newburyport, MA), stored in an Ar-filled glovebox, and used as received. Anhydrous heptane and pentane were purchased from Sigma-Aldrich and further dried by soaking over 3 Å molecular sieves. UHP Ar (99.999%), 10% H$_2$/He, and 5% C$_2$H$_2$/He were purchased from Airgas (Radnor, PA) and used as received. 3,3',5,5'-azobenzene tetracarboxylic acid (H$_4$abtc) was synthesized according to literature procedure.[215]

5.9.2 Synthetic Methods

NU-907 Synthesis. 3,3',5,5'-azobenzene tetracarboxylic acid (H$_4$abtc) was synthesized according to literature procedure.[215] NU-907 was synthesized first according to literature procedure at small scale,[215] and then scaled up based on the following modified procedure. Briefly, 773 mg (2.4 mmol) zirconyl chloride octahydrate was dissolved in 192 mL DMF in a 1 L glass bottle. 144 mL (3.8 mol) formic acid was added, and then 859 mg (2.6 mmol) H$_4$abtc was added before sonicating to disperse the ligand. The bottle was then placed in a 120 °C oven for 3 days. The resulting solid was collected by centrifugation and subsequently washed with fresh DMF 3 times with 1 h soak time in between before solvent exchanging to methanol and performing 3 washes as well, including an additional overnight soak. The MOF was then briefly dried in a vacuum oven before being thermally activated on an ASAP 2420 (150 °C, 16 h) and then transferred into an Ar-filled glovebox for storage before metalation.

Cu-NU-907 Synthesis. 132 mg Cu(dmap)$_2$ (0.50 mmol) was dissolved in 20 mL anhydrous heptane under Ar atmosphere in a glovebox. 200 mg (0.09 mmol) activated NU-907 was added to this solution and mixture was shaken to disperse the MOF in the solution. The solution was allowed to stand at room temperature for overnight. After the overnight soak, the solvent was decanted and exchanged for fresh anhydrous heptane 3 times with a 1 h soaking period in between. The supernatant was replaced with acetone upon removing from the glovebox. The supernatant was decanted and replaced with fresh acetone 3 times with a 1 h soaking period in between. The powder was then isolated and thermally activated under dynamic vacuum on an ASAP 2420 (150 °C, 16 h). The recovered material was kept in a desiccator for storage. The Cu loading was determined to be 0.9 ± 0.1 Cu atoms per Zr$_6$ node by ICP-OES.

In-NU-907 Synthesis. 80 mg In(Me)$_3$ (0.50 mmol) was dissolved in 20 mL anhydrous heptane under Ar atmosphere in a glovebox. 200 mg (0.09 mmol) activated NU-907 was added to this solution and mixture was shaken to disperse the MOF in the solution. The solution was allowed to stand at room temperature for overnight. After the overnight soak, the solvent was decanted and exchanged for fresh anhydrous heptane 3 times with a 1 h soaking period in between. The supernatant was replaced with acetone upon removing from the glovebox. The supernatant was decanted and replaced with fresh acetone 3 times with a 1 h soaking period in between. The powder was then isolated and thermally activated under dynamic vacuum on an ASAP 2420 (150 °C, 16 h). The recovered material was kept in a desiccator for storage. The In loading was determined to be 2.6 ± 0.3 In atoms per Zr$_6$ node by ICP-OES.

InCu-NU-907 Synthesis. 132 mg Cu(dmap)$_2$ (0.50 mmol) was dissolved in 20 mL anhydrous heptane under Ar atmosphere in a glovebox. 200 mg (0.09 mmol) activated NU-907 was added to this solution and mixture was shaken to disperse the MOF in the solution. The solution was allowed

to stand at room temperature for overnight. After the overnight soak, the solvent was decanted and exchanged for fresh anhydrous heptane 3 times with a 1 h soaking period in between. 80 mg In(Me)$_3$ (0.50 mmol) was dissolved in 20 mL anhydrous heptane, and then added to the MOF vial after decanting the wash heptane and then shaken to disperse the MOF before allowing to stand at room temperature overnight. After the overnight soak, the solvent was decanted and exchanged for fresh anhydrous heptane 3 times with a 1 h soaking period in between. The supernatant was replaced with acetone upon removing from the glovebox. The supernatant was decanted and replaced with fresh acetone 3 times with a 1 h soaking period in between. The powder was then isolated and thermally activated under dynamic vacuum on an ASAP 2420 (150 °C, 16 h). The recovered material was kept in a desiccator for storage. The Cu loading was determined to be 0.9 ± 0.1 Cu atoms per Zr$_6$ node and the In loading was determined to be 1.7 ± 0.4 In atoms per Zr$_6$ node by ICP-OES.

5.9.3 Acetylene Dimerization Catalysis

Gas-phase catalysis experiments were conducted in a tubular stainless-steel reactor using a fixed-bed. For a typical experiment 60-70 mg of MOF was diluted in ~ 420 mg high purity quartz sand prior to being loaded into the reactor on top of a bed of quartz wool. The catalysts were then pre-treated under dilute H$_2$ flow at 200 °C for 4 h before the gas feed was switched to include dilute acetylene for conducting the catalysis experiments. Previous discussion of Cu nanoparticle formation by this method has been reported in the literature. Subsequent reactions were carried out at 2 bar and products were analyzed by gas chromatography (GC) coupled with a flame ionization detector (FID).

5.9.4 Analytical Measurements

Powder X-ray diffraction (PXRD) data was collected at the IMSERC X-ray Facility at Northwestern University on a STOE-STADI-P powder diffractometer equipped with an

asymmetric curved Germanium monochromator (CuKα1 radiation, λ = 1.54056 Å) and one-dimensional silicon strip detector (MYTHEN2 1K from DECTRIS). The line focused Cu X-ray tube was operated at 40 kV and 40 mA. Powder was packed in a 3 mm metallic mask and sandwiched between two layers of polyimide tape. Intensity data from 1 to 40 degrees 2θ were collected over a period of 5 min.

N_2 adsorption isotherms were measured on a Micromeritics ASAP 2420 (Micromeritics, Norcross, GA) at 77 K with 30-80 mg pre-activated sample at 150 °C for 16 h under high vacuum. BET area was calculated in the region P/P_0 = 0.005-0.05 and pore-size distributions were obtained *via* density functional theory (DFT) calculations using an oxide cylinder-pore model with a N_2 kernel.

Inductively coupled plasma optical-emission spectroscopy (ICP-OES) was performed at the QBIC facility at Northwestern University on a Thermo iCAP 7600 Spectrometer (ThermoFisher, Waltham, MA). In each preparation, ~3 mg samples were digested in 2 mL concentrated nitric acid in a 2-5 mL Biotage (Uppsala, Sweden) microwave vial. Biotage SPX microwave reactor (software version 2.3, build 6250) was used to heat the mixture to 150 °C for 15 min. 300 μL of the digested sample was removed and diluted to 10 mL with ultrapure Millipore water.

CO DRIFTS measurements were carried out using a Nicolet iS50 FT-IR spectrometer equipped with a Harrick Scientific Praying Mantis DRIFTS accessory and a high temperature reaction chamber. The spectral resolution was 4 cm^{-1}, and all the reported spectra were an average of 64 spectra. All samples (pre-treated under dilute H_2 at 200 °C for 4 hours) were diluted to 20 wt% in KBr and loaded in the sample cup of the DRIFTS reaction chamber in an Ar-filled glovebox. The DRIFTS chamber was connected to the gas manifold under a flow of Ar (Airgas, UHP grade). All the measurements were performed at 23 °C. A background spectrum was

collected in flowing Ar for each sample and used as a reference against itself for the subsequent conditions. CO in balance He (Airgas, 5% certified mixture) was flown through the chamber at about 800 mbar. Evolution of gas phase CO was monitored in the course of about 15 min until spectral changes in the 2000-2200 cm^{-1} region were negligible. Then, the chamber was purged with Ar for about 15 min until the gas phase CO was flushed out and an equilibrium (surface) spectrum was established. The final spectrum was collected at the end of this final step. The collected spectra were processed using the Kubelka-Munk function.

X-ray photoelectron spectra were collected at the Keck-II/NUANCE facility at Northwestern University using a Thermo Scientific ESCALAB 250 Xi (Al Kα radiation, 1486.6 eV). All measurements were performed with an electron flood gun. Collected data was processed using the Thermo Scientific Avantage Data System software and all spectra were referenced to the C 1s peak (284. 8 eV).

X-ray absorption spectroscopy measurements were performed at Sector 10 BM-D of the Advanced Photon Source at Argonne National Laboratory. Samples were ground into a fine powder before being pressed into a barrel stainless steel-sample holder and loaded into a quartz tube equipped with Kapton windows and a thermocouple. Heating was enabled using a tube furnace and temperature controller. Samples were first purged with He before initial spectra were taken. Then, samples were exposed to 3% H_2/He flow over the course of the temperature ramp at 2 °C/min. up to 200 °C. Spectra were collected during the H_2 treatment and after the treatment when cooled down to temperature under flowing He. The final He purged spectra were used to determine Cu nanoparticle sizes. Two independent experiments with the same samples were conducted for the Cu-K edge and In-K edge experiments. Data analysis was performed using the Demeter XAS software package (v 0.9.26).
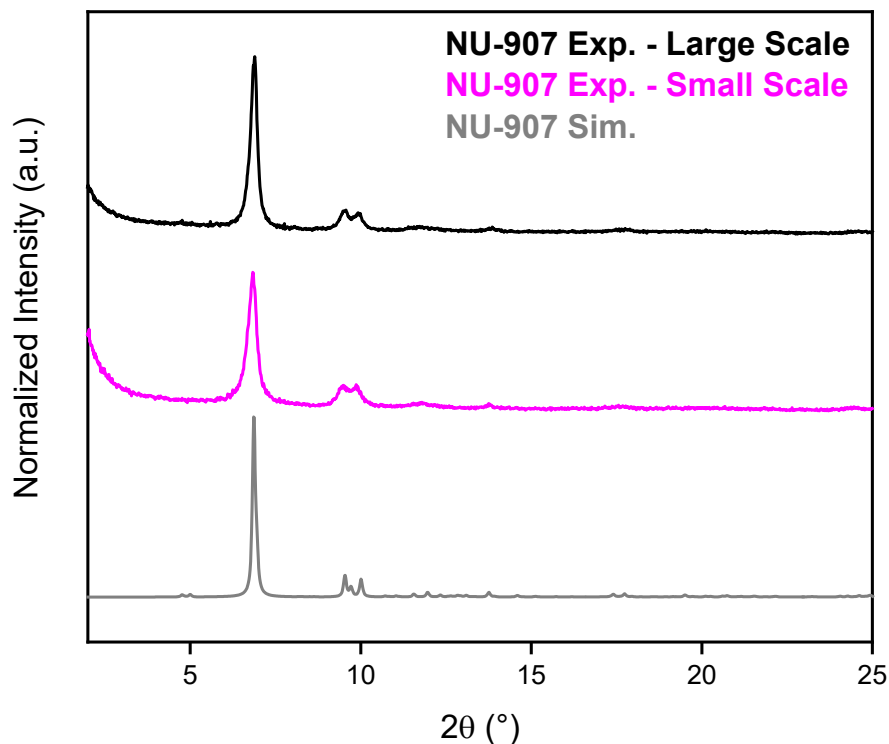
Figure 5.8 Simulated PXRD pattern for NU-907 (gray) compared to patterns for small-scale NU-907 (magenta) and large-scale NU-907 (black) syntheses.
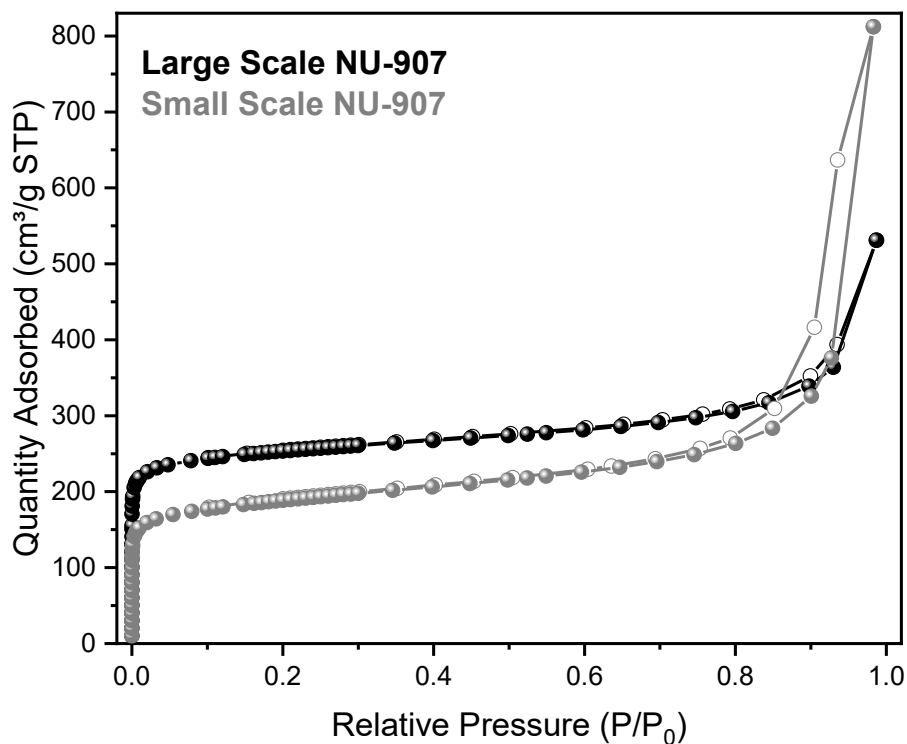
Figure 5.9 N_2 adsorption isotherms for small-scale NU-907 (gray) compared to large-scale NU-907 (black) syntheses.
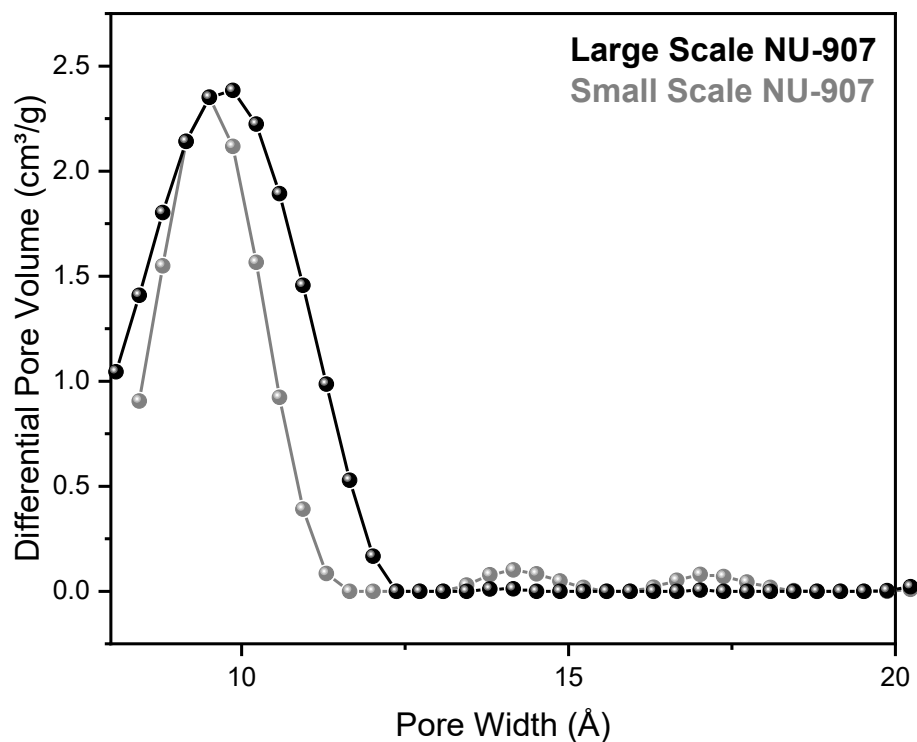
Figure 5.10 DFT calculated pore size distributions for small-scale NU-907 (gray) compared to large-scale NU-907 (black) syntheses.
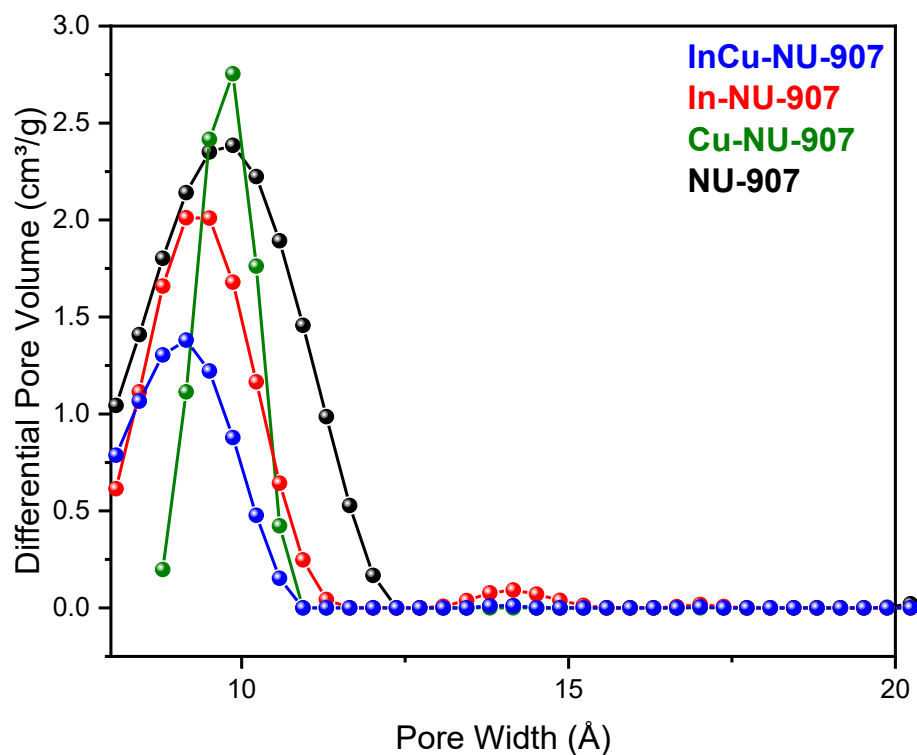
Figure 5.11 DFT calculated pore size distributions for large-scale NU-907 (black), Cu-NU-907 (green), In-NU-907 (red), and InCu-NU-907 (blue).

Table 5.2 BET area, pore volume, and DFT pore sizes for relevant materials.

Material	BET Area (m²/g)	Pore Volume (cm³/g)	DFT Pore Size (Å)
NU-907	980	0.41	10
Cu-NU-907	500	0.31	10
In-NU-907	660	0.33	8.5
InCu-NU-907	540	0.29	8
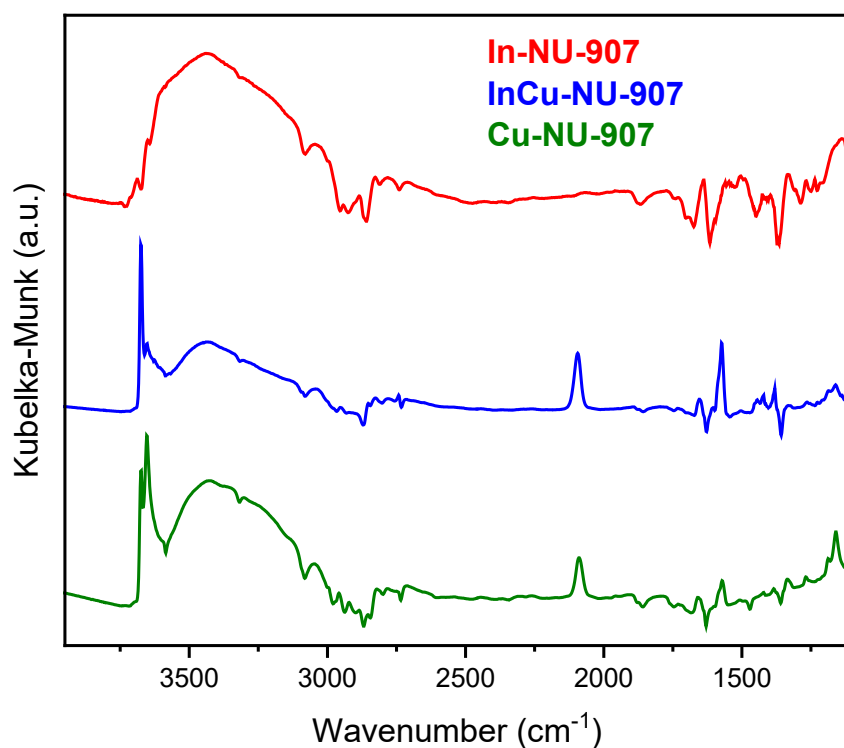
Figure 5.12 Ar purged DRIFT spectra after CO treatment for Cu-NU-907 (green), InCu-NU-907 (blue), and In-NU-907 (red).
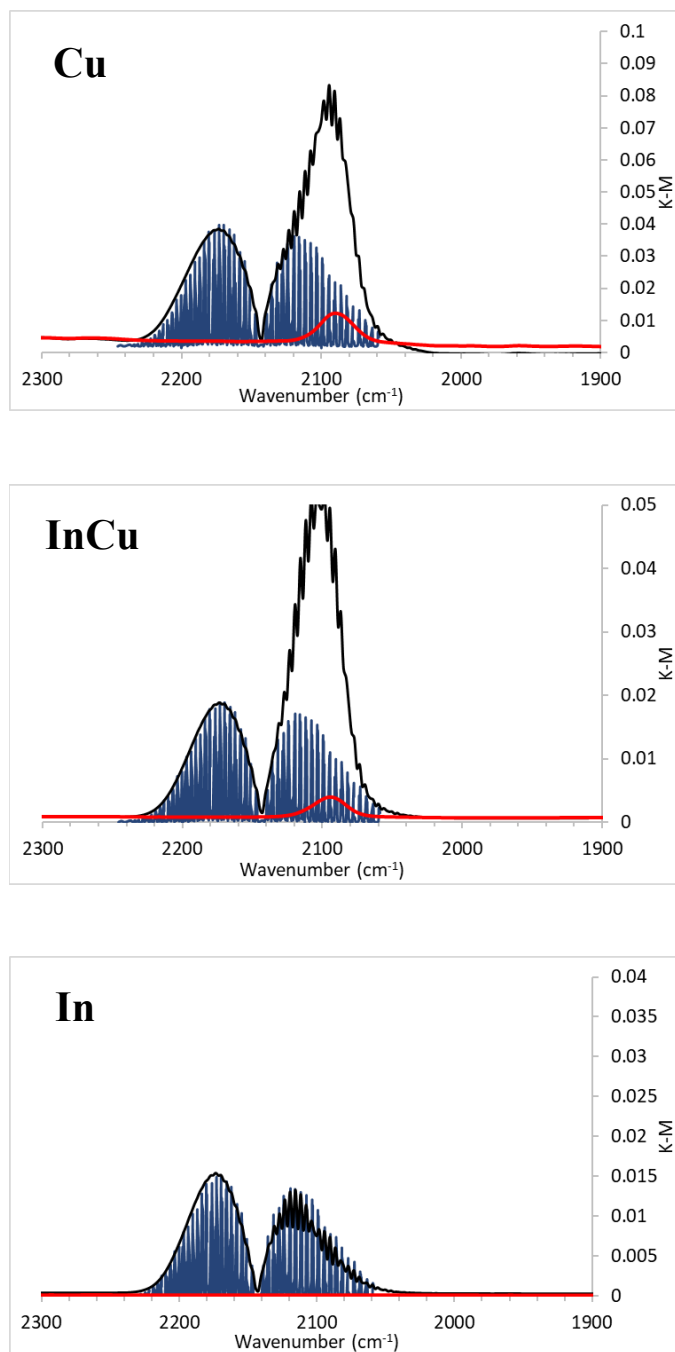
Figure 5.13 CO-DRIFT spectra of Cu, InCu and In samples in CO (black) and after Ar purge (red), compared to the spectrum of gas phase CO (blue).
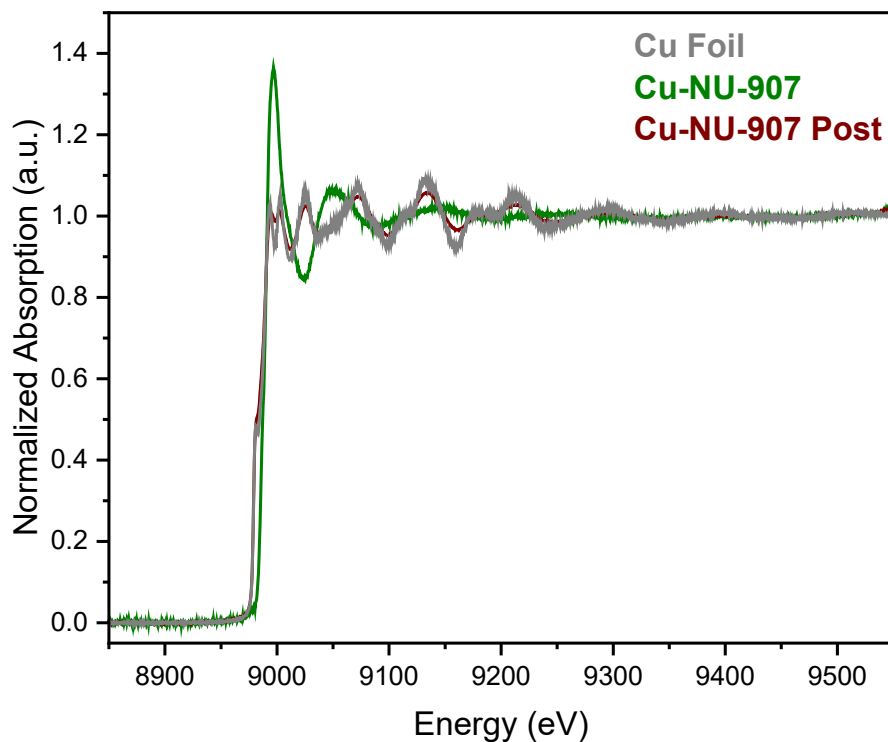
Figure 5.14 Full Cu-K edge XAS spectra for Cu foil reference (gray), Cu-NU-907 (green), and post-reduction Cu-NU-907 (brown).
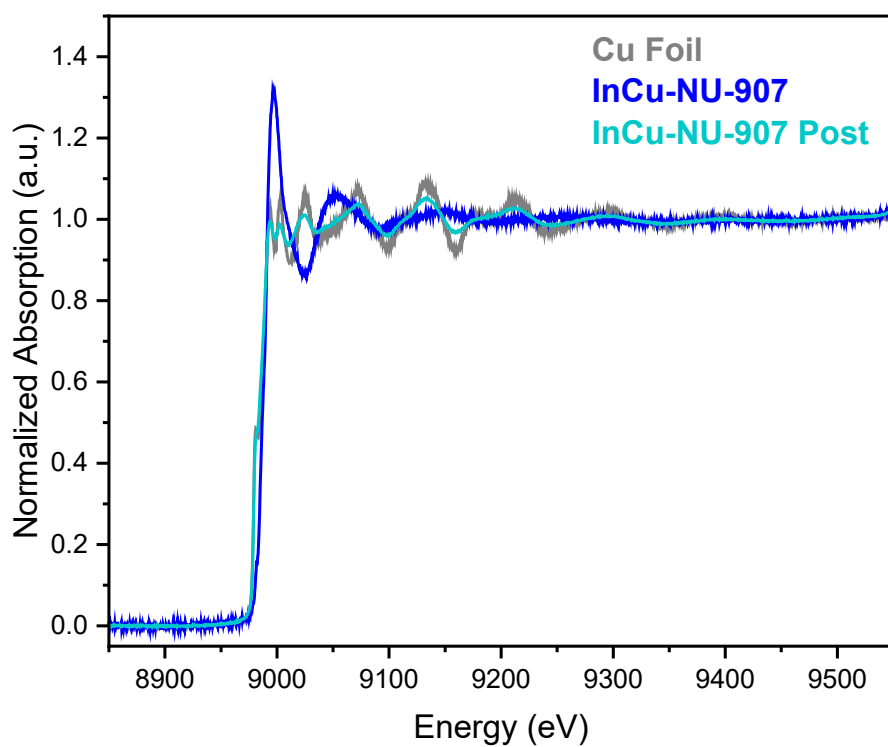
Figure 5.15 Full Cu-K edge XAS spectra for Cu foil reference (gray), InCu-NU-907 (blue), and post-reduction InCu-NU-907 (light blue).
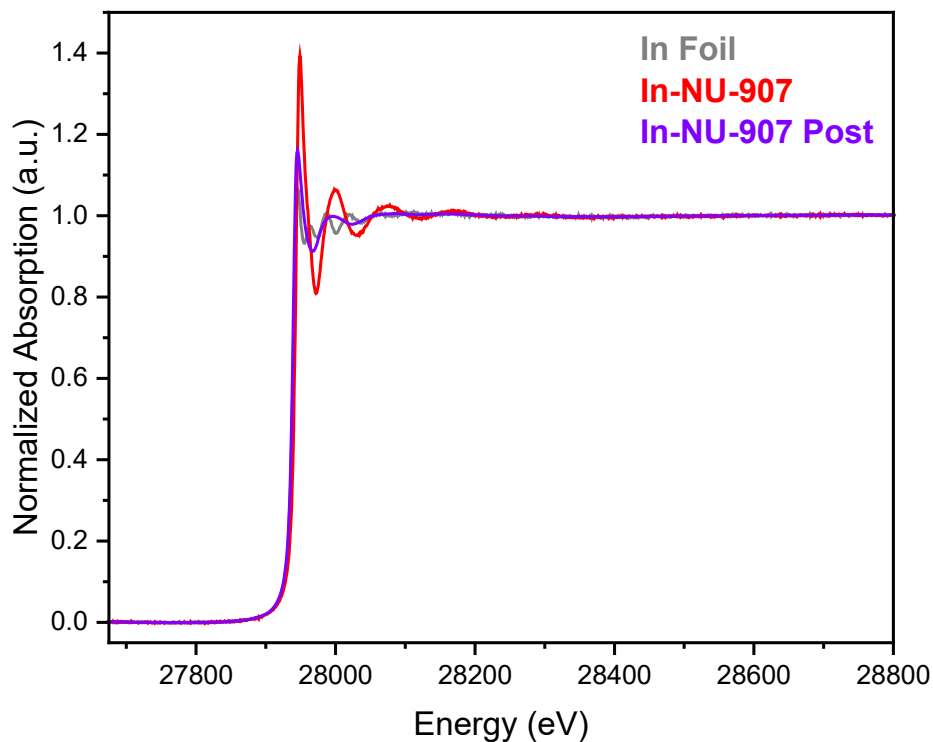
Figure 5.16 Full In-K edge XAS spectra for In foil reference (gray), In-NU-907 (red), and post-reduction In-NU-907 (purple).
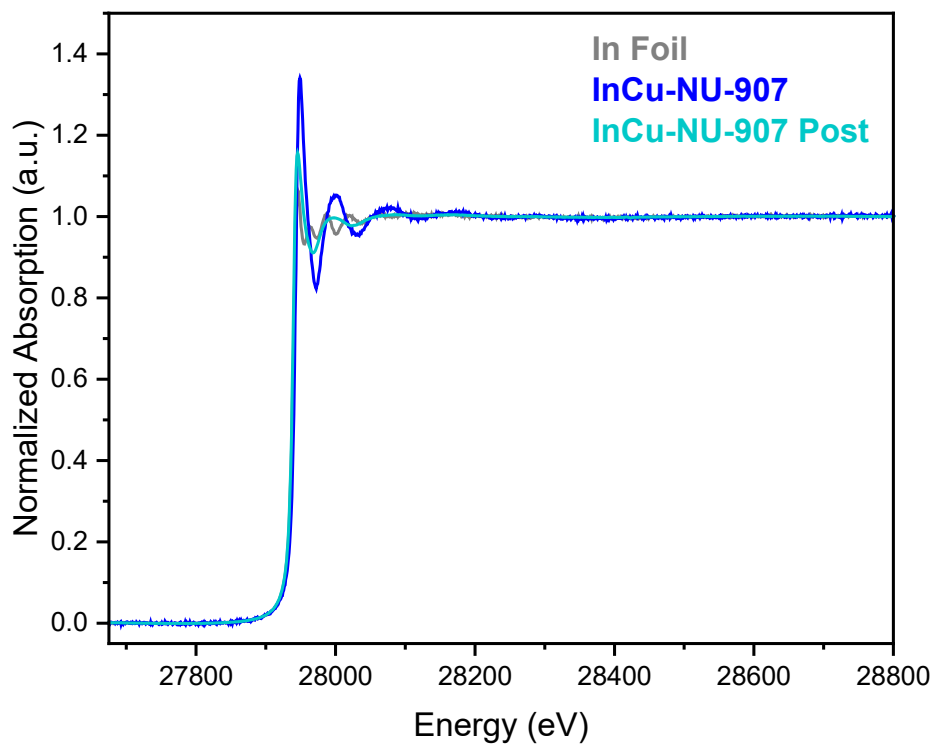
Figure 5.17 Full In-K edge XAS spectra for In foil reference (gray), InCu-NU-907 (blue), and post-reduction InCu-NU-907 (light blue).
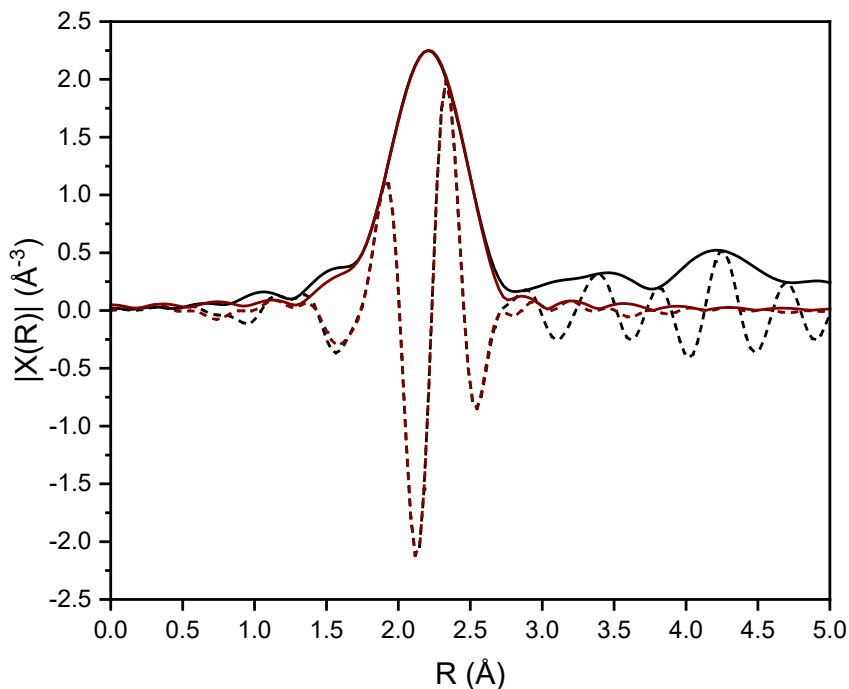
Figure 5.18 R-space Cu-K edge EXAFS spectrum of post-reduction Cu-NU-907 magnitude (solid black) and imaginary (dashed black) components and R space fit of the EXAFS magnitude (solid brown) and imaginary (dashed brown) components. FT generated with k^2-weighting and using a k-range of 3 – 11.5 Å^{-1}. Fit conducted across the range of 1 – 3 Å in R-space.
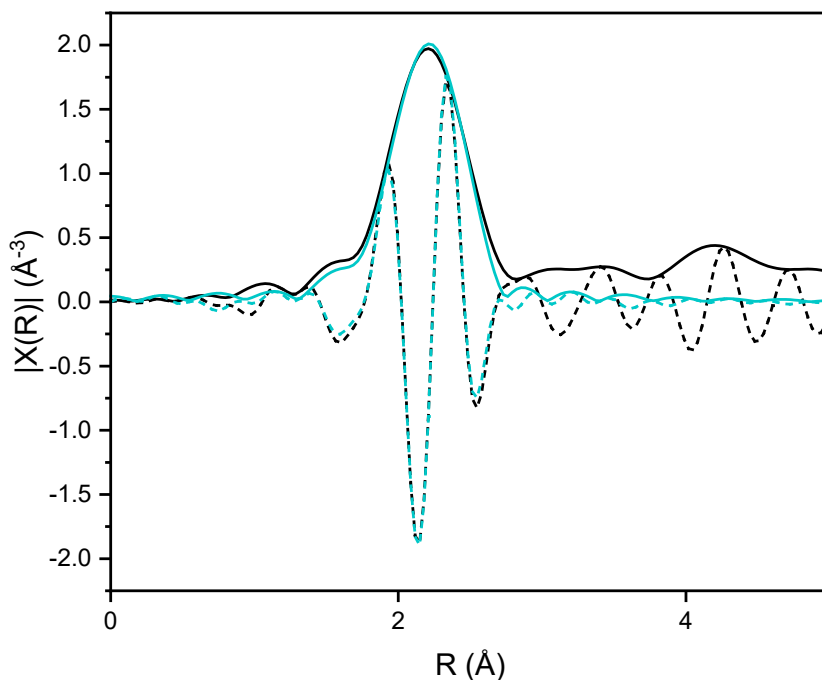
Figure 5.19 R-space Cu-K edge EXAFS spectrum of post-reduction InCu-NU-907 magnitude (solid black) and imaginary (dashed black) components and R space fit of the EXAFS magnitude (solid light blue) and imaginary (dashed light blue) components. FT generated with k^2-weighting and using a k-range of 3 – 11.5 Å^{-1}. Fit conducted across the range of 1 – 3 Å in R-space.
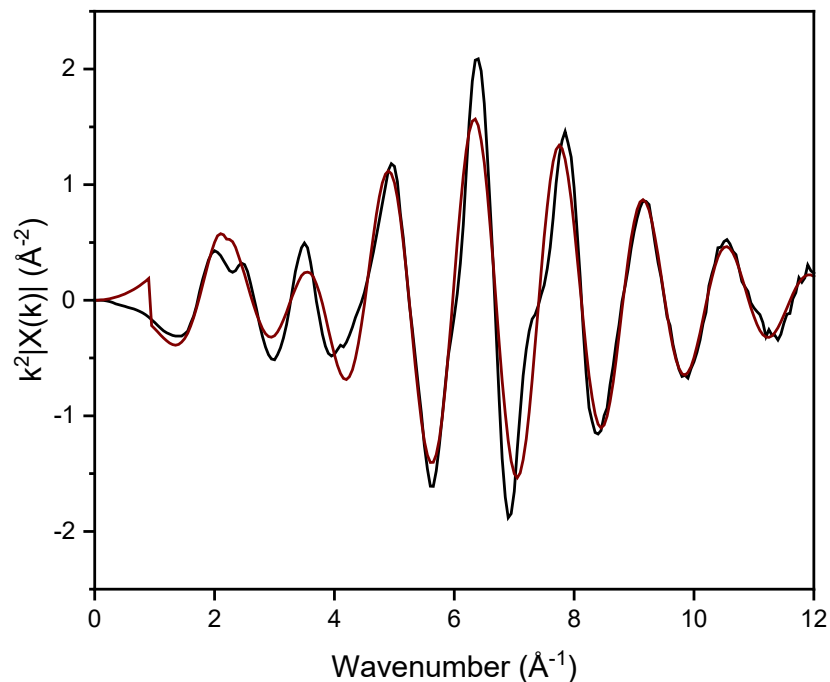
Figure 5.20 Cu-K edge EXAFS spectrum of post-reduction Cu-NU-907 in k-space (black) and k-space fit (brown). Fit generated with k^2-weighting and using a k-range of 3 – 11.5 Å^{-1}.
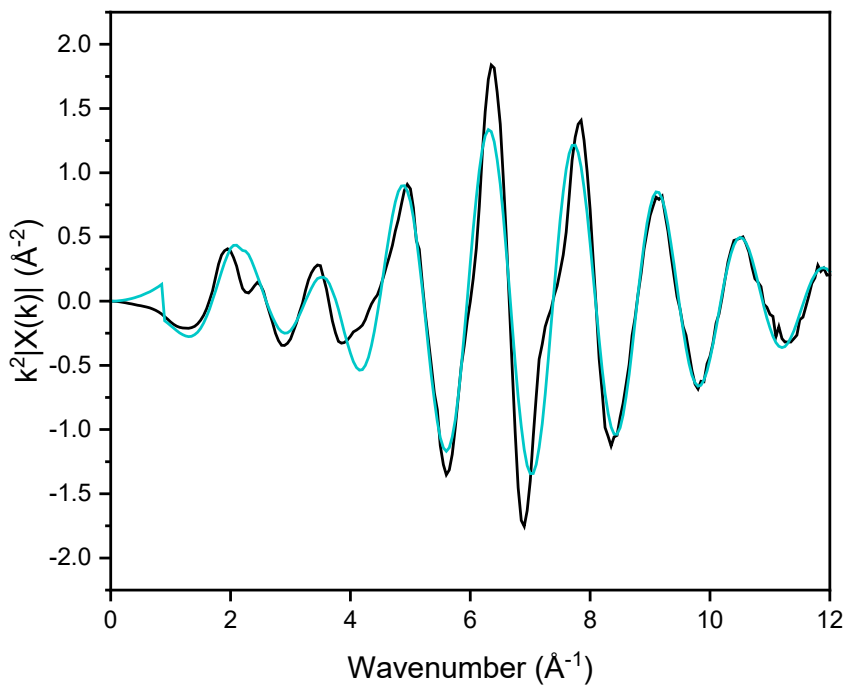
Figure 5.21 Cu-K edge EXAFS spectrum of post-reduction InCu-NU-907 in k-space (black) and k-space fit (light blue). Fit generated with k^2-weighting and using a k-range of 3 – 11.5 Å^{-1}.
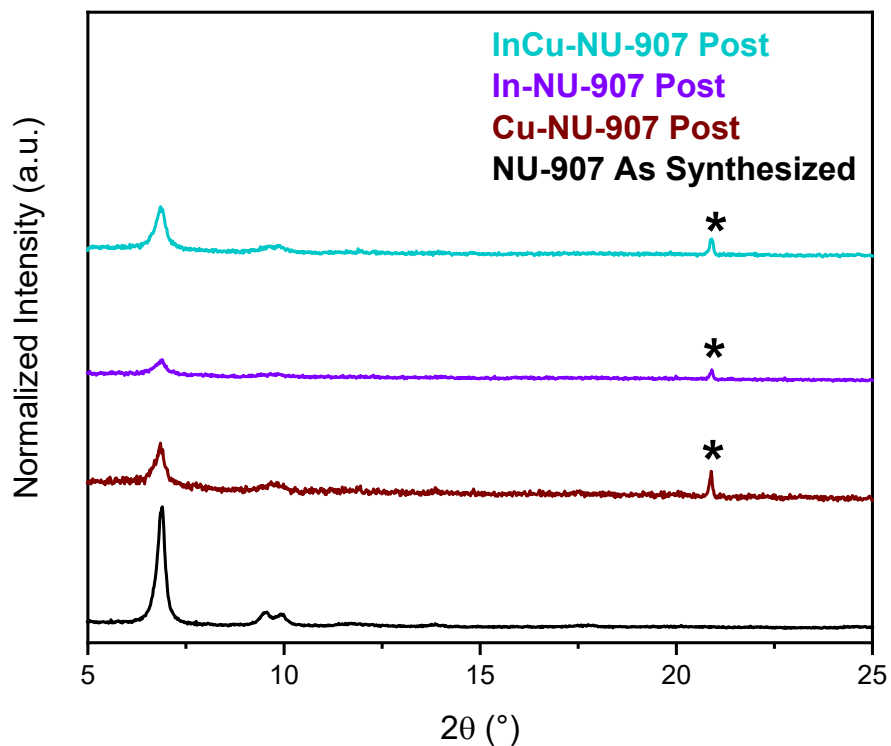
Figure 5.22 PXRD patterns for post-catalysis Cu-NU-907 (brown), In-NU-907 (purple), and InCu-NU-907 (light blue) compared to the as-synthesized NU-907 pattern (black). *Additional peak due to residual SiO_2 in post-catalysis samples. Note: some diminished overall intensity in post-catalysis samples is due to the residual amorphous SiO_2.

Chapter 6. Conclusions and Outlook

6.1 Conclusions

In summary, this work showcases the development of structurally well-defined catalyst platforms for the determination of structure-function relationships in heterogeneous catalyst systems. Advancements of atomic-level characterization of heterogeneous catalysts were made by using structurally well-defined supports, metal–organic frameworks (MOFs). Initial work sought to explore the reactivity of a Cr-based catalyst installed at the Zr_6 node of a MOF for ethylene oligomerization to a Schulz-Flory distribution of liquid hydrocarbon products. Through single-crystal X-ray diffraction measurements, we elucidated the structure of the as-synthesized catalyst, which can be used for further determination of structure-function relationships by catalyst modification. Subsequent work utilized the versatile Cr catalyst for ethylene polymerization, where produced polyethylene had defined properties including a polydispersity characteristic of a single-site catalyst. Additional X-ray diffraction measurements led to the determination of the co-catalyst treated crystal structure, identifying the replacement of the Cr–Cl by Cr–C when exposed to the co-catalyst. With extensive characterization, a plausible mechanism was proposed.

While single-crystal X-ray diffraction studies yield impressive results in terms of the determination of atomic-level structures of catalysts, these measurements are performed under *ex-situ* conditions rather than those during the reaction. Therefore, in the next study, we turned to *operando* X-ray absorption spectroscopy, using a newly built high-pressure capillary reactor, coupled with kinetic experiments to collect information on the evolution of the catalyst structure under relevant reaction conditions and probe further into the mechanism. In this case, the catalyst

structure under reaction conditions remains the same as the pre-catalyst, confirming the active site structure and providing additional evidence for the linear chain insertion mechanism.

6.2 Outlook and Future Opportunities

We anticipate the application of MOFs within the field of heterogeneous catalysis will continue to expand as they provide unique opportunities for fundamental research into catalyst structure-function relationships. Already, MOFs have been studied and proven effective for a wide range of catalytic reactions, in some cases exhibiting unique reactivity or selectivity due to confinement effects or stabilizing a catalyst structure not feasible in other traditional supports. Their crystalline nature allows for atomic-level characterization of the catalysts by single-crystal X-ray diffraction and their uniform structures facilitate the use of *operando* techniques such as X-ray absorption spectroscopy under relevant reaction conditions. We envision that the use of these structurally well-defined catalyst platforms will identify structure-function relationships in heterogeneous catalysis reactions and will contribute to the development of design rules for next-generation catalysts.

Appendix 1 – Embedding a Molecular Catalyst within a Metal–Organic Framework for Ethylene Polymerization

The following work is unfinished due to discrepancies between the amount of ethylene consumed and polymer formed, therefore indicating substantial oligomer formation rather than complete polymer formation. Investigation into the mechanism of operation and replication of catalysis experiments is needed.

A1.1 Introduction

The field of homogeneous catalysis has been working with molecular compounds that have well-defined structures and therefore well-defined active sites.[165] However, these molecular species often suffer from drawbacks such as issues with recyclability and separation from products, due to their inherent need to be solubilized within the reaction system. On the other hand, heterogeneous catalysts provide facile methods of separation from products and typically enhanced recyclability but tend to suffer from non-uniform active sites which makes the elucidation of mechanistic insights and structure-function relationships non-trivial.[158] Supporting molecular catalysts on traditional heterogeneous supports such as silica or alumina (or other bulk metal oxides) alleviates the issue of recyclability in the homogeneous catalytic systems but does not retain the structural definition of the original molecular species due to the potential of non-uniform catalyst deposition sites. Therefore, catalyst supports with a high degree of structural uniformity that can serve to anchor molecular catalysts are desired to further this bridging of the gap between

homogeneous and heterogeneous catalysis, a realm often referred to as supported organometallic chemistry.[171]

Metal–organic frameworks offer unique opportunities to embed molecular catalysts within a structurally well-defined catalyst support, either through encapsulation within the pore environment or by ligation to the organic linker itself.[140] Utilization of the linker as an anchoring site for the catalytic species can be inspired by the ligands of the molecular catalysts themselves. For instance, nitrogen containing ligands such as bipyridine and phenanthroline are moieties that are readily installed into MOFs after being functionalized with carboxylic acids.[216] These bidentate nitrogen donor ligands allow for the coordination of a wide range of catalytic metals while still offering the chance for open metal sites and additional ligands or substrates to interact with the catalytic metal species of interest. Moreover, with these ligands spatially isolated in the organic linkers and periodically arrayed within the framework, harmful intermolecular deactivation pathways such as dimerization, often seen in homogeneous systems, can be shut off.

The Zr-based MOF, UiO-67 (UiO, University of Oslo; [Zr6(μ_3-OH)4(μ_3-O)4(OH)4(OH2)4](BPDC)2; BPDC, biphenyl dicarboxylate; see **Figure A1.1** for node and linker structure),[37] can serve as a model system for the incorporation of bipyridine or phenanthroline ligands as structural building units in place of the original biphenyl dicarboxylate linkers (see **Figure A1.2**). To date, multiple studies of partial or full incorporation of bipyridine dicarboxylate into the UiO-67 structure as well as phenanthroline dicarboxylate have been reported.[24, 85, 180, 217-220] This has led to studies on the ligation of Ni, Ir, Cu, etc. into the nitrogen containing ligands for catalyst immobilization. Due to these successes, it stands to reason that attempting to incorporate Cr-based catalysts in a similar fashion should be straightforward.
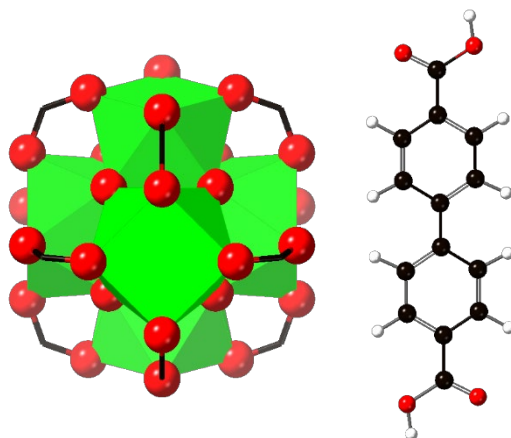
Figure A1.1 Zirconium cluster node (left) and biphenyl dicarboxylic acid linker (right) of UiO-67.
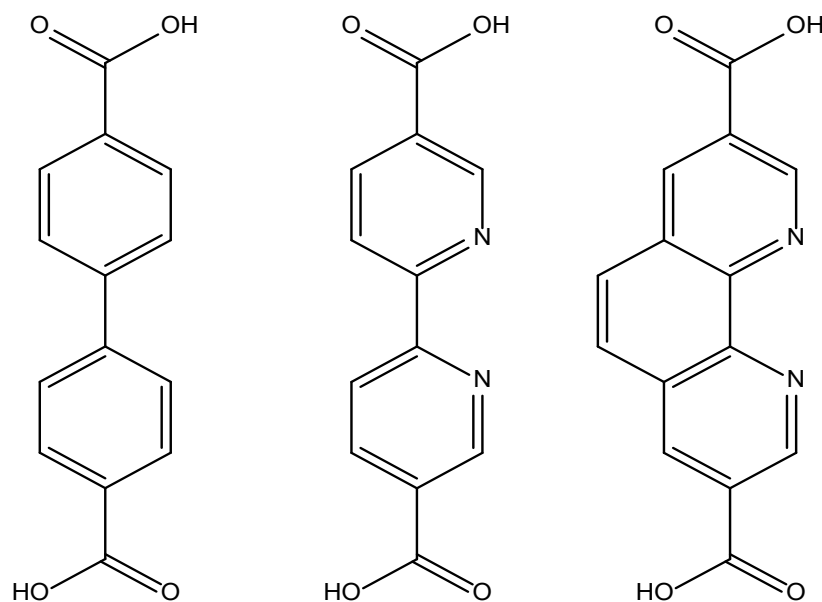
Figure A1.2 Structures of biphenyl dicarboxylic acid (BPDC, left), bipyridine dicarboxylic acid (BPYDC, middle), and phenanthroline dicarboxylic acid (PHENDC, right)

Therefore, this study aims to identify candidate Cr-based catalysts that can be installed in UiO-67-bpy to build upon the library of rigorously studied molecular catalysts for olefin polymerization. Akin to modifying the ligand environment of a molecular catalyst, incorporation of phenanthroline into the UiO-67 structure is also desired to systematically modify catalyst properties within the same structure and pore environment. These well-defined solid supported

catalysts will be crucial for elucidating structure-function relationships in heterogeneous olefin polymerization systems, and subsequently driving the design of next-generation catalysts.

A1.2 Catalyst Support Synthesis

UiO-67, with the original biphenyl linker, was synthesized according to a procedure which yields low-defect material. The idea behind synthesizing this MOF is to use it as a control model because the installation of metals can occur at the Zr_6 node, as shown many times in the literature, and therefore there is a need for a baseline of metal incorporation and reactivity. Aiming for the low defect synthesis limits the number of open deposition sites at the node, since nominally UiO-67 has a 12-connected node – meaning that if the structure is perfect there are no open terminal ligands for grafting. Based on comparison of experimental and simulated PXRD patterns (**Figure A1.3**) as well as an experimental N_2 adsorption isotherm and DFT calculated pore size distribution (**Figure A1.4**), UiO-67 with low defect density was successfully synthesized.
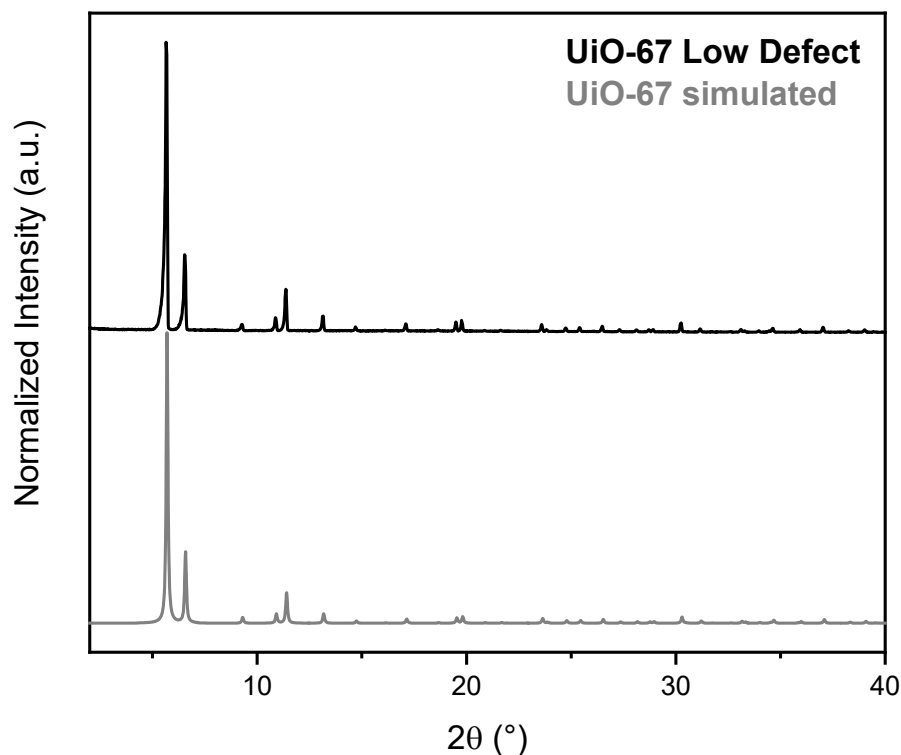
Figure A1.3 PXRD patterns of as-synthesized UiO-67 using a low defect method (black) and simulated UiO-67 from a crystal structure (gray).
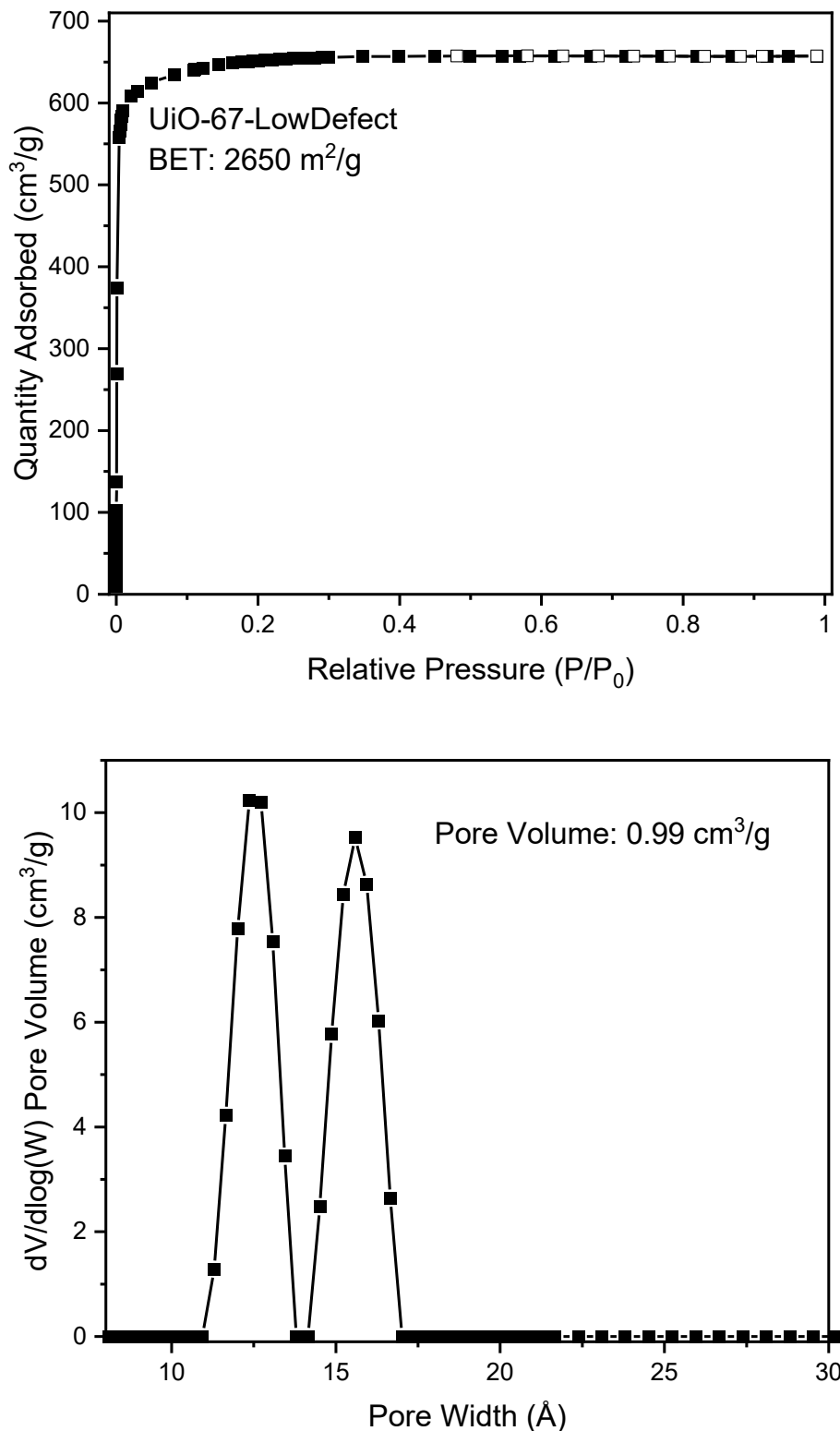
Figure A1.4 Experimental N_2 adsorption isotherm of UiO-67 synthesized by a low defect procedure (top) and DFT calculated pore size distribution showing the two expected pores of low defect UiO-67 (bottom).

UiO-67-bpy was synthesized based on a procedure adapted from the literature. While partial occupancy of the bipyridine can be accomplished, also termed a mixed linker system, a pure material was originally targeted in order to leverage as many deposition sites within the MOF framework as possible. PXRD patterns, N₂ adsorption isotherms, and DFT pore size distributions matched well with the simulated pattern and literature examples (**Figures A1.5** and **A1.6**).
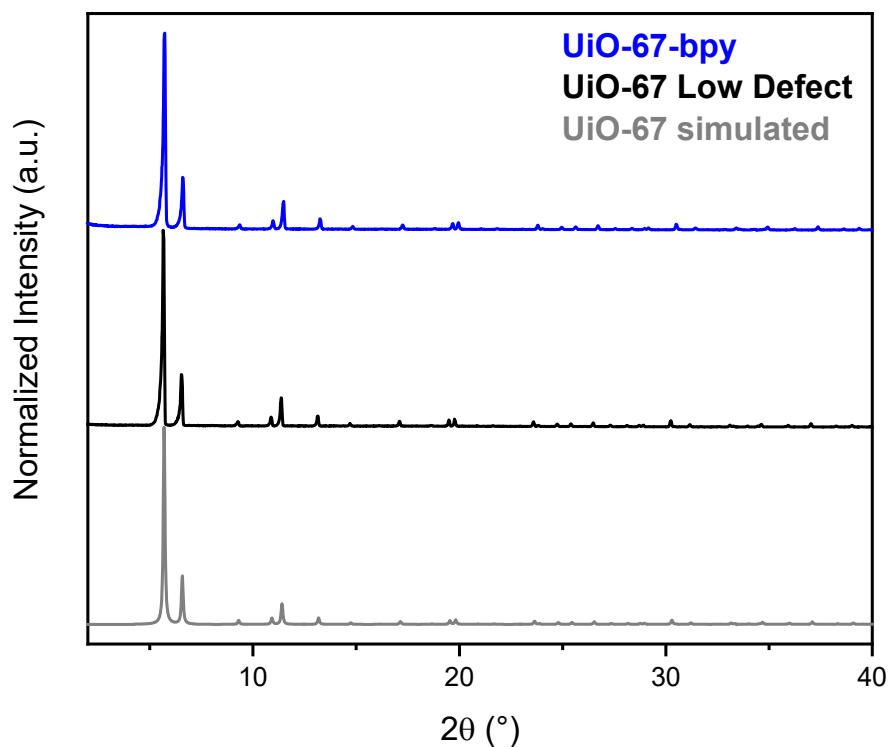
Figure A1.5 PXRD patterns of as-synthesized UiO-67-bpy (blue), UiO-67 synthesized using a low defect method (black) and simulated UiO-67 from a crystal structure (gray).
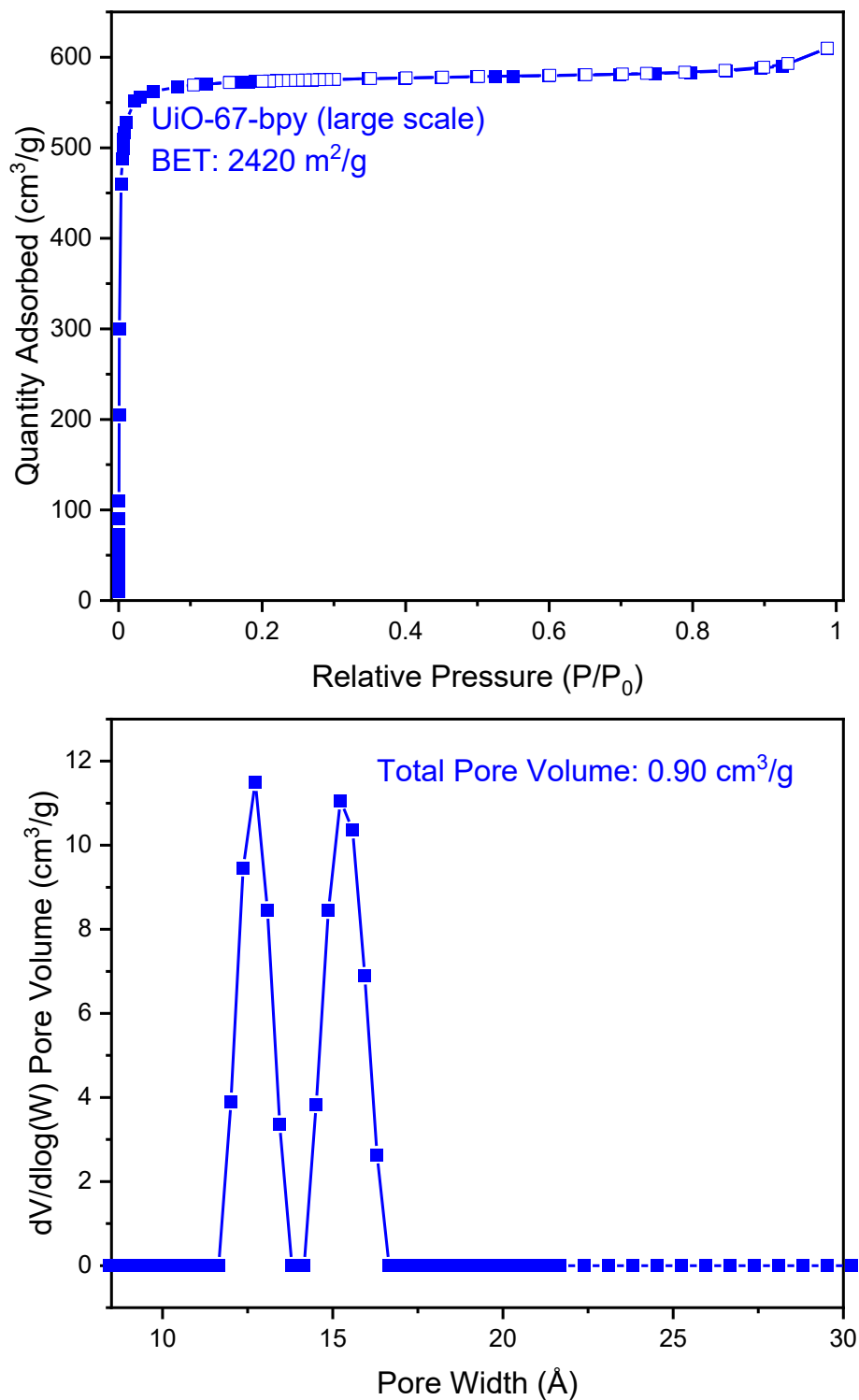
Figure A1.6 Experimental N_2 adsorption isotherm of UiO-67-bpy (top) and DFT calculated pore size distribution showing the two expected pores of UiO-67-bpy (bottom).

Synthesis of pure UiO-67-phen according to different literature procedures[85, 218] was not successfully reproduced (see **Figures A1.7** and **A1.8**) and was limited due to availability of the phenanthroline dicarboxylate linker. Therefore, it may be more feasible to target a mixed linker system which will utilize biphenyl and phenanthroline moieties to lessen the amount of phenanthroline required as well as allow for a templating effect of the biphenyl ligand to encourage uniform growth of the framework.
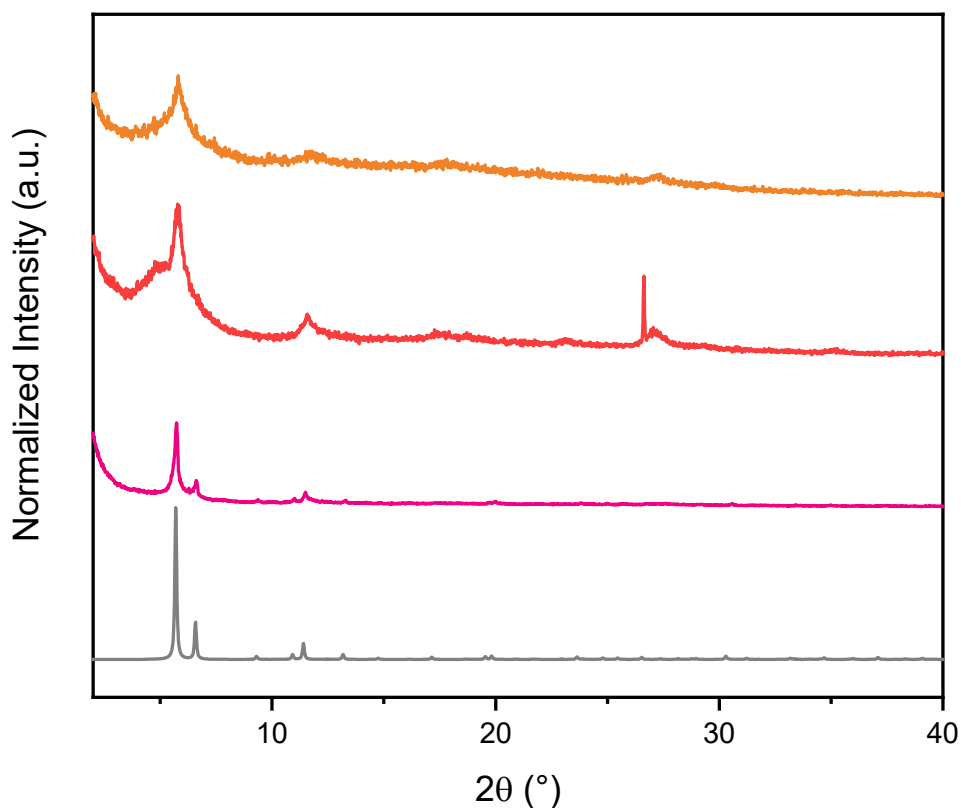
Figure A1.7 PXRD patterns of simulated UiO-67 (gray) and UiO-67-phen synthesis attempts. Crystallinity varies amongst the different trials (pink, red, orange).
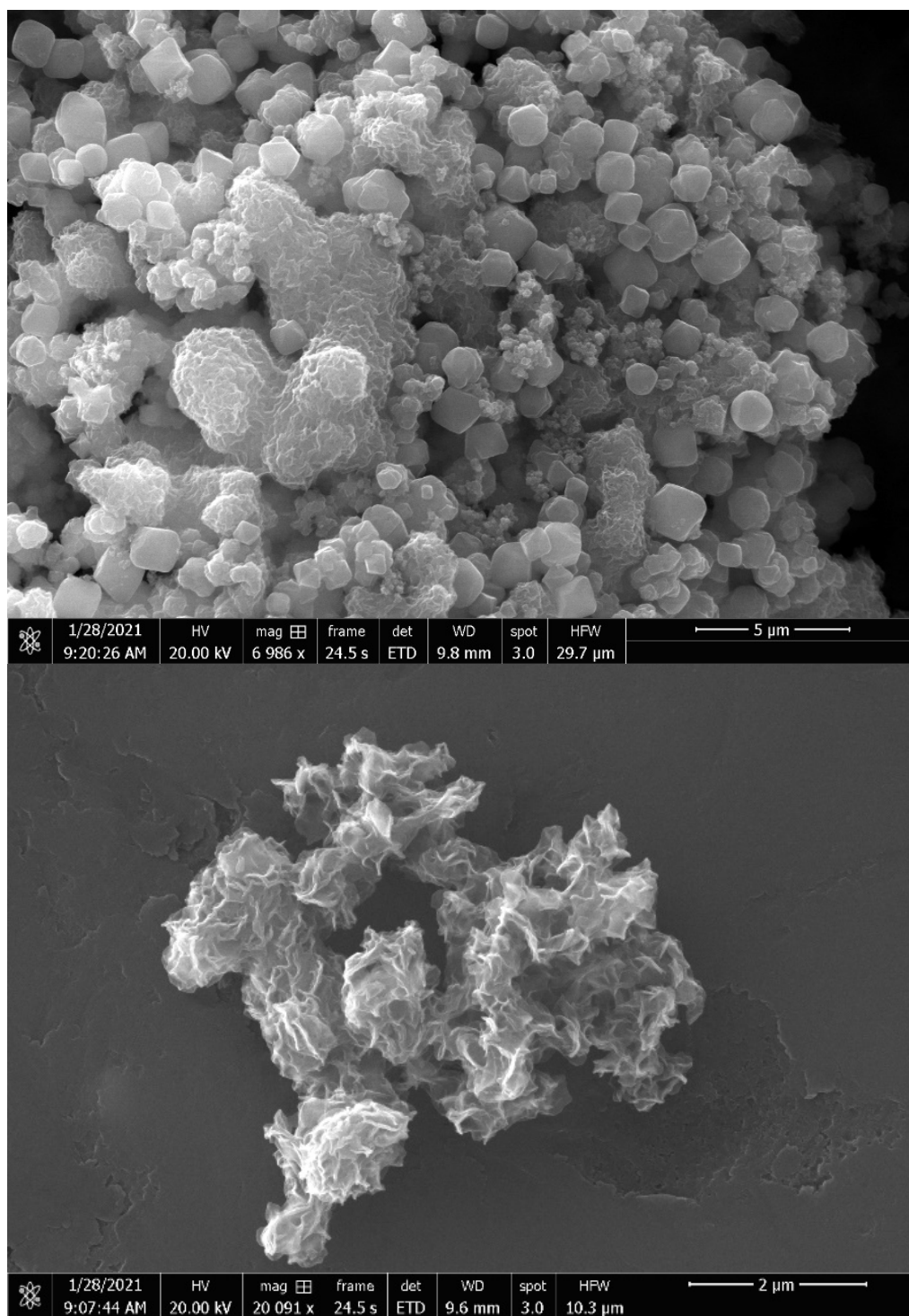
Figure A1.8 Representative SEM images of a synthesis trial of UiO-67-phen containing some octahedron-like particles and other nonuniform morphologies.

A1.3 Installation of Cr Species

Firstly, a simple Cr catalyst species was targeted for incorporation into the series of MOF, $CrCl_3 \cdot 3THF$. The reason for this being starting out with a small metal species, given the pore size of the MOF only reaches roughly 16 Å, with a smaller pore aperture. Additionally, the bipyridine ligand environment is already provided by the structure of the MOF itself. Initial attempts at metal installation targeted the bipyridine material to optimize metal loading conditions before using the biphenyl version as a control. Cr deposition was performed by solvothermal deposition in MOFs (SIM) using THF as a solvent at room temperature.

Loading of Cr into UiO-67-bpy was unsuccessful at first, yielding Cr loading of 0.002 Cr atoms per bipyridine ligand by ICP-OES. After then collecting SEM images of UiO-67-bpy it was readily apparent that there was residual organic ligand deposited on the MOF crystallites (**Figure A1.9**). Therefore, a washing procedure was necessary prior to further Cr loading attempts. After washing with hot DMF, UiO-67-bpy retained bulk crystallinity and porosity, meanwhile SEM images showed significant removal of residual organic buildup (**Figure A1.9**). Retention of porosity was confirmed by N_2 adsorption isotherm likely indicating that the residual organic was not substantially blocking the pores of the MOF (**Figure A1.10**).
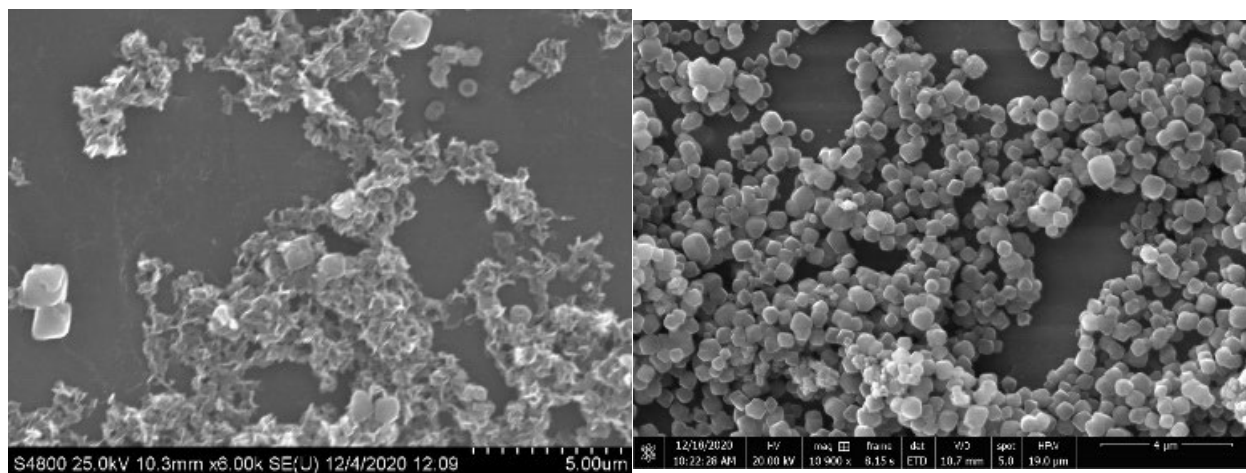
Figure A1.9 SEM images of as-synthesized UiO-67-bpy (left) and UiO-67-bpy after washing with hot DMF (right) showing removal of residual organic material.
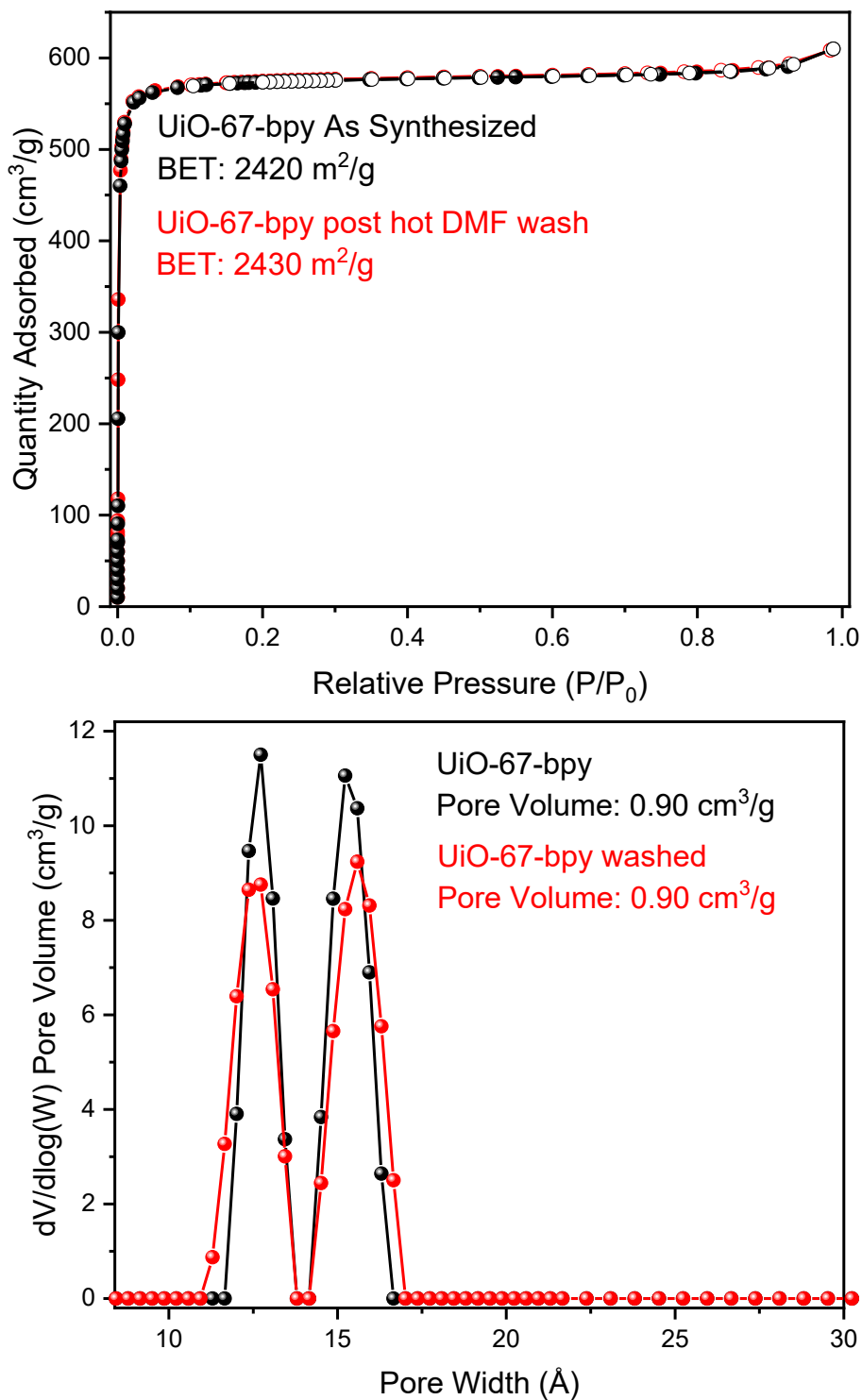
Figure A1.10 Comparison between experimental N_2 adsorption isotherms (top) of as-synthesized UiO-67-bpy (black) and hot DMF washed UiO-67-bpy (red). Comparison between DFT calculated pore size distributions (bottom).

Through iterative screening of Cr loading conditions, eventually between 0.40 – 1.45 Cr atoms per linker were installed, depending on Cr exposure. With roughly linear loading vs. Cr exposure, there is a handle to tune the amount of installed Cr (**Figure A1.11**). The time of exposure also had an impact on the loading, eventually causing more than 1 Cr atom per linker to be installed, likely indicating that there is excess deposition at defect sites at the nodes. The control low defect UiO-67 had Cr loading at similar conditions of 0.27 ± 0.10 Cr atoms per linker, even at a range of exposure levels from 3.4 – 8.3 Cr per linker and 48 h exposure time (**Figure A1.12**). With a moderately effective Cr loading method that yields enhanced incorporation in UiO-67-bpy over UiO-67, the catalysis could then be screened to test if the system would be a viable candidate that is active for ethylene polymerization.
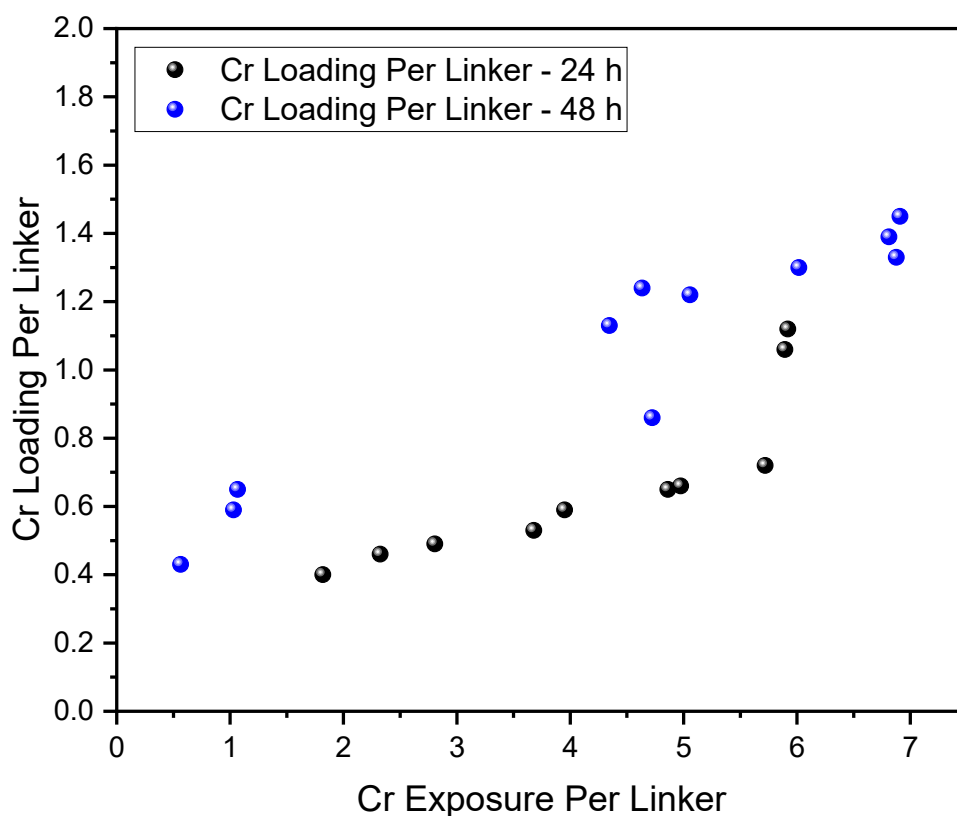
Figure A1.11 Dependence of Cr loading per linker of UiO-67-bpy measured by ICP-OES on the initial exposure level of Cr per linker over a 24 (black) or 48 (blue) h exposure period.
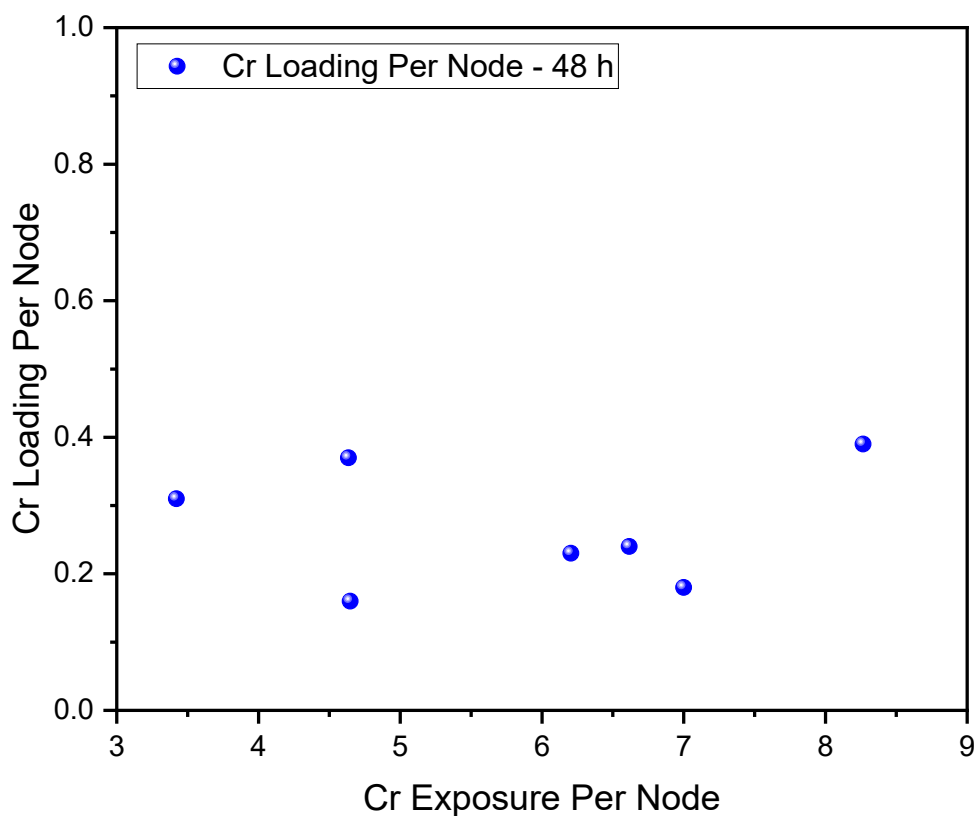
Figure A1.12 Dependence of Cr loading per node of low defect UiO-67 measured by ICP-OES on the initial exposure level of Cr per node over a 48 h (blue) exposure period.

A1.4 Ethylene Polymerization Activity

Using a Parr pressure reactor, the ethylene polymerization activity of Cr-SIM-UiO-67-bpy was screened. The catalyst, along with heptane solvent and diethylaluminum chloride co-catalyst were placed in the reactor inside of an Ar-filled glovebox before being transferred to the gas manifold to be charged with ethylene. After exposure to high-pressure ethylene at 40 bar, the reactor was opened and polymer yield was determined by isolated yield. The polymer productivity, determined by the isolated yield, was found to be $11,300 \pm 3,000$ g PE mol^{-1} Cr h^{-1} with an ethylene consumption turnover frequency of 6400 ± 100 h^{-1}. The catalyst therefore is active for this chemical transformation, however the polymer productivity does not align with the expected amount given the turnover frequency. This can be explained by the significant formation of oligomers as liquid products, undesirable when targeting solid polymer. While this catalyst does

form some polymer, it does not nearly reach the amount expected, therefore the oligomer liquid products make up the majority of products, even when the catalyst is exposed to 40 bar of ethylene. Additional effort is needed to investigate this system, identify if the product distribution can be tuned towards polymer, or if another type of catalytic Cr species should be targeted instead.

A1.5 Future Work

Further efforts into many aspects of this project can lead towards a complete story and understanding of the targeted catalyst system. Replicates of the catalysis data as well as tuning of the catalysis conditions to yield solely polymer are needed. Given the fact that even at 40 bar of ethylene, polymer is not the main product, there needs to be some additional change rather than driving force of substrate pressure.

Whatever is done with the catalysis conditions, the polyethylene produced still needs to be thoroughly characterized to identify the polymer properties such as melting point, % crystallinity, linearity, and molecular weight to name a few. These properties can subsequently be correlated to catalyst structure through structure-function relationships. This segues nicely into discussion of the need for single-crystal X-ray diffraction data of this catalyst to identify the active site structure and ligand environment. Single crystals of UiO-67 and UiO-67-bpy have previously been reported in the literature therefore it should be as straightforward as replicating literature procedures to yield single crystals of sufficient quality and size for X-ray diffraction.

Of course, in addition to all the previously mentioned work left to be done on this study, there is always a need for post-catalysis characterizations. For MOF catalysts, this ends up being PXRD to determine retention of bulk crystallinity, N_2 adsorption to confirm porosity retention, ICP-OES to identify if Cr leached during the catalysis, and SEM to observe if there are any changes to catalyst crystallite morphology. This post-catalysis characterization, tied in with the previously

mentioned efforts for the investigation of a molecular catalyst installed within a MOF linker can yield an interesting publication that will benefit the community through the dissemination of knowledge of structure-function relationships in heterogeneous catalysis that can feed into the development of next-generation catalysts.

A1.6 Additional Information

A1.6.1 Materials

Acetone, *N,N*-dimethylformamide (DMF), tetrahydrofuran (THF), triethylamine (TEA), and hydrochloric acid were purchased from Fisher Scientific (Waltham, MA) and used as received. Benzoic acid (BA), acetic acid (AA), trifluoroacetic acid (TFA), zirconyl chloride octahydrate, chromium(III) chloride tetrahydrofuran complex (1:3), and biphenyl-4,4′-dicarboxylic acid (BPDC) were purchased from Sigma-Aldrich (St. Louis, MO) and used as received. *N,N*-diethylformamide (DEF) was purchased from TCI America (Portland, OR) and used as received. Zirconium(IV) chloride was purchased from Strem Chemicals (Newburyport, MA) and used as received. UHP N_2 (99.999%), UHP Ar (99.999%), and UHP ethylene (99.9%) were purchased from Airgas (Radnor, PA) and used as received.

A1.6.2 Synthetic Methods

UiO-67 low defect powder synthesis. In a 1-L glass bottle 660 mg biphenyl-4,4'-dicarboxylic acid was mixed into 630 mL DMF, 64.4 mL acetic acid, and 70 µL TEA, and subsequently heated at 100 °C for 15 min. In a separate 50 mL centrifuge tube, 630 mg $ZrCl_4$ was dissolved in 45 mL DMF. Once the linker solution was cooled to room temperature, the zirconium solution was added to the 1-L bottle and then heated in an oven at 100 °C overnight. The solid white powder was then collected by centrifugation and washed 3 times with fresh DMF before being solvent exchanged to acetone with an additional 3 washes with fresh acetone and one overnight soak. The isolated powder was then dried in a vacuum oven at 80 °C before being thermally activated on an ASAP 2420 at 150 °C overnight.

UiO-67-bpy powder synthesis. In a 500-mL glass bottle, 490 mg $ZrCl_4$, 520 mg biphenyl-4,4'-dicarboxylic acid, and 3.6 mL acetic acid were combined along with 80 mL DMF. The bottle was then placed in an oven at 120 °C overnight. The solid white powder was then collected by

centrifugation and washed 3 times with fresh DMF before being solvent exchanged to acetone with an additional 3 washes with fresh acetone and one overnight soak. The isolated powder was then dried in a vacuum oven at 80 °C before being thermally activated on an ASAP 2420 at 150 °C overnight.

UiO-67-phen powder synthesis. Multiple literature methods were attempted,[85, 218] but no successful highly crystalline product was formed. Typical syntheses involved mixing $ZrCl_4$ and 1,10-phenanthroline-3,8-dicarboxylic acid in DMF, and adding a monocarboxylic acid modulator such as benzoic acid or acetic acid. Synthesis temperature was 120 °C and reaction time varied from 1 – 3 days.

Cr-SIM Method. First, $CrCl_3 \cdot 3THF$ was dissolved in THF and a stir bar was added. Then, the MOF was added and the mixture was stirred at room temperature for 24 – 48 h.

A1.6.3 Catalysis Details

Ethylene polymerization. In an Ar filled glovebox, 10 - 30 mg Cr-SIM-UiO-67-bpy, 5 mL anhydrous heptane, and 1.0 mL of diethylaluminum chloride (1.0 M in heptane) were charged into a 50 mL 4590 micro bench top autoclave Parr reactor. The reactor was then sealed, transferred out of the glovebox and connected to the gas inlet, pressure gauge, and thermocouple at the reactor station. The reactor was then set to stir at 200 rpm and pressurized to between 5 and 40 bar with C_2H_4. After 1 hour, the reaction was vented and opened, after which the solid polymer was recovered for analysis.

A1.6.4 Physical Characterization and Instrumentation

Powder X-ray diffraction (PXRD) data was collected at the IMSERC X-ray Facility at Northwestern University on a STOE-STADI-P powder diffractometer equipped with an asymmetric curved germanium monochromator (CuKα1 radiation, λ = 1.54056 Å) and one-dimensional silicon strip detector (MYTHEN2 1K from DECTRIS). The line focused Cu X-ray

tube was operated at 40 kV and 40 mA. Powder was packed in a 3 mm metallic mask and sandwiched between two layers of polyimide tape. Intensity data from 1 to 40 degrees 2θ were collected over a period of 5 min.

N_2 adsorption isotherms were measured on a Micromeritics ASAP 2420 (Micromeritics, Norcross, GA) at 77 K with 30–80 mg pre-activated sample at 120 °C for 16 h under high vacuum using the ASAP 2420. BET area was calculated in the region $P/P_0 = 0.005$–0.05 and pore-size distributions were obtained via density functional theory (DFT) calculations using a carbon slit-pore model with a N_2 kernel.

Inductively coupled plasma optical-emission spectroscopy (ICP-OES) was performed at the QBIC facility at Northwestern University on a Thermo iCAP 7600 spectrometer (ThermoFisher, Waltham, MA). In each preparation, ~3 mg samples were digested in 2 mL concentrated nitric acid in a 2–5 mL Biotage (Uppsala, Sweden) microwave vial. Biotage SPX microwave reactor (software version 2.3, build 6250) was used to heat the mixture to 150 °C for 15 min. 300 μL of the digested sample was removed and diluted to 10 mL with ultrapure Millipore water.

Scanning electron microscopy (SEM) images were collected at Northwestern University's EPIC/NUANCE facility using an FEI Quanta 650 ESEM microscope. All samples were coated with 9 nm OsO_4 before imaging.

Appendix 2 – Systematic Study of the Effect of Brønsted Acid Strength and Pore Size on Biomass Esterification

Portions of this chapter appear in the following manuscript:

Wang, F.; Chen, Z.; Chen, H.; **Goetjen, T. A.**; Li, P.; Wang, X.; Alayoglu, S.; Ma, K.; Chen, Y.; Wang, T.; Islamoglu, T.; Fang, Y.; Snurr, R. Q.; Farha, O. K., Interplay of Lewis and Brønsted Acid Sites in Zr-Based Metal–Organic Frameworks for Efficient Esterification of Biomass-Derived Levulinic Acid. *ACS Appl. Mater. Interfaces* **2019**, *11* (35), 32090-32096.

The additional work beyond that from the above publication is unfinished due to lack of progress

in the development of synthetic protocols. Optimization of the MOF linker and MOF syntheses

is a suitable starting point for the continuation of this project.

A2.1 Introduction

The finite nature of fossil fuels and increased efforts toward sustainable development, along with environmental deterioration, have stimulated the search for renewable energy resources.[221-222] Biomass is a rising renewable fuel source and has great potential to replace fossil resources for sustainable biofuel or chemical production.[223-225] In particular, levulinic acid has been identified in the list of top 12 biomass-derived building block chemicals as identified by the United States Department of Energy.[226-228] Converting renewable biomass-derived levulinic acid to ethyl levulinate has attracted considerable attention owing to its extensive applications as a solvent, polymer, and plasticizer, in addition to significant use as a biofuel in the energy industry.[229-231] Therefore, efficient conversion of levulinic acid to ethyl levulinate is highly desirable to provide incentive for the replacement of fossil fuel-derived chemical resources.

Typically, ethyl levulinate is produced through esterification of levulinic acid, which can be catalyzed by various homogenous and heterogeneous catalysts in ethanol.[232] Unfortunately, traditional homogeneous catalysts such as H_2SO_4, HCl, and H_3PO_4 are unrecyclable and inevitably suffer from drawbacks including severe equipment corrosion, higher safety risks, complicated product separation, and environmental pollution.[233] Therefore, there is a high demand to develop efficient heterogeneous solid acid catalysts which will allow for facile catalyst separation and increased catalyst recyclability. To date, various heterogeneous catalysts such as zeolites,[234-235] heteropoly acids,[236-238] WO_x/mesoporous-SiO_2,[239] and sulfated metal oxides[227, 231] have been utilized to produce ethyl levulinate from levulinic acid with ethanol. However, these promising heterogeneous catalysts are still subject to high mass transfer resistance, easy leaching of active sites, and low catalytic activity. Thus, improving upon these known issues by exploring

environmentally friendly, reusable, stable, and efficient solid acid catalysts is the key to increase the efficiency for production of ethyl levulinate.

Metal–organic frameworks (MOFs), comprised of metal ions/clusters and polydentate organic ligands, are a group of highly porous materials that has recently shown high interest for a host of applications due to inherently high surface areas, uniform and tunable pore sizes, and ample opportunities for functionalization.[240-244] So far, MOFs have been thoroughly explored for versatile applications, such as gas storage and separation,[243, 245-246] chemical sensing,[247-249] and heterogeneous catalysis.[250-251] In particular, both the surface area and permanent porosity of MOFs provide access to the interior of the crystals through channels, which facilitate diffusion, having a crucial enhancing effect in heterogeneous catalysis.[252-255.] Given the advantageous structural tunability and enhanced transport, MOFs have tremendous potential from the perspective of designing an efficient heterogeneous catalyst for a targeted application.[244]

A2.2 Previous Work on UiO-66-(COOH)$_2$

A2.2.1 Background

In particular, UiO-66,[37] a MOF with Zr$_6$ nodes highly connected by benzene dicarboxylate linkers, is very attractive owing to its exceptional thermal, chemical, and mechanical stability, versatile synthesis methods, ease of functionalization, and exposed Zr sites which exhibit excellent catalytic performance in various acid-catalyzed reactions.[256-257] More recently, reports have indicated attempts to functionalize UiO-66 MOFs with complementary catalytic moieties, such as Brønsted acids, so that the resulting UiO-66 MOF-based catalyst materials possess desired catalytic performances.[258-259] Furthermore, esterification of levulinic acid with ethanol over Brønsted acidic catalysts has also been widely reported.[235-239] With this in mind, we hypothesized

that incorporating Brønsted acid sites, such as a carboxylic acid group, into the framework of UiO-66 would improve the catalytic activity towards levulinic acid esterification (**Scheme A2.1**).[260-262]
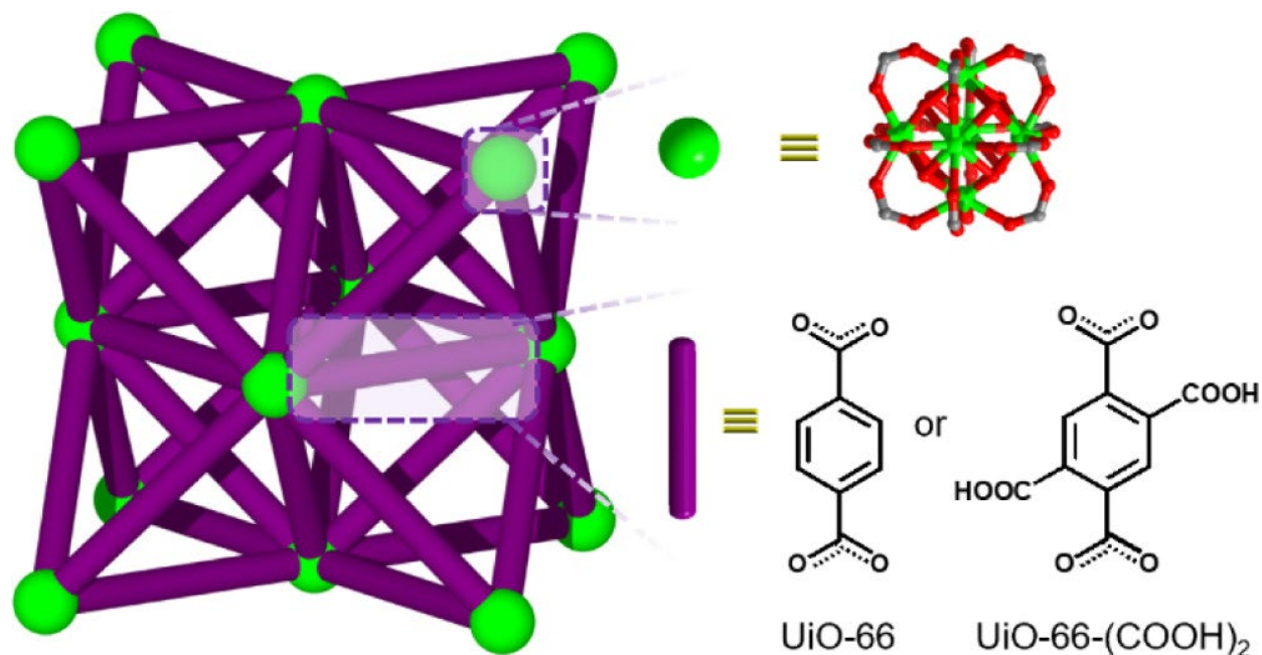
Scheme A2.1 Illustration of the Structure of UiO-66 and UiO-66-(COOH)$_2$.

A2.2.2 Initial Catalytic Results

Pristine UiO-66, with exposed Zr active sites serving as a Lewis acid catalyst for this reaction, afforded only 4.2% yield of ethyl levulinate under identical conditions (*entry 2*, **Table A2.1**). Although UiO-66 has been reported to have higher catalytic activity than that found in our study, this can be attributed to different levulinic acid concentration and catalyst loading. (36) Interestingly, despite the reduced BET surface area, UiO-66-(COOH)$_2$, with two free carboxylic acid groups per phenyl unit, exhibited an enhanced ethyl levulinate yield of 23.9% at 78 °C for 8 h, and thus we inferred that the addition of a Brønsted acid could further facilitate the esterification reaction (*entry 4*, **Table A2.1**). In order to elucidate the role of the free carboxylic acid group on the catalytic activity, another experiment by using only free 1,4-benzendicarboxylate (BDC) as the catalyst was performed, and it was observed that the catalytic activity fell far below that of UiO-

66-(COOH)$_2$, only giving rise to an ethyl levulinate yield of 2.6% (*entry 3*, **Table A2.1**). Furthermore, physically mixing free BDC (equimolar in −COOH groups to UiO-66-(COOH)$_2$) with UiO-66 (equimolar in Zr to UiO-66-(COOH)$_2$) resulted in an ethyl levulinate yield of 10.8% under identical conditions, indicating that Brønsted acid sites were critical and can enhance the yield of ethyl levulinate (*entry 5*, **Table A2.1**). Based on the experimental results above, it was speculated that the significantly improved catalytic activity was most likely due to simultaneously containing both Lewis acid sites (Zr nodes) and Brønsted acid sites (free carboxylic acids) spatially isolated within UiO-66-(COOH)$_2$, which generated a synergistic effect for the esterification reaction. (48)

Table A2.1 Catalytic Performance of Various Catalysts for Esterification of Levulinic Acid to Ethyl Levulinate

entry	catalyst	T (°C)	time (h)	yield of ethyl levulinate (%)
1	blank	78	8	2.3 ± 1.1
2	UiO-66	78	8	4.2 ± 1.4
3	BDC	78	8	2.6 ± 1.2
4	UiO-66-(COOH)$_2$	78	8	23.9 ± 1.9
5	UiO-66 + BDC	78	8	10.8 ± 1.7

Reaction conditions: levulinic acid 2.2 mmol, catalyst (0.39 mol % MOFs or 2.3 mol % BDC based on levulinic acid), ethanol 43 mmol.

A2.2.3 Computational Support by Density Functional Theory

To support or refute the interpretation of the experimental results, and obtain atomistic-level insights into the catalytic mechanism, we carried out DFT calculations to search for the reaction pathways. We first investigated the binding mode of levulinic acid on the node of UiO-66, as both the carbonyl and carboxylic acid groups can bind to the open Zr sites. From our calculations, we found that the carboxylic acid binding mode was 5.1 kJ/mol more favorable than the carbonyl

mode, and we therefore chose to map out the entire catalytic pathway based on this binding mode. Once levulinic acid is adsorbed on the node, the subsequent nucleophilic attack can occur in two ways (**Figure A2.1a**): (1) A Langmuir–Hinshelwood type mechanism where the ethoxide adsorbed on the adjacent Zr site is the nucleophile or (2) an Eley–Rideal type mechanism where a free ethanol molecule from the solvent attacks the bound levulinic acid.
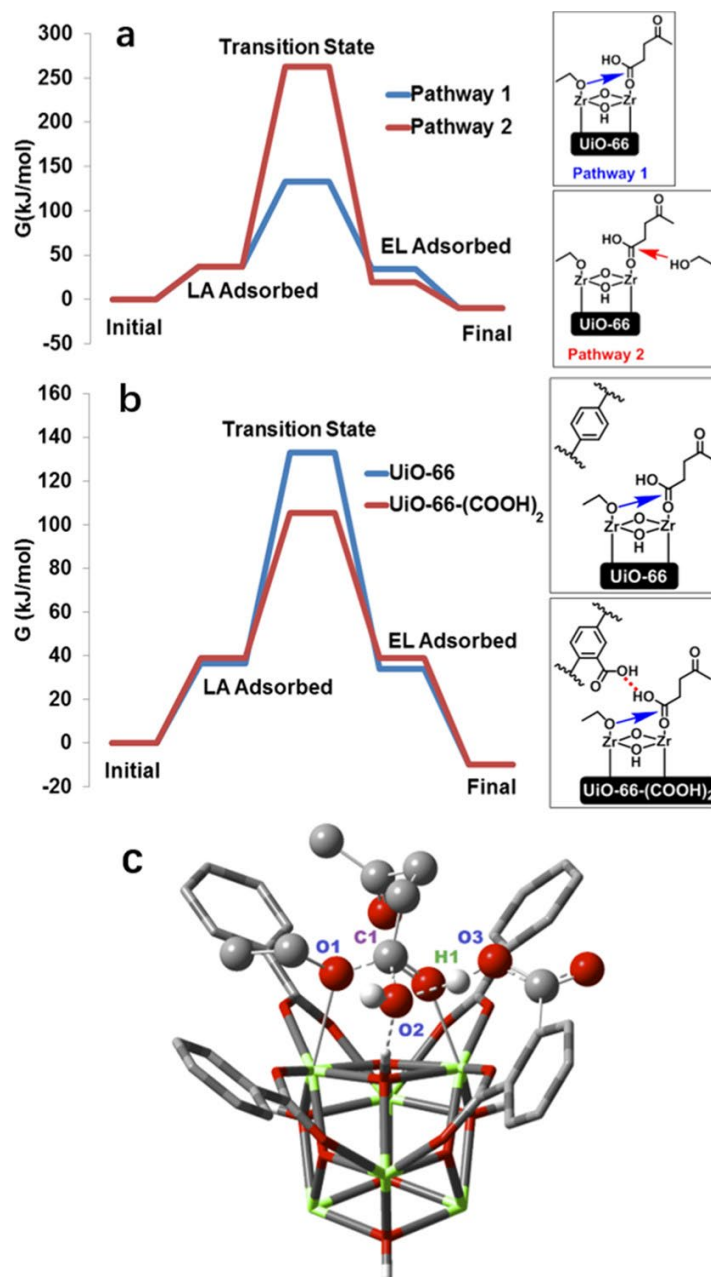
Figure A2.1 (a) Reaction free energy profiles for the esterification of levulinic acid to ethyl levulinate on UiO-66 in the Langmuir–Hinshelwood (pathway 1) and Eley–Rideal (pathway 2) reaction mechanisms. (b) Reaction free energy profiles for the esterification of levulinic acid to ethyl levulinate on UiO-66 (blue) and UiO-66-(COOH)$_2$ (red). (c) Transition state structure of the levulinic acid esterification by UiO-66-(COOH)$_2$ in which the key atoms in the active site are depicted in a ball-and-stick format while other atoms are illustrated in a tube format. For clarity, most hydrogen atoms have been omitted and the linkers far from the active site are not shown. Color code: H—white, C—grey, O—red, Zr—green. O1, O2, and O3 correspond to the oxygen in the ethoxide nucleophile, the oxygen in the leaving group, and the oxygen that stabilizes the leaving group via hydrogen bonding, respectively. The forming O1–C1 bond and the O3–H1–O2 hydrogen bond correspond to the blue arrow and the red dashed line in the bottom right panel of (b), respectively.

Our results show that pathway (1) has a much lower energy barrier (96.5 versus 226.1 kJ/mol) than pathway (2) because ethoxide (activated from ethanol by the Zr site) is a much stronger nucleophile than ethanol. We then modeled pathway (1) on the functionalized UiO-66-$(COOH)_2$ catalyst and found that the energy barrier is significantly lower than on unfunctionalized UiO-66 (66.2 vs 96.5 kJ/mol), which agrees with the experimental finding that the reaction rate is much faster on UiO-66-$(COOH)_2$ than UiO-66 (**Figure A2.1b**). From the analysis of the transition state structure (**Figure A2.1c**), we find that the −COOH group on the linker acts as a Brønsted acid that facilitates the departure of the −OH leaving group in the −COOH group of levulinic acid.

A2.2.4 Optimization of Catalytic Conditions

Considering the fact that varying reaction conditions can have a significant influence on the yield of ethyl levulinate, an experimental series was conducted using UiO-66-$(COOH)_2$ as the catalyst. The effects of catalyst loading, the molar ratio of levulinic acid/ethanol, and the reaction time on the yield of ethyl levulinate were systemically investigated, keeping all other parameters constant. Based on the previous reports, the reaction temperature was fixed at 78 °C (boiling point of ethanol). As shown in **Table A2.2**, it can be clearly seen that increasing the catalyst loading from 0.12 to 0.39 mol % (with respect to the moles of levulinic acid) afforded more available active sites to the reactant, and the ethyl levulinate yield substantially increased from 25.6 to 97.0%. However, increasing the catalyst loading further to 0.5 mol % resulted in a slightly reduced ethyl levulinate yield (83.4%), which was most likely due to excess catalyst contributing to the formation of more water and facilitating the reverse reaction. Additionally, increasing the mole ratio of levulinic acid/ethanol from 1:10 to 1:20 gave rise to an increasing yield of ethyl levulinate from 70.2 to 97.0%, and this may also be attributed to the fact that the esterification reaction of levulinic acid is a reversible reaction, with the forward reaction favored by excess ethanol. (18)

Table A2.2 The Esterification of Levulinic Acid over UiO-66-(COOH)$_2$ under Different Reaction Conditions

entry	catalyst loading (mol %)	levulinic acid/ethanol (molar ratio)	time (h)	yield of ethyl levulinate (mol %)
1	0.12	1:20	24	25.6 ± 1.2
2	0.25	1:20	24	55.3 ± 1.6
3	0.39	1:20	24	97.0 ± 1.1
4	0.50	1:20	24	83.4 ± 1.3
5	0.39	1:10	24	70.2 ± 1.5
6	0.39	1:20	8	23.9 ± 1.4
7	0.39	1:20	14	52.8 ± 1.7
8	0.39	1:20	16	62.9 ± 2.1
9	0.39	1:20	18	80.2 ± 1.2
10	0.39	1:20	20	85.8 ± 1.1
11	0.39	1:20	22	90.2 ± 1.3

Reaction conditions: levulinic acid 2.2 mmol, ethanol 43 mmol, 78 °C.

Conversion of levulinic acid to ethyl levulinate versus reaction time was further analyzed using UiO-66, BDC, and UiO-66-(COOH)$_2$ as catalysts keeping other parameters constant, with the results illustrated in **Figure A2.2**. It was observed that the yield of ethyl levulinate increased progressively with extending the reaction time from 8 to 24 h, with UiO-66-(COOH)$_2$ exhibiting a superior yield of ethyl levulinate compared to that of sole UiO-66. Despite strong Lewis acidity in UiO-66, only a 25.6% yield of ethyl levulinate was observed after 24 h. BDC also afforded a relatively low yield of ethyl levulinate of 17.3% under the same reaction conditions. The remarkably enhanced ethyl levulinate yield of 97.0% from UiO-66-(COOH)$_2$ was significantly higher than that of separate BDC and UiO-66.
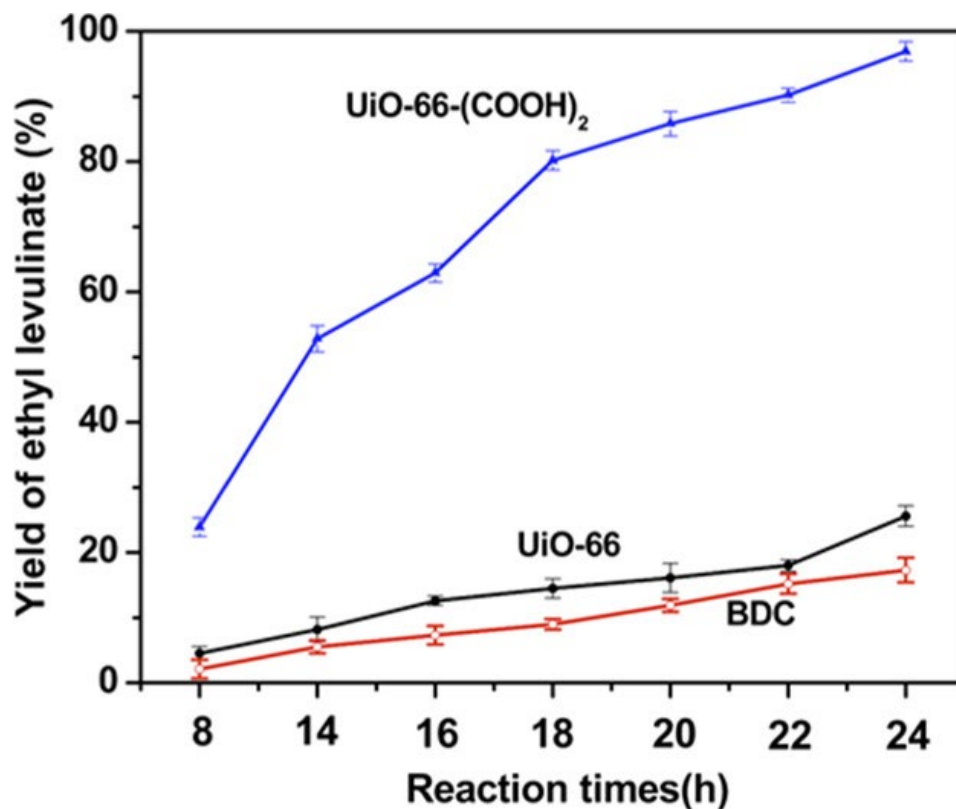
Figure A2.2 The effect of reaction time on catalytic performance of UiO-66, BDC, and UiO-66-(COOH)$_2$. Reaction conditions: levulinic acid 2.2 mmol, 0.39 mol % MOFs or 2.3 mol % BDC based on levulinic acid, ethanol 43 mmol, 78 °C.

A2.2.5 Initial Conclusions of Previous Work

In summary, the Zr-based MOF, UiO-66-(COOH)$_2$, was synthesized and tested as a heterogeneous catalyst for esterification of levulinic acid with ethanol. It exhibited excellent catalytic activity because of the synergistic effect between the Lewis acidic Zr clusters and Brønsted acidic free carboxylic acid functionality within the framework. According to computational results, the Zr sites coordinate with the carbonyl group of levulinic acid, while the free −COOH group from the linker hydrogen bonds with the substrate, facilitating the departure of the −OH leaving group in levulinic acid. This research opens up new avenues for the use of Zr-based MOF materials and functionalized analogues as promising heterogeneous catalysts for transformation of biomass feedstocks to biofuels and value-added chemicals.

A2.3 Expanding the Scope of Study

A2.3.1 Effect of Pore Size

As demonstrated by the previous work detail in Section 8.2 of this chapter,[263] the addition of a Brønsted acid to the organic structural building unit of the MOF synergistically enhanced the efficacy of biomass esterification. Given the nature of the UiO family of MOFs there are many opportunities for systematic study of isostructural catalysts to elucidate the effect of specific changes to the catalyst or catalyst environment. Due to this, we can systematically lengthen the organic linker from benzene dicarboxylic acid to biphenyl dicarboxylic acid, making UiO-67. In addition, we can add the same pendant carboxylic acids to the biphenyl version and compare all four catalysts – UiO-66, UiO-67, UiO-66-$(COOH)_2$, and UiO-67-$(COOH)_2$. This provides an opportunity to study solely the impact of the pore size increase while maintaining all other structural components of the framework. There potentially will be a balance of hastened reactivity due to enhanced diffusion through a larger pore, along with diminished reactivity due to a farther distance for the substrates to travel to the active sites.

A2.3.2 Effect of Acid Strength

Similar to expanding the pore size, we can swap out the pendant Brønsted acid group on the organic linker to screen acid strength as a parameter. The benefits of decades of organic synthesis research enables us to synthesize a series of these analogs creating a range of functional groups including -NH_2, -OH, -NO_3, -SO_3H, and -CO_2H. Therefore, we can screen UiO-66-$(NH_2)_2$, UiO-66-$(OH)_2$, UiO-66-$(NO_3)_2$, and UiO-66-$(SO_3H)_2$ in addition to the already studied UiO-66-$(COOH)_2$. This isolates the acid identity/strength as the sole variable between the different catalysts, allowing for structure-property relationships to be derived within this system. This screening can be taken a step further to even include the analogous UiO-67 series.

A2.3.4 Substrate Scope

Akin to traditional synthetic organic studies, a substrate scope study would determine how versatile these catalysts are for esterification of a variety of carboxylic acid biomass derivatives. These derivatives could include substrates such as succinic acid, fumaric acid, gluconic acid, aconitic acid, and more. A wide enough substrate scope would confirm the broad application of this type of MOF-based catalyst, given substrate scope tolerance.

A2.4 Catalyst Synthesis

UiO-66 and UiO-67 syntheses were done based on previous procedures to yield low defect density products. UiO-66-$(COOH)_2$ was synthesized by a newly adapted DMF-based procedure described in the additional information of this chapter. Synthetic screening was performed, including a scale-up test, which yielded desirable results with lower defect density than aqueous procedures. PXRD patterns (**Figure A2.3**) and N_2 adsorption isotherms (**Figure A2.4**) matched well with the simulated pattern and literature isotherms, and DFT pore size distributions matched expected pore sizes (**Figure A2.5**). Before attempting synthesis of UiO-66-$(SO_3H)_2$, the linker was first synthesized since it is not readily commercially available. Impure BDC-$(SO_3H)_2$ was synthesized and confirmed by ^{1}H- and ^{13}C-NMR (**Figure A2.6** and **A2.7**) but was not used in synthesis screening since further linker synthesis and purification needed be performed. Initial synthesis screening yielded mild success based on PXRD (**Figure A2.8**).
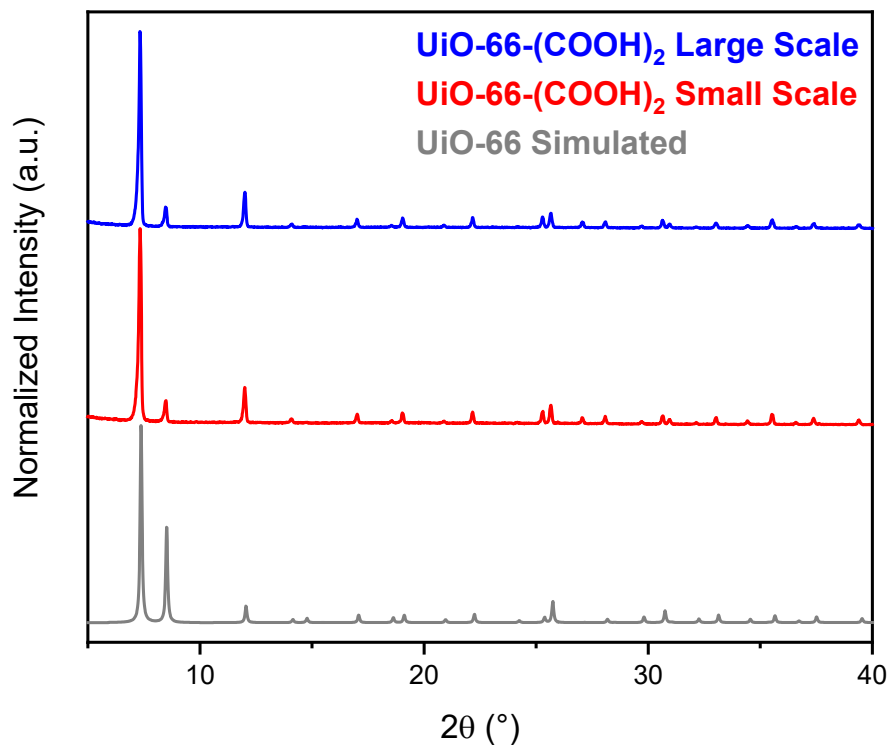
Figure A2.3 PXRD patterns of UiO-66 simulated from crystal structure (gray) and experimental UiO-66-(COOH)$_2$ from small scale (red) and large scale (blue) syntheses.
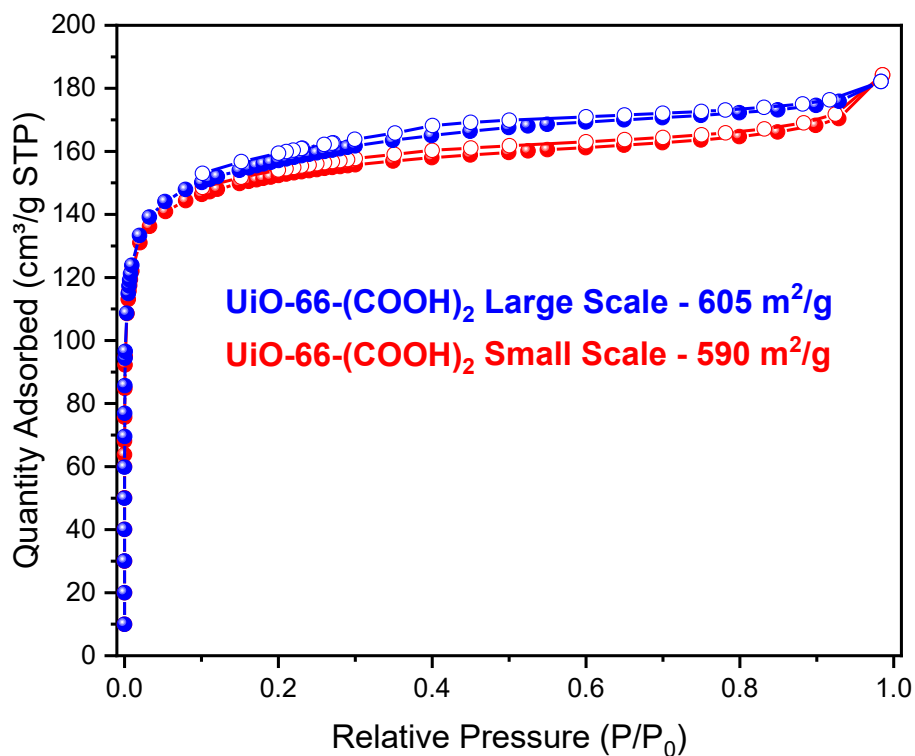
Figure A2.4 N$_2$ adsorption isotherms of experimental UiO-66-(COOH)$_2$ from small scale (red) and large scale (blue) syntheses.
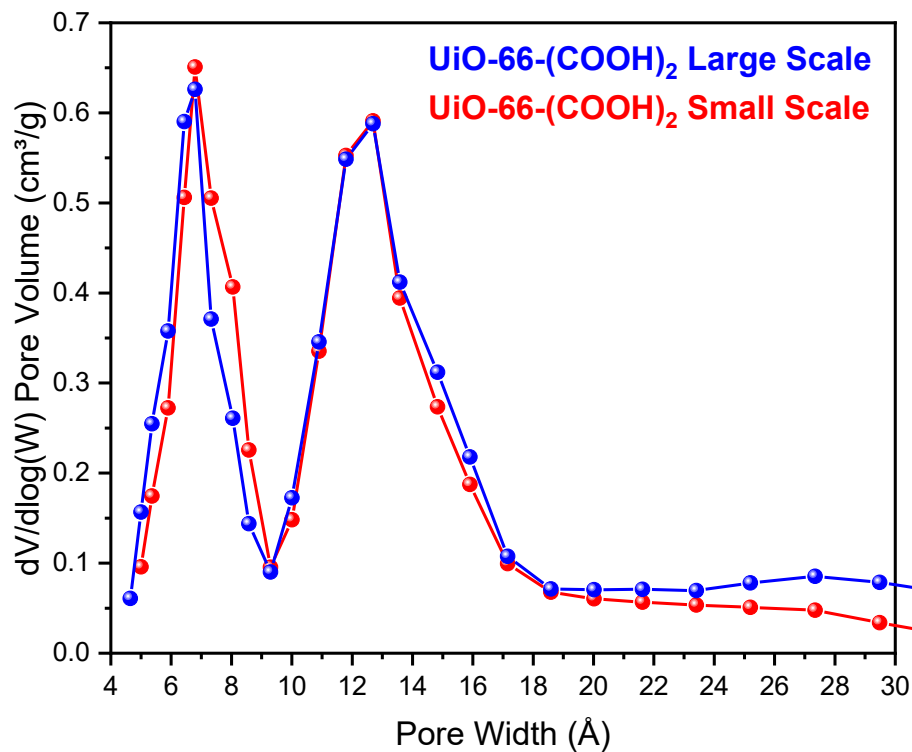
Figure A2.5 DFT calculated pore size distributions of experimental UiO-66-(COOH)$_2$ from small scale (red) and large scale (blue) syntheses.
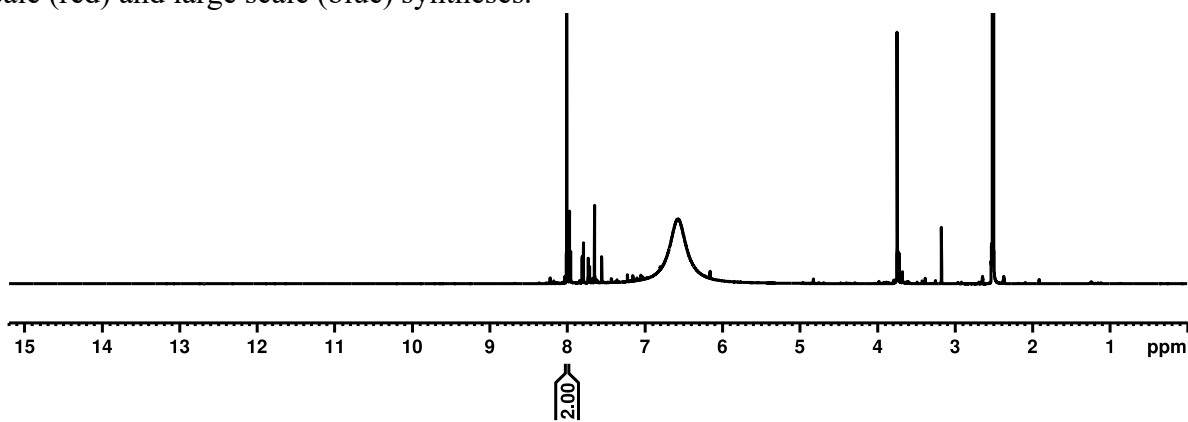
Figure A2.6 ^{1}H-NMR spectrum of impure BDC-(SO$_3$H)$_2$ in DMSO-d$_6$.
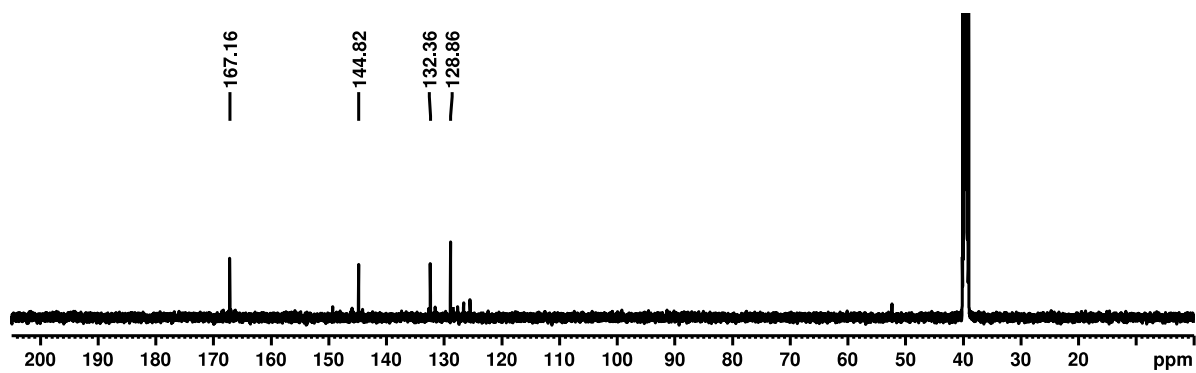
Figure A2.7 ^{13}C-NMR spectrum of impure BDC-$(SO_3H)_2$ in DMSO-d_6.
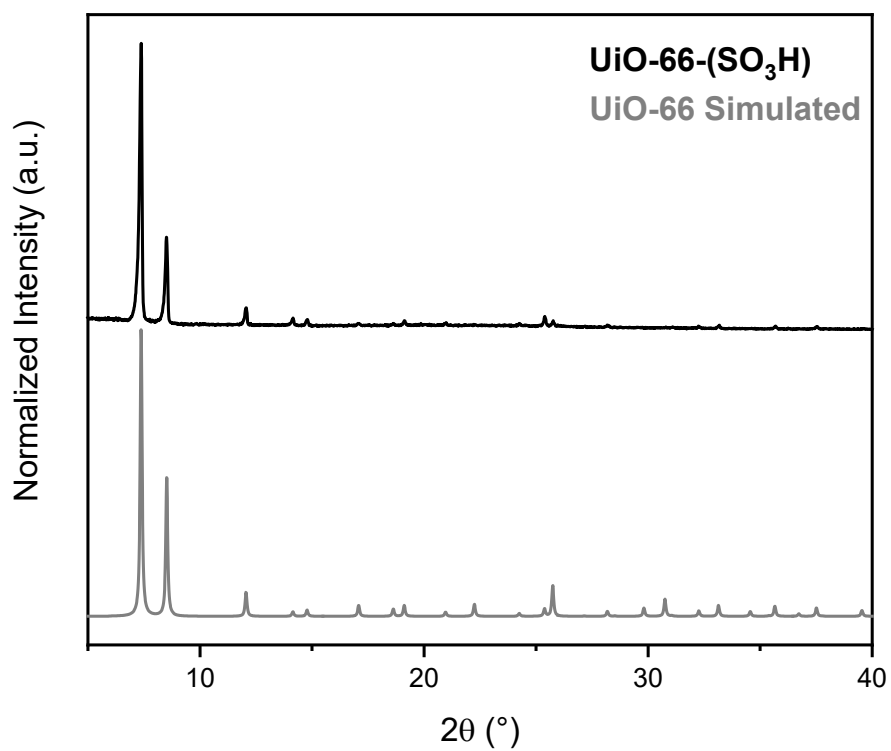
Figure A2.8 PXRD patterns of UiO-66 simulated from crystal structure (gray) and experimental UiO-66-(SO_3H) from initial synthesis screening (black).

Similarly, BPDC-(SO$_3$H) was synthesized and confirmed by ^{1}H-NMR (**Figure A2.9**) before being used in synthesis screening. Initial synthetic screening was potentially successful based on observation of a white powder precipitate before requiring the synthesis of more linker.
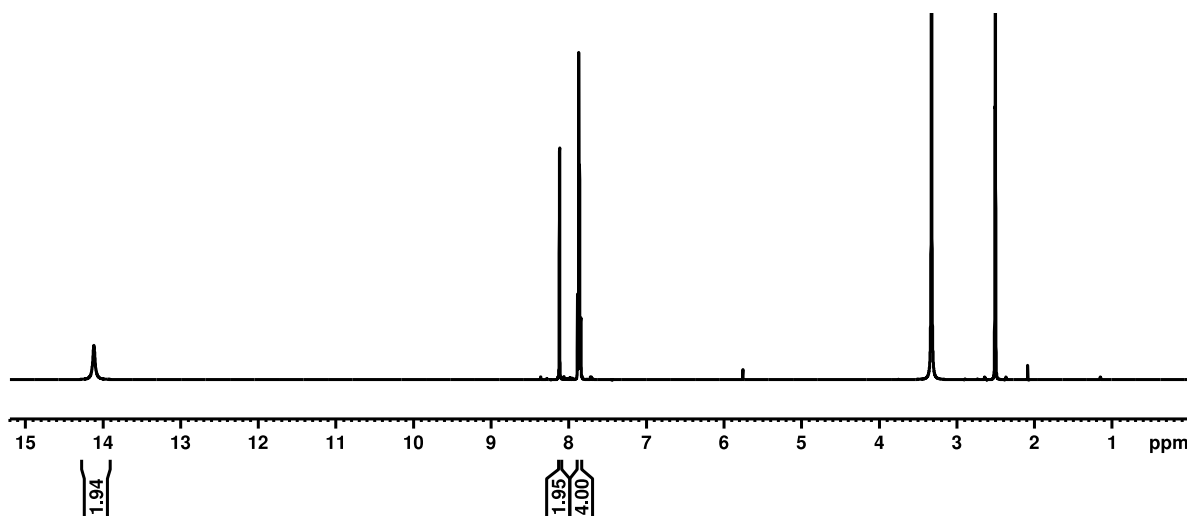
Figure A2.9 ^{1}H-NMR spectrum of as-synthesized BPDC-(SO$_3$H)$_2$ in DMSO-d$_6$.

UiO-67-(COOH)$_2$ has not yet been synthesized for this project due to delays in ligand synthesis/purchase, but we anticipate similar synthetic conditions to UiO-66-(COOH)$_2$ and therefore less lengthy synthetic screening procedures.

A2.5 Future Work

This project is in the starting stages of linker and catalyst synthesis and characterization. Therefore, substantial future work is required to complete the scope of this study. Firstly, synthesis and purification of the organic linkers required for MOF synthesis is necessary. The initial ligand scope can be limited to –(COOH)$_2$ and –(SO$_3$H)$_2$ for the sake of time (see **Figure A2.10** for structures). In addition to the ligand synthesis, MOF synthesis itself will require further optimization to yield highly crystalline material by PXRD and having the proper pore structure based on N$_2$ adsorption isotherms and DFT pore size distributions.
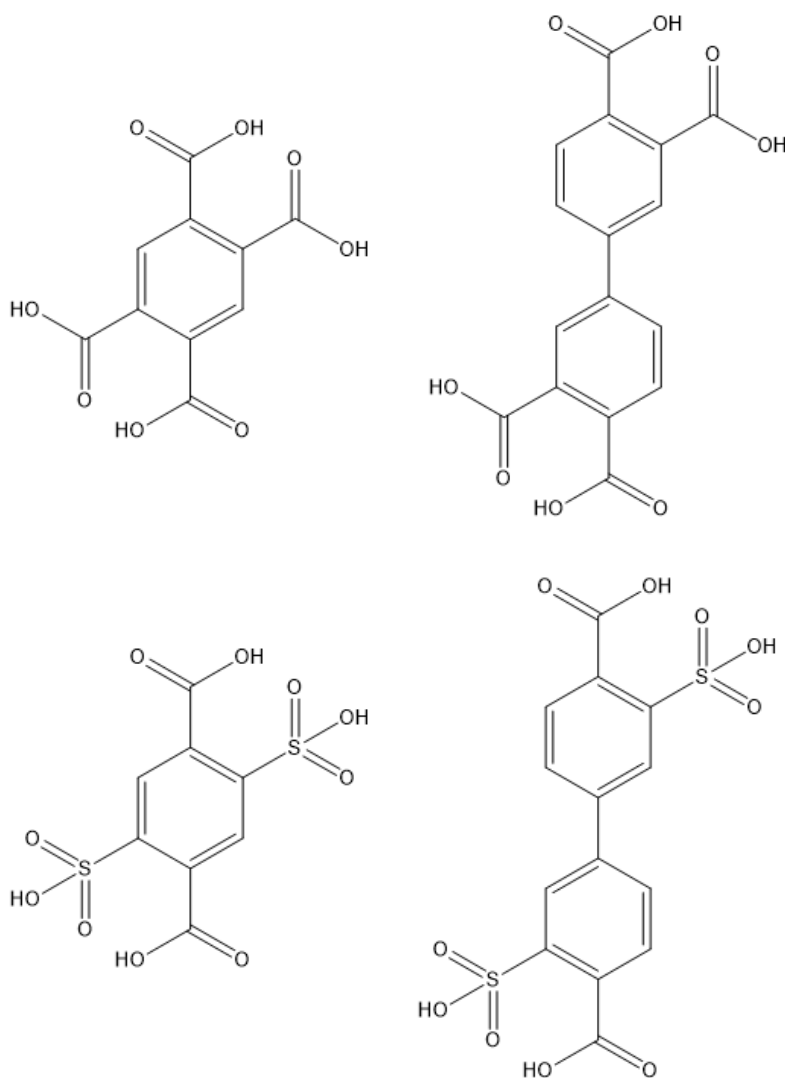
Figure A2.10 Structures of initial scope of MOF catalyst linkers.

With the catalysts in hand, it is important to properly characterize the materials before using them in the catalysis. In particular, Brønsted acid sites can be characterized in numerous ways including titrations, the Hammett indicator test, trimethyl phosphine oxide chemisorption coupled with ^{31}P-NMR, and ammonia or pyridine adsorption measurements coupled with infrared spectroscopy to name a few.[264]

The experimental characterization of acid nature and strength in these materials with give a handle on the correlation between the acid sites and catalytic activity. Meanwhile, fruitful collaborations with computational chemists can yield insights into reaction free energy profiles,

potential mechanisms, and even expected Brønsted acid strength in these systems. The marriage of theory and computations with experimental data make both sides all the more convincing and substantial.

Furthermore, the catalysis activity itself can be evaluated for the esterification of levulinic acid, comparing the variety of catalysts – UiO-66, UiO-66-(COOH)$_2$, UiO-66-(SO$_3$H)$_2$, UiO-67, UiO-67-(COOH)$_2$, and UiO-67-(SO$_3$H)$_2$. Results from this will glean insights into the impact of pore size and Brønsted acid identity/strength in this esterification reaction by a solid catalyst. Of course, proper post-catalysis characterization of the materials is necessary to confirm that the materials are stable under reaction conditions and do not change their physical or chemical properties that are explored pre-catalysis. Lastly, if the scope of the study allows, a substrate scope screen can be performed to include a variety of carboxylic acid-based biomass derivatives such as succinic acid, fumaric acid, and more. I envision this study to aid the catalysis community in definitively determining the structure-function relationships in biomass esterification through a methodic and systematic study on the effect of pore size and Brønsted acid identity/strength.

A2.6 Additional Information

A2.6.1 Materials

Acetone, methanol, *N,N*-dimethylformamide (DMF), triethylamine (TEA), hydrochloric acid, potassium permanganate, 30% hydrogen peroxide, and 2,5-dimercaptoterephthalic acid were purchased from Fisher Scientific (Waltham, MA) and used as received. Benzoic acid (BA), acetic acid (AA), trifluoroacetic acid (TFA), zirconyl chloride octahydrate, terephthalic acid, biphenyl-4,4′-dicarboxylic acid (BPDC), and 1,2,4,5-benzenetetracarboxylic acid were purchased from Sigma-Aldrich (St. Louis, MO) and used as received. 3,3'-Disulfo-[1,1'-biphenyl]-4,4'-dicarboxylic acid and [1,1'-Biphenyl]-3,3',4,4'-tetracarboxylic acid were purchased from AmBeed (Arlington Heights, IL) and used as received. *N,N*-diethylformamide (DEF), 1,1'-dimethylbiphenyl, and monosodium-2-sulfoterephthalate were purchased from TCI America (Portland, OR) and used as received. Zirconium(IV) chloride was purchased from Strem Chemicals (Newburyport, MA), stored in an Ar-filled glovebox, and used as received.

A2.6.2 Synthetic Methods

UiO-66 low defect powder synthesis. In a 1-L glass bottle 450 mg terephthalic acid was mixed into 630 mL DMF, 64.4 mL acetic acid, and 70 µL TEA, and subsequently heated at 100 °C for 15 min. In a separate 50 mL centrifuge tube, 630 mg $ZrCl_4$ was dissolved in 45 mL DMF. Once the linker solution was cooled to room temperature, the zirconium solution was added to the 1-L bottle and then heated in an oven at 100 °C overnight. The solid white powder was then collected by centrifugation and washed 3 times with fresh DMF before being solvent exchanged to acetone with an additional 3 washes with fresh acetone and one overnight soak. The isolated powder was then dried in a vacuum oven at 80 °C before being thermally activated on an ASAP 2420 at 150 °C overnight.

UiO-66-(COOH)$_2$ powder synthesis. Small scale synthesis was done in a 4-dram vial by combining 70 mg ZrCl$_4$ and 76 mg 1,2,4,5-benzenetetracarboxylic acid in 6 mL DMF and 4 mL formic acid. Large scale synthesis was a 10-fold scale up to a 500-mL bottle with 700 mg ZrCl$_4$ and 760 mg 1,2,4,5-benzenetetracarboxylic acid in 60 mL DMF and 40 mL formic acid. In both scales of synthesis the vessels were put in an oven at 120 °C overnight. The solid white powder was then collected by centrifugation and washed 3 times with fresh DMF before being solvent exchanged to acetone with an additional 3 washes with fresh acetone and one overnight soak. The isolated powder was then dried in a vacuum oven at 80 °C before being thermally activated on an ASAP 2420 at 150 °C overnight.

Synthesis of BDC-(SO$_3$H)$_2$. Impure material was synthesized by the following procedure. 50 mg 2,5-dimercaptoterephthalic acid was put in 12 mL methanol and 0.3 mL 30% H$_2$O$_2$ was added before stirring overnight at room temperature.

UiO-66-(SO$_3$H)$_2$ powder synthesis. Due to a lack of substantial linker for synthesis screening, monosodium-2-sulfoterephthalate was used instead. The procedure that gave the most crystalline product was the following. In a 1.5-dram vial 14 mg ZrCl$_4$ and 16.6 mg monosodium-2-sulfoterephthalate were combined in 3 mL DMF and 0.6 mL acetic acid. The vial was placed in a sand bath inside a 120 °C oven for 2 days. The solid white powder was then collected by centrifugation and washed 3 times with fresh DMF before being solvent exchanged to acetone with an additional 3 washes with fresh acetone and one overnight soak. The isolated powder was then dried in a vacuum oven at 80 °C.

UiO-67 low defect powder synthesis. In a 1-L glass bottle 660 mg biphenyl-4,4'-dicarboxylic acid was mixed into 630 mL DMF, 64.4 mL acetic acid, and 70 µL TEA, and subsequently heated at 100 °C for 15 min. In a separate 50 mL centrifuge tube, 630 mg ZrCl$_4$ was dissolved in 45 mL

DMF. Once the linker solution was cooled to room temperature, the zirconium solution was added to the 1-L bottle and then heated in an oven at 100 °C overnight. The solid white powder was then collected by centrifugation and washed 3 times with fresh DMF before being solvent exchanged to acetone with an additional 3 washes with fresh acetone and one overnight soak. The isolated powder was then dried in a vacuum oven at 80 °C before being thermally activated on an ASAP 2420 at 150 °C overnight.

UiO-67-(COOH)$_2$ powder synthesis. This synthesis was not yet attempted but a good starting point would be the following. Mix 35 mg ZrCl$_4$ and 50 mg [1,1'-biphenyl]-3,3',4,4'-tetracarboxylic acid in a 6-dram vial with 3 mL DMF and 2 mL formic acid, and subsequently heat in a 120 °C oven overnight. The solid white powder was then collected by centrifugation and washed 3 times with fresh DMF before being solvent exchanged to acetone with an additional 3 washes with fresh acetone and one overnight soak. The isolated powder was then dried in a vacuum oven at 80 °C.

Synthesis of BPDC-(SO$_3$H)$_2$. 4,4'-dimethylbiphenyl was treated with concentrated sulfuric acid overnight at 90 °C to yield 3,3'-disulfo-4,4'-dimethylbiphenyl. 3,3'-disulfo-4,4'-dimethylbiphenyl was then treated with potassium permanganate in aqueous sodium hydroxide at 90 °C for 3 days before being acidified with hydrochloric acid and BPDC-(SO$_3$H)$_2$ was collected as an off-white solid. This synthesis was performed before finding a commercial supplier for 3,3'-disulfo-[1,1'-biphenyl]-4,4'-dicarboxylic acid.

UiO-67-(SO$_3$H)$_2$ powder synthesis. An attempt at the synthesis of UiO-67-(SO$_3$H) was made, but crystallinity was not confirmed of the powder product. Briefly, 35 mg ZrCl$_4$ and 60 mg BPDC-(SO$_3$H)$_2$ were combined in a 6-dram vial with 3 mL DMF and 2 mL formic acid, and subsequently heated in a 120 °C oven overnight. The solid white powder was then collected by centrifugation and washed 3 times with fresh DMF before being solvent exchanged to acetone with an additional

3 washes with fresh acetone and one overnight soak. The isolated powder was then dried in a vacuum oven at 80 °C.

A2.6.3 Physical Characterization and Instrumentation

Powder X-ray diffraction (PXRD) data was collected at the IMSERC X-ray Facility at Northwestern University on a STOE-STADI-P powder diffractometer equipped with an asymmetric curved germanium monochromator (CuKα1 radiation, λ = 1.54056 Å) and one-dimensional silicon strip detector (MYTHEN2 1K from DECTRIS). The line focused Cu X-ray tube was operated at 40 kV and 40 mA. Powder was packed in a 3 mm metallic mask and sandwiched between two layers of polyimide tape. Intensity data from 1 to 40 degrees 2θ were collected over a period of 5 min.

N_2 adsorption isotherms were measured on a Micromeritics ASAP 2420 (Micromeritics, Norcross, GA) at 77 K with 30–80 mg pre-activated sample at 120 °C for 16 h under high vacuum using the ASAP 2420. BET area was calculated in the region P/P_0 = 0.005–0.05 and pore-size distributions were obtained via density functional theory (DFT) calculations using a carbon slit-pore model with a N_2 kernel.

^{1}H and ^{13}C solution state NMR spectroscopy was conducted on a Bruker Avance III 600 MHz system equipped with two RF channels (^{1}H = 600 MHz, ^{13}C = 150 MHz). Sample data was acquired using TopSpin™ by Bruker. All collected spectra were referenced to residual solvent signals. NMR spectra were processed and integrated using Mnova by Mestrelab Research, following phase correction and baseline correction (Whittaker smoother).

References

1. Vedrine, J. C., Metal Oxides in Heterogeneous Oxidation Catalysis: State of the Art and Challenges for a More Sustainable World. *ChemSusChem* **2019,** *12* (3), 577-588.
2. Anderson, R. B., *Fischer-Tropsch synthesis*. Academic Press,London, England: United Kingdom, 1984.
3. Foster, S. L.; Bakovic, S. I. P.; Duda, R. D.; Maheshwari, S.; Milton, R. D.; Minteer, S. D.; Janik, M. J.; Renner, J. N.; Greenlee, L. F., Catalysts for nitrogen reduction to ammonia. *Nat. Catal.* **2018,** *1* (7), 490-500.
4. Lloyd, L., Industrial Catalysts. In *Handbook of Industrial Catalysts*, Springer US: Boston, MA, 2011; pp 1-22.
5. Ertl, G., Primary Steps in Catalytic Synthesis of Ammonia. *J Vac Sci Technol A* **1983,** *1* (2), 1247-1253.
6. Groppo, E.; Martino, G. A.; Piovano, A.; Barzan, C., The Active Sites in the Phillips Catalysts: Origins of a Lively Debate and a Vision for the Future. *ACS Catal.* **2018,** *8* (11), 10846-10863.
7. McDaniel, M. P., *A Review of the Phillips Supported Chromium Catalyst and Its Commercial Use for Ethylene Polymerization*. 1 ed.; Elsevier Inc.: 2010; Vol. 53, p 123-606.
8. Bennett, T. D.; Horike, S., Liquid, glass and amorphous solid states of coordination polymers and metal–organic frameworks. *Nat. Rev. Mater.* **2018,** *3* (11), 431-440.
9. Moosavi, S. M.; Nandy, A.; Jablonka, K. M.; Ongari, D.; Janet, J. P.; Boyd, P. G.; Lee, Y.; Smit, B.; Kulik, H. J., Understanding the diversity of the metal-organic framework ecosystem. *Nat. Commun.* **2020,** *11* (1), 4068.
10. Haldoupis, E.; Nair, S.; Sholl, D. S., Efficient calculation of diffusion limitations in metal organic framework materials: a tool for identifying materials for kinetic separations. *J Am Chem Soc* **2010,** *132* (21), 7528-39.
11. Chung, Y. G.; Haldoupis, E.; Bucior, B. J.; Haranczyk, M.; Lee, S.; Zhang, H.; Vogiatzis, K. D.; Milisavljevic, M.; Ling, S.; Camp, J. S.; Slater, B.; Siepmann, J. I.; Sholl, D. S.; Snurr, R. Q., Advances, Updates, and Analytics for the Computation-Ready, Experimental Metal–Organic Framework Database: CoRE MOF 2019. *J. Chem. Eng. Data* **2019,** *64* (12), 5985-5998.
12. Liu, J.; Goetjen, T. A.; Wang, Q.; Knapp, J. G.; Wasson, M. C.; Yang, Y.; Syed, Z. H.; Delferro, M.; Notestein, J. M.; Farha, O. K.; Hupp, J. T., MOF-enabled confinement and related effects for chemical catalyst presentation and utilization. *Chem. Soc. Rev.* **2022,** *51* (3), 1045-1097.
13. Kalmutzki, M. J.; Hanikel, N.; Yaghi, O. M., Secondary building units as the turning point in the development of the reticular chemistry of MOFs. *Sci Adv* **2018,** *4* (10), eaat9180.
14. Howarth, A. J.; Liu, Y.; Li, P.; Li, Z.; Wang, T. C.; Hupp, J. T.; Farha, O. K., Chemical, thermal and mechanical stabilities of metal-organic frameworks. *Nat. Rev. Mater.* **2016,** *1* (15018), 1-15.
15. Yang, D.; Gates, B. C., Catalysis by Metal Organic Frameworks: Perspective and Suggestions for Future Research. *ACS Catal.* **2019,** *9* (3), 1779-1798.
16. Mondloch, J. E.; Katz, M. J.; Planas, N.; Semrouni, D.; Gagliardi, L.; Hupp, J. T.; Farha, O. K., Are Zr(6)-based MOFs water stable? Linker hydrolysis vs. capillary-force-driven channel collapse. *Chem. Comm.* **2014,** *50* (64), 8944-6.

17. Li, Z.; Peters, A. W.; Platero-Prats, A. E.; Liu, J.; Kung, C. W.; Noh, H.; DeStefano, M. R.; Schweitzer, N. M.; Chapman, K. W.; Hupp, J. T.; Farha, O. K., Fine-Tuning the Activity of Metal-Organic Framework-Supported Cobalt Catalysts for the Oxidative Dehydrogenation of Propane. *J. Am. Chem. Soc.* **2017,** *139* (42), 15251-15258.

18. Nguyen, H. G. T.; Schweitzer, N. M.; Chang, C.-Y.; Drake, T. L.; So, M. C.; Stair, P. C.; Farha, O. K.; Hupp, J. T.; Nguyen, S. T., Vanadium-Node-Functionalized UiO-66: A Thermally Stable MOF-Supported Catalyst for the Gas-Phase Oxidative Dehydrogenation of Cyclohexene. *ACS Catal.* **2014,** *4* (8), 2496-2500.

19. Ma, Y.; Han, X.; Xu, S.; Wang, Z.; Li, W.; da Silva, I.; Chansai, S.; Lee, D.; Zou, Y.; Nikiel, M.; Manuel, P.; Sheveleva, A. M.; Tuna, F.; McInnes, E. J. L.; Cheng, Y.; Rudic, S.; Ramirez-Cuesta, A. J.; Haigh, S. J.; Hardacre, C.; Schroder, M.; Yang, S., Atomically Dispersed Copper Sites in a Metal-Organic Framework for Reduction of Nitrogen Dioxide. *J. Am. Chem. Soc.* **2021,** *143* (29), 10977-10985.

20. Abdel-Mageed, A. M.; Rungtaweevoranit, B.; Parlinska-Wojtan, M.; Pei, X.; Yaghi, O. M.; Behm, R. J., Highly Active and Stable Single-Atom Cu Catalysts Supported by a Metal-Organic Framework. *J. Am. Chem. Soc.* **2019,** *141* (13), 5201-5210.

21. He, X.; Looker, B. G.; Dinh, K. T.; Stubbs, A. W.; Chen, T.; Meyer, R. J.; Serna, P.; Román-Leshkov, Y.; Lancaster, K. M.; Dincă, M., Cerium(IV) Enhances the Catalytic Oxidation Activity of Single-Site Cu Active Sites in MOFs. *ACS Catal.* **2020,** *10* (14), 7820-7825.

22. Yang, L.; Cai, P.; Zhang, L.; Xu, X.; Yakovenko, A. A.; Wang, Q.; Pang, J.; Yuan, S.; Zou, X.; Huang, N.; Huang, Z.; Zhou, H. C., Ligand-Directed Conformational Control over Porphyrinic Zirconium Metal-Organic Frameworks for Size-Selective Catalysis. *J. Am. Chem. Soc.* **2021,** *143* (31), 12129-12137.

23. Zhang, J.; An, B.; Li, Z.; Cao, Y.; Dai, Y.; Wang, W.; Zeng, L.; Lin, W.; Wang, C., Neighboring Zn-Zr Sites in a Metal-Organic Framework for CO2 Hydrogenation. *J. Am. Chem. Soc.* **2021,** *143* (23), 8829-8837.

24. Kømurcu, M.; Lazzarini, A.; Kaur, G.; Borfecchia, E.; Øien-Ødegaard, S.; Gianolio, D.; Bordiga, S.; Lillerud, K. P.; Olsbye, U., Co-catalyst free ethene dimerization over Zr-based metal-organic framework (UiO-67) functionalized with Ni and bipyridine. *Catal. Today* **2021,** *369*, 193-202.

25. Yang, Y.; Noh, H.; Ma, Q.; Wang, R.; Chen, Z.; Schweitzer, N. M.; Liu, J.; Chapman, K. W.; Hupp, J. T., Engineering Dendrimer-Templated, Metal-Organic Framework-Confined Zero-Valent, Transition-Metal Catalysts. *ACS Appl. Mater. Interfaces* **2021,** *13* (30), 36232-36239.

26. Wang, X.; Zhang, X.; Pandharkar, R.; Lyu, J.; Ray, D.; Yang, Y.; Kato, S.; Liu, J.; Wasson, M. C.; Islamoglu, T.; Li, Z.; Hupp, J. T.; Cramer, C. J.; Gagliardi, L.; Farha, O. K., Insights into the Structure–Activity Relationships in Metal–Organic Framework-Supported Nickel Catalysts for Ethylene Hydrogenation. *ACS Catal.* **2020,** *10* (16), 8995-9005.

27. Mian, M. R.; Redfern, L. R.; Pratik, S. M.; Ray, D.; Liu, J.; Idrees, K. B.; Islamoglu, T.; Gagliardi, L.; Farha, O. K., Precise Control of Cu Nanoparticle Size and Catalytic Activity through Pore Templating in Zr Metal–Organic Frameworks. *Chem. Mater.* **2020,** *32* (7), 3078-3086.

28. Buru, C. T.; Lyu, J.; Liu, J.; Farha, O. K., Restricting Polyoxometalate Movement Within Metal-Organic Frameworks to Assess the Role of Residual Water in Catalytic Thioether Oxidation Using These Dynamic Composites. *Front. Mater. Sci.* **2019,** *6*.

29. Zhang, Y.; Zhang, X.; Lyu, J.; Otake, K. I.; Wang, X.; Redfern, L. R.; Malliakas, C. D.; Li, Z.; Islamoglu, T.; Wang, B.; Farha, O. K., A Flexible Metal-Organic Framework with 4-Connected Zr6 Nodes. *J. Am. Chem. Soc.* **2018,** *140* (36), 11179-11183.

30. Chen, Y.; Zhang, X.; Mian, M. R.; Son, F. A.; Zhang, K.; Cao, R.; Chen, Z.; Lee, S. J.; Idrees, K. B.; Goetjen, T. A.; Lyu, J.; Li, P.; Xia, Q.; Li, Z.; Hupp, J. T.; Islamoglu, T.; Napolitano, A.; Peterson, G. W.; Farha, O. K., Structural Diversity of Zirconium Metal-Organic Frameworks and Effect on Adsorption of Toxic Chemicals. *J. Am. Chem. Soc.* **2020,** *142* (51), 21428-21438.

31. Furukawa, H.; Gandara, F.; Zhang, Y. B.; Jiang, J.; Queen, W. L.; Hudson, M. R.; Yaghi, O. M., Water adsorption in porous metal-organic frameworks and related materials. *J. Am. Chem. Soc.* **2014,** *136* (11), 4369-81.

32. Islamoglu, T.; Otake, K.-I.; Li, P.; Buru, C. T.; Peters, A. W.; Akpinar, I.; Garibay, S. J.; Farha, O. K., Revisiting the structural homogeneity of NU-1000, a Zr-based metal–organic framework. *CrystEngComm* **2018,** *20* (39), 5913-5918.

33. He, T.; Zhang, Y. Z.; Kong, X. J.; Yu, J.; Lv, X. L.; Wu, Y.; Guo, Z. J.; Li, J. R., Zr(IV)-Based Metal-Organic Framework with T-Shaped Ligand: Unique Structure, High Stability, Selective Detection, and Rapid Adsorption of Cr2O7(2-) in Water. *ACS Appl. Mater. Interfaces* **2018,** *10* (19), 16650-16659.

34. Zhao, Y.; Qi, S.; Niu, Z.; Peng, Y.; Shan, C.; Verma, G.; Wojtas, L.; Zhang, Z.; Zhang, B.; Feng, Y.; Chen, Y. S.; Ma, S., Robust Corrole-Based Metal-Organic Frameworks with Rare 9-Connected Zr/Hf-Oxo Clusters. *J. Am. Chem. Soc.* **2019,** *141* (36), 14443-14450.

35. Peters, A. W.; Otake, K.; Platero-Prats, A. E.; Li, Z.; DeStefano, M. R.; Chapman, K. W.; Farha, O. K.; Hupp, J. T., Site-Directed Synthesis of Cobalt Oxide Clusters in a Metal-Organic Framework. *ACS Appl. Mater. Interfaces* **2018,** *10* (17), 15073-15078.

36. Pang, J.; Di, Z.; Qin, J. S.; Yuan, S.; Lollar, C. T.; Li, J.; Zhang, P.; Wu, M.; Yuan, D.; Hong, M.; Zhou, H. C., Precisely Embedding Active Sites into a Mesoporous Zr-Framework through Linker Installation for High-Efficiency Photocatalysis. *J. Am. Chem. Soc.* **2020,** *142* (35), 15020-15026.

37. Cavka, J. H.; Jakobsen, S.; Olsbye, U.; Guillou, N.; Lamberti, C.; Bordiga, S.; Lillerud, K. P., A new zirconium inorganic building brick forming metal organic frameworks with exceptional stability. *J Am Chem Soc* **2008,** *130* (42), 13850-1.

38. Lu, Z.; Liu, J.; Zhang, X.; Liao, Y.; Wang, R.; Zhang, K.; Lyu, J.; Farha, O. K.; Hupp, J. T., Node-Accessible Zirconium MOFs. *J. Am. Chem. Soc.* **2020,** *142* (50), 21110-21121.

39. Yang, D.; Ortuno, M. A.; Bernales, V.; Cramer, C. J.; Gagliardi, L.; Gates, B. C., Structure and Dynamics of Zr6O8 Metal-Organic Framework Node Surfaces Probed with Ethanol Dehydration as a Catalytic Test Reaction. *J. Am. Chem. Soc.* **2018,** *140* (10), 3751-3759.

40. Liu, J.; Lu, Z.; Chen, Z.; Rimoldi, M.; Howarth, A. J.; Chen, H.; Alayoglu, S.; Snurr, R. Q.; Farha, O. K.; Hupp, J. T., Ammonia Capture within Zirconium Metal-Organic Frameworks: Reversible and Irreversible Uptake. *ACS Appl. Mater. Interfaces* **2021,** *13* (17), 20081-20093.

41. Peterson, G. W.; Wagner, G. W.; Balboa, A.; Mahle, J.; Sewell, T.; Karwacki, C. J., Ammonia Vapor Removal by Cu(3)(BTC)(2) and Its Characterization by MAS NMR. *J Phys Chem C Nanomater Interfaces* **2009,** *113* (31), 13906-13917.

42. Rieth, A. J.; Dinca, M., Controlled Gas Uptake in Metal-Organic Frameworks with Record Ammonia Sorption. *J. Am. Chem. Soc.* **2018,** *140* (9), 3461-3466.

43.   Jiang, J.; Gandara, F.; Zhang, Y. B.; Na, K.; Yaghi, O. M.; Klemperer, W. G., Superacidity in sulfated metal-organic framework-808. *J. Am. Chem. Soc.* **2014,** *136* (37), 12844-7.

44.   Trickett, C. A.; Osborn Popp, T. M.; Su, J.; Yan, C.; Weisberg, J.; Huq, A.; Urban, P.; Jiang, J.; Kalmutzki, M. J.; Liu, Q.; Baek, J.; Head-Gordon, M. P.; Somorjai, G. A.; Reimer, J. A.; Yaghi, O. M., Identification of the strong Bronsted acid site in a metal-organic framework solid acid catalyst. *Nat. Chem.* **2019,** *11* (2), 170-176.

45.   Howarth, A. J.; Wang, T. C.; Al-Juaid, S. S.; Aziz, S. G.; Hupp, J. T.; Farha, O. K., Efficient extraction of sulfate from water using a Zr-metal-organic framework. *Dalton Trans.* **2016,** *45* (1), 93-7.

46.   Yang, D.; Babucci, M.; Casey, W. H.; Gates, B. C., The Surface Chemistry of Metal Oxide Clusters: From Metal-Organic Frameworks to Minerals. *ACS Cent. Sci.* **2020,** *6* (9), 1523-1533.

47.   Burtch, N. C.; Walton, I. M.; Hungerford, J. T.; Morelock, C. R.; Jiao, Y.; Heinen, J.; Chen, Y. S.; Yakovenko, A. A.; Xu, W.; Dubbeldam, D.; Walton, K. S., In situ visualization of loading-dependent water effects in a stable metal-organic framework. *Nat. Chem.* **2020,** *12* (2), 186-192.

48.   Liu, J.; Ye, J.; Li, Z.; Otake, K. I.; Liao, Y.; Peters, A. W.; Noh, H.; Truhlar, D. G.; Gagliardi, L.; Cramer, C. J.; Farha, O. K.; Hupp, J. T., Beyond the Active Site: Tuning the Activity and Selectivity of a Metal-Organic Framework-Supported Ni Catalyst for Ethylene Dimerization. *J. Am. Chem. Soc.* **2018,** *140* (36), 11174-11178.

49.   Wang, X.; Zhang, X.; Li, P.; Otake, K. I.; Cui, Y.; Lyu, J.; Krzyaniak, M. D.; Zhang, Y.; Li, Z.; Liu, J.; Buru, C. T.; Islamoglu, T.; Wasielewski, M. R.; Li, Z.; Farha, O. K., Vanadium Catalyst on Isostructural Transition Metal, Lanthanide, and Actinide Based Metal-Organic Frameworks for Alcohol Oxidation. *J. Am. Chem. Soc.* **2020,** *141* (20), 8306-8314.

50.   Goetjen, T. A.; Zhang, X.; Liu, J.; Hupp, J. T.; Farha, O. K., Metal-Organic Framework Supported Single Site Chromium(III) Catalyst for Ethylene Oligomerization at Low Pressure and Temperature. *ACS Sustain. Chem. Eng.* **2019,** *7* (2), 2553-2557.

51.   Liu, J.; Li, Z.; Zhang, X.; Otake, K.-i.; Zhang, L.; Peters, A. W.; Young, M. J.; Bedford, N. M.; Letourneau, S. P.; Mandia, D. J.; Elam, J. W.; Farha, O. K.; Hupp, J. T., Introducing Nonstructural Ligands to Zirconia-like Metal–Organic Framework Nodes To Tune the Activity of Node-Supported Nickel Catalysts for Ethylene Hydrogenation. *ACS Catal.* **2019,** *9* (4), 3198-3207.

52.   Li, J.; Han, X.; Kang, X.; Chen, Y.; Xu, S.; Smith, G. L.; Tillotson, E.; Cheng, Y.; McCormick McPherson, L. J.; Teat, S. J.; Rudic, S.; Ramirez-Cuesta, A. J.; Haigh, S. J.; Schroder, M.; Yang, S., Purification of Propylene and Ethylene by a Robust Metal-Organic Framework Mediated by Host-Guest Interactions. *Angew. Chem. Int. Ed.* **2021,** *60* (28), 15541-15547.

53.   Wang, H.; Shi, Z.; Yang, J.; Sun, T.; Rungtaweevoranit, B.; Lyu, H.; Zhang, Y. B.; Yaghi, O. M., Docking of Cu(I) and Ag(I) in Metal-Organic Frameworks for Adsorption and Separation of Xenon. *Angew. Chem. Int. Ed.* **2021,** *60* (7), 3417-3421.

54.   Lv, X. L.; Feng, L.; Xie, L. H.; He, T.; Wu, W.; Wang, K. Y.; Si, G.; Wang, B.; Li, J. R.; Zhou, H. C., Linker Desymmetrization: Access to a Series of Rare-Earth Tetracarboxylate Frameworks with Eight-Connected Hexanuclear Nodes. *J. Am. Chem. Soc.* **2021,** *143* (7), 2784-2791.

55.   Feng, X.; Song, Y.; Chen, J. S.; Xu, Z.; Dunn, S. J.; Lin, W., Rational Construction of an Artificial Binuclear Copper Monooxygenase in a Metal-Organic Framework. *J. Am. Chem. Soc.* **2021,** *143* (2), 1107-1118.

56.   Lee, J. S.; Kapustin, E. A.; Pei, X.; Llopis, S.; Yaghi, O. M.; Toste, F. D., Architectural Stabilization of a Gold(III) Catalyst in Metal-Organic Frameworks. *Chem.* **2020,** *6* (1), 142-152.

57.   Yang, Y.; Zhang, X.; Kanchanakungwankul, S.; Lu, Z.; Noh, H.; Syed, Z. H.; Farha, O. K.; Truhlar, D. G.; Hupp, J. T., Unexpected "Spontaneous" Evolution of Catalytic, MOF-Supported Single Cu(II) Cations to Catalytic, MOF-Supported Cu(0) Nanoparticles. *J. Am. Chem. Soc.* **2020,** *142* (50), 21169-21177.

58.   Otake, K.-I.; Ye, J.; Mandal, M.; Islamoglu, T.; Buru, C. T.; Hupp, J. T.; Delferro, M.; Truhlar, D. G.; Cramer, C. J.; Farha, O. K., Enhanced Activity of Heterogeneous Pd(II) Catalysts on Acid-Functionalized Metal–Organic Frameworks. *ACS Catal.* **2019,** *9* (6), 5383-5390.

59.   Otake, K. I.; Cui, Y.; Buru, C. T.; Li, Z.; Hupp, J. T.; Farha, O. K., Single-Atom-Based Vanadium Oxide Catalysts Supported on Metal-Organic Frameworks: Selective Alcohol Oxidation and Structure-Activity Relationship. *J. Am. Chem. Soc.* **2018,** *140* (28), 8652-8656.

60.   Mandal, M.; Cramer, C. J.; Truhlar, D. G.; Sauer, J.; Gagliardi, L., Structure and Reactivity of Single-Site Vanadium Catalysts Supported on Metal–Organic Frameworks. *ACS Catal.* **2020,** *10* (17), 10051-10059.

61.   Wen, M.; Kuwahara, Y.; Mori, K.; Zhang, D.; Li, H.; Yamashita, H., Synthesis of Ce ions doped metal–organic framework for promoting catalytic H2 production from ammonia borane under visible light irradiation. *J. Mater. Chem. A* **2015,** *3* (27), 14134-14141.

62.   Ji, P.; Manna, K.; Lin, Z.; Feng, X.; Urban, A.; Song, Y.; Lin, W., Single-Site Cobalt Catalysts at New Zr12(mu3-O)8(mu3-OH)8(mu2-OH)6 Metal-Organic Framework Nodes for Highly Active Hydrogenation of Nitroarenes, Nitriles, and Isocyanides. *J. Am. Chem. Soc.* **2017,** *139* (20), 7004-7011.

63.   Piszczek, P.; Radtke, A.; Wojtczak, A.; Muzioł, T.; Chojnacki, J., Synthesis, structure characterization and thermal properties of [Zr6(µ3-O)4(µ3-OH)4(OOCCH2tBu)9(µ2-OH)3]2. *Polyhedron* **2009,** *28* (2), 279-285.

64.   Park, J. G.; Collins, B. A.; Darago, L. E.; Runcevski, T.; Ziebel, M. E.; Aubrey, M. L.; Jiang, H. Z. H.; Velasquez, E.; Green, M. A.; Goodpaster, J. D.; Long, J. R., Magnetic ordering through itinerant ferromagnetism in a metal-organic framework. *Nat. Chem.* **2021,** *13* (6), 594-598.

65.   Rieth, A. J.; Tulchinsky, Y.; Dinca, M., High and Reversible Ammonia Uptake in Mesoporous Azolate Metal-Organic Frameworks with Open Mn, Co, and Ni Sites. *J. Am. Chem. Soc.* **2016,** *138* (30), 9401-4.

66.   Dou, J. H.; Arguilla, M. Q.; Luo, Y.; Li, J.; Zhang, W.; Sun, L.; Mancuso, J. L.; Yang, L.; Chen, T.; Parent, L. R.; Skorupskii, G.; Libretto, N. J.; Sun, C.; Yang, M. C.; Dip, P. V.; Brignole, E. J.; Miller, J. T.; Kong, J.; Hendon, C. H.; Sun, J.; Dinca, M., Atomically precise single-crystal structures of electrically conducting 2D metal-organic frameworks. *Nat. Mater.* **2021,** *20* (2), 222-228.

67.   Li, Z.; Schweitzer, N. M.; League, A. B.; Bernales, V.; Peters, A. W.; Getsoian, A. B.; Wang, T. C.; Miller, J. T.; Vjunov, A.; Fulton, J. L.; Lercher, J. A.; Cramer, C. J.; Gagliardi,

L.; Hupp, J. T.; Farha, O. K., Sintering-Resistant Single-Site Nickel Catalyst Supported by Metal-Organic Framework. *J. Am. Chem. Soc.* **2016,** *138* (6), 1977-82.

68. Kim, I. S.; Li, Z.; Zheng, J.; Platero-Prats, A. E.; Mavrandonakis, A.; Pellizzeri, S.; Ferrandon, M.; Vjunov, A.; Gallington, L. C.; Webber, T. E.; Vermeulen, N. A.; Penn, R. L.; Getman, R. B.; Cramer, C. J.; Chapman, K. W.; Camaioni, D. M.; Fulton, J. L.; Lercher, J. A.; Farha, O. K.; Hupp, J. T.; Martinson, A. B. F., Sinter-Resistant Platinum Catalyst Supported by Metal-Organic Framework. *Angew. Chem. Int. Ed.* **2018,** *57* (4), 909-913.

69. Marsh, C.; Han, X.; Li, J.; Lu, Z.; Argent, S. P.; da Silva, I.; Cheng, Y.; Daemen, L. L.; Ramirez-Cuesta, A. J.; Thompson, S. P.; Blake, A. J.; Yang, S.; Schroder, M., Exceptional Packing Density of Ammonia in a Dual-Functionalized Metal-Organic Framework. *J. Am. Chem. Soc.* **2021,** *143* (17), 6586-6592.

70. Wang, Q.; Pengmei, Z.; Pandharkar, R.; Gagliardi, L.; Hupp, J. T.; Notestein, J. M., Investigating the effect of metal nuclearity on activity for ethylene hydrogenation by metal-organic-framework-supported oxy-Ni(II) catalysts. *J. Catal.* **2022,** *407*, 162-173.

71. Bavykina, A.; Kolobov, N.; Khan, I. S.; Bau, J. A.; Ramirez, A.; Gascon, J., Metal-Organic Frameworks in Heterogeneous Catalysis: Recent Progress, New Trends, and Future Perspectives. *Chem. Rev.* **2020,** *120* (16), 8468-8535.

72. Lauer, N. E.; Hower, J. C.; Hsu-Kim, H.; Taggart, R. K.; Vengosh, A., Naturally Occurring Radioactive Materials in Coals and Coal Combustion Residuals in the United States. *Environ Sci Technol* **2015,** *49* (18), 11227-33.

73. National Academies of Sciences, E.; Medicine, *The Changing Landscape of Hydrocarbon Feedstocks for Chemical Production: Implications for Catalysis: Proceedings of a Workshop*. The National Academies Press: Washington, DC, 2016; p 136.

74. Vogt, E. T.; Weckhuysen, B. M., Fluid catalytic cracking: recent developments on the grand old lady of zeolite catalysis. *Chem. Soc. Rev.* **2015,** *44* (20), 7342-70.

75. Liu, Y.; Deng, D.; Bao, X., Catalysis for Selected C1 Chemistry. *Chem.* **2020,** *6* (10), 2497-2514.

76. Koval, C. A.; Lercher, J.; Scott, S. L.; Coates, G. W.; Iglesia, E.; Bullock, R. M.; Jaramillo, T. F.; Flytzani-Stephanopoulos, M.; Resasco, D.; Tway, C. L.; Batista, V.; Chapman, K. W.; Dai, S.; Dumesic, J.; Friend, C.; Hille, R.; Johnson, K.; Nørskov, J.; Rekoske, J.; Sarkar, R.; Bradley, C.; Garrett, B.; Henderson, C.; Miranda, R.; Peden, C.; Schwartz, V.; Runkles, K.; Fellner, K.; Jenks, C.; Nelson, M.; Appel, A. M.; Bare, S.; Bartlett, B. M.; Bligaard, T.; Chandler, B. D.; Davis, R. J.; Glezakou, V.-A.; Gregoire, J.; Hille, R.; Hock, A. S.; Kitchin, J.; Kung, H. H.; Rousseau, R.; Sadow, A. D.; Schaak, R. E.; Shaw, W. J.; Stacchiola, D. J.; Delferro, M.; Bunel, E.; Holladay, J.; Houle, F.; Jenks, C.; Krause, T.; Marshall, C.; Neale, N.; Parks, J.; Schaidle, J.; VandeLagemaat, J.; Wang, Y.; Weber, R. *Basic Research Needs for Catalysis Science to Transform Energy Technologies*; U.S. Department of Energy, Office of Basic Energy Sciences: Gaithersburg, MD, 2017.

77. Morgan, G. M.; Apt, J.; Lave, L. *U.S. electric power sector and climate change mitigation*; United States, 2005; pp Medium: X; Size: 95; 626 KB pages 2010-06-03 Pew Center on Global Climate Change, 2101 Wilson Boulevard, suite 550, Arlington, VA 22201, USA, Tel: (703)516-4146. Internet in full from: www.pewclimate.org.

78. Elvidge, C.; Ziskin, D.; Baugh, K.; Tuttle, B.; Ghosh, T.; Pack, D.; Erwin, E.; Zhizhin, M., A Fifteen Year Record of Global Natural Gas Flaring Derived from Satellite Data. *Energies* **2009,** *2* (3), 595-622.

79. Jarvis, J.; He, P.; Wang, A.; Song, H., Pt-Zn/HZSM-5 as a highly selective catalyst for the Co-aromatization of methane and light straight run naphtha. *Fuel* **2019,** *236*, 1301-1310.

80. Chica, A.; Corma, A., Hydroisomerization of Pentane, Hexane, and Heptane for Improving the Octane Number of Gasoline. *J. Catal.* **1999,** *187* (1), 167-176.

81. Demirbas, A.; Balubaid, M. A.; Basahel, A. M.; Ahmad, W.; Sheikh, M. H., Octane Rating of Gasoline and Octane Booster Additives. *Petroleum Science and Technology* **2015,** *33* (11), 1190-1197.

82. Maurice, L. Q.; Lander, H.; Edwards, T.; Harrison, W. E., Advanced aviation fuels: a look ahead via a historical perspective. *Fuel* **2001,** *80* (5), 747-756.

83. Knothe, G., Biodiesel and renewable diesel: A comparison. *Progress in Energy and Combustion Science* **2010,** *36* (3), 364-373.

84. Alam, M. S.; Zeraati-Rezaei, S.; Liang, Z.; Stark, C.; Xu, H.; MacKenzie, A. R.; Harrison, R. M., Mapping and quantifying isomer sets of hydrocarbons ($\geq C_{12}$) in diesel exhaust, lubricating oil and diesel fuel samples using GC × GC-ToF-MS. *Atmospheric Measurement Techniques* **2018,** *11* (5), 3047-3058.

85. Zhang, X.; Huang, Z.; Ferrandon, M.; Yang, D.; Robison, L.; Li, P.; Wang, T. C.; Delferro, M.; Farha, O. K., Catalytic chemoselective functionalization of methane in a metal−organic framework. *Nat. Catal.* **2018,** *1* (5), 356-362.

86. Wood, D. A.; Nwaoha, C.; Towler, B. F., Gas-to-liquids (GTL): A review of an industry offering several routes for monetizing natural gas. *J. Nat. Gas Sci. Eng.* **2012,** *9*, 196-208.

87. Alferov, K. A.; Belov, G. P.; Meng, Y., Chromium catalysts for selective ethylene oligomerization to 1-hexene and 1-octene: Recent results. *Applied Catalysis A: General* **2017,** *542*, 71-124.

88. Hirscher, N. A.; Agapie, T., Stoichiometrically Activated Catalysts for Ethylene Tetramerization using Diphosphinoamine-Ligated Cr Tris(hydrocarbyl) Complexes. *Organometallics* **2017,** *36* (21), 4107-4110.

89. Kissin, Y. V.; Beach, D. L., Oligomerization of ethylene with a homogeneous sulfonated nickel ylide–aluminum alkoxide catalyst. *Journal of Polymer Science Part A: Polymer Chemistry* **1989,** *27* (1), 147-155.

90. McGuinness, D. S., Olefin oligomerization via metallacycles: dimerization, trimerization, tetramerization, and beyond. *Chem Rev* **2011,** *111* (3), 2321-41.

91. Comito, R. J.; Fritzsching, K. J.; Sundell, B. J.; Schmidt-Rohr, K.; Dinca, M., Single-Site Heterogeneous Catalysts for Olefin Polymerization Enabled by Cation Exchange in a Metal-Organic Framework. *J Am Chem Soc* **2016,** *138* (32), 10232-7.

92. Corma, A.; García, H.; Llabrés I Xamena, F. X., Engineering metal organic frameworks for heterogeneous catalysis. *Chem. Rev.* **2010,** *110* (8), 4606-4655.

93. Madrahimov, S. T.; Gallagher, J. R.; Zhang, G.; Meinhart, Z.; Garibay, S. J.; Delferro, M.; Miller, J. T.; Farha, O. K.; Hupp, J. T.; Nguyen, S. T., Gas-Phase Dimerization of Ethylene under Mild Conditions Catalyzed by MOF Materials Containing (bpy)NiII Complexes. *ACS Catal.* **2015,** *5* (11), 6713-6718.

94. Mondloch, J. E.; Bury, W.; Fairen-Jimenez, D.; Kwon, S.; DeMarco, E. J.; Weston, M. H.; Sarjeant, A. A.; Nguyen, S. T.; Stair, P. C.; Snurr, R. Q.; Farha, O. K.; Hupp, J. T., Vapor-phase metalation by atomic layer deposition in a metal-organic framework. *J. Am. Chem. Soc.* **2013,** *135* (28), 10294-7.

95. Deria, P.; Mondloch, J. E.; Karagiaridi, O.; Bury, W.; Hupp, J. T.; Farha, O. K., Beyond post-synthesis modification: evolution of metal-organic frameworks via building block replacement. *Chem Soc Rev* **2014,** *43* (16), 5896-912.

96. Wang, T. C.; Vermeulen, N. A.; Kim, I. S.; Martinson, A. B.; Stoddart, J. F.; Hupp, J. T.; Farha, O. K., Scalable synthesis and post-modification of a mesoporous metal-organic framework called NU-1000. *Nat Protoc* **2016,** *11* (1), 149-62.

97. Gunasekara, T.; Kim, J.; Preston, A.; Steelman, D. K.; Medvedev, G. A.; Delgass, W. N.; Sydora, O. L.; Caruthers, J. M.; Abu-Omar, M. M., Mechanistic Insights into Chromium-Catalyzed Ethylene Trimerization. *ACS Catal.* **2018,** *8* (8), 6810-6819.

98. Liu, L.; Liu, Z.; Cheng, R.; He, X.; Liu, B., Unraveling the Effects of H2, N Substituents and Secondary Ligands on Cr/PNP-Catalyzed Ethylene Selective Oligomerization. *Organometallics* **2018,** *37* (21), 3893-3900.

99. Liu, S.; Zhang, Y.; Han, Y.; Feng, G.; Gao, F.; Wang, H.; Qiu, P., Selective Ethylene Oligomerization with Chromium-Based Metal–Organic Framework MIL-100 Evacuated under Different Temperatures. *Organometallics* **2017,** *36* (3), 632-638.

100. Dolomanov, O. V.; Bourhis, L. J.; Gildea, R. J.; Howard, J. A. K.; Puschmann, H., OLEX2: a complete structure solution, refinement and analysis program. *Journal of Applied Crystallography* **2009,** *42* (2), 339-341.

101. Sheldrick, G. M., A short history of SHELX. *Acta Crystallogr A* **2008,** *64* (Pt 1), 112-22.

102. Sheldrick, G. M., Crystal structure refinement with SHELXL. *Acta Crystallogr C Struct Chem* **2015,** *71* (Pt 1), 3-8.

103. Utracki, L. A., History of commercial polymer alloys and blends (from a perspective of the patent literature). *Polymer Engineering and Science* **1995,** *35* (1), 2-17.

104. Friend, C. M.; Xu, B., Heterogeneous Catalysis: A Central Science for a Sustainable Future. *Acc Chem Res* **2017,** *50* (3), 517-521.

105. Brown, C.; Lita, A.; Tao, Y.; Peek, N.; Crosswhite, M.; Mileham, M.; Krzystek, J.; Achey, R.; Fu, R.; Bindra, J. K.; Polinski, M.; Wang, Y.; van de Burgt, L. J.; Jeffcoat, D.; Profeta, S.; Stiegman, A. E.; Scott, S. L., Mechanism of Initiation in the Phillips Ethylene Polymerization Catalyst: Ethylene Activation by Cr(II) and the Structure of the Resulting Active Site. *ACS Catal.* **2017,** *7* (11), 7442-7455.

106. Zecchina, A.; Groppo, E., Surface chromium single sites: open problems and recent advances. *Proceedings of the Royal Society A: Mathematical, Physical and Engineering Sciences* **2012,** *468* (2143), 2087-2098.

107. Morra, E.; Martino, G. A.; Piovano, A.; Barzan, C.; Groppo, E.; Chiesa, M., In Situ X- and Q-Band EPR Investigation of Ethylene Polymerization on Cr/SiO2 Phillips Catalyst. *The Journal of Physical Chemistry C* **2018,** *122* (37), 21531-21536.

108. McDaniel, M. P., Controlling polymer properties with the Phillips chromium catalysts. *Ind. Eng. Chem. Res.* **2002,** *27* (9), 1559-1564.

109. van Deelen, T. W.; Hernández Mejía, C.; de Jong, K. P., Control of metal-support interactions in heterogeneous catalysts to enhance activity and selectivity. *Nat. Catal.* **2019,** *2* (11), 955-970.

110. Zhou, H. C.; Long, J. R.; Yaghi, O. M., Introduction to metal-organic frameworks. *Chem. Rev.* **2012,** *112* (2), 673-674.

111. Feng, L.; Day, G. S.; Wang, K.-Y.; Yuan, S.; Zhou, H.-C., Strategies for Pore Engineering in Zirconium Metal-Organic Frameworks. *Chem* **2020,** *6* (11), 2902-2923.

112. Islamoglu, T.; Goswami, S.; Li, Z.; Howarth, A. J.; Farha, O. K.; Hupp, J. T., Postsynthetic Tuning of Metal-Organic Frameworks for Targeted Applications. *Acc. Chem. Res.* **2017,** *50* (4), 805-813.

113. Wang, Z.; Cohen, S. M., Postsynthetic modification of metal-organic frameworks. *Chem Soc Rev* **2009,** *38* (5), 1315-29.

114. Song, Y. F.; Cronin, L., Postsynthetic covalent modification of metal-organic framework (MOF) materials. *Angew Chem Int Ed Engl* **2008,** *47* (25), 4635-7.

115. Kirchon, A.; Feng, L.; Drake, H. F.; Joseph, E. A.; Zhou, H. C., From fundamentals to applications: a toolbox for robust and multifunctional MOF materials. *Chem. Soc. Rev.* **2018,** *47* (23), 8611-8638.

116. Furukawa, H.; Cordova, K. E.; O'Keeffe, M.; Yaghi, O. M., The chemistry and applications of metal-organic frameworks. *Science* **2013,** *341* (6149), 1230444.

117. Lin, R.-B.; Xiang, S.; Xing, H.; Zhou, W.; Chen, B., Exploration of porous metal–organic frameworks for gas separation and purification. *Coord. Chem. Rev.* **2019,** *378*, 87-103.

118. Li, H.; Li, L.; Lin, R.-B.; Zhou, W.; Zhang, Z.; Xiang, S.; Chen, B., Porous metal-organic frameworks for gas storage and separation: Status and challenges. *EnergyChem* **2019,** *1* (1).

119. Li, H.; Wang, K.; Sun, Y.; Lollar, C. T.; Li, J.; Zhou, H. C., Recent advances in gas storage and separation using metal–organic frameworks. *Materials Today* **2018,** *21* (2), 108-121.

120. Koo, W.-T.; Jang, J.-S.; Kim, I.-D., Metal-Organic Frameworks for Chemiresistive Sensors. *Chem* **2019,** *5* (8), 1938-1963.

121. Zhang, Y.; Yuan, S.; Day, G.; Wang, X.; Yang, X.; Zhou, H. C., Luminescent sensors based on metal-organic frameworks. *Coord. Chem. Rev.* **2018,** *354* (18), 28-45.

122. Drout, R. J.; Robison, L.; Chen, Z.; Islamoglu, T.; Farha, O. K., Zirconium Metal–Organic Frameworks for Organic Pollutant Adsorption. *Trends in Chemistry* **2019,** *1* (3), 304-317.

123. Dias, E. M.; Petit, C., Towards the use of metal–organic frameworks for water reuse: a review of the recent advances in the field of organic pollutants removal and degradation and the next steps in the field. *J. Mater. Chem. A* **2015,** *3* (45), 22484-22506.

124. Carraro, F.; Chapman, K.; Chen, Z.; Dincă, M.; Easun, T.; Eddaoudi, M.; Farha, O.; Forgan, R.; Gagliardi, L.; Haase, F.; Harris, D.; Kitagawa, S.; Knichal, J.; Lamberti, C.; Lee, J. S. M.; Leus, K.; Li, J.; Lin, W.; Lloyd, G.; Long, J. R.; Lu, C.; Ma, S.; McHugh, L.; Perez, J. P. H.; Ranocchiari, M.; Rosi, N.; Rosseinsky, M.; Ryder, M. R.; Ting, V.; Van Der Veen, M.; Van Der Voort, P.; Volkmer, D.; Walsh, A.; Woods, D.; Yaghi, O. M., Catalysis in MOFs: General discussion. *Faraday Discussions* **2017,** *201*, 369-394.

125. Wang, C.; An, B.; Lin, W., Metal–Organic Frameworks in Solid–Gas Phase Catalysis. *ACS Catal.* **2018,** *9* (1), 130-146.

126. Rimoldi, M.; Howarth, A. J.; DeStefano, M. R.; Lin, L.; Goswami, S.; Li, P.; Hupp, J. T.; Farha, O. K., Catalytic Zirconium/Hafnium-Based Metal–Organic Frameworks. *ACS Catal.* **2016,** *7* (2), 997-1014.

127. Drake, T.; Ji, P.; Lin, W., Site Isolation in Metal-Organic Frameworks Enables Novel Transition Metal Catalysis. *Acc Chem Res* **2018,** *51* (9), 2129-2138.

128. Ren, F.; Ji, P., Recent Advances in the Application of Metal–Organic Frameworks for Polymerization and Oligomerization Reactions. *Catalysts* **2020,** *10* (12).

129. Kirlikovali, K. O.; Chen, Z.; Islamoglu, T.; Hupp, J. T.; Farha, O. K., Zirconium-Based Metal-Organic Frameworks for the Catalytic Hydrolysis of Organophosphorus Nerve Agents. *ACS Appl Mater Interfaces* **2020,** *12* (13), 14702-14720.

130. Liu, Y.; Howarth, A. J.; Vermeulen, N. A.; Moon, S. Y.; Hupp, J. T.; Farha, O. K., Catalytic degradation of chemical warfare agents and their simulants by metal-organic frameworks. *Coord. Chem. Rev.* **2017,** *346*, 101-111.

131. de Koning, M. C.; van Grol, M.; Breijaert, T., Degradation of Paraoxon and the Chemical Warfare Agents VX, Tabun, and Soman by the Metal-Organic Frameworks UiO-66-NH2, MOF-808, NU-1000, and PCN-777. *Inorg Chem* **2017,** *56* (19), 11804-11809.

132. Syed, Z. H.; Chen, Z.; Idrees, K. B.; Goetjen, T. A.; Wegener, E. C.; Zhang, X.; Chapman, K. W.; Kaphan, D. M.; Delferro, M.; Farha, O. K., Mechanistic Insights into C–H Borylation of Arenes with Organoiridium Catalysts Embedded in a Microporous Metal–Organic Framework. *Organometallics* **2020,** *39* (7), 1123-1133.

133. Feng, X.; Song, Y.; Li, Z.; Kaufmann, M.; Pi, Y.; Chen, J. S.; Xu, Z.; Li, Z.; Wang, C.; Lin, W., Metal-Organic Framework Stabilizes a Low-Coordinate Iridium Complex for Catalytic Methane Borylation. *J. Am. Chem. Soc.* **2019,** *141* (28), 11196-11203.

134. Goetjen, T. A.; Liu, J.; Wu, Y.; Sui, J.; Zhang, X.; Hupp, J. T.; Farha, O. K., Metal-organic framework (MOF) materials as polymerization catalysts: a review and recent advances. *Chem. Comm.* **2020,** *56* (72), 10409-10418.

135. Park, H. D.; Comito, R. J.; Wu, Z.; Zhang, G.; Ricke, N.; Sun, C.; Van Voorhis, T.; Miller, J. T.; Román-Leshkov, Y.; Dincă, M., Gas-Phase Ethylene Polymerization by Single-Site Cr Centers in a Metal-Organic Framework. *ACS Catal.* **2020,** *10* (6), 3864-3870.

136. Jongkind, M. K.; Rivera-Torrente, M.; Nikolopoulos, N.; Weckhuysen, B. M., Influence of Pore Structure and Metal-Node Geometry on the Polymerization of Ethylene over Cr-Based Metal-Organic Frameworks. *Chem.* **2021,** *27* (18), 5769-5781.

137. Chen, Y.; Zhang, X.; Wang, X.; Drout, R. J.; Mian, M. R.; Cao, R.; Ma, K.; Xia, Q.; Li, Z.; Farha, O. K., Insights into the Structure-Activity Relationship in Aerobic Alcohol Oxidation over a Metal-Organic-Framework-Supported Molybdenum(VI) Catalyst. *J Am Chem Soc* **2021,** *143* (11), 4302-4310.

138. Zhou, G.; Wang, B.; Cao, R., Acid Catalysis in Confined Channels of Metal-Organic Frameworks: Boosting Orthoformate Hydrolysis in Basic Solutions. *J Am Chem Soc* **2020,** *142* (35), 14848-14853.

139. Syed, Z. H.; Sha, F.; Zhang, X.; Kaphan, D. M.; Delferro, M.; Farha, O. K., Metal–Organic Framework Nodes as a Supporting Platform for Tailoring the Activity of Metal Catalysts. *ACS Catal.* **2020,** *10* (19), 11556-11566.

140. Wasson, M. C.; Buru, C. T.; Chen, Z.; Islamoglu, T.; Farha, O. K., Metal–organic frameworks: A tunable platform to access single-site heterogeneous catalysts. *Applied Catalysis A: General* **2019,** *586* (May), 117214-117214.

141. Otake, K. I.; Ahn, S.; Knapp, J.; Hupp, J. T.; Notestein, J. M.; Farha, O. K., Vapor-Phase Cyclohexene Epoxidation by Single-Ion Fe(III) Sites in Metal-Organic Frameworks. *Inorg Chem* **2021,** *60* (4), 2457-2463.

142. Blitz, J. P.; Diebel, R. E.; Deakyne, C. A.; Christensen, J. M.; Gun'ko, V. M., Experimental and computational studies of trialkylaluminum and alkylaluminum chloride reactions with silica. *J Phys Chem B* **2005,** *109* (12), 5667-77.

143. Champagne, B. t.; Mosley, D. H.; Fripiat, J. G.; Jean-Marie, A.; Bernard, A.; Bettonville, S.; François, P.; Momtaz, A., Dimerization versus complexation of triethylaluminum and diethylaluminum chloride: an ab initio determination of structures, energies of formation, and vibrational spectra. *Journal of Molecular Structure: THEOCHEM* **1998,** *454* (2-3), 149-159.

144. Rottler, R.; Kreiter, C. G.; Fink, G., 13C NMR-spektroskopische Untersuchungen an Äthylaluminiumverbindungen / 13C NMR Spectroscopic Investigations of Ethylaluminium Compounds. *Zeitschrift für Naturforschung B* **1976,** *31* (6), 730-736.

145. Agirrezabal-Telleria, I.; Iglesia, E., Stabilization of active, selective, and regenerable Ni-based dimerization catalysts by condensation of ethene withinordered mesopores. *J. Catal.* **2017,** *352*, 505-514.

146. Agirrezabal-Telleria, I.; Luz, I.; Ortuno, M. A.; Oregui-Bengoechea, M.; Gandarias, I.; Lopez, N.; Lail, M. A.; Soukri, M., Gas reactions under intrapore condensation regime within tailored metal-organic framework catalysts. *Nat Commun* **2019,** *10* (1), 2076.

147. Pollard, M.; Klimke, K.; Graf, R.; Spiess, H. W.; Wilhelm, M.; Sperber, O.; Piel, C.; Kaminsky, W., Observation of Chain Branching in Polyethylene in the Solid State and Melt via 13C NMR Spectroscopy and Melt NMR Relaxation Time Measurements. *Macromolecules* **2004,** *37* (3), 813-825.

148. Kaji, A.; Yamanaka, A.; Murano, M., Structural Analysis of Polyethylene Fibers by Solid State High Resolution NMR; the Distribution of 13C Spin-Lattice Relaxation Times. *Polymer Journal* **1990,** *22* (10), 893-900.

149. Tapash, A.; DesLauriers, P. J.; White, J. L., Simple NMR Experiments Reveal the Influence of Chain Length and Chain Architecture on the Crystalline/Amorphous Interface in Polyethylenes. *Macromolecules* **2015,** *48* (9), 3040-3048.

150. Jarrett, W. L.; Mathias, L. J.; Porter, R. S., Solid-state carbon-13 NMR study of polyethylene reactor powders. *Macromolecules* **2002,** *23* (24), 5164-5166.

151. Mirabella, F. M.; Bafna, A., Determination of the crystallinity of polyethylene/?-olefin copolymers by thermal analysis: Relationship of the heat of fusion of 100% polyethylene crystal and the density. *Journal of Polymer Science Part B: Polymer Physics* **2002,** *40* (15), 1637-1643.

152. Bergstra, M. F.; Weickert, G., Ethylene Polymerization Kinetics with a Heterogeneous Metallocene Catalyst - Comparison of Gas and Slurry Phases. *Macromolecular Materials and Engineering* **2005,** *290* (6), 610-620.

153. Kim, I.; Kim, J. H.; Woo, S. I., Kinetic study of ethylene polymerization by highly active silica supported TiCL4/MgCl2 catalysts. *Journal of Applied Polymer Science* **1990,** *39* (4), 837-854.

154. Gates, D. P.; Svejda, S. A.; Oñate, E.; Killian, C. M.; Johnson, L. K.; White, P. S.; Brookhart, M., Synthesis of Branched Polyethylene Using (α-Diimine)nickel(II) Catalysts: Influence of Temperature, Ethylene Pressure, and Ligand Structure on Polymer Properties. *Macromolecules* **2000,** *33* (7), 2320-2334.

155. Fong, A.; Yuan, Y.; Ivry, S. L.; Scott, S. L.; Peters, B., Computational Kinetic Discrimination of Ethylene Polymerization Mechanisms for the Phillips (Cr/SiO2) Catalyst. *ACS Catal.* **2015,** *5* (6), 3360-3374.

156. Budzelaar, P. H. M., Mechanisms of branch formation in metal-catalyzed ethene polymerization. *Wiley Interdisciplinary Reviews: Computational Molecular Science* **2012,** *2* (2), 221-241.

157. Białek, M., Effect of catalyst composition on chain-end-group of polyethylene produced by salen-type complexes of titanium, zirconium, and vanadium. *Journal of Polymer Science Part A: Polymer Chemistry* **2010,** *48* (14), 3209-3214.

158. Schlogl, R., Heterogeneous catalysis. *Angew Chem Int Ed Engl* **2015,** *54* (11), 3465-520.

159. Descorme, C.; Gallezot, P.; Geantet, C.; George, C., Heterogeneous Catalysis: A Key Tool toward Sustainability. *ChemCatChem* **2012,** *4* (12), 1897-1906.

160. Blaser, H.-U., Heterogeneous catalysis for fine chemicals production. *Catal. Today* **2000,** *60* (3-4), 161-165.

161. Dhakshinamoorthy, A.; Opanasenko, M.; Čejka, J.; Garcia, H., Metal organic frameworks as heterogeneous catalysts for the production of fine chemicals. *Catal. Sci. Technol.* **2013,** *3* (10).

162. Fechete, I.; Wang, Y.; Védrine, J. C., The past, present and future of heterogeneous catalysis. *Catal. Today* **2012,** *189* (1), 2-27.

163. de Vries, J. G.; Jackson, S. D., Homogeneous and heterogeneous catalysis in industry. *Catal. Sci. Technol.* **2012,** *2* (10).

164. Schlexer Lamoureux, P.; Winther, K. T.; Garrido Torres, J. A.; Streibel, V.; Zhao, M.; Bajdich, M.; Abild-Pedersen, F.; Bligaard, T., Machine Learning for Computational Heterogeneous Catalysis. *ChemCatChem* **2019,** *11* (16), 3581-3601.

165. van Leeuwen, P. W. N. M., *Homogeneous Catalysis*. 2004.

166. Delley, M. F.; Nunez-Zarur, F.; Conley, M. P.; Comas-Vives, A.; Siddiqi, G.; Norsic, S.; Monteil, V.; Safonova, O. V.; Coperet, C., Proton transfers are key elementary steps in ethylene polymerization on isolated chromium(III) silicates. *Proc Natl Acad Sci U S A* **2014,** *111* (32), 11624-9.

167. Peters, B.; Scott, S. L.; Fong, A.; Wang, Y.; Stiegman, A. E., Reexamining the evidence for proton transfers in ethylene polymerization. *Proc Natl Acad Sci U S A* **2015,** *112* (31), E4160-1.

168. Delley, M. F.; Nunez-Zarur, F.; Conley, M. P.; Comas-Vives, A.; Siddiqi, G.; Norsic, S.; Monteil, V.; Safonova, O. V.; Coperet, C., Reply to Peters et al.: Proton transfers are plausible initiation and termination steps on Cr(III) sites in ethylene polymerization. *Proc Natl Acad Sci U S A* **2015,** *112* (31), E4162-3.

169. Coperet, C.; Chabanas, M.; Petroff Saint-Arroman, R.; Basset, J. M., Homogeneous and heterogeneous catalysis: bridging the gap through surface organometallic chemistry. *Angew Chem Int Ed Engl* **2003,** *42* (2), 156-81.

170. Coperet, C.; Comas-Vives, A.; Conley, M. P.; Estes, D. P.; Fedorov, A.; Mougel, V.; Nagae, H.; Nunez-Zarur, F.; Zhizhko, P. A., Surface Organometallic and Coordination Chemistry toward Single-Site Heterogeneous Catalysts: Strategies, Methods, Structures, and Activities. *Chem Rev* **2016,** *116* (2), 323-421.

171. Copéret, C.; Fedorov, A.; Zhizhko, P. A., Surface Organometallic Chemistry: Paving the Way Beyond Well-Defined Supported Organometallics and Single-Site Catalysis. *Catalysis Letters* **2017,** *147* (9), 2247-2259.

172. Xu, C.; Fang, R.; Luque, R.; Chen, L.; Li, Y., Functional metal–organic frameworks for catalytic applications. *Coord. Chem. Rev.* **2019,** *388*, 268-292.

173. Liu, J.; Yang, Y.; Goetjen, T. A.; Hupp, J. T., Carbon-efficient conversion of natural gas and natural-gas condensates to chemical products and intermediate feedstocks via catalytic metal–organic framework (MOF) chemistry. *Energy Environ. Sci.* **2022**.

174. Corma, A.; Garcia, H.; Llabres i Xamena, F. X., Engineering metal organic frameworks for heterogeneous catalysis. *Chem Rev* **2010,** *110* (8), 4606-55.

175. Houk, M. K. N.; Kessler, C. A. H. H.; Ley, L. S. V.; Thiem, M. O. J.; Venturi, B. M. T. M.; Wong, P. V. H., Functional metal-organic fameworks: gas storage, separation, and catalysis. 2014; Vol. 2014, pp 8-8.

176. Goetjen, T. A.; Knapp, J. G.; Syed, Z. H.; Hackler, R. A.; Zhang, X.; Delferro, M.; Hupp, J. T.; Farha, O. K., Ethylene polymerization with a crystallographically well-defined metal–organic framework supported catalyst. *Catal. Sci. Technol.* **2022,** *12* (5), 1619-1627.

177. Hall, J. N.; Bollini, P., Structure, characterization, and catalytic properties of open-metal sites in metal organic frameworks. *Reaction Chemistry & Engineering* **2019,** *4* (2), 207-222.

178. O'Keeffe, M.; Peskov, M. A.; Ramsden, S. J.; Yaghi, O. M., The Reticular Chemistry Structure Resource (RCSR) database of, and symbols for, crystal nets. *Acc. Chem. Res.* **2008,** *41* (12), 1782-9.

179. Yuan, N.; Pascanu, V.; Huang, Z.; Valiente, A.; Heidenreich, N.; Leubner, S.; Inge, A. K.; Gaar, J.; Stock, N.; Persson, I.; Martin-Matute, B.; Zou, X., Probing the Evolution of Palladium Species in Pd@MOF Catalysts during the Heck Coupling Reaction: An Operando X-ray Absorption Spectroscopy Study. *J Am Chem Soc* **2018,** *140* (26), 8206-8217.

180. Braglia, L.; Borfecchia, E.; Maddalena, L.; Øien, S.; Lomachenko, K. A.; Bugaev, A. L.; Bordiga, S.; Soldatov, A. V.; Lillerud, K. P.; Lamberti, C., Exploring structure and reactivity of Cu sites in functionalized UiO-67 MOFs. *Catal. Today* **2017,** *283*, 89-103.

181. Liu, L.; Meira, D. M.; Arenal, R.; Concepcion, P.; Puga, A. V.; Corma, A., Determination of the Evolution of Heterogeneous Single Metal Atoms and Nanoclusters under Reaction Conditions: Which Are the Working Catalytic Sites? *ACS Catal* **2019,** *9* (12), 10626-10639.

182. Bucior, B. J.; Rosen, A. S.; Haranczyk, M.; Yao, Z.; Ziebel, M. E.; Farha, O. K.; Hupp, J. T.; Siepmann, J. I.; Aspuru-Guzik, A.; Snurr, R. Q., Identification Schemes for Metal–Organic Frameworks To Enable Rapid Search and Cheminformatics Analysis. *Cryst. Growth Des.* **2019,** *19* (11), 6682-6697.

183. Dashti, A.; Mazloumi, S. H.; Akbari, A.; Ahadiyan, H. R.; Emami, A. R., Solubility of Ethene in n-Hexane and n-Heptane as Common Slurry-Phase Polymerization Solvents: Experimental Measurement and Modeling. *J. Chem. Eng. Data* **2016,** *61* (1), 693-697.

184. Ravel, B.; Newville, M., ATHENA, ARTEMIS, HEPHAESTUS: data analysis for X-ray absorption spectroscopy using IFEFFIT. *J Synchrotron Radiat* **2005,** *12* (Pt 4), 537-41.

185. de Jong, K. P., General Aspects. In *Synthesis of Solid Catalysts*, 2009; pp 1-11.

186. Cui, W.-G.; Zhang, G.-Y.; Hu, T.-L.; Bu, X.-H., Metal-organic framework-based heterogeneous catalysts for the conversion of C1 chemistry: CO, CO2 and CH4. *Coord. Chem. Rev.* **2019,** *387*, 79-120.

187. Wang, Q.; Astruc, D., State of the Art and Prospects in Metal-Organic Framework (MOF)-Based and MOF-Derived Nanocatalysis. *Chem. Rev.* **2020,** *120* (2), 1438-1511.

188. Hall, J. N.; Bollini, P., Low-Temperature, Ambient Pressure Oxidation of Methane to Methanol Over Every Tri-Iron Node in a Metal-Organic Framework Material. *Chem.* **2020,** *26* (70), 16639-16643.

189. Wen, X.; Guan, J., Recent progress on MOF-derived electrocatalysts for hydrogen evolution reaction. *Applied Materials Today* **2019,** *16*, 146-168.

190. Yang, Q.; Xu, Q.; Jiang, H. L., Metal-organic frameworks meet metal nanoparticles: synergistic effect for enhanced catalysis. *Chem Soc Rev* **2017,** *46* (15), 4774-4808.

191. Falcaro, P.; Ricco, R.; Yazdi, A.; Imaz, I.; Furukawa, S.; Maspoch, D.; Ameloot, R.; Evans, J. D.; Doonan, C. J., Application of metal and metal oxide nanoparticles@MOFs. *Coord. Chem. Rev.* **2016,** *307*, 237-254.

192.   Astruc, D., Introduction: Nanoparticles in Catalysis. *Chem Rev* **2020,** *120* (2), 461-463.

193.   Bartholomew, C. H., Mechanisms of catalyst deactivation. *Applied Catalysis A: General* **2001,** *212* (1-2), 17-60.

194.   Goodman, E. D.; Johnston-Peck, A. C.; Dietze, E. M.; Wrasman, C. J.; Hoffman, A. S.; Abild-Pedersen, F.; Bare, S. R.; Plessow, P. N.; Cargnello, M., Supported Catalyst Deactivation by Decomposition into Single Atoms Is Suppressed by Increasing Metal Loading. *Nat Catal* **2019,** *2*.

195.   Otor, H. O.; Steiner, J. B.; García-Sancho, C.; Alba-Rubio, A. C., Encapsulation Methods for Control of Catalyst Deactivation: A Review. *ACS Catal.* **2020,** *10* (14), 7630-7656.

196.   Thiam, Z.; Abou-Hamad, E.; Dereli, B.; Liu, L.; Emwas, A. H.; Ahmad, R.; Jiang, H.; Isah, A. A.; Ndiaye, P. B.; Taoufik, M.; Han, Y.; Cavallo, L.; Basset, J. M.; Eddaoudi, M., Extension of Surface Organometallic Chemistry to Metal-Organic Frameworks: Development of a Well-Defined Single Site [(identical withZr-O-)W(horizontal lineO)(CH2(t)Bu)3] Olefin Metathesis Catalyst. *J Am Chem Soc* **2020,** *142* (39), 16690-16703.

197.   Korzynski, M. D.; Consoli, D. F.; Zhang, S.; Roman-Leshkov, Y.; Dinca, M., Activation of Methyltrioxorhenium for Olefin Metathesis in a Zirconium-Based Metal-Organic Framework. *J Am Chem Soc* **2018,** *140* (22), 6956-6960.

198.   Temkin, O. N., "Golden Age" of Homogeneous Catalysis Chemistry of Alkynes: Dimerization and Oligomerization of Alkynes. *Kinetics and Catalysis* **2020,** *60* (6), 689-732.

199.   Janiak, C., Metallocene and related catalysts for olefin, alkyne and silane dimerization and oligomerization. *Coord. Chem. Rev.* **2006,** *250* (1-2), 66-94.

200.   Borodziński, A.; Bond, G. C., Selective Hydrogenation of Ethyne in Ethene-Rich Streams on Palladium Catalysts. Part 1. Effect of Changes to the Catalyst During Reaction. *Catalysis Reviews* **2006,** *48* (2), 91-144.

201.   Borodziński, A.; Bond, G. C., Selective Hydrogenation of Ethyne in Ethene-Rich Streams on Palladium Catalysts, Part 2: Steady-State Kinetics and Effects of Palladium Particle Size, Carbon Monoxide, and Promoters. *Catalysis Reviews* **2008,** *50* (3), 379-469.

202.   Makshina, E. V.; Dusselier, M.; Janssens, W.; Degreve, J.; Jacobs, P. A.; Sels, B. F., Review of old chemistry and new catalytic advances in the on-purpose synthesis of butadiene. *Chem Soc Rev* **2014,** *43* (22), 7917-53.

203.   Li, C.; Luo, J.; Zhang, Q.; Xie, J.; Zhang, J.; Dai, B., Cu(II)Cu(I)/AC Catalysts for Gas–Solid Acetylene Dimerization. *Ind. Eng. Chem. Res.* **2019,** *59* (1), 110-117.

204.   Redfern, L. R.; Li, Z.; Zhang, X.; Farha, O. K., Highly Selective Acetylene Semihydrogenation Catalyzed by Cu Nanoparticles Supported in a Metal–Organic Framework. *ACS Applied Nano Materials* **2018,** *1* (9), 4413-4417.

205.   Redfern, L. R.; Lo, W. S.; Dillingham, I. J.; Eatman, J. G.; Mian, M. R.; Tsung, C. K.; Farha, O. K., Enhancing Four-Carbon Olefin Production from Acetylene over Copper Nanoparticles in Metal-Organic Frameworks. *ACS Appl Mater Interfaces* **2020,** *12* (28), 31496-31502.

206.   Jung, H.-J.; Cho, Y.; Kim, D.; Mehrkhodavandi, P., Cationic aluminum, gallium, and indium complexes in catalysis. *Catal. Sci. Technol.* **2021,** *11* (1), 62-91.

207.   Sharma, S. K.; Paul, B.; Pal, R. S.; Bhanja, P.; Banerjee, A.; Samanta, C.; Bal, R., Influence of Indium as a Promoter on the Stability and Selectivity of the Nanocrystalline Cu/CeO2

Catalyst for CO2 Hydrogenation to Methanol. *ACS Appl Mater Interfaces* **2021,** *13* (24), 28201-28213.

208. Loza, K.; Heggen, M.; Epple, M., Synthesis, Structure, Properties, and Applications of Bimetallic Nanoparticles of Noble Metals. *Advanced Functional Materials* **2020,** *30* (21).

209. Duan, M.; Jiang, L.; Zeng, G.; Wang, D.; Tang, W.; Liang, J.; Wang, H.; He, D.; Liu, Z.; Tang, L., Bimetallic nanoparticles/metal-organic frameworks: Synthesis, applications and challenges. *Applied Materials Today* **2020,** *19*.

210. Lu, J.; Elam, J. W.; Stair, P. C., Synthesis and stabilization of supported metal catalysts by atomic layer deposition. *Acc Chem Res* **2013,** *46* (8), 1806-15.

211. Kappers, M. J.; van der Maas, J. H., Correlation between CO frequency and Pt coordination number. A DRIFT study on supported Pt catalysts. *Catalysis Letters* **1991,** *10* (5-6), 365-373.

212. Bazin, D.; Bensaddik, A.; Briois, V.; Sainctavit, P., Multiple Scattering Calculation of Absorption Spectrum and Diffraction Calculation: Application to Nanometer Scale Copper Metallic Particle. *Le Journal de Physique IV* **1996,** *06* (C4), C4-481-C4-485.

213. Marinkovic, N. S.; Sasaki, K.; Adzic, R. R., Determination of Single- and Multi-Component Nanoparticle Sizes by X-ray Absorption Spectroscopy. *Journal of The Electrochemical Society* **2018,** *165* (15), J3222-J3230.

214. Beale, A. M.; Weckhuysen, B. M., EXAFS as a tool to interrogate the size and shape of mono and bimetallic catalyst nanoparticles. *Phys Chem Chem Phys* **2010,** *12* (21), 5562-74.

215. Wang, H.; Dong, X.; Lin, J.; Teat, S. J.; Jensen, S.; Cure, J.; Alexandrov, E. V.; Xia, Q.; Tan, K.; Wang, Q.; Olson, D. H.; Proserpio, D. M.; Chabal, Y. J.; Thonhauser, T.; Sun, J.; Han, Y.; Li, J., Topologically guided tuning of Zr-MOF pore structures for highly selective separation of C6 alkane isomers. *Nat Commun* **2018,** *9* (1), 1745.

216. Feng, X.; Ren, Y.; Jiang, H., Metal-bipyridine/phenanthroline-functionalized porous crystalline materials: Synthesis and catalysis. *Coord. Chem. Rev.* **2021,** *438*.

217. Øien, S.; Agostini, G.; Svelle, S.; Borfecchia, E.; Lomachenko, K. A.; Mino, L.; Gallo, E.; Bordiga, S.; Olsbye, U.; Lillerud, K. P.; Lamberti, C., Probing Reactive Platinum Sites in UiO-67 Zirconium Metal–Organic Frameworks. *Chem. Mater.* **2015,** *27* (3), 1042-1056.

218. Li, J.; Liao, J.; Ren, Y.; Liu, C.; Yue, C.; Lu, J.; Jiang, H., Palladium Catalysis for Aerobic Oxidation Systems Using Robust Metal-Organic Framework. *Angew Chem Int Ed Engl* **2019,** *58* (48), 17148-17152.

219. Li, B.; Ju, Z.; Zhou, M.; Su, K.; Yuan, D., A Reusable MOF-Supported Single-Site Zinc(II) Catalyst for Efficient Intramolecular Hydroamination of o-Alkynylanilines. *Angew Chem Int Ed Engl* **2019,** *58* (23), 7687-7691.

220. Fei, H.; Cohen, S. M., A robust, catalytic metal-organic framework with open 2,2'-bipyridine sites. *Chem Commun (Camb)* **2014,** *50* (37), 4810-2.

221. Faaij, A., Modern Biomass Conversion Technologies. *Mitigation and Adaptation Strategies for Global Change* **2006,** *11* (2), 343-375.

222. Gallezot, P., Conversion of biomass to selected chemical products. *Chem Soc Rev* **2012,** *41* (4), 1538-58.

223. Maki-Arvela, P.; Simakova, I. L.; Salmi, T.; Murzin, D. Y., Production of lactic acid/lactates from biomass and their catalytic transformations to commodities. *Chem Rev* **2014,** *114* (3), 1909-71.

224. Alonso, D. M.; Bond, J. Q.; Dumesic, J. A., Catalytic conversion of biomass to biofuels. *Green Chemistry* **2010,** *12* (9).

225. Wang, F.; Wen, Y.; Fang, Y.; Ji, H., Synergistic Production of Methyl Lactate from Carbohydrates Using an Ionic Liquid Functionalized Sn-Containing Catalyst. *ChemCatChem* **2018,** *10* (18), 4154-4161.

226. Weingarten, R.; Kim, Y. T.; Tompsett, G. A.; Fernández, A.; Han, K. S.; Hagaman, E. W.; Conner, W. C.; Dumesic, J. A.; Huber, G. W., Conversion of glucose into levulinic acid with solid metal(IV) phosphate catalysts. *J. Catal.* **2013,** *304*, 123-134.

227. Kuwahara, Y.; Kaburagi, W.; Nemoto, K.; Fujitani, T., Esterification of levulinic acid with ethanol over sulfated Si-doped ZrO2 solid acid catalyst: Study of the structure–activity relationships. *Applied Catalysis A: General* **2014,** *476*, 186-196.

228. Li, S.; Wang, Y.; Yang, Y.; Chen, B.; Tai, J.; Liu, H.; Han, B., Conversion of levulinic acid to γ-valerolactone over ultra-thin TiO2 nanosheets decorated with ultrasmall Ru nanoparticle catalysts under mild conditions. *Green Chemistry* **2019,** *21* (4), 770-774.

229. Hu, X.; Li, C.-Z., Levulinic esters from the acid-catalysed reactions of sugars and alcohols as part of a bio-refinery. *Green Chemistry* **2011,** *13* (7).

230. Fernandes, D. R.; Rocha, A. S.; Mai, E. F.; Mota, C. J. A.; Teixeira da Silva, V., Levulinic acid esterification with ethanol to ethyl levulinate production over solid acid catalysts. *Applied Catalysis A: General* **2012,** *425-426*, 199-204.

231. Yadav, G. D.; Yadav, A. R., Synthesis of ethyl levulinate as fuel additives using heterogeneous solid superacidic catalysts: Efficacy and kinetic modeling. *Chem. Eng. J.* **2014,** *243*, 556-563.

232. Ogino, I.; Suzuki, Y.; Mukai, S. R., Esterification of levulinic acid with ethanol catalyzed by sulfonated carbon catalysts: Promotional effects of additional functional groups. *Catal. Today* **2018,** *314*, 62-69.

233. Chang, C.; Xu, G.; Jiang, X., Production of ethyl levulinate by direct conversion of wheat straw in ethanol media. *Bioresour Technol* **2012,** *121*, 93-9.

234. Nandiwale, K. Y.; Bokade, V. V., Esterification of Renewable Levulinic Acid ton-Butyl Levulinate over Modified H-ZSM-5. *Chemical Engineering & Technology* **2015,** *38* (2), 246-252.

235. Patil, C. R.; Niphadkar, P. S.; Bokade, V. V.; Joshi, P. N., Esterification of levulinic acid to ethyl levulinate over bimodal micro–mesoporous H/BEA zeolite derivatives. *Catalysis Communications* **2014,** *43*, 188-191.

236. Dharne, S.; Bokade, V. V., Esterification of levulinic acid to n-butyl levulinate over heteropolyacid supported on acid-treated clay. *Journal of Natural Gas Chemistry* **2011,** *20* (1), 18-24.

237. Ramli, N. A. S.; Sivasubramaniam, D.; Amin, N. A. S., Esterification of Levulinic Acid Using ZrO2-Supported Phosphotungstic Acid Catalyst for Ethyl Levulinate Production. *BioEnergy Research* **2017,** *10* (4), 1105-1116.

238. Yan, K.; Wu, G.; Wen, J.; Chen, A., One-step synthesis of mesoporous H4SiW12O40-SiO2 catalysts for the production of methyl and ethyl levulinate biodiesel. *Catalysis Communications* **2013,** *34*, 58-63.

239. Enumula, S. S.; Gurram, V. R. B.; Chada, R. R.; Burri, D. R.; Kamaraju, S. R. R., Clean synthesis of alkyl levulinates from levulinic acid over one pot synthesized WO3-SBA-16 catalyst. *Journal of Molecular Catalysis A: Chemical* **2017,** *426*, 30-38.

240. Cui, X.; Chen, K.; Xing, H.; Yang, Q.; Krishna, R.; Bao, Z.; Wu, H.; Zhou, W.; Dong, X.; Han, Y.; Li, B.; Ren, Q.; Zaworotko, M. J.; Chen, B., Pore chemistry and size control in hybrid porous materials for acetylene capture from ethylene. *Science* **2016,** *353* (6295), 141-4.

241. Yaghi, O. M.; O'Keeffe, M.; Ockwig, N. W.; Chae, H. K.; Eddaoudi, M.; Kim, J., Reticular synthesis and the design of new materials. *Nature* **2003,** *423* (6941), 705-14.

242. Chen, Z.; Hanna, S. L.; Redfern, L. R.; Alezi, D.; Islamoglu, T.; Farha, O. K., Reticular chemistry in the rational synthesis of functional zirconium cluster-based MOFs. *Coord. Chem. Rev.* **2019,** *386*, 32-49.

243. Adil, K.; Belmabkhout, Y.; Pillai, R. S.; Cadiau, A.; Bhatt, P. M.; Assen, A. H.; Maurin, G.; Eddaoudi, M., Gas/vapour separation using ultra-microporous metal-organic frameworks: insights into the structure/separation relationship. *Chem Soc Rev* **2017,** *46* (11), 3402-3430.

244. Bai, Y.; Dou, Y.; Xie, L. H.; Rutledge, W.; Li, J. R.; Zhou, H. C., Zr-based metal-organic frameworks: design, synthesis, structure, and applications. *Chem Soc Rev* **2016,** *45* (8), 2327-67.

245. Yang, Q.; Vaesen, S.; Ragon, F.; Wiersum, A. D.; Wu, D.; Lago, A.; Devic, T.; Martineau, C.; Taulelle, F.; Llewellyn, P. L.; Jobic, H.; Zhong, C.; Serre, C.; De Weireld, G.; Maurin, G., A water stable metal-organic framework with optimal features for CO2 capture. *Angew Chem Int Ed Engl* **2013,** *52* (39), 10316-20.

246. Liao, P. Q.; Huang, N. Y.; Zhang, W. X.; Zhang, J. P.; Chen, X. M., Controlling guest conformation for efficient purification of butadiene. *Science* **2017,** *356* (6343), 1193-1196.

247. Cui, Y.; Yue, Y.; Qian, G.; Chen, B., Luminescent functional metal-organic frameworks. *Chem Rev* **2012,** *112* (2), 1126-62.

248. Kreno, L. E.; Leong, K.; Farha, O. K.; Allendorf, M.; Van Duyne, R. P.; Hupp, J. T., Metal-organic framework materials as chemical sensors. *Chem Rev* **2012,** *112* (2), 1105-25.

249. Hu, Z.; Deibert, B. J.; Li, J., Luminescent metal-organic frameworks for chemical sensing and explosive detection. *Chem Soc Rev* **2014,** *43* (16), 5815-40.

250. Zhang, T.; Lin, W., Metal-organic frameworks for artificial photosynthesis and photocatalysis. *Chem Soc Rev* **2014,** *43* (16), 5982-93.

251. Chughtai, A. H.; Ahmad, N.; Younus, H. A.; Laypkov, A.; Verpoort, F., Metal-organic frameworks: Versatile heterogeneous catalysts for efficient catalytic organic transformations. *Chem. Soc. Rev.* **2015,** *44* (19), 6804-6849.

252. Valekar, A. H.; Cho, K.-H.; Chitale, S. K.; Hong, D.-Y.; Cha, G.-Y.; Lee, U. H.; Hwang, D. W.; Serre, C.; Chang, J.-S.; Hwang, Y. K., Catalytic transfer hydrogenation of ethyl levulinate to γ-valerolactone over zirconium-based metal–organic frameworks. *Green Chemistry* **2016,** *18* (16), 4542-4552.

253. Rojas-Buzo, S.; Garcia-Garcia, P.; Corma, A., Catalytic Transfer Hydrogenation of Biomass-Derived Carbonyls over Hafnium-Based Metal-Organic Frameworks. *ChemSusChem* **2018,** *11* (2), 432-438.

254. Xie, W.; Wan, F., Basic ionic liquid functionalized magnetically responsive Fe3O4@HKUST-1 composites used for biodiesel production. *Fuel* **2018,** *220*, 248-256.

255. Chen, J.; Liu, R.; Guo, Y.; Chen, L.; Gao, H., Selective Hydrogenation of Biomass-Based 5-Hydroxymethylfurfural over Catalyst of Palladium Immobilized on Amine-Functionalized Metal–Organic Frameworks. *ACS Catal.* **2014,** *5* (2), 722-733.

256. Cirujano, F. G.; Corma, A.; Llabrés i Xamena, F. X., Conversion of levulinic acid into chemicals: Synthesis of biomass derived levulinate esters over Zr-containing MOFs. *Chemical Engineering Science* **2015,** *124*, 52-60.

257. Song, J. Y.; Ahmed, I.; Seo, P. W.; Jhung, S. H., UiO-66-Type Metal-Organic Framework with Free Carboxylic Acid: Versatile Adsorbents via H-bond for Both Aqueous and Nonaqueous Phases. *ACS Appl Mater Interfaces* **2016,** *8* (40), 27394-27402.

258. Xie, W.; Yang, X.; Hu, P., Cs2.5H0.5PW12O40 Encapsulated in Metal–Organic Framework UiO-66 as Heterogeneous Catalysts for Acidolysis of Soybean Oil. *Catalysis Letters* **2017,** *147* (11), 2772-2782.

259. Xie, W.; Wan, F., Immobilization of polyoxometalate-based sulfonated ionic liquids on UiO-66-2COOH metal-organic frameworks for biodiesel production via one-pot transesterification-esterification of acidic vegetable oils. *Chem. Eng. J.* **2019,** *365*, 40-50.

260. Jiang, J.; Yaghi, O. M., Bronsted acidity in metal-organic frameworks. *Chem Rev* **2015,** *115* (14), 6966-97.

261. Miao, Z.; Qi, C.; Wensley, A. M.; Luan, Y., Development of a novel Brønsted acid UiO-66 metal–organic framework catalyst by postsynthetic modification and its application in catalysis. *RSC Advances* **2016,** *6* (71), 67226-67231.

262. Yang, F.; Huang, H.; Wang, X.; Li, F.; Gong, Y.; Zhong, C.; Li, J.-R., Proton Conductivities in Functionalized UiO-66: Tuned Properties, Thermogravimetry Mass, and Molecular Simulation Analyses. *Cryst. Growth Des.* **2015,** *15* (12), 5827-5833.

263. Wang, F.; Chen, Z.; Chen, H.; Goetjen, T. A.; Li, P.; Wang, X.; Alayoglu, S.; Ma, K.; Chen, Y.; Wang, T.; Islamoglu, T.; Fang, Y.; Snurr, R. Q.; Farha, O. K., Interplay of Lewis and Bronsted Acid Sites in Zr-Based Metal-Organic Frameworks for Efficient Esterification of Biomass-Derived Levulinic Acid. *ACS Appl Mater Interfaces* **2019,** *11* (35), 32090-32096.

264. Zheng, A.; Huang, S. J.; Liu, S. B.; Deng, F., Acid properties of solid acid catalysts characterized by solid-state 31P NMR of adsorbed phosphorous probe molecules. *Phys Chem Chem Phys* **2011,** *13* (33), 14889-901.